A Ph.D. dissertation on

GLOBAL DAMAGE INDICES FOR RC STRUCTURES: A NUMERICAL RESPONSE-DRIVEN TRAINING APPROACH

submitted by

Subhadip Naskar

DEPARTMENT OF CIVIL ENGINEERING
INDIAN INSTITUTE OF TECHNOLOGY GUWAHATI
ASSAM, INDIA

September 2023

A Ph.D. dissertation on

GLOBAL DAMAGE INDICES FOR RC STRUCTURES: A NUMERICAL RESPONSE-DRIVEN TRAINING APPROACH

in Partial Fulfillment of the Requirements
for the Degree of
DOCTOR OF PHILOSOPHY

submitted by

Subhadip Naskar

DEPARTMENT OF CIVIL ENGINEERING
INDIAN INSTITUTE OF TECHNOLOGY GUWAHATI
ASSAM, INDIA
September 2023

Declaration

I hereby declare that the works presented in this thesis entitled **"Global Damage Indices for RC Structures: A Numerical Response-Driven Training Approach"**, submitted in partial fulfillment of the requirement for the award of the degree of *Doctor of Philosophy (Ph.D.)* in *Department of Civil Engineering* with the specialization in *Structural Engineering*, is an original record of my own research works carried out at the Indian Institute of Technology Guwahati under the supervision of *Dr. Sandip Das* and *Dr. Hemant B. Kaushik*, Department of Civil Engineering, IIT Guwahati.

The research output embodied in this thesis work has not been submitted by me for the award of any other degree, diploma associate-fellowship, fellowship or its equivalent to any University or Institute.

Date: September 13, 2023
Place: Guwahati

Subhadip Naskar

Subhadip Naskar
Research Scholar
Department of Civil Engineering
Indian Institute of Technology Guwahati
Pin - 781039, Assam, India

Certificate

It is certified that the work contained in the dissertation entitled **"Global Damage Indices for RC Structures: A Numerical Response-Driven Training Approach"**, by **Subhadip Naskar (156104037)** for the partial fulfillment of the requirements for the award of the *Doctor of Philosophy (Ph.D.)* in *Department of Civil Engineering* with the specialization in *Structural Engineering* at the Indian Institute of Technology Guwahati, India is an authentic work. This work has been carried out under our sole supervisions, and it has not been submitted elsewhere for the award of a degree.

Date: September 13, 2023
Place: Guwahati

Dr. Sandip Das
Associate Professor
Department of Civil Engineering
Indian Institute of Technology Guwahati
Pin - 781039, Assam, India

Dr. Hemant B. Kaushik
Professor
Department of Civil Engineering
Indian Institute of Technology Guwahati
Pin - 781039, Assam, India

Acknowledgements

As I stand at the culmination of this educational voyage that has spanned years, the sentiment of Swami Vivekananda in his own words *"Education is the manifestation of the perfection already in man"* resonate deeply in my mind. This journey of knowledge has been a revelation of the latent potential within, a journey not only of academic growth but also of personal transformation. I am acutely aware that this achievement is the harmonious symphony of efforts, sacrifices, and unwavering support from a constellation of individuals.

In the realm of academia, the significance of mentors is immeasurable. Foremost, I extend my heartfelt gratitude and utmost appreciation to my esteemed supervisors, *Dr. Sandip Das* and *Dr. Hemant B. Kaushik*. They have stood as the navigators of the most crucial expedition of my life through the ocean of knowledge. Their profound grasp of the technical subjects, combined with their dedication to cultivating my potential, has illuminated my path through the intricate landscape of research. Their mentorship has extended beyond academics, enriching my intellectual and personal growth. I am particularly thankful to *Dr. Sandip Das*, as his ideology and way of life have truly helped me become a better version of myself as a human being in reality.

In addition to my supervisors, I extend my gratitude to the members of my Doctoral Committee: *Dr. Anjan Dutta*, *Dr. Arunasis Chakraborty*, and *Dr. Satyajit Panda*. Their insights, suggestions, and guidance have greatly contributed to the continuous improvement of this thesis. Moreover, I sincerely acknowledge the scholarship from the Ministry of Education, Government of India, and IIT Guwahati, India, which greatly aided the successful thesis completion.

At IIT Guwahati, the academic community cultivates an environment where knowledge thrives. Engaging dialogues, collaborative endeavours, and shared intellectual pursuits among my peers have significantly deepened my comprehension and expanded my perspectives. A heartfelt commendation to my friends at NDT Laboratory who have fostered a blend of free-spirited camaraderie and healthy competition, making this journey both enjoyable and memorable in myriad ways.

As Rabindranath Tagore eloquently put it, *"The butterfly counts not month but moments, and has time enough."* Each moment of learning and growth has been nurtured by the strength of my family. The blessings of my parents have been a constant source of strength, with their unconditional belief and encouragement fostering a foundation since my childhood. The love and wisdom of my elder sisters have illuminated my life. They have consistently shown me the significance of embracing the journey of life itself, transcending the focus solely on the ultimate destination. Furthermore, I extend a heartfelt toast to my beloved nieces and endearing daughter, whose presence has infused my life with boundless joy and wonderful moments.

In the journey of life, my wife has stood as my steadfast pillar of support. Her patience, profound understanding, and unshakable faith in my dreams have provided sustenance during moments of adversity. Her encouragement, even when faced with my self-doubt, has been the wind beneath my wings. She has shared not only in the victories but also in the struggles, reminding me that every step forward is a step closer to my aspirations.

This thesis is dedicated to the people who lost their lives due to earthquakes

Abstract

The seismic damage index (SDI) is mainly used to quantify the earthquake-induced damage at the local and global levels for civil structures. Such quantification of damage has various practical applications in structural engineering, such as assessing post-earthquake damage conditions of a structure, predicting seismic performances for novel types of structures with great importance, damage-based seismic design, and carrying out reliability studies of existing structures. Researchers have developed several SDI models for different types of material, i.e., homogeneous material (e.g., steel), heterogeneous material (e.g., reinforced concrete or RC), and composite material. However, the scope of the present research work is limited to RC buildings only.

The SDIs are generally classified as local damage index (LDI) and global damage index (GDI) based on whether an SDI quantifies damage at the local level (i.e., section or member) or the global level (i.e., an assemblage of members or complete structure), respectively. Among the available LDIs (non-cumulative, cumulative and combined), the combined ones are more comprehensive as they can capture the structural damage due to maximum and cyclic deformations for any ground motion. The computation of the GDI of a structure using such LDI involves using any suitable weighted average method based on dissipated hysteresis energy at each section or gravity loads at each member. Generally, the demand parameters used for computing combined LDIs (and GDIs) are required at the section level (e.g., sectional stress and strain resultants, dissipated hysteresis energy) obtained through nonlinear time-history analysis. Therefore, the available combined SDI models rely exclusively on sectional responses and do not consider global responses (e.g., the lateral behaviour of floors). Nowadays, different sensors are available to record global dynamic responses for structures with satisfactory accuracy and precision during an earthquake. So, there is a scope to develop a new combined GDI evaluation method which utilizes such recorded data and bypasses the requirement of numerically obtained sectional responses. For the new GDI evaluation method to be viable like other existing SDI models, it should successfully predict the damage state for a structure due to any seismic event.

For computing structural damage using any SDI model, the required inputs are obtained either through direct experimental observations (for very limited cases) or through responses of the representative finite element model, which is essentially calibrated with some experimental results. Usually, the response of a finite element model is preferred for estimating damage index (especially using combined damage models) because the collection of compulsory dynamic responses for real-life structures due to earthquakes is not always possible. In this case, the acceptability of the computed damage index depends on the authenticity of the experimental results with which the corresponding finite element model is calibrated. The lateral behaviour of a building is highly dependent on the lateral load-deformation be-

haviour of columns, which is generally obtained experimentally by considering a cantilever column of half the length of the actual one based on a symmetric double-curvature deformation profile. For most of the available experimental setups regarding such axially loaded cantilever columns due to unidirectional or bidirectional horizontal loading(s), the true cantilever behaviour is altered due to the undesirable orientations of the actuators, and the fixing arrangements between the actuator heads and the free end of the column during the experiment. Therefore, rectifying the experimentally obtained load-deformation curve through some mechanics-based formulation to get the true lateral behaviour is obligatory. The rectified curve for the cantilever column should be used to calibrate the material properties associated with a representative finite element model. Finally, the finite element models for different structures incorporating the material properties calibrated with the rectified (or true) lateral load-deformation curve must be used to find LDI and GDI values.

Based on the above discussions, the primary objectives of this dissertation work are to address the necessity of rectifying experimental data obtained for axially loaded cantilever columns due to quasi-static horizontal loading and the development of novel combined GDI evaluation method for RC buildings equipped with floor response measuring sensors. Therefore, a novel mechanics-based formulation is proposed in this thesis to get the true lateral load-deformation behaviour for cantilever columns subjected to constant axial load and unidirectional lateral load by identifying the effects of fixity and interactions between the actuators and the specimen. An overall underestimation and overestimation of lateral strength and lateral displacement capacity for cantilever columns are observed if the experimental data are not rectified. The analytical models for predicting the lateral load-deformation behaviour of the columns can be calibrated using the rectified data without changing the experimentally obtained material properties. Also, the proposed formulation can directly identify the yield parameters for a column, which are required for quantification of SDI subsequently.

A novel method for predicting combined GDI for instrumented RC buildings utilizing the recorded floor-displacement data during earthquakes (along with some readily obtainable structural capacity terms) is attempted in the present research work. For two-dimensional (2D) RC frames, two different combined 2D GDI formulae are proposed to predict the GDI obtained from the dissipated hysteresis energy-based weighted average of the modified Park and Ang local damage model. The difference in those formulae is the type of capacity parameter required (i.e., displacement ductility or curvature ductility of columns). Further, the scope of the proposed method is extended for three-dimensional (3D) RC buildings by introducing another two combined 3D GDI formulae, which can accommodate the effect of structural responses considering biaxial bending and axial load due to bidirectional ground motions. These two 3D GDI formulae can predict the GDI computed through the biaxial dissipated hysteresis energy-based weighted average of the three-dimensional extension of the modified Park and Ang local damage model. The main advantage of applying the new GDI formulae is that they do not need dynamic responses from any complex and time-consuming nonlinear

time-history analysis. Explicit expressions for the global damage coefficients (available in the new GDI formulae) are also provided in terms of structural properties (e.g., fundamental period, total building height, total bay widths along orthogonal directions, number of floors and bays) and the local soil type for wider applicability of the GDI formulae.

Finally, the performances of the new formulae to predict the global damage states based on post-disaster restoration of a building (i.e., no damage, repairable, irreparable and collapse) from the estimated GDI values are cross-checked and found satisfactory. For 2D GDI formulae, the global damage states are checked using the available limiting values for GDI obtained from the modified Park and Ang damage model. In the case of 3D GDI formulae, the limiting values for GDI are established in the absence of any such limiting ranges in the literature to connect the global damage states with the physical damage conditions for the structural members. The performances of 3D GDI formulae are checked using the established limiting values.

Table of Contents

List of Figures

List of Tables

Nomenclature

All abbreviations and symbols used in the present research work are enlisted here along with their definitions. The symbols used for literature review in Chapter 1 and mathematical formulae in Appendix A are excluded from the following lists.

List of Abbreviations

2D	Two-dimensional, *see* Page 4
3D	Three-dimensional, *see* Page 4
DOF	Degree of freedom, *see* Page 29
DSCBGM	Design spectrum-compatible bidirectional ground motion, *see* Page 82
DSCUGM	Design spectrum-compatible unidirectional ground motion, *see* Page 54
GDC	Global damage coefficient, *see* Page 26
GDI	Global damage index, *see* Page 3
GF	Ground floor, *see* Page 55
LDI	Local damage index, *see* Page 3
PSA	Pseudo spectral acceleration, *see* Page 58
RC	Reinforced concrete, *see* Page 2
SDOF	Single degree of freedom, *see* Page 8

List of Greek Symbols

α	Angle between horizontal actuator and horizontal axis, *see* Page 33
α_s	Level of significance considered for statistical tests, *see* Page 68
$\bar{\mu}_d(s\Delta t)$	Normalized global displacement ductility factor for 3D RC building at time $s\Delta t$, *see* Page 90
$\bar{\mu}_{\phi_n}$	Weighted average (based on the axial load demand of columns due to gravity loads) of curvature ductility values for all columns situated between Floor n and Floor $(n-1)$ of 2D RC frame, *see* Page 63
$\bar{\mu}_{\phi}$	Weighted average (based on the axial load demand of columns due to gravity loads) of curvature ductility values for all columns present in 2D

	RC frame, *see* Page 63
$\bar{\mu}_{\phi}(s\Delta t)$	Curvature ductility factor for 3D RC building at time $s\Delta t$, *see* Page 94
$\bar{\mu}_{d_n}$	Weighted average (based on the axial load demand of columns due to gravity loads) of displacement ductility values for all columns situated between Floor n and Floor $(n-1)$ of 2D RC frame, *see* Page 61
$\bar{\mu}_{\phi,m}$	Maximum curvature ductility factor for 3D RC building, *see* Page 94
$\bar{\mu}_{\phi_n}^{(x)}, \bar{\mu}_{\phi_n}^{(y)}$	Weighted average (based on the axial load demand of columns due to gravity loads) of curvature ductility values for all columns situated between Floor n and Floor $(n-1)$ corresponding to global x- and y-directions, respectively, for 3D RC building, *see* Page 95
$\bar{\mu}_{\phi}^{(x)}, \bar{\mu}_{\phi}^{(y)}$	Weighted average (based on the axial load demand of columns due to gravity loads) of curvature ductility values for all columns corresponding to global x- and y-directions, respectively, for 3D RC building, *see* Page 95
$\bar{\mu}_{d,m}$	Maximum normalized global displacement ductility factor for 3D RC building, *see* Page 89
$\bar{\mu}_{d_n}^{(x)}, \bar{\mu}_{d_n}^{(y)}$	Weighted average (based on the axial load demand of columns due to gravity loads) of displacement ductility values for all columns situated between Floor n and Floor $(n-1)$ along x- and y-directions, respectively, of 3D RC building, *see* Page 93
β_{KRL}	Non-negative parameter in modified Park and Ang-type 2D local damage model [1] representing the energy-based strength degradation of material in the case of cyclic loading, *see* Page 11
Δ_e, Δ_p	Elastic and plastic portions of Δ, respectively, *see* Page 33
δ_h	Incremental displacement readings of horizontal actuator, *see* Page 34
Δt	Small-time interval for recorded displacement data, *see* Page 60
$\Delta u_n(s\Delta t)$	Difference between the absolute interstory drifts of Floor n and Floor $(n-1)$ at time $s\Delta t$ and $(s-1)\Delta t$ along x-direction of 3D RC building, *see* Page 91
$\Delta v_n(s\Delta t)$	Difference between the absolute interstory drifts of Floor n and Floor $(n-1)$ at time $s\Delta t$ and $(s-1)\Delta t$ along y-direction of 3D RC building, *see* Page 91
Δ	Lateral displacement of cantilever column tip, *see* Page 31
Δ'	Displacement of cantilever column due to tip moment, M, *see* Page 41
Δ'_e	$\Delta_e/\cos\theta_p$, *see* Page 36
Δ_r	Rectified lateral displacement of cantilever column, *see* Page 41
δ_v	Incremental displacement readings of vertical actuator, *see* Page 36
Δ_{L_c}	Vertical displacement of cantilever column tip during total deformation, *see* Page 33

ϵ_u	Strains corresponding to ultimate stress of steel, *see* Page 48
$\epsilon_{cu}, \epsilon_{cc}$	Unconfined and confined concrete strains at f_{cu} and f_{cc}, respectively, *see* Page 48
ϵ_{sh}	Strains corresponding to initial strain hardening of steel, *see* Page 48
$\kappa_1, \kappa_2, \cdots, \kappa_{11}$	Regression coefficients associated with global damage coefficients for proposed 2D GDI formulae, *see* Page 71
$\kappa_{12}, \kappa_{13}, \cdots, \kappa_{55}$	Regression coefficients associated with global damage coefficients for proposed 3D GDI formulae, *see* Page 104
$\lambda_{2D\text{-}1}, \psi_{2D\text{-}1}$	Regression coefficients (or GDCs) for $GDI_{2D\text{-}1}$, *see* Page 60
$\lambda_{2D\text{-}2}, \psi_{2D\text{-}2}, \gamma_{2D\text{-}2}$	Regression coefficients (or GDCs) for $GDI_{2D\text{-}2}$, *see* Page 63
$\lambda_{3D\text{-}1}, \psi_{3D\text{-}1}$	Regression coefficients (or GDCs) for $GDI_{3D\text{-}1}$, *see* Page 89
$\lambda_{3D\text{-}2}, \psi_{3D\text{-}2}, \gamma_{3D\text{-}2}$	Regression coefficients (or GDCs) for $GDI_{3D\text{-}2}$, *see* Page 94
$\mu_{\phi_n}^{(d)}$	Curvature ductility value for dth column situated between Floor n and Floor $(n-1)$ of 2D RC frame, *see* Page 63
$\mu_{d_n}^{(d)}$	Displacement ductility value for dth column between Floor n and Floor $(n-1)$ of 2D RC frame, *see* Page 61
$\mu_{\phi_n}^{(d,x)}, \mu_{\phi_n}^{(d,y)}$	Curvature ductility values for dth column situated between Floor n and Floor $(n-1)$ corresponding to global x- and y-directions, respectively, for 3D RC building, *see* Page 95
$\mu_{d_n}^{(d,x)}, \mu_{d_n}^{(d,y)}$	Displacement ductility values for dth column situated between Floor n and Floor $(n-1)$ along x- and y-directions, respectively, of 3D RC building, *see* Page 93
$\omega_n(t)$	Rotational DOF associated with nth floor $(n \geq 1)$ of 3D RC building, *see* Page 83
ρ_a	Actual axial stress ratio, *see* Page 31
ρ_d	Design axial stress ratio, *see* Page 31
ρ_{SM}	Spearman's rank correlation coefficient between a particular new GDI formula and the corresponding target modified Park and Ang global damage model, *see* Page 70
θ_e, θ_p	Elastic and plastic portions of θ, respectively, *see* Page 33
θ	Tip rotation of cantilever column, *see* Page 31
φ	Angle between vertical actuator and vertical axis, *see* Page 35
ϑ	Angle oriented from $\ddot{u}_g(t)$ to $\ddot{r}_g(t, \vartheta)$ in the counterclockwise sense, *see* Page 87
ξ, η, ζ	Indices to represent various null and alternative hypotheses corresponding to explicit expressions of GDCs, *see* Page 73

List of Roman Symbols

(x, y, z)	Right-handed Cartesian coordinate system, *see* Page 56
$\ddot{r}_g(t, \vartheta)$	Time-history of resultant of $\ddot{u}_g(t)$ and $\ddot{v}_g(t)$ along the direction making an angle of ϑ with $\ddot{u}_g(t)$ in counterclockwise sense, *see* Page 87
$\ddot{u}_g(t), \ddot{v}_g(t)$	Time-histories of bidirectional ground motion recorded along two orthogonal horizontal directions, *see* Page 87
$\det(\bullet)$	Determinant of a matrix, *see* Page 37
$\mathbf{K_e}$	Elastic stiffness matrix of cantilever column, *see* Page 36
$\mathbf{K_g}$	Geometric stiffness matrix of cantilever column, *see* Page 36
$\mathbf{K}$	$\mathbf{K_e} + \mathbf{K_g}$, *see* Page 37
SE$(\bullet)$	Standard error, *see* Page 69
RotDnn	nnth percentile value of response parameter associated with the resultant motion of the recorded bidirectional ground motion for all orientations ranging from 0° to 180°, *see* Page 87
$\overline{GDI}^{(j,k)}_{2D\text{-ST}}$	Mean of all $GDI_{2D\text{-ST}}$ values in the case of the jth soil type and the kth 2D RC frame, *see* Page 68
$\tilde{x}_{2D\text{-}i}, \tilde{y}_{2D\text{-}i}$	Numerical values of independent variables present in the ith 2D GDI formula, *see* Page 69
$\tilde{x}_{3D\text{-}i}, \tilde{y}_{3D\text{-}i}$	Numerical values of independent variables present in the ith 3D GDI formula, *see* Page 103
$\widetilde{GDI}_{3D\text{-GWLZD}}$	Normalized value of $GDI_{3D\text{-GWLZD}}$ for 3D RC building, *see* Page 99
a_1, a_2, a_3, a_4	Geometric parameters depending on each incremental load-step during cantilever column experiment used in the new mechanics-based formulation for the purpose of deformation compatibility, *see* Page 34
a_5, a_6, a_7	Geometric parameters depending on each incremental load-step during cantilever column experiment used in the new mechanics-based formulation for the purposes of constitutive laws and equilibrium equations, *see* Page 38
A_c	Area of column cross-section, *see* Page 31
b	Width of cantilever column stub, *see* Page 33
b_1, b_2, b_3, b_4	Trigonometric parameters depending on each incremental load-step during cantilever column experiment used in the new mechanics-based formulation for the purposes of constitutive laws and equilibrium equations, *see* Page 38
c	$\theta_e L_c / \Delta_e$, *see* Page 37
c_0	Initial value of the parameter c, *see* Page 39
c_1, c_2	Indices to represent all possible linear regression models considered for explicit expressions of various GDCs associated with 2D GDI formulae, *see* Page 71

c_3, c_4, c_5	Indices to represent all possible linear regression models considered for explicit expressions of various GDCs associated with 3D GDI formulae, *see* Page 104
C_{frame}	Total number of columns present at each floor of 2D RC frame, *see* Page 61
C_{building}	Total number of columns present at each floor of 3D RC building, *see* Page 93
$C_{\phi}(s\Delta t)$	Overall curvature ductility-based capacity of 3D RC building at time $s\Delta t$, *see* Page 94
$C_{\phi_n}(s\Delta t)$	Curvature ductility-based capacity for Floor n of 3D RC building at time $s\Delta t$, *see* Page 94
$C_{d_n}(s\Delta t)$	Displacement ductility-based capacity for Floor n of 3D RC building at time $s\Delta t$, *see* Page 89
d	Index to represent columns of a particular floor for 2D RC frame, *see* Page 61
d_b	Maximum diameter (in m) of longitudinal reinforcement in a beam or a column, *see* Page 33
$D^2_{d_n}(s\Delta t)$	Displacement-based demand for Floor n of 3D RC building at time $s\Delta t$, *see* Page 89
E_c	Elastic modulus of concrete, *see* Page 36
E_s	Initial elastic modulus of steel, *see* Page 48
$E_{2D\text{-}h_p}$	Total dissipated hysteresis energy due to uniaxial bending associated with pth plastic hinge location in a 2D RC frame, *see* Page 64
$E_{3D\text{-}h_p}$	Total dissipated hysteresis energy due to biaxial bending associated with pth plastic hinge location in a 3D RC building, *see* Page 96
E_{sh}	Initial strain hardening modulus of steel, *see* Page 48
F	Force reading of horizontal actuator, *see* Page 33
f_0	F-test statistic value, *see* Page 68
f_c	Actual compressive strength of concrete cube, *see* Page 31
F_H, F_V	Horizontal and vertical components of F, respectively, *see* Page 33
$F_n^{(d)}$	Axial load demand due to gravity loads for the dth column between Floor n and Floor $(n-1)$ of 2D RC frame or 3D RC building, *see* Page 61
F_r	Frame ratio for 2D RC frame, *see* Page 71
f_u	Ultimate strength of steel, *see* Page 48
f_y	Yield strength of steel, *see* Page 33
f_{α_s}	Value of the percentage point of the F-distribution at the α_s level of significance, *see* Page 68
f_{ck}	Characteristic (design) compressive strength of concrete cube, *see* Page 31
f_{cr}	Modulus of rupture of concrete, *see* Page 37

f_{cu}, f_{cc}	Unconfined and confined compressive strengths of concrete, respectively, *see* Page 48
g	Index to represent individual data available in regression dataset, *see* Page 68
$g(\bullet)$	Algebraic function, *see* Page 71
$GDI_{2D\text{-}1}$	Proposed global damage index formula based on displacement ductility of columns for 2D RC frame, *see* Page 60
$GDI_{2D\text{-}2}$	Proposed global damage index formula based on curvature ductility of columns for 2D RC frame, *see* Page 63
$GDI_{2D\text{-}ST}$	Global damage index estimated through dissipated hysteresis energy-based weighted average of modified Park and Ang-type local damage model [1] for 2D RC frame, *see* Page 64
$GDI_{3D\text{-}1}$	Proposed global damage index formula based on displacement ductility of columns for 3D RC building, *see* Page 89
$GDI_{3D\text{-}2}$	Proposed global damage index formula based on curvature ductility of columns for 3D RC building, *see* Page 94
$GDI_{3D\text{-}GWLZD}$	Global damage index estimated through dissipated hysteresis energy-based weighted average of modified Park and Ang-type local damage model [2] for 3D RC building, *see* Page 96
H	Net horizontal force at cantilever column tip, *see* Page 36
h	Height of each story in 2D RC frame or 3D RC building, *see* Page 55
H_0	Null hypothesis for ANOVA test, *see* Page 68
h_1	Length of vertical actuator heads, *see* Page 35
h_2	Lengths of horizontal actuator heads, *see* Page 33
H_a	Alternative hypothesis for ANOVA test, *see* Page 68
h_v	Distance between cantilever column tip and bottom of vertical actuator, *see* Page 35
h_{total}	Total height of 2D RC frame or 3D RC building, *see* Page 56
i	Index to represent proposed 2D or 3D GDI formulae, *see* Page 65
I_e	Effective moment of inertia for cantilever column, *see* Page 36
I_{cr}, I_t	Crack and transformed moment of inertia for cantilever column, respectively, *see* Page 37
j	Index to represent the type of soil, *see* Page 65
k	Index to represent the training 2D RC frames or 3D RC buildings, *see* Page 65
K_{ij}	Element of $\mathbf{K}$ corresponding to ith row and jth column, *see* Page 37
l	Length of each bay in 2D RC frame, *see* Page 55
L_c	Length of cantilever column, *see* Page 33
L_h	Initial length of horizontal actuators, *see* Page 34

L_o	Length of cantilever column participating in elasto-plastic deformation, *see* Page 33
L_p	Plastic hinge length of a beam or a column, *see* Page 33
L_v	Initial length of vertical actuators, *see* Page 36
l_x, l_y	Length of each bay along x- and y-directions, respectively, in 3D RC building, *see* Page 83
$l_{x,\text{total}}, l_{y,\text{total}}$	Total width of bays along x- and y-directions, respectively, for 3D RC building, *see* Page 84
$LDI_{2D\text{-ST}}$	Modified Park and Ang-type local damage index model [1] for 2D RC frame, *see* Page 11
$LDI_{3D-\text{GWLZD}}$	Modified Park and Ang-type local damage index model [2] for 3D RC building, *see* Page 17
M	Net moment at cantilever column tip, *see* Page 36
m	Index used to represent bays for 2D RC frame, *see* Page 55
M_F	Moment at cantilever column tip due to eccentricity of horizontal actuator, *see* Page 33
M_P	Moment at cantilever column tip due to eccentricity of vertical actuator, *see* Page 35
M_{cr}	Cracked moment capacity for column cross-section, *see* Page 37
$M_{O'}$	Moment acting at lumped plastic hinge location of cantilever column, *see* Page 37
N	Axial compressive load, *see* Page 31
n	Index used to represent floors for 2D RC frame and 3D RC building, *see* Page 55
N_b	Number of bays available in 2D RC frame, *see* Page 55
N_s	Number of storeys available in 2D RC frame or 3D RC building, *see* Page 55
N_{bx}, N_{by}	Number of bays available along x- and y-directions, respectively, in 3D RC building, *see* Page 82
P	Force reading of vertical actuator, *see* Page 35
p	Index to represent plastic hinge locations for 2D RC frame and 3D RC building, *see* Page 64
P_h	Total number of plastic hinge locations, *see* Page 64
P_H, P_V	Horizontal and vertical components of P, respectively, *see* Page 35
q	Total number of data points in regression dataset, *see* Page 68
r	Ratio between the elastic lateral and total lateral displacements of cantilever column, *see* Page 32
r_0	Initial value of the parameter r, *see* Page 39
R_0, cR_1, cR_2	Parameters used in `Steel02` controlling stress-strain transition during

	elastic to plastic behaviour, *see* Page 47
R_1, R_2, R_3	Parameters used in `ReinforcingSteel` controlling stress-strain transition during elastic to plastic behaviour, *see* Page 83
$r_n(s\Delta t)$	Resultant displacement value for Floor n of 3D RC building at time $s\Delta t$, *see* Page 93
$R^2_{\text{adj.}}$	Adjusted R^2 value for multilinear regression analysis, *see* Page 70
$R^2_{\text{pred.}}$	Predicted R^2 value for multilinear regression analysis, *see* Page 70
R_{d1}, R_{d2}, R_{d3}	Building dimensional ratios for 3D RC building, *see* Page 104
$r_{N_s,u}(s\Delta t)$	Resultant global ultimate displacement for 3D RC building at time $s\Delta t$, *see* Page 90
$r_{N_s,y}(s\Delta t)$	Resultant global yield displacement for 3D RC building at time $s\Delta t$, *see* Page 90
R_{s1}, R_{s2}, R_{s3}	Building shape ratios for 3D RC building, *see* Page 104
S	Parameter representing local soil type, *see* Page 71
s	Index to represent incremental time-steps, *see* Page 60
S_d	Spectral displacement values corresponding to the fundamental period, T_p, obtained using IS 1893: 2016 [3], *see* Page 61
$S_d^{\prime(x)}, S_d^{\prime(y)}$	Spectral displacement values corresponding to fundamental periods, $T_p^{\prime(x)}$ and $T_p^{\prime(y)}$, respectively, obtained using IS 1893: 2016 [3], *see* Page 95
$S_d, S_d^{\prime}$	Spectral displacement value corresponding to the fundamental period, $T_p^{\prime}$, obtained using IS 1893: 2016 [3], *see* Page 63
$S_d^{(x)}, S_d^{(y)}$	Spectral displacement values corresponding to fundamental periods, $T_p^{(x)}$ and $T_p^{(y)}$, respectively, obtained using IS 1893: 2016 [3], *see* Page 93
$T_p^{\prime}$	Fundamental period of 2D RC frame obtained from eigen analysis by assuming the frame as shear frame with masses lumped at each floor, *see* Page 63
t_0	Student's t-test statistic value, *see* Page 69
T_d	Total duration of displacement time-history record for instrumented RC frame or building, *see* Page 60
T_p	Fundamental period of 2D RC frame obtained using eigenvalue analysis of the corresponding finite element model, *see* Page 61
$T_p^{\prime}$	Fundamental period of torsionally uncoupled 3D RC building obtained using eigenvalue analysis of the building assuming two translational and one in-plane rotational DOFs are attached at the center of mass for each floor, *see* Page 96
$T_p^{\prime(x)}, T_p^{\prime(y)}$	Fundamental periods of 3D RC building along x- and y-directions, respectively, obtained using eigenvalue analysis of the building assuming two translational and one in-plane rotational DOFs are attached at the center of mass for each floor, *see* Page 95

$T_p^{(x)}, T_p^{(y)}$	Fundamental periods of 3D RC building along x- and y-directions, respectively, obtained using eigenvalue analysis of the corresponding finite element model, *see* Page 93
$t_{\alpha_s/2}$	Value of the percentage point of the Student's t-distribution at the $\alpha_s/2$ level of significance, *see* Page 69
$u_n(s\Delta t)$	Displacement values recorded at Floor n along x-direction of 2D RC Frames or 3D RC building, at time $s\Delta t$, *see* Page 60
$u_n(t)$	Translational DOF along x-direction associated with nth floor ($n \geqslant 1$) of 2D RC frame and 3D RC building, *see* Page 55
u_u, u_y	Ultimate displacement and yield displacement values, respectively, along x-direction for 2D RC frame and 3D RC building, *see* Page 60
V	Net vertical force at cantilever column tip, *see* Page 36
v	Number of GDCs present in proposed GDI formula, *see* Page 68
$v_n(s\Delta t)$	Displacement values recorded at Floor n along y-direction of 3D RC building, respectively, at time $s\Delta t$, *see* Page 91
$v_n(t)$	Translational DOF along y-direction associated with nth floor ($n \geq 1$) of 3D RC building, *see* Page 83
v_u, v_y	Ultimate displacement and yield displacement values, respectively, along y-direction for 3D RC building, *see* Page 90
w	Number of independent variables used in proposed GDI formulae, *see* Page 68
y_t	Distance between centroidal axis and extreme tension fiber of transformed column section, *see* Page 37
z_c	Distance (in m) from critical section to point of contraflexure for a beam or a column, *see* Page 33

1. Introduction and State-of-Art

Contents

1.1 General Overview

Earthquakes are one of the most powerful and destructive natural forces on Earth. There are evidences of triggering other secondary natural disasters due to earthquakes. For example, the earthquakes occurred at Chile (1960) [4], Northern Sumatra (2004) [5] and Japan (2011) [6] were responsible for devastating tsunamis and floods affecting the areas near the surrounding oceans, the earthquakes at Hawaii (1868, 1975) [7, 8] and Philippines (1990) [9] triggered volcanic eruptions, whereas the earthquakes at southern Alaska (1964) [10], Mount St. Helens (1980) [11] and Los Angeles (1994) [12] caused massive landslides and avalanches. Therefore, earthquakes are responsible for relatively more human life and economic losses, among other natural hazards. According to World Health Organization [13], during 1998-2017, more people were affected (either directly or indirectly) by earthquakes than the total number of people affected by all other natural hazards. The growth of the human population and rapid urbanization, especially in the seismically active regions, will only increase such losses in the future [14]. Besides life loss, earthquakes can impact the socio-economic condition of a region/country by disrupting essential and life-saving services through damage to critical structures, e.g., bridges, highways, power plants, underground and underwater pipelines, sewerage systems, communication facilities, and hospitals. Studying the reasons and extent of structural damages due to past earthquakes will help to minimize human life loss and monetary loss in future seismic events. Therefore, research works on structural damages became very common a long time back, and such research

introduced many new advanced engineering subjects, e.g., damage quantification using seismic damage indices [15–17], damage detection (or identification) through structural health monitoring [18–21], construction of new earthquake-resistant engineering structures through performance-based structural design methodology [22–25]. Although those subjects are interconnected with each other, the focus of this thesis will be on the damage quantification of reinforced concrete (RC) structures.

Damage function can be defined as a non-decreasing and non-dimensional formula for quantifying the damage state of a structure or its components using some representative state variables (or damage parameters) [26]. Therefore, the selected state variables must describe the evolution of the real state of structural degradation due to seismic loading [27]. The state variables are generally related to inelastic deformation at section or member-level (e.g., strain, curvature, rotation) or at structural-level (e.g., horizontal floor-displacement, interstory drift), stress resultant (e.g., base shear, member force), energy dissipated during cyclic loading. A damage function incorporates specific state variables to permit indications of the proximity of some limit states in structures such as collapse. The numerical value represented by the damage function at a particular stage of seismic loading is considered the seismic damage index (SDI). Usually, the values of SDIs range from 0 for an undamaged structure to 1 for a structure near or at collapse, with intermediate values representing different states of damage (e.g., minor damage, moderate damage, severe damage). SDI is mainly used to scale the level of structural damage or identify the damage state of structure, along with some other applications [28–30] in

(i) *performance-based seismic design of structures* to obtain an economical design by allowing some structural damage within repairable range due to large and less frequent earthquakes,

(ii) *structural health monitoring* for numerical representation of damage of an identified damaged location,

(iii) *post-earthquake damage assessment* [31–33] to determine required measures for repair and/or strengthening of a structure based on its performance due to the earthquake,

(iv) *reliability studies of existing structures due to future earthquake scenarios* [34] to decide the necessity of structural strengthening as a pre-earthquake damage prevention strategy,

(v) *development of optimal intensity measures* [35–38] by correlating ground motion parameters with engineering demand parameters, and

(vi) *preparedness and planning for disasters* [39–41] by predicting plausible cost, amount of vulnerable casualties, number of required temporary accommodation due to earthquake vis-à-vis structural damage estimation.

1.2 Literature Reviews

1.2.1 Seismic Damage Indices for RC Structures

The earthquake-induced damage to any structure is governed by the load-deformation relationship of the structure, the amount of inelastic deformation, and the characteristics (e.g., temporal and frequency contents) of ground motions. Based on these governing factors, several SDI models as a systematic approach to quantify the extent of seismic damage sustained by structures or their members have been proposed by many researchers for the last fifty years. Different well-documented papers, reports, state-of-the-art reviews about the development of those damage models are available in the literature [15–17, 25, 26, 28, 42–45]. The existing SDIs can be classified following different types of approach as described below.

(i) **Classification based on the type of structural material properties:** (a) damage index for homogeneous material, e.g., steel [46–55], (b) damage index for heterogeneous material, e.g., reinforced concrete, or (c) damage index for composite material [26, 56–61]. Further explorations of damage indices for steel and other metals, and composite materials are not in the scope of this dissertation works, and therefore, the SDIs applicable for RC structures only will be discussed in this thesis.

(ii) **Classification based on the definition of the damage index:** (a) capacity-demand type damage index [62–68], or (b) degradation type damage index [16, 69–75]. The demand associated with a specific damage parameter (e.g., deformation, energy) due to seismic loading is related to the corresponding capacity of a member or a structure in the case of the former type of damage index, whereas the degradation of a structure is quantified via relating the value of specific damage parameter (e.g., strength, stiffness, modal parameters, dissipated energy) to a predefined threshold value (representing the structural collapse) in the case of the latter type of damage index.

(iii) **Classification based on the part of the structure whose damage is determined:** (a) local damage index or LDI, or (b) global damage index or GDI. LDI is associated with the damage that occurred at the local level, i.e., sections of a member or a single member itself, whereas GDI is associated with the damage that occurred at the global level, i.e., a storey in a building, sub-assemblage of members or substructure, whole structure. LDIs usually incorporate a single or combination of damage parameters. GDIs are computed using global parameters, modal parameters [76–78] considering two modes [79] or more, some suitable weighing functions [66, 80–83] on LDI values of individual members. Some damage parameter such as displacement ductility can be utilized both as LDI when associated with a member, or GDI when associated with complete structure. On the other hand, other damage parameters such as curvature ductility or interstory drift can only be used as either LDI or GDI. It is

obvious that the accuracy of the estimated damage index decreases as one shift from a critical region (such as plausible plastic hinge location of RC member) to the structure in its entirety [29].

(iv) **Classification based on the type of damage parameter's value, i.e., maximum or cyclic, incorporated in the (local) damage index:** (a) non-cumulative LDI, (b) cumulative LDI, or (c) combined LDI. At the initial stage of developing SDIs, the non-cumulative LDIs were introduced based on peak absolute deformation (usually normalized to the corresponding yield deformation, i.e., ductility terms such as displacement ductility, rotational ductility, curvature ductility) or maximum values of any other suitable damage parameter. Later, the cumulative LDIs are developed to compute accumulated damage due to plastic deformation through dissipation of hysteresis energy during cyclic loading. Finally, combined LDIs (as their name suggests) are introduced to consider the effects of both maximum and cyclic deformations due to seismic loading on the total structural damage.

(v) **Classification based on the mathematical formulation used to compute the damage index:** (a) deterministic damage index, or (b) probabilistic damage index [53, 77, 79, 84, 85]. The probabilistic formulation is a more rigorous choice to get the damage index because of the uncertainties involved in seismic action and the behaviour of RC members against cyclic loading are accounted for by this formulation. On the other hand, deterministic formulation offers a more straightforward evaluation of damage based on predetermined criteria without considering variations in input parameters. Despite its disadvantage arising from no uncertainty characterization, the deterministic formulation is explored predominantly mainly because of its direct applicability to damage assessment and seismic design of structures at the expense of less computational cost.

(vi) **Classification based on the dimension of the structural model whose numerical responses are utilized to get the damage index:** (a) two-dimensional or 2D seismic damage index, or (b) three-dimensional or 3D seismic damage index. Frameworks for most of the developed SDIs utilize the structural responses (incorporating the effect of uniaxial bending and axial load) obtained from a representative 2D finite element model subjected to unidirectional ground motion. However, due to bidirectional ground motions, such damage indices cannot capture the actual extent of the damage that occurred in a real (3D) building. Therefore, a few research groups proposed 3D SDI models by combining the effects of biaxial bending and axial loading on structural damages either at member level [44, 86, 87] or cross-section level [2].

(vii) **Classification based on the function of the part whose damage is quantified:** (a) structural damage index, or (b) non-structural damage index [88–92]. Although

most of the developed SDIs concentrate on the damage occurred in structural members due to their utmost importance for active participation in the load-transfer mechanism, several researchers have introduced damage index models applicable for non-structural elements (e.g., partition walls, cladding members, false ceilings, various necessary installations for different functionality). Because the cost of the non-structural members exceeds around three-fourths of the total cost of the corresponding building, especially for hospital or commercial buildings [92], also, non-structural members such as masonry infill panels cannot follow the overall deformation profile of RC structural system, and therefore, necessitates the development of separate suitable SDI model.

(viii) **Classification based on the purpose for quantifying the damage occurred:** (a) structural damage index, or (b) economic or financial damage index [93–98]. Structural damage index is mainly used to study the performance of a structure due to earthquake(s) in terms of sustained damages and predict its vulnerability for future earthquake scenarios in terms of reserved strength, whereas economic damage index is typically used for deciding insurance policies for a structure against seismic activities. The economic damage index is generally represented as the repair cost ratio to the corresponding replacement cost for a member or a structure. Therefore, its value might exceed unity while a structure is not physically collapsed.

(ix) **Classification based on the type of analysis required:** for computing the existing structural damage indices, structural responses obtained using either numerical analysis (static/dynamic and linear elastic/inelastic) or no analysis, i.e., alternative approaches without any analysis (e.g., in-situ measurements, on-site observations) is mandatory. Inelastic dynamic analysis should be incorporated to find SDI for a structure as it can capture post-yield nonlinear responses of a structure (or its member) due to time-varying seismic loading. However, other types of analysis are also explored, especially when the engineering judgement and computational framework for carrying out nonlinear time-history analysis for multi-storey RC building other than flexure-dominated plane frames are highly demanding. Also, 'no analysis' refers to the damage index represented as a function of earthquake measures (i.e., magnitude or intensity).

A detailed literature review of different types of available SDI models based on the classification strategies mentioned above is beyond the scope of this dissertation work. Figure 1.1 is a succinct representation of various SDIs based on different classification strategies suitable for establishing the scope of the current research works. In this figure, structural SDI is first classified according to the dimension of the required structural model for which the damage index would be computed. Then the SDIs are classified according to the damage calculated at which part of the structural model. Further, 2D LDI models are classified according to

the type of damage parameter's value, whereas 2D GDI models are classified according to the types of weighing functions and global response parameters. Different types of 2D LDI models are also classified according to the type of state variables used in the models. Finally, 3D LDI models are classified according to the methodology for combining the effects of bi-axial bending and axial loading developed due to bidirectional ground motions. Necessary references of the research works associated with different types of SDIs considered in the present works are provided in Figure 1.1 for the sake of completeness.

1.2.1.1 Local damage index for 2D RC frames

Non-cumulative LDI

The earliest development of damage indices originated from the simple ductility concept, which refers to the ratio between the maximum and yield values of a particular parameter. Newmark and Rosenblueth [99] considered different types of ductility factors (displacement ductility, rotational ductility and curvature ductility) to quantify the damage. Banon et al. [70], and Roufaiel and Meyer [100] modified the expression of rotational ductility considering concentrated plastic hinge and the finite size of the plastic region, respectively. The curvature ductility can be applied (instead of rotational ductility) when the yielding of a member does not occur due to anti-symmetric bending. However, the curvature ductility can be applied to the most damaged section along the length of a member and not to the member as a whole [28]. Blejwas and Bresler [63] introduced a capacity-demand type damage index with normalized deformation terms. Powell and Allahabadi [65], and Cosenza et al. [101] introduced different displacement ductility-based normalized damage functionals.

Shibata and Sozen [69] introduced the stiffness parameter as a state variable for the first time. They represented damage in terms of the ratio between the initial tangent stiffness (calculated using the assumption of anti-symmetric bending) and the reduced secant stiffness corresponding to the maximum curvature obtained from the moment-curvature relationship. Later, Kunnath and Jenne [103] and Khashaee [104] attempted some modifications to the stiffness-based damage index, and Carrillo [105] extended the scope of the stiffness-based damage index for RC structural walls. Although these indices can incorporate some effect of cyclic loading in terms of final stiffness and strength degradation, it fails to consider the impact of the sequence of applied loading and the pinching effect due to high shear stress. Banon et al. [70] have used stiffness terms related to ultimate and maximum curvatures to represent flexural damage ratio, a better damage indicator than rotational and curvature ductility. Later, Roufaiel and Meyer [71] proposed a modified flexural damage ratio to consider the effect of strength degradation (along with stiffness degradation) by removing stiffness value associated with recoverable curvature from the reduced secant stiffness values associated with maximum and ultimate curvatures during cyclic loading. The flexural damage ratio and its modified version do not consider the effect of cumulative damage obtained

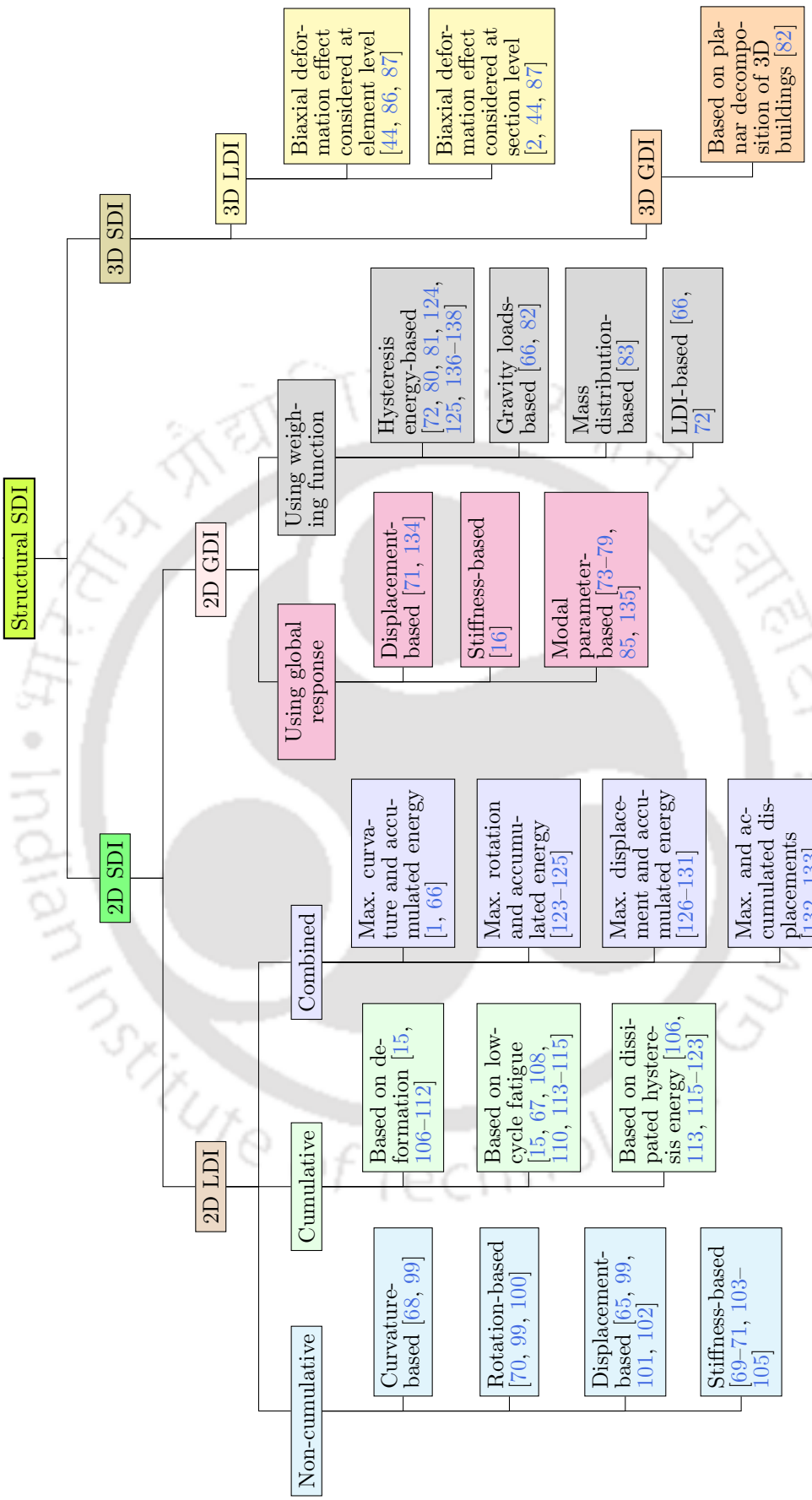

Figure 1.1: Classification of structural seismic damage indices

by repeated load reversals.

Gupta et al. [102] introduced a capacity-demand type damage index with the help of displacement response obtained by a modified Clough-Johnston single degree of freedom (SDOF) type elasto-plastic oscillator. The applicability of the LDI holds good only if a structure undergoes large plastic deformation in one cycle and negligible plastic deformations in other cycles during an earthquake. Mergos and Kappos [68] proposed a new capacity-demand type damage index (in terms of flexural curvature and shear distortion) to compute the damage due to bending-shear interactions in the inelastic range.

The non-cumulative damage indices are likely to provide an approximate measure of structural damage sustained during earthquakes by neglecting the effect of temporal features (e.g., total duration, number of loading cycles) and frequency content (e.g., patterns of occurrence of loading cycles) of the ground motions. Therefore, they are usually not implemented despite being easy to compute.

Cumulative LDI

Cumulative damage indices consider damage as a function of accumulated plastic deformation and can include the effect of dissipated hysteresis energy during earthquakes. Initially, researchers extended the scope of the ductility concept to capture the cumulative damage due to repetitive cyclic loading. Gosain et al. [106] proposed a simple damage index (applicable for pure bending) defined as the sum of the ratio between the displacement during a particular cycle and the yield displacement for all loading cycles. Banon and Veneziano [107] introduced normalized cumulative rotation, which is defined as the ratio of the sum of plastic rotations (i.e., the difference between maximum rotation and yield rotation) during all half cycles to the yield rotation. They have also proposed a normalized dissipated energy term as a function of time, and the term is represented by the ratio between the energy dissipated up to a specific time and the maximum elastically stored energy.

Low-cycle fatigue (refers to the failure of members at deformation levels with significantly low amplitudes compared to the corresponding ultimate deformation capacity due to unidirectional loading [42]) is considered one of the main reasons for member failures. Therefore, Stephens and Yao [108] introduced the concept of low-cycle fatigue (usually used to model damage in metals) in their cumulative plastic deformation damage function in terms of positive and negative changes in plastic deformations for all loading cycles as demand, and positive change in plastic deformation in a one-cycle test to collapse conducted at each relative deformation ratio as capacity. The computation of the fatigue exponent coefficient and the capacity term used in the damage function is challenging and subjected to large statistical scatter. Later, Jeong and Iwan [110] proposed another damage index based on low-cycle fatigue formulation considering the number of cycles to failure at a particular ductility value obtained from a relationship similar to Coffin-Manson law. Chung et al. [15, 67] also used a fatigue formulation (considering Miner's Law) to propose a new combined damage index

including damage modifiers to reflect the loading history effect. This index considers the difference in member responses from positive and negative deformation cycles separately. Chung et al. [137] also used this damage index for setting criteria to check the acceptability of a design (following the strong-column weak-beam concept) of beam and column members. The design of individual elements is acceptable only if the corresponding damage index due to design earthquakes is less than 0.30($\pm$0.03) and 0.01, respectively, for the beam and column. McCabe and Hall [113], Kunnath et al. [114], Hindi and Sexsmith [115] introduced other damage indices based on low-cycle fatigue theory.

Wang and Shah [109] proposed a cumulative damage model (as a measure of strength degradation [28]) assuming that the development of damage is a function of maximum deformation occurred in a cycle, and the rate of damage accumulation is proportional to the sustained damage during the previous loading cycles. Later, Wang and Wang [111] used this damage model for RC structures with shear walls. This damage model is of limited use due to the required calibration against observed seismic damages [139].

During the dynamic motion of a structure due to an earthquake, the structure absorbs some portion of the energy imparted to it by the ground excitations. Some amount of the absorbed energy is stored (temporarily) in the form of kinetic and strain energy, and the rest is dissipated by damping and inelastic deformations in various members of the structure [140]. Eventually, all imparted energy is dissipated and results in some damage if the absorbed energy exceeds the corresponding elastic limit. Therefore, as a first attempt to consider the absorbed energy, Gosain et al. [106] proposed a damage index represented by the sum of the ratio of the absorbed energy associated with a particular loading cycle to the energy absorbed in yielding over those hysteresis loops for which the applied lateral load is more than equal to 75% of the yield force. A similar damage index was also proposed by Darwin and Nmai [118, 119] with an additional modification factor for reinforcement arrangement. Hwang and Scribner [116, 117] proposed a *work index* (due to its dependency on the product of force and displacement) based on some modifications to the damage index of Gosain et al. [106]. The upper limit of this index is not bounded, unlike other damage indices. Prakash and Belarbi [123] made necessary changes to the work index so that their indices do not suffer from unbounded upper limit and can quantify damage due to bending-shear and torsion separately.

Krätzig et al. [120] developed another energy-based damage index based on the definition of primary and follower half-cycles to distinguish loading history effects. A primary half-cycle is defined as the first half-cycle of loading at a given amplitude, with subsequent half-cycles referred to as follower half-cycles unless they exceed the previous maximum amplitude. This LDI considers the effect of both deformation (through a single high-amplitude cycle) and fatigue-type damage (through repeated cycles at lower amplitude). Later, Mehanny and Deierlein [112] developed a new damage index using the same approach (involving primary and follower half cycles) in terms of cumulative inelastic deformations instead of dissipated

hysteresis energy.

Colombo and Negro [121] attempted to a uniform definition of damage (i.e., independent of material properties) based on the ratio between the initial and the reduced capacity to pave the way for general design and assessment method applicable to any structures. The damage index, proposed by these authors, considers the maximum attained deformation, the dissipated hysteresis energy and the loading history and requires several parameters in terms of ductility and energy dissipation. Rodríguez-Gómez and Cakmak [122] proposed a capacity-demand type damage index for SDOF system represented as the ratio of absorbed energy and hysteresis energy at collapse.

Combined LDI

The earthquake-induced damage to any structure generally occurs due to combined effects of maximum deformation, number of load cycles, and absorbed hysteresis energy [70, 107, 121, 122]. Depending on this philosophy, Park and Ang [126] introduced a combined LDI considering the nonuniform cyclic loading effect at different displacement levels as

$$LDI_{2D\text{-PA}} = \frac{\delta_m}{\delta_u} + \beta_{\text{PA}} \int \left(\frac{\delta}{\delta_u}\right)^{\alpha_{\text{PA}}} \frac{\mathrm{d}E_h}{E_c(\delta)} \tag{1.1}$$

where δ_m and δ_u are the maximum absolute displacement due to unidirectional seismic loading and the ultimate displacement under monotonic loading condition, respectively, $\mathrm{d}E_h$ is incremental absorbed hysteresis energy, $E_c(\delta)$ is the dissipated hysteresis energy per loading cycle at displacement level δ, α_{PA} and β_{PA} are the non-negative parameters representing the effect of cyclic loading on structural damage. For simplicity, the authors assumed a uniform cyclic loading effect at different displacement levels and proposed the best-known and most widely studied damage index as

$$LDI_{2D\text{-PA}} = \frac{\delta_m}{\delta_u} + \frac{\beta_{\text{PA}} E_h}{F_y \delta_u} \tag{1.2}$$

where F_y is the yield force under lateral monotonic loading conditions and E_h is the total amount of absorbed hysteresis energy due to seismic loading (i.e., the sum of the area enclosed within the hysteresis curve). Park et al. [142] identified two parameters (δ_u and β_{PA}) of the above equation as component characteristics and other three parameters (δ_m, F_y and E_h) as response parameters. The component characteristics can be computed from empirical relationships [80, 126], and the response parameters can be obtained from the responses of nonlinear dynamic analysis.

The calibration of the strength degradation parameter, β_{PA}, was discussed in detail by the authors in a separate report [143]. A low value of the parameter refers to the seismic damage governed by the maximum displacement demand (of a properly designed and detailed structure [144]), whereas a high value refers to the seismic damage due to cumulative inelastic

displacements (of a poorly designed and detailed structure [144]). Many researchers have used different values for the parameter, ranging from 0.025 [144] to 0.23 [127] for steel structures and 0.05 [136] to 0.24 [145] for RC structures. Another group of researchers reported the parameter value ranging from 0.20 to 0.40 for systems showing substantial strength and stiffness degradation [28, 101, 108]. Ciampoli et al. [84] used a probabilistic approach assuming random values for the parameter with a mean value of 0.27 and a coefficient of variation of 0.60. Cosenza et al. [101] reported that the parameter ranges from -0.30 to 1.20, with a median value of 0.15.

After the introduction of the Park and Ang combined damage index, $LDI_{2D\text{-PA}}$, many researchers provided necessary modifications to improve the applicability of the original model based on its several limitations. Table 1.1 enlisted the (year-wise) details of those modified Park and Ang-type 2D local damage models. A practical problem for using $LDI_{2D\text{-PA}}$ is to determine the relationship between δ_u, local plastic rotations and the damage index. Because inelastic behaviour is usually confined within plastic zones near the ends of a member. Therefore, Kunnath et al. [124], and Stone and Taylor [1] replaced the force-displacement terms (in $LDI_{2D\text{-PA}}$) with moment-rotation and moment-curvature terms, respectively, and introduced two new damage indices ($LDI_{2D\text{-KRL}}$ and $LDI_{2D\text{-ST}}$ in Table 1.1) for implementing in IDARC Version 3.0 [124]. The researchers have also removed the yield value from the maximum and ultimate values in the non-cumulative part to generate non-zero damage only due to inelastic structural responses. Although the term $A_{M\text{-}\phi}$ in $LDI_{2D\text{-ST}}$ represents an implicit measure of dissipated energy, it correlates well with the original strength degradation parameter (β_{PA}) when normalized with the term $M_y\phi_u$. The range of values for the parameter β_{KRL} is from 0.0 (for no deterioration) to 0.4 (for severe deterioration), and $\beta_{\text{KRL}} = 0.1$ is used for nominal deterioration. Later, Ghosh et al. [144] kept the displacement term of the original Park and Ang damage model to modify it following the framework similar to $LDI_{2D\text{-KRL}}$ or $LDI_{2D\text{-ST}}$. The authors used the modified damage model to explore the concept of implementing an equivalent SDOF system to get a storey or global damage index of a multiple degree of freedom system.

Theoretically, the value of a local damage model should be equal to 1.0 (indicating a failure) when ultimate deformation capacity is utilized under monotonic loading conditions. However, it is not possible to satisfy the criteria for $LDI_{2D\text{-PA}}$ (refer to Equation (1.2)). As a remedy to this limitation, Chai et al. [127] introduced $LDI_{2D\text{-CRB}}$ (see Table 1.1) by removing the dissipated plastic strain energy due to monotonic response from the total dissipated plastic strain energy. Accordingly, the authors also modified the parameter, $\beta_{2D\text{-PA}}$, in terms of displacement ductility capacity for an elasto-plastic system to capture the same effect of strength degradation behaviour as in the case of original Park and Ang damage model. But this modified model was verified for experimental results of small-scaled notched steel cantilever beams and cannot be applicable for RC structural members without any uncertainty. Therefore, Jiang et al. [130] developed another modified Park and Ang-type

Table 1.1: Various modified Park and Ang-type local damage indices for 2D RC frames

Sl. No.	Authors	LDI formula	Remarks
1(a)	Kunnath et al. [124]	$LDI_{2D\text{-KRL}} = \frac{\theta_m - \theta_r}{\theta_u - \theta_r} + \frac{\beta_{\text{KRL}} E_h}{M_y \theta_u}$	θ_m: maximum absolute rotation, θ_r : recoverable rotation, θ_u: ultimate rotation, M_y : flexural yield moment
1(b)	Stone and Taylor [1]	$LDI_{2D\text{-ST}} = \frac{\phi_m - \phi_y}{\phi_u - \phi_y} + \frac{\beta_{\text{KRL}} A_{M\text{-}\phi}}{M_y \phi_u}$	ϕ_m: maximum absolute curvature, ϕ_y : yield curvature, ϕ_u: ultimate curvature, $A_{M\text{-}\phi}$: total area enclosed within M-ϕ loops
2	Chai et al. [127]	$LDI_{2D\text{-CRB}} = \frac{\delta_m}{\delta_u} + \frac{\beta_{\text{CRB}}(E_h - E_{hm})}{F_y \delta_u}$	$\beta_{\text{CRB}} = \mu_\delta \beta_{\text{PA}} / [\mu_\delta + (1 - \mu_\delta)\beta_{\text{PA}}]$, μ_δ : displacement ductility capacity (δ_u/δ_y), E_{hm} : dissipated plastic strain energy under monotonic loading
3	Fajfar and Gašperšič [125]	$LDI_{2D\text{-FG}} = \frac{\theta}{\theta_u}\left[1 + \beta_{\text{FG}} \frac{E_h(\theta - \theta_y)}{E_{hs}\,\theta}\right]$	E_{hs} : static hysteresis energy (i.e., dissipated hysteresis energy in the case of monotonic loading)
4	Bozorgnia and Bertero [128]	$LDI_{2D\text{-BB1}} = (1 - \alpha_{\text{BB1}}) \frac{\mu_{\delta,d} - \mu_{\delta,e}}{\mu_\delta - 1} + \alpha_{\text{BB1}} \frac{E_h}{E_{hm}}$ $LDI_{2D\text{-BB2}} = (1 - \alpha_{\text{BB2}}) \frac{\mu_{\delta,d} - \mu_{\delta,e}}{\mu_\delta - 1} + \alpha_{\text{BB2}} \sqrt{\frac{E_h}{E_{hm}}}$	α_{BB1} and α_{BB2} : constant coefficients (with ranges from 0 to 1) depending on the mechanical characteristics of structure and input ground motion $\mu_{\delta,d}$: displacement ductility demand (δ_m/δ_y), $\mu_{\delta,e}$ is equal to 1 and μ_{δ_d} for inelastic and elastic responses, respectively
5	Ladjinovic and Folic [129]	$LDI_{2D\text{-LF}} = \frac{\delta - \delta_y}{\delta_u - \delta_y} + \frac{\alpha_{\text{LF}} \beta_{\text{LF}} E_h}{F_y(\delta_u - \delta_y)}$	δ_y : yield displacement, $\alpha_{\text{LF}} = 1 - \mu_c/\mu_{ac}$, μ_c : cyclic displacement ductility[(a)] [146], μ_{ac} : accumulative displacement ductility[(b)]
6	Prakash and Belarbi [123]	$LDI_{2D\text{-PB}} = \frac{\theta_{m,t}}{\theta_{u,t}} + \frac{\beta_{PB} E_{h,t}}{T_y \theta_{u,t}}$	$\theta_{m,t}$: maximum absolute twist, $\theta_{u,t}$: ultimate twist, T_y : torsional yield value, $E_{h,t}$: total torsional dissipated hysteresis energy
7	Ghosh et al. [144]	$LDI_{2D\text{-GDK}} = \frac{\delta_m - \delta_y}{\delta_u - \delta_y} + \frac{\beta_{\text{GDK}} E_h}{F_y \delta_u}$	$LDI_{2D\text{-PA}}$ is modified using global displacement terms in the framework similar to $LDI_{2D\text{-KRL}}$ and $LDI_{2D\text{-ST}}$.
8	Jiang et al. [130]	$LDI_{2D\text{-JFLC}} = (1 - \beta_{\text{JFLC}}) \frac{\delta_m - \delta_c}{\delta_u - \delta_c} + \beta_{JFLC} \frac{E_h}{E_{hm}}$	δ_c : displacement at initial cracking of concrete, $\delta_m - \delta_c = 0$ when $\delta_m \leqslant \delta_c$
9	Huang et al. [131]	$LDI_{2D\text{-HQZ}} = (1 - \beta_{\text{HQZ}}) \frac{\delta_m - \delta_y}{\delta_u - \delta_y} + \frac{\beta_{HQZ} E_h}{F_y(\delta_u - \delta_y)}$	$\delta_m - \delta_y = 0$ when $\delta_m \leqslant \delta_y$
10	Xiao et al. [83]	$LDI_{2D\text{-XXL}} = (1 - \beta_{\text{XXL}}) \left(\frac{\delta_m - \delta_y}{\delta_u - \delta_y}\right)^{\alpha_{\text{XXL}}} + \beta_{XXL} \left(\frac{E_h}{F_y \delta_u}\right)^{1 - \alpha_{\text{XXL}}}$	α_{XXL} : combination parameter reflecting the interrelation between deformation and hysteresis energy of a member

Note: (a) cyclic displacement ductility is the ratio of the maximum absolute displacement demand due to unidirectional motion to the yield displacement, (b) accumulative displacement ductility is the ratio of the sum of the absolute inelastic displacements (in both positive and negative directions) during all plastic excursions to the yield displacement.

damage model ($LDI_{2D\text{-JFLC}}$ in Table 1.1) to counter the non-normalization issue and calibrated its combination coefficient (β_{JFLC}) with various cyclic experimental results of RC members. Since the displacement of RC members at first cracking is significantly smaller than yield displacement (i.e., $\delta_c/\delta_y \approx 0$) and plastic strain energy due to monotonic loading, $E_{hm} = F_y(\delta_u - \delta_y)$ for an elasto-plastic system, the authors further simplified the damage model in terms of displacement ductility capacity and maximum displacement ductility demand. Later Huang et al. [131] extended the scope of $LDI_{2D\text{-JFLC}}$ for steel RC members (more ductile material in comparison to common RC members) and replaced the term δ_c with δ_y (refer to $LDI_{2D\text{-HQZ}}$ in Table 1.1). Xiao et al. [83] also modified the damage index $LDI_{2D\text{-JFLC}}$ to incorporate the mutual effect of maximum deformation and hysteresis energy (through continuum mechanics-based damage dissipation potential function [147]) for different types of members during different loading stages in the final damage.

Fajfar and Gašperšič [125] has considered $LDI_{2D\text{-PA}}$ in terms of moment and rotation, and used static hysteresis energy (i.e., the dissipated energy in the case of static loading) for an elasto-plastic M-θ relationship to propose $LDI_{2D\text{-FG}}$ (as shown in Table 1.1). Further, assuming the distribution of dissipated hysteresis energy throughout a structure is similar for both dynamic and static analyses, the authors have provided another expression for $LDI_{2D\text{-FG}}$ as a function of ductility terms, and a non-dimensional parameter related to equivalent SDOF system.

Bozorgnia and Bertero [128] provided two new LDIs ($LDI_{2D\text{-BB1}}$ and $LDI_{2D\text{-BB1}}$ in Table 1.1) by improvising $LDI_{2D\text{-PA}}$ to generate two different damage spectra (defined as a plot of computed damage index versus structural period, or a plot of required strength or maximum deformation versus structural period for constant values of damage indices) for performance-based damage assessment of existing structures and performance-based design for new structures. The authors have further simplified their LDIs in the case of an elastic-perfectly-plastic system. Similarly, Ladjinovic and Folic [129] came with a modified Park and Ang-type damage index ($LDI_{2D\text{-LF}}$ in Table 1.1) which can be used in the design of earthquake resistant structures by keeping a necessary balance between strength capacity, stiffness and ductility, and the damage level within acceptable prescribed limits. A corrective coefficient, α_{LF}, is introduced in the cumulative terms of the LDI to eliminate the effect of hysteresis energy due to monotonically increasing lateral deformation. The authors have also expressed their LDI in a more convenient form as a function of maximum ductility demand (δ/δ_y) during an earthquake, monotonic ductility capacity (δ_u/δ_y) and normalized hysteresis energy ($E_h/F_y\delta_y$) for directly using in earthquake resistant design of structures.

All modified Park and Ang-type 2D local damage models, till discussed, are developed to measure structural damages due to flexure-shear and axial loadings and neglect the contribution of torsional response to the damage. So, Prakash and Belarbi [123] investigated the damages developed in circular RC columns due to combined loadings, i.e., bending, shear, axial and torsion, and modified the original Park and Ang damage model by replacing force-

displacement terms with torsion-twist relationship (refer to $LDI_{2D\text{-}PB}$ in Table 1.1).

Apart from original and modified Park and Ang-type damage indices, other combined LDIs are also available in the literature. For example, Mizuhata and Nishigaki [132, 133] introduced a combined LDI assuming the local damage as the linear combination of the damages due to maximum displacement and the accumulated displacement resulting from cyclic loading as

$$LDI_{2D\text{-MN}} = \frac{|\delta_m|}{\delta_f} + \begin{cases} \sum_{i=1}^{k} \left(\frac{n_i}{N_{fi}}\right)^{0.715} \cdot 0.609 \cdot \left(1 - \frac{\delta_i}{\delta_f}\right), & \text{for} \quad 0.078 \geqslant \frac{n_i}{N_{fi}} \geq 0 \\ \sum_{i=1}^{k} \left(\frac{n_i}{N_{fi}}\right)^{0.910} \left(1 - \frac{\delta_i}{\delta_f}\right), & \text{for} \quad 1.0 \geqslant \frac{n_i}{N_{fi}} > 0.078 \end{cases} \tag{1.3}$$

where δ_i is ith specified displacement level, δ_f is displacement at failure under monotonic loading, k is the number of different displacement levels, n_i is the number of cycles with displacement level δ_i, and N_{fi} is the number of cycles to failure with displacement level δ_i. The above LDI expression was derived based on low-cycle fatigue tests performed under constant displacement amplitudes. Bracci et al. [66] represented the damage in terms of irrecoverable deformations and strength degradation, and accordingly proposed a new combined damage index as

$$LDI_{2D\text{-BRMK}} = D_M + D_\phi - D_M D_\phi \quad \text{with } D_M = \frac{S_{sd} E_h}{M_y \phi_y},\ D_\phi = \frac{\phi_m - \phi_y}{\phi_u - \phi_y} \tag{1.4}$$

where S_{sd} is the strength degradation parameter, and its mathematical expression is obtained (in terms of the axial load, the longitudinal and confinement steel percentages, material strength) using regression analysis of various test results.

1.2.1.2 Local damage index for 3D RC buildings

The LDI models mentioned in the previous section (refer to Figure 1.1) can accommodate structural responses (along a particular direction) due to unidirectional loadings only and cannot be used directly to measure damages that occurred in members of 3D buildings as the corresponding responses (along two orthogonal horizontal directions) are generated due to bidirectional ground motions. Therefore, many researchers attempted new combined LDI models for which the corresponding demand and capacity terms must utilize the structural responses at the element level (e.g., force, displacement) or the section level (e.g., moment, rotation or curvature) due to bidirectional lateral loadings. The elementary 3D LDI models achieve this condition by combining any suitable 2D LDI model (i.e., $LDI_{2D}^{(x)}$ and $LDI_{2D}^{(y)}$) for a member due to individual unidirectional ground motions (i.e., along x- and y-directions)

through various functions generally represented as

$$LDI_{3D} = f\left(LDI_{2D}^{(x)}, LDI_{2D}^{(y)}, E_h^{(x)}, E_h^{(y)}\right) \tag{1.5}$$

where $E_h^{(x)}$ and $E_h^{(y)}$ are the cumulative dissipated hysteresis energies of the member when subjected to lateral loadings along x- and y-directions, respectively. For example, Qiu et al. [86] introduced three different 3D LDI models using $LDI_{2D\text{-PA}}$ and the corresponding E_h in terms of force-displacement relationship (refer to Equation (1.2)) as

$$LDI_{3D\text{-QLPQ1}} = LDI_{2D\text{-PA}}^{(x)} + LDI_{2D\text{-PA}}^{(y)} - 0.5\min\left(LDI_{2D\text{-PA}}^{(x)}, LDI_{2D\text{-PA}}^{(y)}\right) \tag{1.6}$$

$$LDI_{3D\text{-QLPQ2}} = \max\left(LDI_{2D\text{-PA}}^{(x)}, LDI_{2D\text{-PA}}^{(y)}\right) + \frac{E_h^{(x)} \text{ or } E_h^{(y)}}{E_h^{(x)} + E_h^{(y)}}\min\left(LDI_{2D\text{-PA}}^{(x)}, LDI_{2D\text{-PA}}^{(y)}\right) \tag{1.7}$$

$$LDI_{3D\text{-QLPQ3}} = \max\left(LDI_{2D\text{-PA}}^{(x)}, LDI_{2D\text{-PA}}^{(y)}\right) + \frac{LDI_{2D\text{-PA}}^{(x)} \text{ or } LDI_{2D\text{-PA}}^{(y)}}{LDI_{2D\text{-PA}}^{(x)} + LDI_{2D\text{-PA}}^{(y)}}\min\left(LDI_{2D\text{-PA}}^{(x)}, LDI_{2D\text{-PA}}^{(y)}\right) \quad . \tag{1.8}$$

Apart from the above damage index models, the authors also proposed another model assuming the damage is determined by the maximum displacement and accounts for the coupling effect of the other direction. The 3D LDI is expressed as

$$LDI_{3D\text{-QLPQ4}} = \begin{cases} \dfrac{\delta_m^{(x)}}{\delta_u^{(x)}} + \beta_{\text{PA}}\dfrac{E_h^{(x)} + E_h^{(y)}}{F_y^{(x)}\delta_u^{(x)}}, & \text{when} \quad \delta_m^{(x)} \geqslant \delta_m^{(y)} \\ \dfrac{\delta_m^{(y)}}{\delta_u^{(y)}} + \beta_{\text{PA}}\dfrac{E_h^{(x)} + E_h^{(y)}}{F_y^{(y)}\delta_u^{(y)}}, & \text{otherwise} \end{cases} \tag{1.9}$$

where $\delta_m^{(x)}$, $\delta_u^{(x)}$ and $F_y^{(x)}$ are maximum displacement, ultimate displacement and yield force of a structural member, respectively, when subjected to the corresponding loading along x-direction only, whereas $\delta_m^{(y)}$, $\delta_u^{(y)}$ and $F_y^{(y)}$ denote same displacement and force parameters due to the loadings along y-direction only. For simplicity, the authors considered the yield force values as 0.80 times the corresponding ultimate strength, e.g. $F_y^{(x)} = 0.80F_u^{(x)}$. Later, Rodrigues et al. [87] proposed the following 3D LDI models by directly combining $LDI_{2D\text{-PA}}$ along two orthogonal directions without involving the energy terms as

$$LDI_{3D\text{-RAVC1}} = LDI_{2D\text{-PA}}^{(x)} + LDI_{2D\text{-PA}}^{(y)} \tag{1.10}$$

$$LDI_{3D\text{-RAVC2}} = \sqrt{\left(LDI_{2D\text{-PA}}^{(x)}\right)^2 + \left(LDI_{2D\text{-PA}}^{(y)}\right)^2} \quad . \tag{1.11}$$

The 3D LDI models represented by Equations (1.6)-(1.11) suffer from non-normalization related problem for using $LDI_{2D\text{-PA}}$ values within their framework. Therefore, Roy et al. [44]

utilized one of the modified Park and Ang-type 2D damage model capable of solving the problem, $LDI_{2D\text{-JFLC}}$, to propose four new 3D LDIs (similar to Equations (1.6)-(1.8) and (1.11)) as

$$LDI_{3D\text{-RBR1}} = LDI^{(x)}_{2D\text{-JFLC}} + LDI^{(y)}_{2D\text{-JFLC}} - 0.5 \min\left(LDI^{(x)}_{2D\text{-JFLC}}, LDI^{(y)}_{2D\text{-JFLC}}\right) \tag{1.12}$$

$$LDI_{3D\text{-RBR2}} = \max\left(LDI^{(x)}_{2D\text{-JFLC}}, LDI^{(y)}_{2D\text{-JFLC}}\right) + \frac{E^{(x)}_h \text{ or } E^{(y)}_h}{E^{(x)}_h + E^{(y)}_h} \min\left(LDI^{(x)}_{2D\text{-JFLC}}, LDI^{(y)}_{2D\text{-JFLC}}\right) \tag{1.13}$$

$$LDI_{3D\text{-RBR3}} = \max\left(LDI^{(x)}_{2D\text{-JFLC}}, LDI^{(y)}_{2D\text{-JFLC}}\right) + \frac{LDI^{(x)}_{2D\text{-JFLC}} \text{ or } LDI^{(y)}_{2D\text{-JFLC}}}{LDI^{(x)}_{2D\text{-JFLC}} + LDI^{(y)}_{2D\text{-JFLC}}} \min\left(LDI^{(x)}_{2D\text{-JFLC}}, LDI^{(y)}_{2D\text{-JFLC}}\right) \tag{1.14}$$

$$LDI_{3D\text{-RBR4}} = \sqrt{\left(LDI^{(x)}_{2D\text{-JFLC}}\right)^2 + \left(LDI^{(y)}_{2D\text{-JFLC}}\right)^2}\ . \tag{1.15}$$

Also, the authors modified the expression of $LDI_{3D\text{-QLPQ4}}$ accordingly and introduced another damage index as

$$LDI_{3D\text{-RBR5}} = \begin{cases} (1-\beta_{JFLC})\dfrac{\delta^{(x)}_m}{\delta^{(x)}_u} + \dfrac{\beta_{\text{JFLC}}\left(E^{(x)}_h + E^{(y)}_h\right)}{F^{(x)}_y\left(\delta^{(x)}_u - \delta^{(x)}_y\right)}, & \text{when} \quad \delta^{(x)}_m \geqslant \delta^{(y)}_m \\ (1-\beta_{\text{JFLC}})\dfrac{\delta^{(y)}_m}{\delta^{(y)}_u} + \dfrac{\beta_{\text{JFLC}}\left(E^{(x)}_h + E^{(y)}_h\right)}{F^{(y)}_y\left(\delta^{(y)}_u - \delta^{(y)}_y\right)}, & \text{otherwise} \quad . \end{cases} \tag{1.16}$$

Instead of combining the responses due to individual unidirectional loadings at element level (as in the cases of Equations (1.6)-(1.16)), it is better to get more realistic damage measure by combining the necessary responses at section level due to bidirectional ground motions. Therefore, Rodrigues et al. [87] introduced a new damage index based on the resultant maximum displacement ($\delta_{m,r}$) and total energy as

$$LDI_{3D\text{-RAVC3}} = \frac{\delta_{m,r}}{\delta_{u,r}} + \beta_{\text{PA}}\frac{E^{(x)}_h + E^{(y)}_h}{F_{y,r}\delta_{u,r}} \tag{1.17}$$

where $\delta_{m,r}$ is computed for each loading step, and for this resultant direction, the resultant ultimate displacement ($\delta_{u,r}$) and the resultant yield force ($F_{y,r}$) are also estimated based on an assumed parabolic resultant surface. Equation (1.17) considered only partial combination of the sectional responses due to bidirectional motions for computing the damage. Because the dissipated hysteresis energies due to individual unidirectional motions are used in the cumulative term to get the desired combined effect. Also, the estimation of resultant maximum displacement assumes that the maximum displacements along two orthogonal directions will

occur together, which is not practical. Therefore, as an improvement to this model, Roy et al. [44] considered complete combination of the sectional responses and maximum resultant displacement, $\delta_{r,m}$, instead of $\delta_{m,r}$ to introduce another 3D LDI as

$$LDI_{3D\text{-RBR6}} = (1 - \beta_{\text{JFLC}}) \frac{\delta_{r,m}}{\delta_{r,u}} + \frac{\beta_{\text{JFLC}} \left(E_{h_1} + E_{h_2}\right)}{F_{r,y} \left(\delta_{r,u} - \delta_{r,y}\right)} \tag{1.18}$$

$$\text{with} \quad \delta_{r,m} = \max \left[\sqrt{\delta_1^2(t) + \delta_2^2(t)} \right] \ \forall \ t \tag{1.19}$$

where $\delta_1(t)$, E_{h_1} and $\delta_2(t)$, E_{h_2} are the displacement time-histories and total dissipated hysteresis energy along two principal axes, respectively, of a member section subjected to bidirectional ground motions. $\delta_{r,y}$, $\delta_{r,u}$ and $F_{r,y}$ are the yield displacement, the ultimate displacement, and the yield strength values, respectively, computed along the direction of $\delta_{r,m}$. The 3D LDIs represented by Equations (1.6)-(1.18) require displacement values from inelastic behaviour within plastic zones, which is a drawback for these models like their 2D counterparts [124]. So, Guo et al. [2] extended the concept of M-θ based modified Park and Ang-type damage model for 3D members and proposed the most comprehensive 3D LDI as

$$LDI_{3D\text{-GWLZD}} = (1 - \beta_{\text{GWLZD}}) \, \bar{\mu}_{\theta,m} + \beta_{\text{GWLZD}} \int \alpha_{\text{GWLZD},m} \frac{\mathrm{d}E_p}{E_{hm}(t)} \tag{1.20}$$

where $\bar{\mu}_{\theta,m}$ is the maximum normalized rotation ductility factor, $\mathrm{d}E_p$ is the incremental dissipated plastic energy, $E_{hm}(t)$ is dissipated plastic strain energy under monotonic loading at failure, $\alpha_{\text{GWLZD},m}$ and β_{GWLZD} are the correction term and the combination factor, respectively, associated with energy dissipation. Further, $\bar{\mu}_{\theta,m}$ is defined as

$$\bar{\mu}_{\theta,m} = \max \underbrace{\left[\frac{\theta_r(t) - \theta_{r,y}(t)}{\theta_{r,u}(t) - \theta_{r,y}(t)} \right]}_{\substack{\text{normalized rotation} \\ \text{ductility, } \bar{\mu}_\theta(\theta_r(t))}} \ \forall \ t \tag{1.21}$$

$$\text{with} \quad \theta_r(t) = \sqrt{\theta_1^2(t) + \theta_2^2(t)} \tag{1.22}$$

where $\theta_1(t)$ and $\theta_2(t)$ are the rotation time-histories along two principle axes of a member section, $\theta_{r,y}(t)$ and $\theta_{r,u}(t)$ are the yield and ultimate rotation, respectively, at a particular loading step estimated along the direction of the corresponding resultant rotation, $\theta_r(t)$, for the section. The authors considered only the plastic energy dissipation increment in the cumulative term assuming that the (reversible) elastic portion of the energy dissipation would cause negligible damage. This assures zero value for the damage index in the case of elastic responses only. $\mathrm{d}E_p$ can be estimated by removing incremental elastic energy dissipation from the incremental total dissipated hysteresis energy. For three-dimensional deformation, incremental elastic energy dissipation is the sum of the recoverable area under M-θ relationships along two sectional principal axes, and the areas are calculated assuming unloading

stiffness is same as the linear loading stiffness. On the other hand, the incremental total dissipated hysteresis energy can be computed from the inner product of M-θ relationships along two sectional principal axes due to biaxial bending. The value of $E_{hm}(t)$ for a particular loading step can be computed assuming ideal elasto-plastic M-θ relationship as

$$E_{hm}(t) = M_{r,y}(t)\left[\theta_{r,u}(t) - \theta_{r,y}(t)\right] \tag{1.23}$$

where $M_{r,y}(t)$ is the yield moment of the section computed along the direction of $\theta_r(t)$. The correction term of the damage model is expressed as

$$\alpha_{\text{GWLZD},m} = \max\left[\alpha(\theta_r(t))\right] \quad \forall\ t \tag{1.24}$$

$$\text{with} \quad \alpha(\theta_r(t)) = \begin{cases} \beta_2\left[\bar{\mu}_\theta\left(\theta_r(t)\right)\right]^{\beta_1}, & \text{when } \theta_r(t) \geqslant \theta_{r,y}(t) \\ 0, & \text{otherwise} \end{cases} . \tag{1.25}$$

The authors prescribed the values of the parameters β_{GWLZD}, β_1 and β_2 as 0.1, 1.5 and 2.5, respectively, based on available experimental data.

1.2.1.3 Global damage index

The global damage index is used to compute the damage sustained in subassemblage of members or substructures, a storey of a building or a whole structure. Although the damage index used for subassemblage of members or a storey is sometimes referred to as intermediate damage index [29], this dissertation work uses the term global damage index for such damages in consistency with most of the available literature. The available GDIs are computed using either global responses and overall structural parameters (e.g., displacement, stiffness properties and modal parameters) or combining local damage indices across a structure with the help of any suitable weighing function (e.g., dissipated hysteresis energy or gravity load demand) as shown in Figure 1.1.

The earliest global damage index was introduced as a function of maximum interstory drift or maximum roof displacement. For example, Sozen [148] presented maximum relative displacement between two storeys normalized with storey height as the global damage parameter of a structure. In contrast, Meyer et al. [134] considered maximum roof displacement and total building height. Later, Roufaiel and Meyer [71] introduced a global damage parameter using the roof displacement at which the first member in the frame reaches its yield capacity other than maximum roof displacement and total frame height. Ghobarah et al. [16] proposed a static pushover analysis-based method to compute the expected damage to structure in terms of stiffness degradation due to various earthquakes. Recently Hait et al. [149] proposed various empirical global damage models in terms of different global engineering demand parameters (e.g., maximum interstory drift ratio, peak roof displacement, stiffness, ductility).

The stiffness degradation during earthquakes results in an increment of the natural period, and therefore, many researchers used the variation of the fundamental period or the first few natural periods of a structure and proposed various softening indices. For example, DiPasquale et al. [76–78, 135] proposed final softening index (as a measure of average reduction in structural stiffness), plastic softening index (as a measure of plastic deformation incorporating soil-structure interaction) and maximum softening index (as a measure of combined effect of stiffness degradation and plastic deformation). Although the maximum softening index is the best indicator (among all softening indices) of global damage [28] and correlates well with a weighted average of other combined LDI models [141], the final softening index has an advantage (over maximum softening index) of being computed directly from the recorded structural responses during earthquakes. However, no softening index can provide information about the distribution of the damage within the structure. So, Mørk [79] introduced two new damage parameters considering the first two modes of vibration. Later, Nielsen et al. [85] used these two damage parameters to get the maximum softening index. Pandey et al. [150], Ko et al. [73] and Wang et al. [74], among many other researchers, explored modal frequency and mode shapes as a measure of global damage, whereas researchers like Massumi and Moshtagh [75] proposed GDI models based on variations of nonlinear fundamental period.

Another way to get the GDI of a structure is by using any suitable weighing functions and computing the weighted average of all LDIs across the structure. The selection of the weighing function is usually based on a subjective assessment of the impact of heavily localized damage on the overall serviceability of structures [28]. Most of the researchers such as Park et al. [80, 136], Chung et al. [137], Kunnath et al. [124, 138], Fajfar and Gašperšič [125], Skjærbæk et al. [72], Tabeshpour et al. [81] used dissipated hysteresis energy at each plausible plastic hinge location as the weighing function to put higher weights on the heavily damaged members. Based on the same concept, Bracci et al. [66] and Skjærbæk et al. [72] used the computed LDI values as the weighing function to find the GDI value. Bracci et al. [66] also proposed the gravity load demand of each member as the weighing function because the damaged columns of lower storeys have a higher chance of causing complete structural collapse than the damaged columns of upper storeys. The same weighing function was adopted by Jeong and Elnashai [82] to propose a new GDI formula for 3D irregular buildings based on the planar decomposition of the structure. The proposed GDI can capture the effect of torsion due to bidirectional ground motions on irregular structures. Xiao et al. [83] have used the mass distribution over the tributary area for each column as the weighing function to provide separate weights to the damaged columns based on their position in the plan (i.e., corner columns, side columns and middle columns).

1.2.2 Seismic damage states for RC structures

The seismic damage state (or condition) of a structure is used to evaluate its post-earthquake status and help to decide the future use of the structure based on its existing condition. There are many definitions of damage states available in the literature. Any damage state must consider detailed or brief damage descriptions (preferably along with a failure mechanism) to make its users understand the post-earthquake situations of a structure. Hill and Rossetto [151, 152] provided a detailed review of the acceptability of available damage states in terms of estimating seismic loss. Now, the ability to predict structural damage is not the only criterion of a practical SDI model unless it also reflects the corresponding damage state or performance level [114]. Therefore, the correlations between the damage indices and the damage in actual buildings must be established through predefined damage states or design performance levels. To achieve this, the damage states are categorized with limiting values of SDI models, which are usually estimated from experimental results, observational studies or both. One group of researchers [87, 123, 130, 136, 153] related their damage indices with the material damage process, whereas others [2, 66, 80, 83, 131] used post-earthquake restoration-based information to define limits of their damage indices. Typical details for two types of damage states (i.e., based on material damage process and post-earthquake restoration information) are provided in Table 1.2. Although the first type of damage states have better physical meaning, the second type of damage states are more useful for performance-based seismic design through their direct interpretations in performance evaluation and financial loss assessment [2]. Further, Kunnath et al. [114] provided a correlation between visually observed damage (during monotonic and cyclic tests conducted by the authors) with some damage limit states (as shown in Table 1.3) to make post-earthquake structural reconnaissance more convenient.

Table 1.2: Details of two different types of damage states

Based on material damage process		Based on post-earthquake restoration	
Damage state	Description	Damage state	Description
No/slight damage	Localized minor cracking	No damage	Localized minor cracking
Minor damage	Light cracking throughout	Repairable	Extensive spalling but inherent stiffness remains
Moderate damage	Severe cracking, localized spalling	Irreparable	Still standing but failure imminent
Severe damage	Crushing of concrete		
Collapse	Total or partial building collapse	Collapse	Total or partial building collapse

Table 1.4 enlisted the ranges of various SDI models associated with some predetermined damage states reported by several researchers. Several researchers [80, 136, 153] provided different ranges of limiting values for $LDI_{2D\text{-PA}}$ (refer to Equation (1.2)) associated with different damage states. Bracci et al. [66] introduced limiting values for $LDI_{2D\text{-BRMK}}$ (refer

Table 1.3: Correlation of damage limit states with visual observations [114]

Sl. No.	Damage state	Description	Visual observation
1	None	No visible damage, either cosmetic or structural	No visible cracks
2	Insignificant	Damage requires cosmetic repair, but no structural repair	Hair-line cracks, minor spalling, no exposed reinforcement
3	Moderate	Repairable structural damage - existing elements can be repaired without substantial demolition/ replacement	Excessive spalling, exposed reinforcement, no buckling of longitudinal bars, no necking of spirals
4	Heavy	Extensive damage - repair of elements is not feasible or requires major demolition/replacement	Buckling/fracture of longitudinal bars, necking/rupture of spirals

to Equation (1.4)) based on test results on columns, model-scale of three- and six-storey frames. Stone and Taylor [1] provided limiting values for $LDI_{2D\text{-ST}}$ (and $LDI_{2D\text{-KRL}}$ as shown in Table 1.1) based on 82 tests conducted on circular bridge columns. Similarly, Jiang et al. [130], Huang et al. [131] and Xiao et al. [83] proposed limiting values for other modified Park and Ang-type 2D LDI models, $LDI_{2D\text{-JFLC}}$ and $LDI_{2D\text{-HQZ}}$ (refer to Table 1.1), respectively, for both material damage and post-earthquake restoration-based damage states, whereas Guo et al. [2] provided limiting values for one of the modified Park and Ang-type 3D LDI model, $LDI_{2D\text{-GWLZD}}$ (refer to Equation (1.20)). On the other hand, Prakash and Belarbi [123] given different limiting values for flexural-shear-based and torsion-based damage indices separately.

1.2.3 Sensors for Measuring Structural Responses

At present time, many new buildings [20, 154, 155] are equipped with sensors at some pre-decided locations from the beginning of their service life, and many existing buildings [156–159] with critical conditions and/or national importance are also getting instrumented. It will help structural engineers to reconnaissance the global damage state and further decide the need for repairing/strengthening the structure immediately after the event [160–162]. Accelerometers are easily implementable and widely used as sensors in strong motion instrumentation programs [163]. Traditional electronic accelerometers can measure three-way acceleration (with limited resolution capacity) of a structure at the cost of a substantial amount of energy [164]. So, such accelerometers were replaced by wireless electrical accelerometers [165] to record the data remotely and economically compared to other sensors. But, the recorded data obtained from this type of sensor is subjected to electromagnetic interference. To tackle this problem, fiber Bragg grating-based optical accelerometers [166, 167] can be used to record the data by measuring changes in light refractivity. These sensors are comparatively fragile and must be handled with proper care during their installa-

Table 1.4: Limiting values for different SDI models and different predetermined damage states

Sl. No.	Authors	Range of various SDI models for different predetermined states of damages or performance levels				
1	Park et al. [80]	Repairable		Irreparable		Collapse
		$[0.0, 0.40)$		$[0.40, 1.0)$		$\geqslant 1.0$
2	Park et al. [136]	No damage	Minor damage	Moderate damage	Severe damage	Collapse
		$[0.0, 0.10)$	$[0.10, 0.25)$	$[0.25, 0.40)$	$[0.40, 1.0)$	$\geqslant 1.0$
3	Bracci et al. [66]	Serviceable	Repairable	Irreparable		Collapse
		$[0.0, 0.33)$	$[0.33, 0.66)$	$[0.66, 1.0)$		$\geqslant 1.0$
4	Ang et al. [153]	No damage	Minor damage	Moderate damage	Severe damage	Collapse
		$[0.0, 0.10)$	$[0.10, 0.25)$	$[0.25, 0.40)$	$[0.40, 0.80)$	$\geqslant 0.80$
5	Stone and Taylor [1]	No damage	Repairable	Irreparable		Collapse
		$[0.0, 0.11)$	$[0.11, 0.40)$	$[0.40, 0.77)$		$\geqslant 0.77$
6(a)	Prakash and Belarbi [123]	Flexural-shear damage index				
		No damage	Minor damage	Moderate damage	Severe damage	Collapse
		$[0.0, 0.10)$	$[0.10, 0.20)$	$[0.20, 0.40)$	$[0.40, 0.90)$	$\geqslant 0.90$
6(b)	Prakash and Belarbi [123]	Torsional damage index				
		No damage	Minor damage	Moderate damage	Severe damage	Collapse
		$[0.0, 0.05)$	$[0.05, 0.10)$	$[0.10, 0.40)$	$[0.40, 0.80)$	$\geqslant 0.80$
7	Jiang et al. [130]	Nominal cracking	Yielding	Ultimate strength	Ultimate limit state	
		$[0.0, 0.05)$	$[0.05, 0.15)$	$[0.15, 0.45)$	$[0.45, 1.0)$	
8	Huang et al. [131]	Basic operation	Repairable	Avoiding collapse		Collapse
		$[0.0, 0.03)$	$[0.03, 0.40)$	$[0.40, 1.0)$		$\geqslant 1.0$
9	Guo et al. [2]	No damage	Can be retrofitted	Should be replaced		Collapse
		$[0.0, 0.08)$	$[0.08, 0.30)$	$[0.30, 0.68)$		$[0.68, 1.0)$
10	Xiao et al. [83]	Without damage	Minor damage	Repairable	Irreparable	Nearly collapsed
		$[0.0, 0.15)$	$[0.15, 0.30)$	$[0.30, 0.60)$	$[0.60, 0.80)$	$\geqslant 0.8$

tions. Kavitha et al. [168] designed a capacitive-based (micro-electro-mechanical system or MEMS) accelerometer for earthquake-related applications with good sensitivity and noise performance. Another type of accelerometer, based on global positioning system [169] and precise point positioning technique [170], with a high-frequency sampling rate, is also used for monitoring responses due to seismic loading. The limitation of these sensors is comparatively high cost and high energy consumption for collecting a bulk number of observations [171].

Apart from accelerometers, researchers have also developed vision-based methods with the help of advanced high-resolution digital cameras to measure relative displacements [172–174] or absolute displacements [175] of different points in a structure. Hutchinson and

Kuester [176] developed an active illumination system to measure global structural displacements (e.g., interstory drift, story level velocities) during any seismic activity. Matsuya and co-workers [177, 178] developed an LED array-based lateral displacement sensor and an optic-based relative displacement sensor to monitor both static and dynamic responses of a building by measuring its relative story displacement in real-time. There are also some laser sensor-based methods for direct measurements of relative displacements [179, 180] and interstory drifts [181, 182] of a building. For further study, some detailed discussions about the use of different types of sensors for monitoring structural responses can be found in the literature [183–188].

1.2.4 Experiments on Cantilever Column

Different capacity parameters, such as lateral strength and lateral displacement capacity, are essential for performance-based seismic design of new civil structures and performance assessment of existing civil structures. Capacity estimation of the structures is also required to evaluate the structural damage, variation of global hysteretic behaviour, stiffness and strength degradation of columns, and energy dissipation due to seismic ground motions. Therefore, studying the effect of unidirectional and bidirectional lateral forces on the ultimate strength, ultimate displacement, and cyclic behaviour of RC structural members under the action of the constant or varying axial load has become a very familiar research topic that has attracted the attention of many researchers in the last few decades [86, 189–200]. A detailed review of such experiments can be found in literature [27, 201, 202]. Generally, most experimental studies use cantilever column specimens to study the behaviour of double curvature specimens (whose damage is dominated by flexural loading) with rigid zones on top and bottom representing a typical building column. An estimate of the number of experiments carried out on RC structural members subjected to unidirectional or bidirectional lateral load with constant or varying axial load obtained from Rodrigues et al. [202] and recently published works is provided in Table 1.5. One of the primary objectives of these experiments is to develop numerical models, including material properties, for representative column specimens. Further, it is essential to capture the behaviour beyond yielding, which enters the large deformation regime for capacity estimation. CEB report [27] provided a detailed report on such validation of different types of modelling.

Table 1.5: Numbers of different types of experiments on RC structural members

Nature of axial load	Types of lateral loading		Total
	Unidirectional load	Bidirectional load	
Constant axial load	381(79.0%)	58(12.1%)	439(91.1%)
Varying axial load	26(5.4%)	17(3.5%)	43(8.9%)
Total	407(84.4%)	75(15.6%)	482(100.0%)

1.3 Need of the Study

The most common classification of the available seismic damage indices is the local and global damage indices based on whether it quantifies the damage at a structure's local or global level, respectively. Among the different types of LDIs (non-cumulative, cumulative and combined), the combined ones are the most comprehensive as they can capture the effects of both maximum and cyclic accumulative deformations on the structural damage for any seismic activity. The computation of the GDI using such LDIs involves using the weighted average method through any suitable weighing function (refer to Figure 1.1). Generally, the demand parameters used for computing combined LDIs (and GDIs) are required at the section level (e.g., sectional stress and strain resultants, dissipated hysteresis energy) through complex and time-consuming nonlinear time-history analysis. Therefore, the available combined SDI models cannot use only global responses instead of sectional ones for their applications. Although a few existing GDIs (e.g., final softening index) can be determined using in-situ vibration records, such modal parameter-based damage indices can provide reasonable global damage estimates only when the damage is quite severe and distributed evenly throughout a structure [28]. Apart from that, engineered supervision and judgement are required every time to produce an equivalent linear system matching the nonlinear dynamic response of the structure due to an earthquake for applying the GDIs based on modal parameters. On the other hand, the modal parameters are mainly used for detecting damage in a structure rather than quantifying it by a single value [74]. Nowadays, various types of sensors are available to record the global dynamic responses for structures with satisfactory accuracy and precision during an earthquake. Relying on such state-of-the-art structural response measuring sensors, it is imperative to utilize the recorded data to compute a combined GDI for any instrumented structure and bypass the requirement of numerically obtained sectional responses through nonlinear dynamic analysis. Also, for the new GDI evaluation method to be widely applicable, it should predict the damage state for a structure obtained from any suitable combined damage index model. However, no such GDI evaluation methodology is available in the literature to date.

For the computation of structural damage at the local or global level, the required inputs are either generated through experimental observations directly (for minimal cases) or obtained through responses of representative finite element model, which must be calibrated with some experimental results. Although the damage calculated from the experimental observations represents the most realistic condition for a structure, the demanding practical arrangements are not always possible, mainly due to financial constraints. Therefore, the nonlinear dynamic responses of finite element models are preferred for computing damages in almost every situation. In this case, the acceptability of the calculated damage index relies on the authenticity of the experimental results with which the corresponding finite element model is calibrated.

The overall lateral behaviour of a building is governed by the combined action of lateral load-deformation behaviours of individual columns, which is generally obtained through experiments on a particular axially-loaded (with constant or varying load values) cantilever column of half the length of the corresponding actual one based on a symmetric double-curvature deformation profile. For most of the available experimental arrangements (as shown in Chapter 2) used for such axially-loaded cantilever columns subjected to unidirectional or bidirectional horizontal loading(s), the true cantilever behaviour is altered due to the undesirable orientations of the actuators (especially under large deformation), and the fixing arrangements between the actuator heads and the free end of the column during the experiment. Many researchers [86, 194, 203] have identified these problems, which must be taken into account, possibly through some kinematic corrections [204]. It should be noted that for most test setups on cantilever columns, it is impossible to carry out some kinematic correction in an isolated manner because the possible geometric configurations are not unique for a given pair of actuator displacements. Therefore, a constitutive model of column specimens is mandatory to satisfy the desired uniqueness in the solution. Hence, applying a mechanics-oriented approach involving equilibrium, deformation compatibility, and constitutive laws (elasto-plastic) is obligatory to get the actual configuration and the acting forces, including their directions, from actuator readings. This way, the obtained rectified curves for cantilever columns should be used to calibrate the material properties associated with a representative finite element model. Finally, the finite element models for different structures using such calibrated material properties must be utilized to find SDI values.

1.4 Objectives and Scope of the Present Work

Based on the discussion in the previous section, the primary objectives of this dissertation work are to address the necessity of rectifying experimental data obtained for axially loaded cantilever columns due to quasi-static [201] (or pseudo-static) monotonic and cyclic loadings and development of novel combined GDI evaluation method for RC buildings equipped with global response recording sensors. The point-wise objectives and scope of this thesis are provided below.

❶ A novel mechanics-based formulation is proposed here to get the true lateral load-deformation behaviour for cantilever columns due to constant axial load and unidirectional lateral load by identifying the effects of fixity and interactions between the actuators and the specimen.

❷ Overestimations of lateral displacement capacity, dissipated hysteresis energy, and underestimation of lateral strength for cantilever columns are observed if the experimental data are not rectified, thus, emphasizing the importance of the proposed rectification formulation, especially in the case of realistic structural damage characterization. Also,

the proposed formulation can directly find the yield parameters for a column from the rectified data by tracing the emergence of its inelastic displacement.

❸ A novel method for predicting combined GDI for instrumented RC buildings using the recorded floor-displacement data during seismic activities along with some readily obtainable structural capacity terms is attempted in the present research work. The main advantage of using the novel method is its independency on the dynamic responses usually obtained from complex and time-consuming nonlinear time-history analysis of RC buildings.

❹ For 2D RC frames, two different combined 2D GDI formulae using the novel method are introduced to predict the GDI obtained from dissipated hysteresis energy-based weighted average of $LDI_{2D\text{-ST}}$ (refer to Table 1.1) values computed at all plausible plastic hinge locations. The difference in those formulae is the type of required capacity terms, i.e., displacement ductility or curvature ductility of columns.

❺ The scope of the novel damage evaluation method is also extended for 3D RC buildings by introducing another two combined 3D GDI formulae, which can accommodate the effect of structural responses considering biaxial bending and axial load due to bidirectional ground motions. These two 3D GDI formulae can predict the GDI computed through the biaxial dissipated hysteresis energy-based weighted average of $LDI_{3D\text{-GWLZD}}$ (refer to Equation (1.20)) values.

❻ The explicit expressions for the global damage coefficients (GDCs), available in the new GDI formulae, are provided in terms of structural properties (e.g., fundamental period, total building height, total bay widths along orthogonal directions, number of floors and bays) and the local type (i.e., hard soil, medium stiff soil or soft soil) for wider applicability of the GDI formulae.

❼ The performances of the new formulae to predict the global damage states based on post-disaster restoration of a building (i.e., no damage, repairable, irreparable and collapse) from the estimated GDI values are also cross-checked and found satisfactory.

1.5 Organization of the Thesis

The main contributions of the present dissertation work are towards the development of a novel mechanics-based formulation to get the true load-deformation behaviour of cantilever columns from experimental data and a novel combined global damage index evaluation method utilizing recorded floor-displacement responses for instrumented RC buildings. The road map of this thesis following the current first chapter, which outlines the motivation for this study through a supporting literature review, is given below.

- ☞ A novel mechanics-based formulation to rectify the experimental results for axially loaded cantilever column due to unidirectional lateral loading and generate the true load-deformation behaviour of the column is discussed in Chapter 2. The new formulation is applicable in those cases when making some special arrangements to accurately record the column movement and actuator rotations during the tests is not possible.

- ☞ A novel combined GDI evaluation method utilizing the recorded floor-displacement data is introduced in Chapter 3. Two GDI formulae based on the new method for 2D RC frames along with explicit expressions for the global damage coefficients are also proposed in this chapter. The performance of the new GDI formulae for predicting well-known global damage states are also verified in the chapter.

- ☞ Further, the scope of the novel combined GDI evaluation method is extended for 3D RC buildings by introducing two new 3D GDI formulae and explicit expressions for the corresponding global damage coefficients in Chapter 4. The performance of the 3D GDI formulae to predict the global damage states are verified in this chapter.

- ☞ Finally, the salient contributions of this research work are concluded and the discussion on the plausible development of the present work are provided in Chapter 5.

2. Rectification of Experimental Data for Cantilever Columns

Contents

2.1 Introduction

In this chapter, a mechanics-based formulation for refining experimental data is attempted to reveal the true cantilever behaviours of an axially loaded column specimen due to unidirectional lateral loading, and further, the onset of yielding and the yield strength are identified for the specimen. Different quasi-static monotonic and cyclic experimental results are considered for full-scale cantilever column specimens. Finally, the implications of extracting true

cantilever behaviour vis-à-vis the material model for the analytical prediction of experimental results are also investigated.

2.2 Details of Experiments

The experiments on axially loaded cantilever column specimens used for demonstrating the proposed methodology were carried out in a separate research work by Yadav [199]. Some essential information about the experiments is presented in this section.

2.2.1 Experimental Arrangement

Experimental results of different nonlinear monotonic and quassi-static cyclic tests on four full-scale cantilever columns subjected to a unidirectional lateral load and along with different levels of compressive axial load (as shown in Figure 2.1a) are used here. The lateral force has been simulated by a displacement controlled MTS actuator of 250 kN capacity, whereas the axial force has been simulated by another force controlled MTS actuator of 1000 kN capacity. The bottom beam, with the moment carrying capacity around four times of that of the column, is provided to achieve the fixed support condition for the cantilever column. Moreover, the bottom beam has been rigidly clamped with the strong floor with additional supports not to allow any degree of freedom (DOF) at the column base. The top end of the column is allowed to move only along the direction of the horizontal actuator and any accidental out-of-plane movement has been prevented by using a roller support mechanism during the cyclic experiments. A rigid prefabricated connection has been provided between the vertical actuator and the top surface of the column in order to facilitate the fixing arrangement of the two actuator heads with the column specimen. Figures 2.1c and 2.1d respectively show the schematic diagram of an undeformed and a deformed column specimen. It should be noted that the system has total four hinges (at B, C, D and E) and, therefore, it will behave as a mechanism in absence of the stiffness provided by the column. So the system can have infinite plausible configurations for a single pair of displacement readings of both actuators when the column stiffness is treated as unknown.

2.2.2 Details of Specimens

The geometry and reinforcement details of a typical cantilever specimen are shown in Figure 2.1b. Four tests were carried out in different combinations of loading type and compressive axial stress level (refer to Table 2.1). The yield stress, ultimate stress, and elongation of the main longitudinal bar of the column (12 mm diameter) were found to be 535 MPa, 656 MPa and 20.33%, respectively.

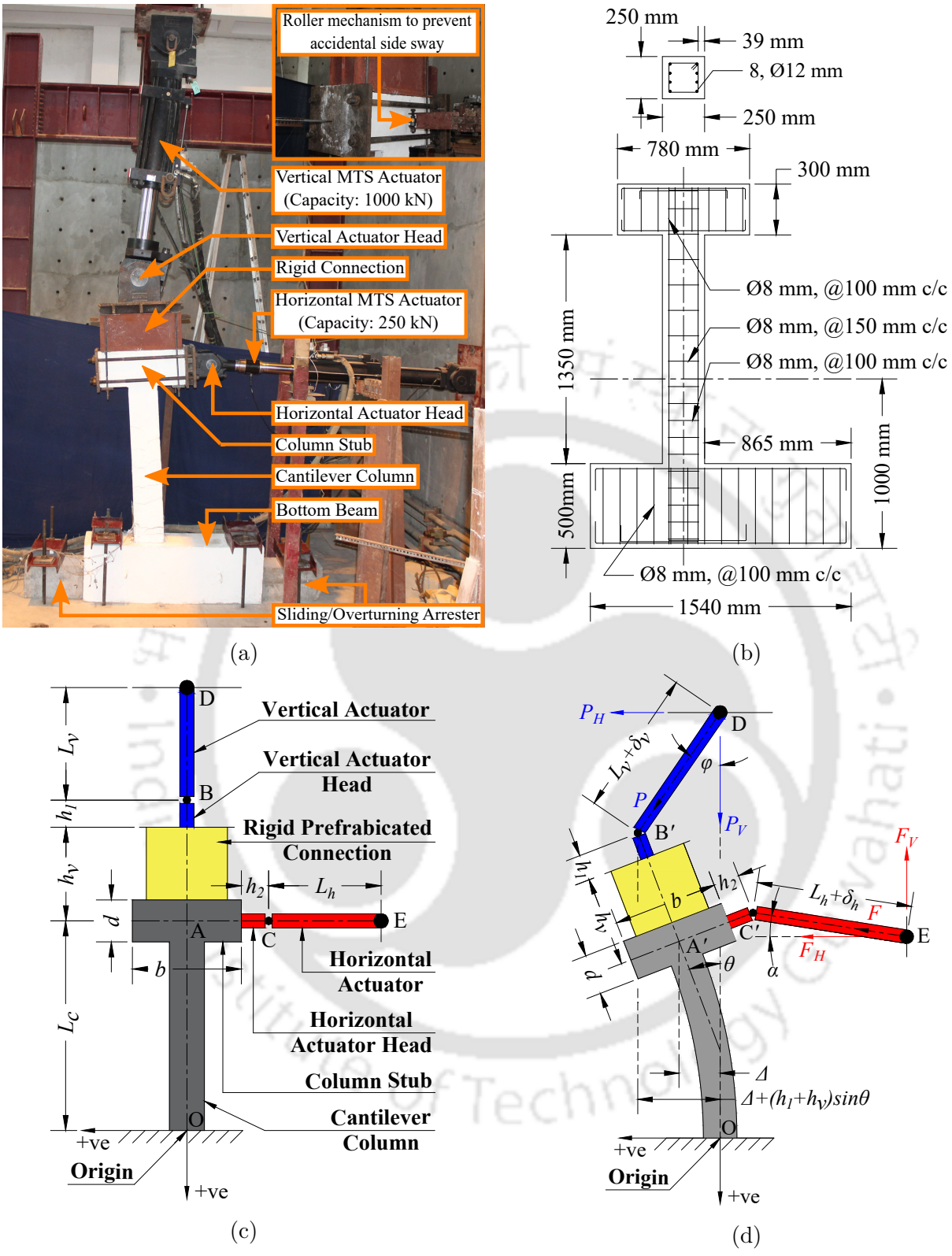

Figure 2.1: (a) Typical experimental arrangement [199], (b) reinforcement detailing of a specimen [199], (c) schematic diagram of an undeformed specimen, (d) schematic diagram of a deformed specimen

Table 2.1: Details of different experiments

Sl. No.	Nomenclature	Loading type	f_c (MPa)	f_{ck} (MPa)	N (kN)	$\rho_a = N/(f_c A_c)$	$\rho_d = N/(f_{ck} A_c)$
1	M1	Monotonic	32	25	100	0.05	0.064
2	M2	Monotonic	24	20	300	0.20	0.24
3	C1	Cyclic	32	25	100	0.05	0.064
4	C2	Cyclic	32	25	200	0.10	0.128

Source: data from Yadav [199]

Note: f_c, f_{ck} = actual and characteristic (design) compressive strength of concrete cube, respectively; N = axial compressive load; ρ_a, ρ_d = actual and design axial stress ratio, respectively; A_c: area of column cross-section.

2.3 Novel Mechanics-based Formulation for Rectification

2.3.1 Philosophy

At the beginning of the experiment, both horizontal and vertical actuators remained along the horizontal and vertical directions, respectively (refer to Figure 2.1c). After some amount of lateral displacement of the column tip, both actuators did not maintain their respective initial directions (as shown in Figure 2.1d) and both of them individually contributed to the horizontal and vertical forces acting on the column. Providing some special arrangement in order to record the column tip movement and actuator rotations during experiments is not possible in many studies, like the present case, due to laboratory constraints and high cost. Therefore, the direction of the applied forces are not known during the analysis and hence directly the lateral displacement and base-shear cannot be extracted. So, the current study is applicable and very important in those cases where such a special arrangement has not been made during the experiment. The inclined positions of the actuators result in eccentric forces with respect to the column tip and therefore an extra moment develops. This extra moment that contributes to an additional deformation of the column tip must be removed to obtain the horizontal displacement of the column tip under the ideal cantilever action subjected to lateral and axial loads only. But the exact force and deformation components are functions of the unknown tip rotation of the column, which cannot be determined directly from the force and displacement readings of actuators. Involving the lengths of actuators (i.e., the initial length plus the displacement reading), an implicit relation between the column tip rotation, θ, and the lateral displacement, Δ, of the column tip can be found by considering the displacement compatibility conditions. However, there are infinite such compatible pairs of θ and Δ given any lengths of actuators and hence, the true (and unique) solution is the one that incorporates the correct resistance offered by the column specimen against the deformation. Since the configuration depends on the loading directions of actuators and vice-versa, an iterative technique is must, which is described succinctly in Figure 2.2.

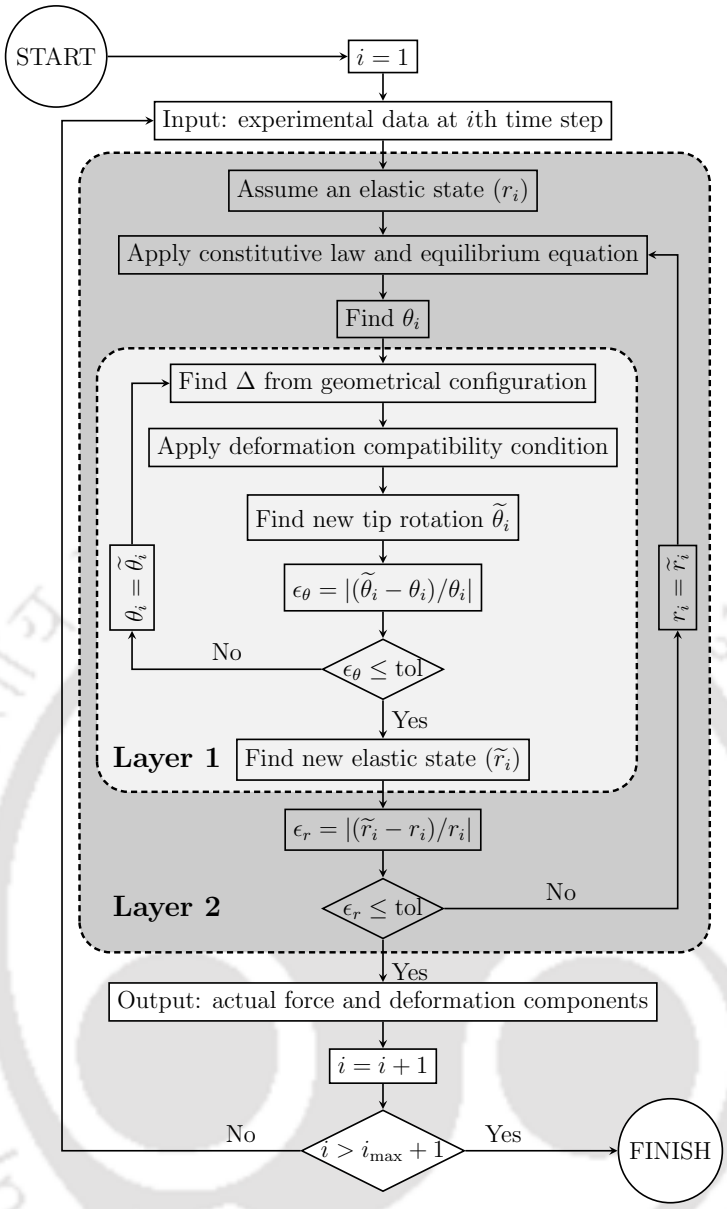

Figure 2.2: Basic iterative framework to find force and deformation components

The constitutive model essentially depends on the proportion of elastic and plastic behaviours of the specimen (which is unknown a priori), and it is quantified by a parameter, r. The parameter r is defined as the ratio between the elastic lateral and total lateral displacements. Hence, the proposed iteration procedure is nested; the inner level (i.e., Layer 1) is to achieve the solution (i.e. the unique configuration) from an assumed r at the outer level (i.e., Layer 2). The convergence for r is achieved when the inferred value of r from Layer 1, based on the elastic and plastic theories of bending, matches that of the assumed one (in Layer 2) within a specified tolerance. Thus, the rectification procedure involves a detailed mechanics-based approach, which is presented in the following sections.

2.3.2 Geometric Configuration and Deformation Compatibility

Locus of the cantilever column tip follows a curvilinear path in the case of monotonic or cyclic experiments with a large amount of displacements as shown in Figure 2.3. Here, the total tip rotation, θ and the total lateral displacement, Δ of the column comprises elastic and plastic portions, i.e.,

$$\theta = \theta_e + \theta_p \tag{2.1}$$

$$\Delta = \Delta_e + \Delta_p \quad . \tag{2.2}$$

The column tip (originally at A) would go to the location A'_p after the plastic rotation by an amount θ_p about the assumed lumped plastic hinge (O′) at the mid-height of the plastic hinge length [205]. Therefore, the length of the column, participated in the elasto-plastic deformation is taken as

$$L_o = L_c - 0.5L_p \tag{2.3}$$

where L_c is the length of the column, and L_p is the plastic hinge length (in m), which can be expressed as [205]

$$L_p = 0.08z_c + 0.022d_b f_y \quad . \tag{2.4}$$

Here z_c (in m) is the distance from the critical section to the point of contraflexure, d_b (in m) is the maximum diameter of the longitudinal reinforcement and f_y (in MPa) is the yield strength of the steel. Since Equation (2.4) is only empirical by nature, z is assumed to be L_c in the present study for simplicity. Within elastic deformation range as well, it is assumed that the portion of the column from the base to the point O′ will remain rigid so that the same formulation can work for both elastic and plastic deformations. This is not a major limitation as the elastic rotation and deformation at O′ is negligible. Now, the column tip at A'_p, in general, further rotates elastically by an amount θ_e and takes the final location at A'_{e+p}. The column tip lowers by an amount Δ_{L_c} during the total deformation, which can be expressed as

$$\Delta_{L_c} = L_o(1 - \cos\theta_p) + \Delta_e \tan\theta_p \quad . \tag{2.5}$$

Figure 2.4a shows the geometric configuration of deformed column along with the horizontal actuator only. The force components (F_H and F_V) and moment (M_F) produced at the deformed column tip, A'_{e+p} due to the inclined horizontal actuator are expressed as

$$F_H = F\cos\alpha \tag{2.6}$$

$$F_V = F\sin\alpha \tag{2.7}$$

$$M_F = F\,(h_2 + 0.5b)\sin(\theta + \alpha) \tag{2.8}$$

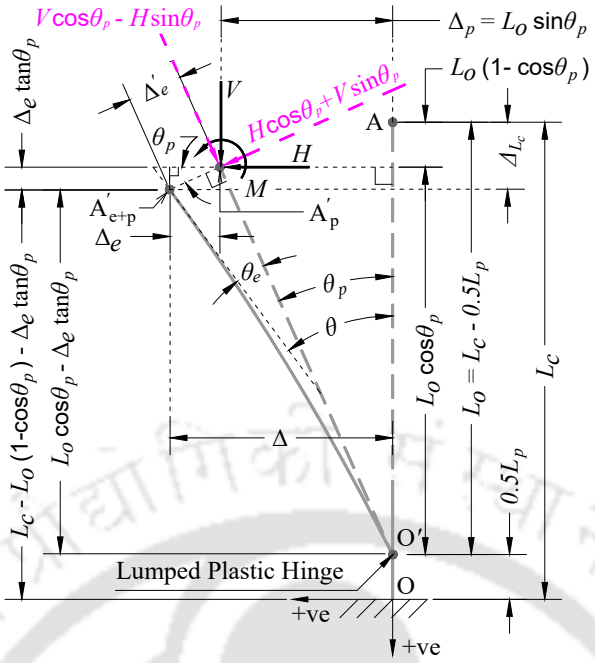

Figure 2.3: Schematic diagram for locus of cantilever column tip

where F is the horizontal actuator's force reading (i.e., the force exerted by the horizontal actuator during experiments). h_2 is the length of the horizontal actuator head, b is the width of the cantilever column stub and α is the inclination angle of the horizontal actuator with horizontal axis (refer to Figures 2.1c and 2.1d). Further, Δ and α, can be expressed from Figures 2.1c, 2.1d and 2.4a as

$$\Delta = \delta_h \cos\alpha - L_h\,(1-\cos\alpha) - (h_2 + 0.5b)\,(1-\cos\theta) \tag{2.9}$$

$$\therefore\ \alpha = \cos^{-1}\{a_1 + a_2(1-\cos\theta)\} \tag{2.10}$$

$$\text{with}\quad a_1 = \frac{L_h + \Delta}{L_h + \delta_h}\quad \text{and}\quad a_2 = \frac{h_2 + 0.5b}{L_h + \delta_h} \tag{2.11}$$

where L_h and δ_h are the initial length and the incremental displacement reading of horizontal actuator, respectively, a_1 and a_2 (and other similar terms with different subscripts to be used in the mechanics-based formulation) are geometric parameters with different values at each incremental load-step during experiment. From Triangles C′GI and C′A'_{e+p}J (Figure 2.4a) one obtains

$$\text{C}'\text{G} = (h_2 + 0.5b) - \frac{L_o(1-\cos\theta_p) + \Delta_e \tan\theta_p}{\sin\theta}\quad . \tag{2.12}$$

Now α and θ can be expressed using the triangles C′GI and C′EI as

$$\alpha = \sin^{-1}\{a_2 \sin\theta - a_3(1-\cos\theta_p) - a_4 \tan\theta_p\} \tag{2.13}$$

$$\text{with}\quad a_3 = \frac{L_o}{L_h + \delta_h}\quad \text{and}\quad a_4 = \frac{\Delta_e}{L_h + \delta_h}\quad . \tag{2.14}$$

By eliminating the parameter α from Equations (2.10) and (2.13), the following relation between θ and Δ can be obtained as

$$(a_1^2 + 2a_1a_2 + 2a_2^2 - 1) + a_4^2 \tan^2\theta_p + a_3^2(1-\cos\theta_p)^2 - 2a_2a_3\sin\theta(1-\cos\theta_p) \\ +2a_3a_4\tan\theta_p(1-\cos\theta_p) - 2a_2a_4\sin\theta\tan\theta_p - 2a_2(a_1+a_2)\cos\theta = 0 \quad . \tag{2.15}$$

Equation (2.15) serves as the deformation compatibility condition for the column specimens for small and large levels of deformations.

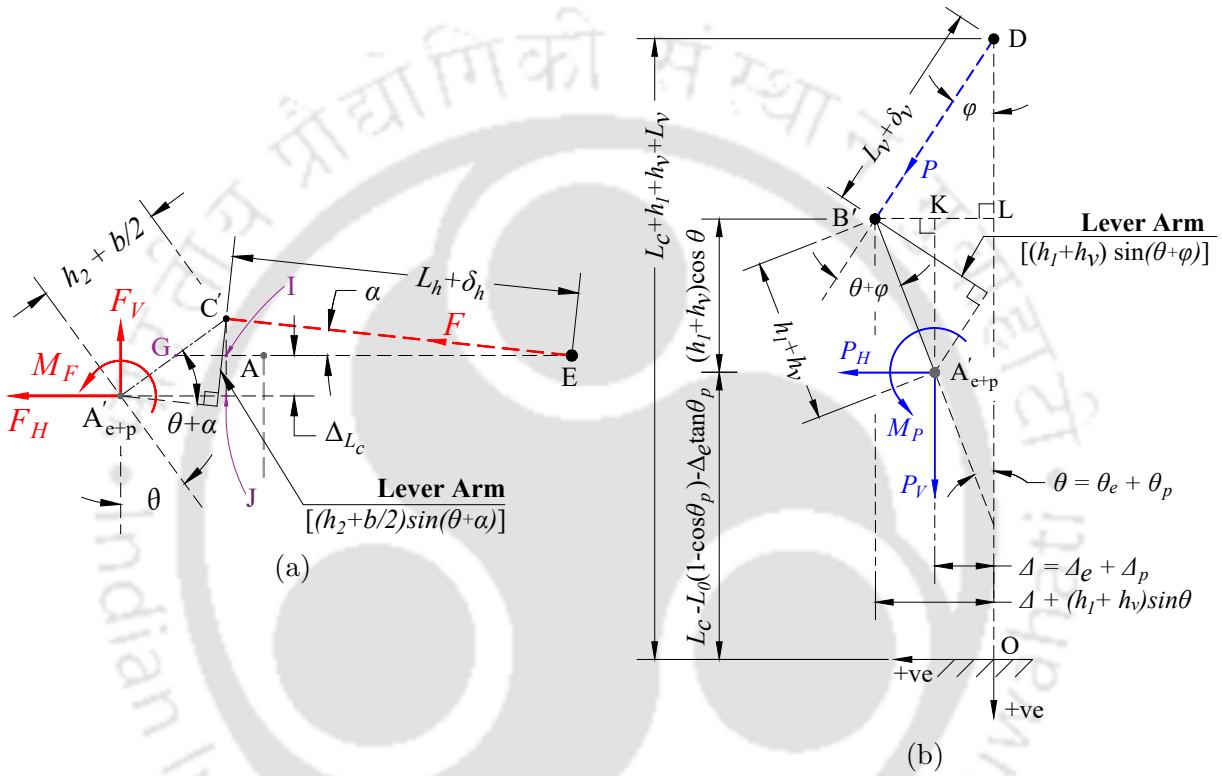

Figure 2.4: Force and moment components due to inclined positions of different actuators [refer Figure 2.1d]: (a) horizontal actuator, and (b) vertical actuator

Figure 2.4b shows the geometric configuration of the deformed column along with the vertical actuator only. The force components (P_H and P_V) and moment (M_P) produced at A'_{e+p} due to the inclined vertical actuator are expressed as

$$P_H = P\sin\varphi \tag{2.16}$$

$$P_V = P\cos\varphi \tag{2.17}$$

$$M_P = P(h_1 + h_v)\sin(\theta+\varphi) \tag{2.18}$$

where P is the vertical actuator's force reading (i.e., the force exerted by the vertical actuator during experiments). h_1 is the length of the vertical actuator head, h_v is the distance between the column tip and the bottom of the vertical actuator, and φ is the inclination angle of the

vertical actuator with vertical axis (refer to Figures 2.1c and 2.1d). The relation between φ and θ can be expressed using the triangles DB′L and A'_{e+p}B′K from Figure 2.4b as

$$\varphi = \sin^{-1}\left\{\frac{\Delta + (h_1 + h_v)\sin\theta}{L_v + \delta_v}\right\} \tag{2.19}$$

where L_v and δ_v are the initial length and the incremental displacement reading of vertical actuator, respectively. In the present study the experimentally obtained total length of the vertical actuator, $(L_v + \delta_v)$, is not used directly in Equation (2.19) not only because δ_v is not available for all the cases but also because the predicted $(L_v + \delta_v)$ can form a basis for verification of the proposed methodology when $(L_v + \delta_v)$ is available from the experimental data. The total length of the vertical actuator is predicted as

$$L_v + \delta_v = \sqrt{x_{B'}^2 + (y_{B'} - y_D)^2} \tag{2.20}$$

with

$$x_{B'} = \Delta_e + L_o \sin\theta_p + (h_1 + h_v)\sin\theta \tag{2.21}$$

$$y_{B'} = -\left\{L_c - \Delta_{L_c} + (h_1 + h_v)\cos\theta\right\} \tag{2.22}$$

$$y_D = -(L_c + h_1 + h_v + L_v) \tag{2.23}$$

where $(x_{B'}, y_{B'})$ and $(0, y_D)$ are the coordinates of the points B' and D, respectively (refer to Figure 2.4b).

2.3.3 Constitutive Laws and Equilibrium Equations

It can be seen from Figure 2.3 that a corotational formulation is adopted to inherently account for the P-Δ effect due to the plastic deformation where the local axis is aligned along the plastically deformed chord. To address the possible P-Δ effect for the additional elastic deformation (with the plastically deformed chord as reference) the geometric stiffness matrix ($\mathbf{K_g}$) is added to the basic elastic stiffness matrix ($\mathbf{K_e}$) of the column. Hence, the elastic force-deformation relationship at the column tip is expressed as

$$\begin{Bmatrix} H\cos\theta_p + V\sin\theta_p \\ M \end{Bmatrix} = (\mathbf{K_e} + \mathbf{K_g}) \begin{Bmatrix} \Delta'_e\,(=\Delta_e/\cos\theta_p) \\ \theta_e \end{Bmatrix} \tag{2.24}$$

with

$$\mathbf{K_e} = \frac{E_c I_e}{L_c^3}\begin{bmatrix} 12 & -6L_c \\ -6L_c & 4L_c^2 \end{bmatrix} \tag{2.25}$$

$$\mathbf{K_g} = -\frac{V\cos\theta_p - H\sin\theta_p}{L_c}\begin{bmatrix} 6/5 & -L_c/10 \\ -L_c/10 & 2L_c^2/15 \end{bmatrix} \tag{2.26}$$

$$H = P_H + F_H \tag{2.27}$$

$$V = P_V - F_V \tag{2.28}$$

$$M = M_P + M_F \tag{2.29}$$

where H, V and M are the net horizontal force, net vertical force and net moment acting at column tip, respectively, E_c is the elastic modulus of concrete, and I_e is the effective moment of inertia for the column specimen. By denoting $(\mathbf{K_e} + \mathbf{K_g})$ by $\mathbf{K}$ the tip deformation quantities are obtained from Equation (2.24) as

$$\begin{Bmatrix} \Delta_e/\cos\theta_p \\ \theta_e \end{Bmatrix} = \mathbf{K}^{-1} \begin{Bmatrix} H\cos\theta_p + V\sin\theta_p \\ M \end{Bmatrix} \quad . \tag{2.30}$$

So, the elastic tip lateral displacement, Δ_e, and elastic tip rotation, θ_e, can be obtained as

$$\Delta_e = \{K_{22}(H\cos\theta_p + V\sin\theta_p) - K_{12}M\}\cos\theta_p/\det(\mathbf{K}) \tag{2.31}$$

$$\theta_e = \{-K_{21}(H\cos\theta_p + V\sin\theta_p) + K_{11}M\}/\det(\mathbf{K}) \tag{2.32}$$

where K_{ij} is the element of $\mathbf{K}$ corresponding to ith row and jth column, and $\det(\bullet)$ denotes the determinant of a matrix. Here, the expression for I_e (as in Equation (2.25)) is obtained as [206, 207]

$$I_e = \left(\frac{M_{cr}}{M_{O'}}\right)^3 I_t + \left\{1 - \left(\frac{M_{cr}}{M_{O'}}\right)^3\right\} I_{cr} \leq I_t \tag{2.33}$$

$$\text{with} \quad M_{cr} = f_{cr} I_t / y_t \tag{2.34}$$

where M_{cr} is the cracked moment capacity of a column section, f_{cr} is the modulus of rupture computed as $0.7\sqrt{f_c}$ [208], y_t is the distance between the centroidal axis of the transformed section and the extreme tension fiber of the column cross-section, and $M_{O'}$ is the moment acting at the lumped plastic hinge location of the column which can be expressed (from Figure 2.3) as

$$M_{O'} = H(L_o\cos\theta_p - \Delta_e\tan\theta_p) + V\Delta + M \quad . \tag{2.35}$$

In the case of cyclic loading the effective moment of inertia is considered separately for positive and negative bending moments. The moment inertia values for cracked and transformed cantilever column section (i.e., I_{cr} and I_t, respectively) are determined by using the well-established theory of reinforced concrete [209] and I_{cr} is found to be around $0.25I_t$.

Now, the elastic portions of θ and Δ can be related as $\theta_e = c\Delta_e/L_c$, where,

$$c = \frac{\{-K_{21}(H\cos\theta_p + V\sin\theta_p) + K_{11}M\}\,L_c}{\{K_{22}(H\cos\theta_p + V\sin\theta_p) - K_{12}M\}\cos\theta_p} \quad . \tag{2.36}$$

Since the elastic portion of the displacement is not known from the experimental data, a parameter r, defined as the ratio between Δ_e and Δ, is assumed. Therefore, Δ_e can be written (using Equation (2.9)) as

$$\Delta_e = r\Delta = r\left\{\delta_h \cos\alpha - L_h(1-\cos\alpha) - (h_2+0.5b)(1-\cos\theta)\right\} \tag{2.37}$$

$$\therefore\ \cos\alpha = a_5\theta_e + a_6 + a_2(1-\cos\theta) \tag{2.38}$$

$$\text{with} \qquad a_5 = \frac{L_c}{cr(L_h+\delta_h)} \quad \text{and} \quad a_6 = \frac{L_h}{L_h+\delta_h} \quad . \tag{2.39}$$

Similarly, Δ_p, θ_p and θ can be expressed as

$$\Delta_p = (1-r)\Delta = \frac{(1-r)\theta_e L_c}{cr} \tag{2.40}$$

$$\theta_p = \sin^{-1}\left(\frac{\Delta_p}{L_o}\right) = \sin^{-1}(a_7\theta_e) \tag{2.41}$$

$$\theta = \theta_e + \sin^{-1}(a_7\theta_e) \tag{2.42}$$

$$\text{with} \quad a_7 = \frac{(1-r)L_c}{crL_o} \quad . \tag{2.43}$$

By eliminating the parameter α from Equations (2.13) and (2.38), θ_e can be solved from the following equation.

$$\begin{aligned} &2a_2^2b_4 + a_3^2b_2^2 + a_4^2b_3^2 + a_5^2\theta_e^2 + a_6^2 - 2a_2a_3b_1b_2 + 2a_3a_4b_2b_3 \\ &\quad - 2a_2a_4b_1b_3 + 2a_5a_6\theta_e + 2a_2b_4(a_5\theta_e + a_6) - 1 = 0 \end{aligned} \tag{2.44}$$

$$\text{with} \qquad b_1 = \sin\left\{\theta_e + \sin^{-1}(a_7\theta_e)\right\} \tag{2.45}$$

$$b_2 = 1 - \cos\left\{\sin^{-1}(a_7\theta_e)\right\} \tag{2.46}$$

$$b_3 = \tan\left\{\sin^{-1}(a_7\theta_e)\right\} \tag{2.47}$$

$$b_4 = 1 - \cos\left\{\theta_e + \sin^{-1}(a_7\theta_e)\right\} \quad . \tag{2.48}$$

Here, b_1, b_2, b_3 and b_4 are trigonometric parameters with different values at each incremental load-step during experiment.

It should be mentioned that Equation (2.44) combines both constitutive laws and equilibrium conditions for any given r and the true solution will be achieved when the choice of r satisfies the deformation compatibility in Equation (2.15) as well. Further, for all practical purpose the usefulness of r comes after the first time it departs from unity during which the sections are already cracked. So, by Δ_e we assume it is the recoverable displacement (while unloading) with the elastic stiffness corresponding to I_{cr}, which accounts for all forces acting on the member and Δ_p is essentially the residual displacement.

2.3.4 Iterative Solution Scheme

The Newton-Raphson method is used to solve θ_e from Equation (2.44) in the present study. Here, the parameters a_5 and a_7 are functions of c and r. At the starting of the experiment, the column tip has not been subjected to any extra moments due to zero eccentricity of the forces applied by the actuators. Also, the plastic deformation does not occur at that time. Therefore, the initial value of c is obtained from Equation (2.36) by considering $\theta_p = 0$, $M = 0$, $I_e = I_t$ and $V = P$, as

$$c_0 = \frac{6E_cI_t - PL_c^2/10}{4E_cI_t - 2PL_c^2/15} \tag{2.49}$$

which is always close to 1.5. On the other hand the initial value of r, denoted by r_0, is considered as 1.0.

For any given loading step, Equation (2.44) is used to find the value of θ_e (at the beginning of layer 2 of Figure 2.2) by obeying the constitutive laws and equilibrium conditions. Then the parameters θ_p and θ are computed using Equations (2.41) and (2.42), respectively. Equation (2.15) is used to solve the parameters iteratively (in Layer 1 of Figure 2.2) satisfying the compatibility condition. The use of constitutive laws, equilibrium and compatibility conditions leads to a unique solution of tip rotation for a particular value of assumed r. Now the value of r is computed from the converged values of the parameters using Equations (2.10), (2.19), (2.31) and (2.37), and checked with the assumed one. The nested iteration continues until the assumed r at the beginning of Layer 2 becomes the same as r obtained at the end of Layer 1. The nested iteration process is repeated for every loading step. The converged values of the parameters in the ith loading step are considered as the trial values for the $(i+1)$th step for effective convergence. The complete flowchart for the proposed mechanics-based formulation is shown in Figure 2.5.

There are a few special cases for which θ_e (or θ) cannot be solved directly from Equation (2.44). Such cases are described in what follows along with the solution strategy on a case-by-case basis.

(a) The non-dimensional parameter c cannot be solved when $K_{22}(H\cos\theta_p + V\sin\theta_p) = K_{12}M$ according to Equation (2.36). The following equations are to be used along with Equation (2.10) to determine the column tip rotation iteratively:

$$\Delta_e = \{K_{22}(H\cos\theta_p + V\sin\theta_p) - K_{12}M\}\cos\theta_p/\det(\mathbf{K}) = 0\ ;\ r = 0 \tag{2.50}$$

$$\theta_e = \{-K_{21}(H\cos\theta_p + V\sin\theta_p) + K_{11}M\}/\det(\mathbf{K}) = M/K_{22} \tag{2.51}$$

$$\Delta = \Delta_p = (L_h + \delta_h)\cos\alpha - L_h - (h_2 + 0.5b)\{1 - \cos(\theta_e + \theta_p)\} \tag{2.52}$$

$$\theta_p = \sin^{-1}\left[\frac{(L_h + \delta_h)\cos\alpha - L_h - (h_2 + 0.5b)\{1 - \cos(\theta_e + \theta_p)\}}{L_o}\right] . \tag{2.53}$$

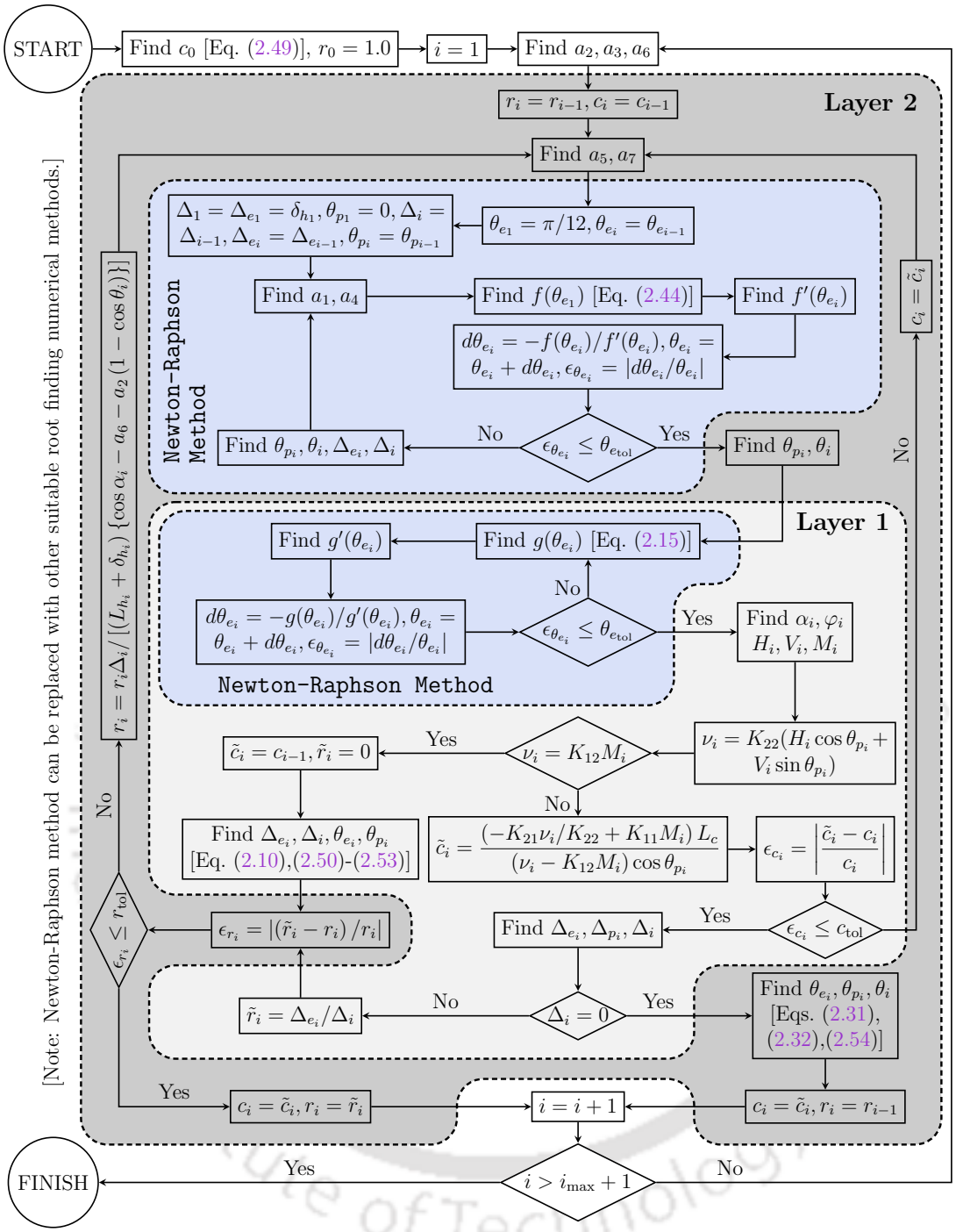

Figure 2.5: Detailed flowchart to find the rectified force and deformation components (refer to Section 2.3)

(b) The non-dimensional parameter r cannot be solved from Equation (2.37) for $\Delta = 0$. The following equations are to be used along with Equations (2.31) and (2.32) to determine the column tip iteratively:

$$\alpha = \cos^{-1}[a_6 + a_2\{1 - \cos(\theta_e + \theta_p)\}] \;;\; \Delta_p = -\Delta_e \;;\; \theta_p = \sin^{-1}\left(\frac{\Delta_p}{L_o}\right) \quad . \tag{2.54}$$

2.3.5 Displacement Rectification for Extra Tip Moment

The eccentricities of the forces applied by both actuators during an experiment produce an extra moment at the column tip. The displacement resulting from this extra moment (Δ') must be removed to obtain the rectified lateral displacement (Δ_r) due to the horizontal force component only. Therefore, Δ_r can be expressed as

$$\Delta_r = \Delta - \Delta' \cos\theta_p \tag{2.55}$$

$$\Delta' = -K_{12} M / \det(\mathbf{K}) \quad . \tag{2.56}$$

2.3.6 Validation of the Proposed Formulation

As mentioned in the previous section, the predicted instantaneous length of the vertical actuator can be used for the purpose of validation in case the actual length is available from the experimental data. For the cyclic tests C1 and C2 the actuator readings are available and hence the total lengths are known at any instant. It should be mentioned here that the overall configuration is dependent on the instantaneous total length of the vertical actuator and not on its incremental reading, so the total lengths are compared. The predicted values from Equation (2.20) are compared with the measured ones over time and the maximum error is found to be less than 0.27% for both the cases. However, this is only an indirect validation because with the same total length of vertical actuator it is possible to have a quite different geometric configuration (from the actual one) in case the constitutive model for the column is grossly simplistic.

To this end an attempt is made to directly validate the proposed method on the basis of observations of various deformation quantities. It is true that ordinary images of the specimens usually do not reveal such deformation quantities unless they are large enough to make them approximately measurable. Since the specimen for test M1 has undergone maximum deformation, the values of various deformation quantities from the image (refer to Figure 2.6) at large deformations are obtained, and these values are compared with the predicted ones using the proposed methodology at that time instant. The values of the angles of vertical and horizontal actuators with respect to their original positions (φ and α, respectively), column tip rotation (θ) and horizontal tip displacement (Δ) are tabulated in Table 2.2. In addition to the deformation quantities the base shear and base moment are computed from the actuator force readings and their observed directions by satisfying equilibrium (i.e., the base moment inherently includes the column tip moment, M, and the moment due to the P-Δ effect). The base shear and base moment computed from the proposed methodology are obtained and also compared with the experimentally obtained ones in Table 2.2. It is clear that the predicted values are reasonably acceptable, which suggests that the various idealizations made in formulating the mechanics-based model are practically valid.

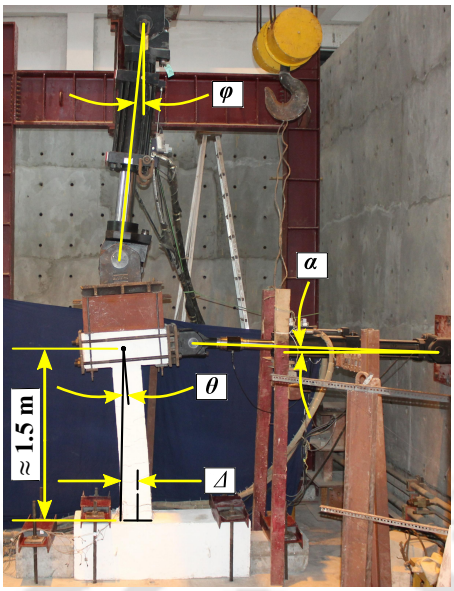

Figure 2.6: Different angles and lateral displacement from test setup for experiment M1

Table 2.2: Comparison of various deformation and force quantities obtained from the experiment and the proposed method in the case of experiment M1

Source	φ	α	θ	Δ (mm)	Base shear (kN)	Base moment (kNm)
Experiment M1	5.36°	2.09°	5.11°	141.30	18.98	56.25
Proposed method	4.97°	1.66°	6.45°	140.44	18.31	55.30

2.4 Results and Discussions

Other than the validation of the proposed algorithm, there are some subtle issues with two physically meaningful parameters, c and r. Their variation patterns with loading steps provide additional insights to the methodology and are hence discussed next.

2.4.1 Variation of the Parameter c

The parameter c represents the linear relation between the elastic tip rotation (θ_e) and the elastic portion of the actual lateral displacement (Δ_e). For monotonic experiments, c will increase monotonically (from around 1.5) and the rate of that change increases in the presence of higher axial load at the column tip (refer to Figure 2.7) as the magnitude of the acting moment at the column tip will be higher in this case. The sudden increase in the value of c in the case of monotonic experiment M1 is due to a sudden drop in the lateral force capacity of the system (refer to Figure 2.8a).

On the other hand, for cyclic experiments, c maintains a value of around 1.5 owing to small lateral drift except at certain instants, as shown in Figure 2.9. At around any such instant, the elastic lateral displacements due to the tip moment and due to the net lateral

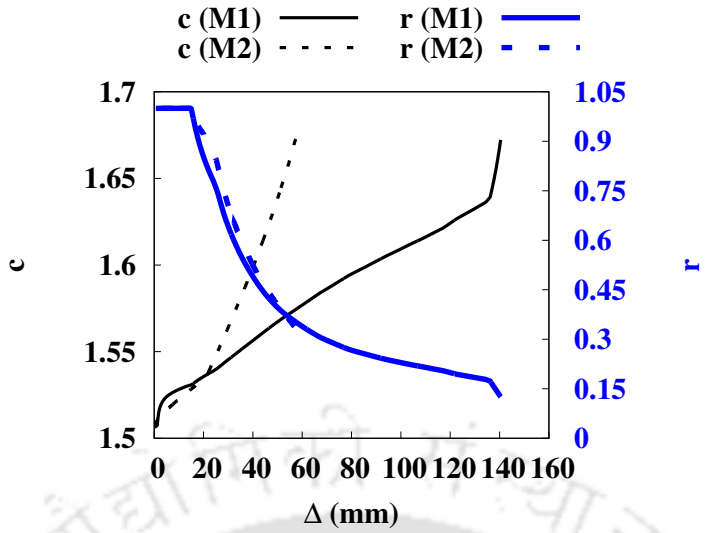

Figure 2.7: Variation of the parameters c and r with respect to Δ for the monotonic experiments

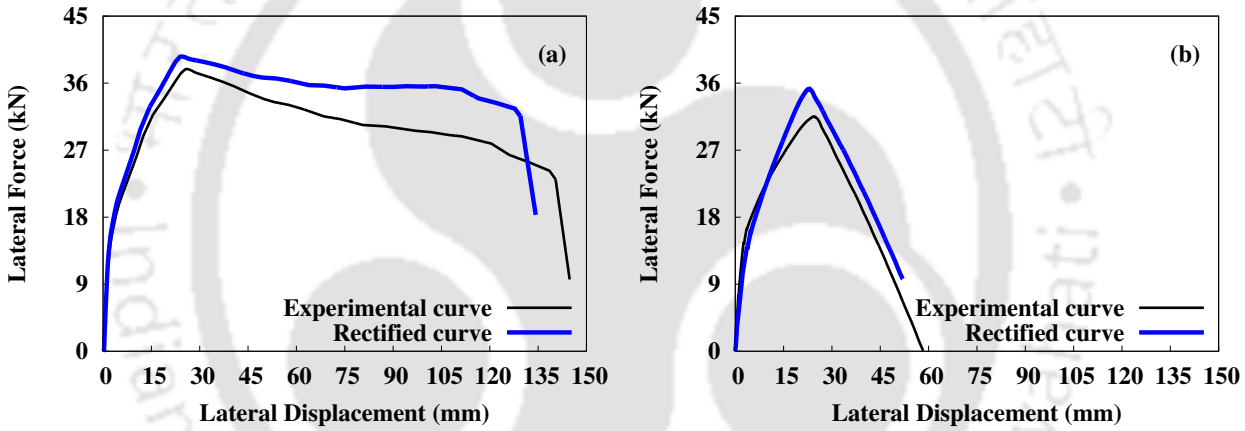

Figure 2.8: Experimental and rectified pushover curves for monotonic experiments: (a) M1, (b) M2

force become very close and opposite to each other, which generates sudden changes in the value of c, as per Equation (2.31).

2.4.2 Variation of the Parameter r

The parameter r is defined as the ratio between Δ_e and Δ. Therefore, $r = 1.0$ at the start of the experiment and gradually decreases for monotonic experiments, as shown in Figure 2.7. For cyclic experiments without any axial force, the value of r should vary for each cycle, as shown in Figure 2.10a, for the following reasons.

- When the direction of the force applied by the horizontal actuator is changed from positive to negative (i.e., Points 2 and 3 in Figure 2.10a), both Δ_e and r tend to zero and Δ is equal to the plastic displacement Δ_p. Also, the sign of Δ_e will change from positive

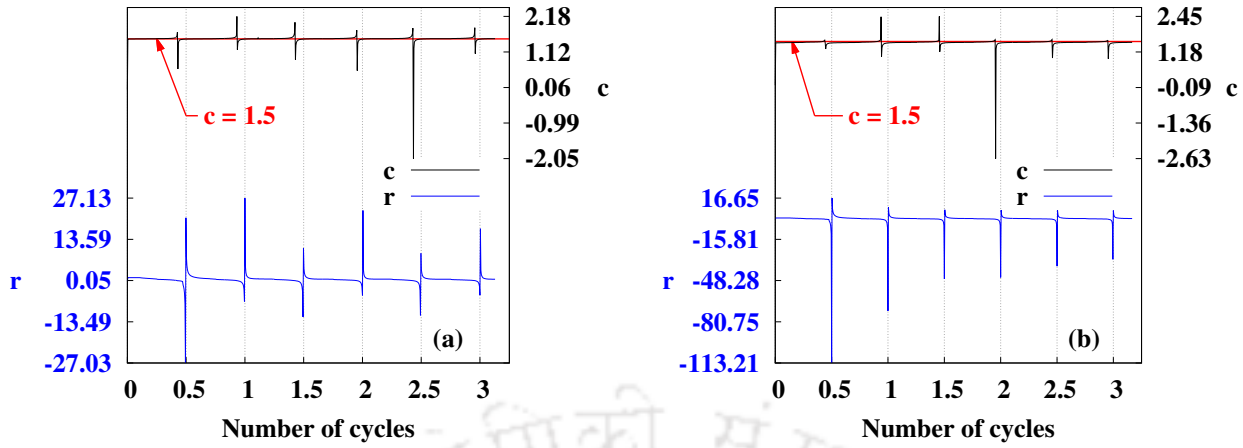

Figure 2.9: Variation of the parameters c and r within the first three cycles of tests: (a) C1, (b) C2

to negative between these two points. Therefore, theoretically, $r_2 \to +\epsilon, r_3 \to -\epsilon$, where $\epsilon \to 0$.

- Similarly, when the direction of the lateral force is changed from negative to positive (i.e., Points 7 and 8 in Figure 2.10a), the sign of Δ_e will also change from negative to positive between these two points, and the sign of Δ will be negative in this case. Hence, $r_7 \to +\epsilon, r_8 \to -\epsilon$.

- On the other hand, when the direction of the displacement of the horizontal actuator changes from positive to negative (i.e., Points 4 and 5 in Figure 2.10a), the value of the parameter r will become very large. Also, Δ will change its sign from positive to negative and Δ_e will have a negative sign between these two points. Therefore, $r_4 \ll -1, r_5 \gg +1$.

- Similarly, when the direction of the displacement of the horizontal actuator changes from negative to positive (i.e., Points 9 and 10 in Figure 2.10a), Δ will change its sign from negative to positive, while Δ_e will have positive sign between these two points. Therefore, $r_9 \ll -1, r_{10} \gg +1$.

- Points 6 and 11 in the figure represent points where r is equal to unity, i.e., where the total and recoverable lateral displacements are the same.

When some vertical load is present, $H = 0$ will not exactly correspond to $\Delta_e = 0$, hence $r = 0$ cases will not lie exactly on the Δ-axis.

Two different cycles (first cycle and an intermediate cycle) for two different cyclic experiments C1 and C2 were considered for comparison with the theoretical values described earlier and are shown in Figures 2.10b and 2.10c. The value of r changes satisfactorily for all the various conditions. Also, the variation of the parameter r with respect to the cycles of the cyclic tests will show a sudden change between Points 4 and 5, and 9 and 10

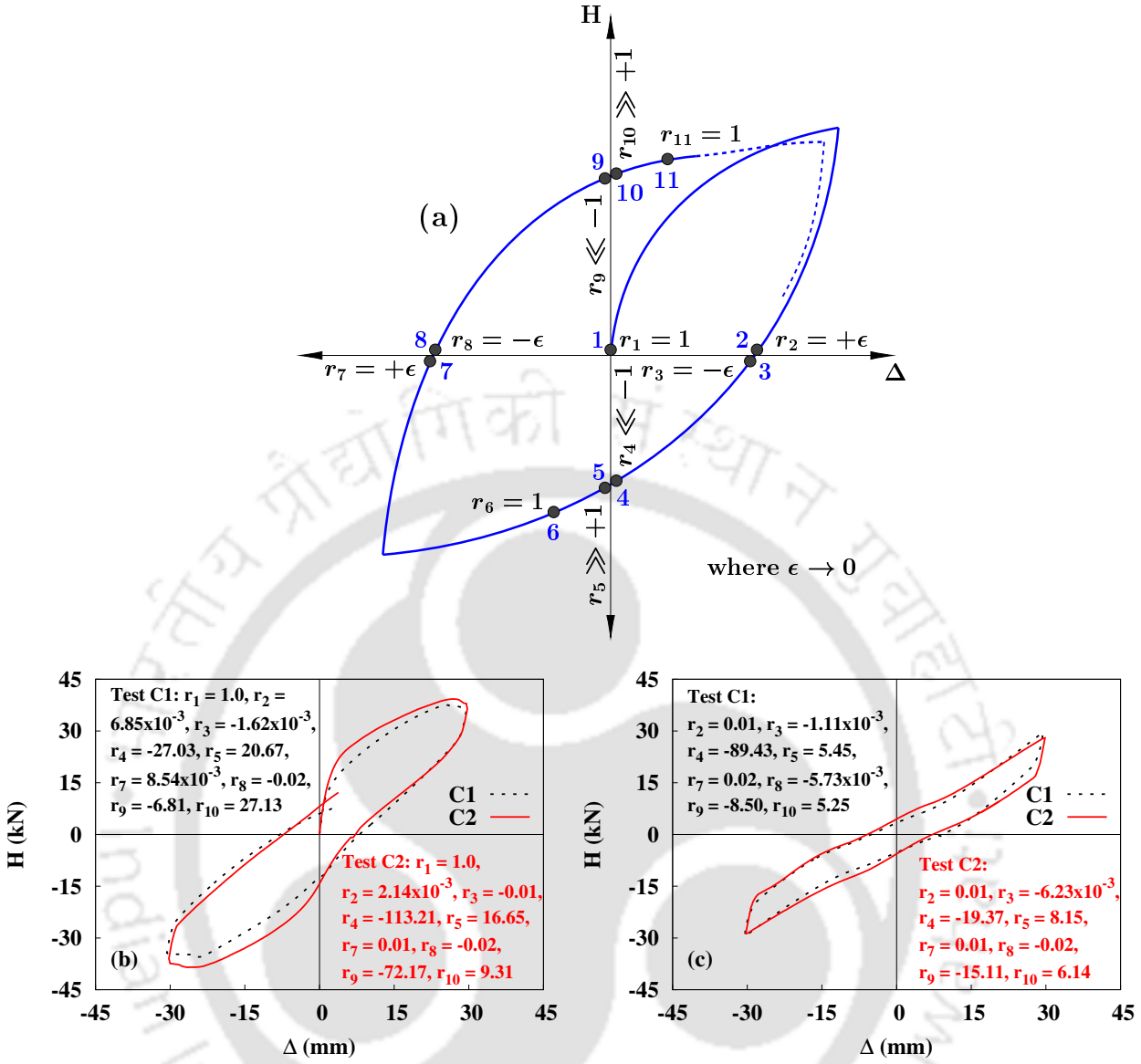

Figure 2.10: Variation of r in H-Δ plot for cyclic experiments: (a) schematic diagram, (b) first cycle of C1 and C2, (c) intermediate cycle of C1 and C2

(of Figure 2.10a), as shown in Figure 2.9, owing to a change in the direction of the lateral displacement. Since the sudden jump in the value of c takes place around $r = 0$ (near the Δ-axis), the sudden change in c is always followed by a sudden jump in r (near the H-axis), as shown in Figure 2.9.

2.4.3 Displacement Contribution from Extra Tip Moment

Table 2.3 shows the contribution of the displacement produced by the extra tip moment to Δ_e for different tests. The contributions are shown separately when H and Δ_r attain their respective maximum values. For monotonic tests, the contribution from the extra tip moment becomes significant during the post-yield behaviour of the cantilever column for high axial load. For cyclic tests, Δ_e reduces with the number of cycles because of cyclic strength

degradation. But the part of the elastic displacement produced by the tip moment does not reduce much because majority of the moment comes from the eccentricity of the axial load. Therefore, the contribution from the tip moment increases with number of cycles, especially in presence of high axial load.

Table 2.3: Contribution of displacement produced by the extra tip moment, Δ', to Δ_e

Test case	Cycle stage	at maximum H			at maximum Δ_r		
		Δ_e (mm)	Δ' (mm)	Δ'/Δ_e (%)	Δ_e (mm)	Δ' (mm)	Δ'/Δ_e (%)
M1	-	19.18	1.56	8.13	17.63	6.16	34.94
M2	-	18.89	1.69	8.95	14.70	5.51	37.48
C1	First	16.77	1.49	8.88	15.90	1.64	10.31
	Middle	13.24	1.50	11.33	13.24	1.50	11.33
	Last	12.77	1.47	11.51	12.65	1.48	11.70
C2	First	18.28	2.98	16.30	16.98	3.18	18.73
	Middle	13.10	2.93	22.37	13.07	2.98	22.80
	Last	7.75	2.75	35.48	7.35	2.77	37.69

2.4.4 Rectified Pushover Curves for Monotonic Experiments

Figure 2.8 shows the experimental and rectified pushover curves for the monotonic tests. The experimental lateral force-displacement curves correspond to F-δ_h curves, whereas the rectified ones correspond to H-Δ_r. It is found that the lateral strength of the system is underestimated where experimental data are used directly. Furthermore, δ_h has a positive contribution of displacement produced by the additional tip moment whose effect is removed from Δ_r. Hence, the displacement capacity of the system is overestimated if rectification is not performed. It was found that the amount of the underestimation of the lateral strength and the overestimation of the displacement capacity increase with increases in the axial stress ratio, as shown in Table 2.4.

Table 2.4: Comparison of lateral strengths and displacement capacities obtained from experimental curves and rectified curves for different experiments

Quantity for comparison	Experiment case			
	M1	M2	C1	C2
$F_{\max}$ (kN)	37.9	31.5	35.9, −34.0	35.8, −35.4
$H_{\max}$ (kN)	39.6	35.2	37.5, −35.5	39.3, −38.5
Percentage change in strength	4.5	11.7	4.5, 4.4	9.8, 8.8
$\delta_{\max}$ (mm)	144.8	58.3	29.8, −30.4	30.1, −30.1
$\Delta_{r_{max}}$ (mm)	134.3	52.0	28.0, −29.6	27.0, −27.8
Percentage change in displacement	−7.3	−10.8	−6.0, −2.6	−10.3, −7.6

2.4.5 Rectified Pushover Curves for Cyclic Experiments

Figure 2.11 shows the experimental and rectified cyclic pushover curves for the tests. In this case underestimation of lateral strength and overestimation of maximum lateral displacement have also been observed, especially in the presence of a high axial stress ratio (refer to

Table 2.4). The experimental curves also overestimate the amount of cumulative energy dissipated during the cyclic tests. It was found that the experimental curve produced around an 8% higher value of dissipated energy when the system is subjected to a 0.10 axial stress ratio. This discrepancy is expected to increase further with larger displacement cycles. Therefore, the use of the proposed formulation on experimental data is necessary to calibrate numerical models associated with RC frames or buildings and get realistic damage quantification of the structures from their nonlinear dynamic responses by using correct values of capacity terms (e.g., yield displacement, yield strength, ultimate displacement) and dissipated hysteresis energy.

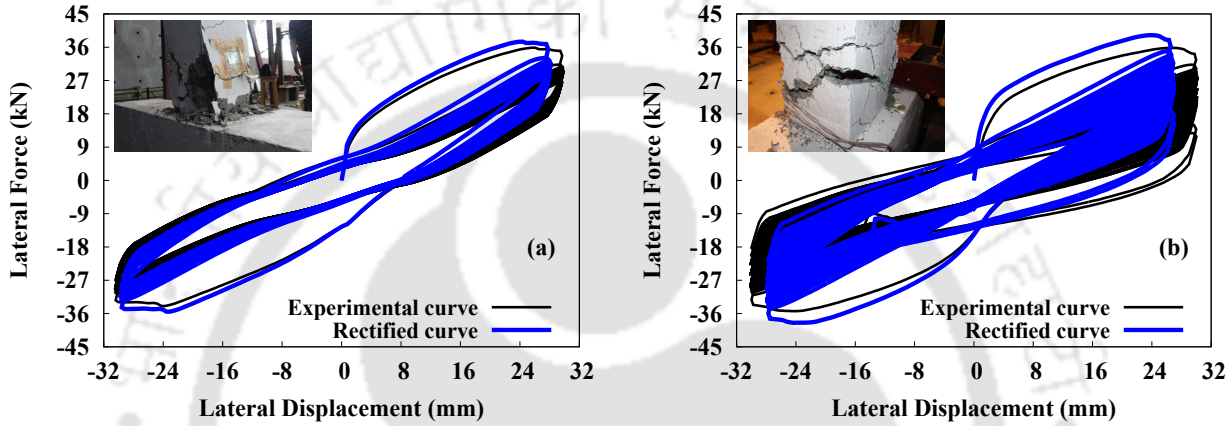

Figure 2.11: Experimental and rectified cyclic pushover curves for cyclic experiments: (a) C1, (b) C2

2.5 Practical Applications

2.5.1 Calibration of Analytical Models and Their Comparison

Two different analytical models were developed in the present research work using the OpenSees framework [210, 211]. The general details required to develop the analytical models are given in Table 2.5. The calibration of analytical model 1 was done with F-δ_h curves for different tests, whereas analytical model 2 was calibrated with H-Δ_r developed in the present study. Figures 2.12 and 2.13 show a comparison of the analytical models with the experimental results and the rectified results, respectively. The material properties used for the analytical models are compared with the actual ones obtained directly or indirectly [212–214], as shown in Table 2.6. In addition, the Giuffré-Menegotto-Pinto model [215, 216] in `Steel02` with the parameters $R_0 = 11.5, cR_1 = 0.125$, and $cR_2 = 0.15$ for analytical model 1 and $R_0 = 20.0, cR_1 = 0.925$, and $cR_2 = 0.15$ for analytical model 2 are used to capture the cyclic strength degradation of the system. It is found that some directly obtained material properties (which are more reliable than indirectly obtained material properties) of steel and

concrete (f_y, f_u, f_c) must be reduced for calibrating analytical model 1 with the experimental results, especially in the specimens with higher axial loads. On the other hand, for the present cases the rectified curves can be predicted through analytical model 2 with good accuracy using those actual material properties of concrete and steel. However, other indirectly obtained material properties may still need to be changed due to the inherent uncertainty in material models and other modeling issues. It should be mentioned that for either analytical model the axial load is kept constant and is equal to the axial load at the instant of the maximum lateral force in the corresponding experimental curve (F-δ_h or H-Δ_r).

Table 2.5: Details of analytical models for cantilever columns developed in OpenSees framework [210]

Object type	Object specific input
Material model for steel	`Steel02` [217] (uniaxialMaterial)
Material model for unconfined cover concrete	`Concrete07` [218] (uniaxialMaterial)
Material model for confined core concrete	`Concrete07` [218] (uniaxialMaterial)
SectionForceDeformation object type	`Fiber` [219, 220]
Geometric-transformation type	`Corotational` [221]
Element object type	`beamWithHinges` [222]
Number of element	1
Number of sections per element	6

Table 2.6: Comparison of material properties used for calibrating analytical model 1 and analytical model 2 with the actual properties obtained directly or indirectly

Material properties	Actual value				Analytical model 1				Analytical model 2			
	M1	M2	C1	C2	M1	M2	C1	C2	M1	M2	C1	C2
Steel:												
f_y(MPa)[a]	**535**	**535**	**535**	**535**	505	400	465	450	535	535	535	535
f_u(MPa)[a]	**641**	**641**	**641**	**641**	600	480	558	540	641	641	641	641
E_s(10^3 MPa)[a]	**216**	**216**	**216**	**216**	216	200	216	216	216	216	216	216
E_{sh}(10^3 MPa)[a]	**2.14**	**2.14**	**2.14**	**2.14**	2.14	2.14	2.14	2.14	2.14	2.14	2.14	2.14
ϵ_{sh}(10^{-3})[a]	**5.23**	**5.23**	**5.23**	**5.23**	5.23	5.23	5.23	5.23	5.23	5.23	5.23	5.23
ϵ_u(10^{-2})[a]	**11.6**	**11.6**	**11.6**	**11.6**	11.6	11.6	11.6	11.6	11.6	11.6	11.6	11.6
Concrete:												
f_c(MPa)[a]	**32**	**24**	**32**	**32**	32	20	32	25	32	24	32	32
E_c(10^3 MPa)[b]	27.7	24.6	27.7	27.7	27.7	21.6	27.7	25.0	27.7	24.6	27.7	27.7
f_{cu}(MPa)[b]	25.7	18.7	25.7	25.7	25.7	13.8	25.7	18.0	25.7	18.7	25.7	25.7
f_{cc}(MPa)[b]	35.6	28.1	35.6	35.6	35.6	24.4	35.6	27.0	35.6	28.1	35.6	35.6
ϵ_{cu}(10^{-3})[b]	1.9	1.8	1.9	1.8	1.9	1.6	2.0	2.0	1.9	1.8	1.9	1.9
ϵ_{cc}(10^{-3})[b]	5.5	6.2	5.5	5.5	5.5	6.5	4.6	4.6	5.5	6.2	4.6	4.6

Note: Numbers in bold font represent the directly (or experimentally) obtained values of material properties that remain unchanged in the case of analytical model 2. f_u = ultimate strength of steel; E_s = initial elastic modulus of steel; E_{sh} = initial strain hardening modulus of steel; ϵ_{sh} = strain corresponding to initial strain hardening; ϵ_u = strain corresponding to ultimate stress; f_{cu} = unconfined concrete compressive strength; f_{cc} = confined concrete compressive strength; ϵ_{cu} = unconfined concrete strain at f_{cu}; ϵ_{cc} = confined concrete strain at f_{cc}.

[a] Directly obtained material properties, [b] Indirectly obtained material properties.

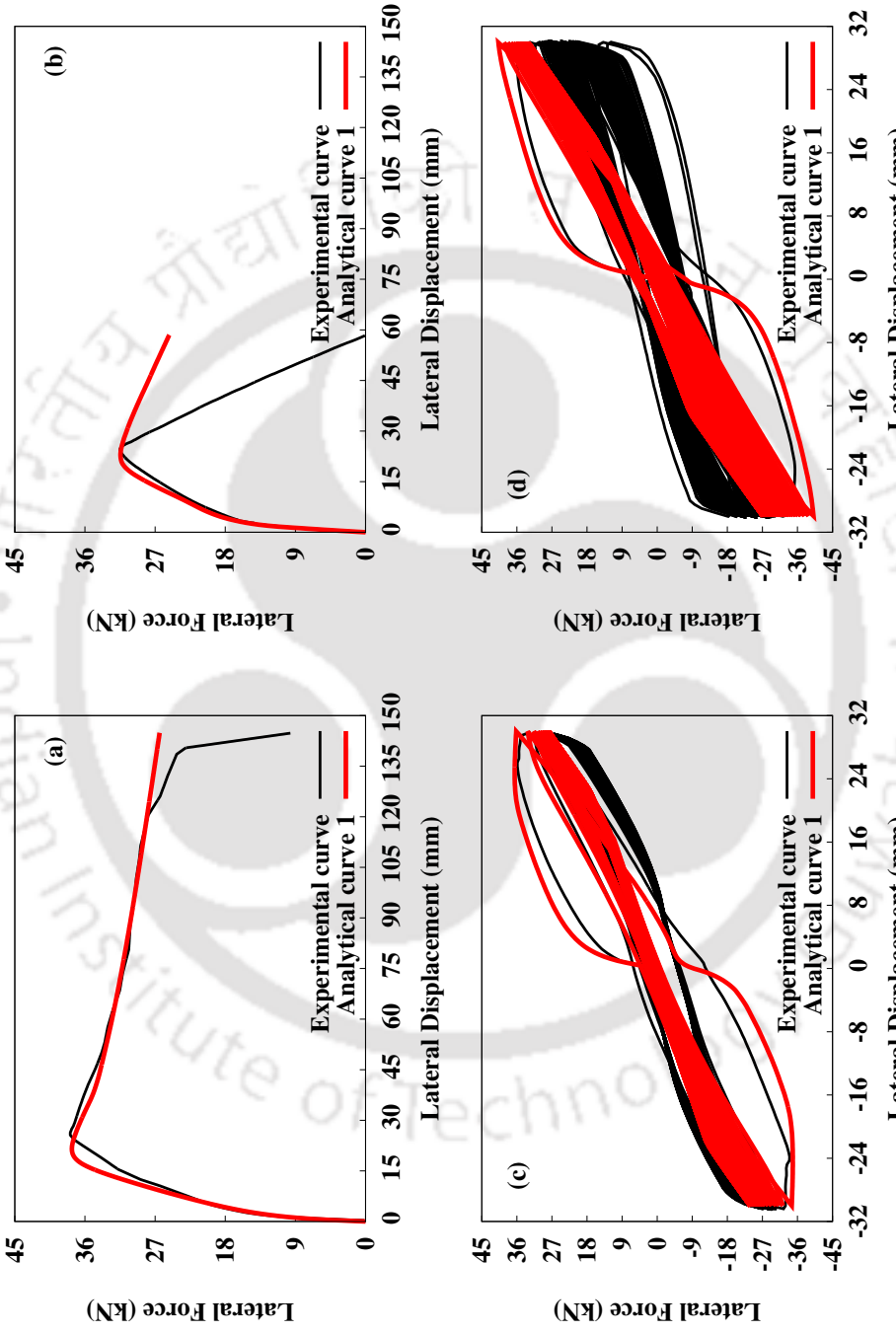

Figure 2.12: Comparison of the experimental and analytical F-δ_h curves for different tests: (a) M1, (b) M2, (c) C1, (d) C2

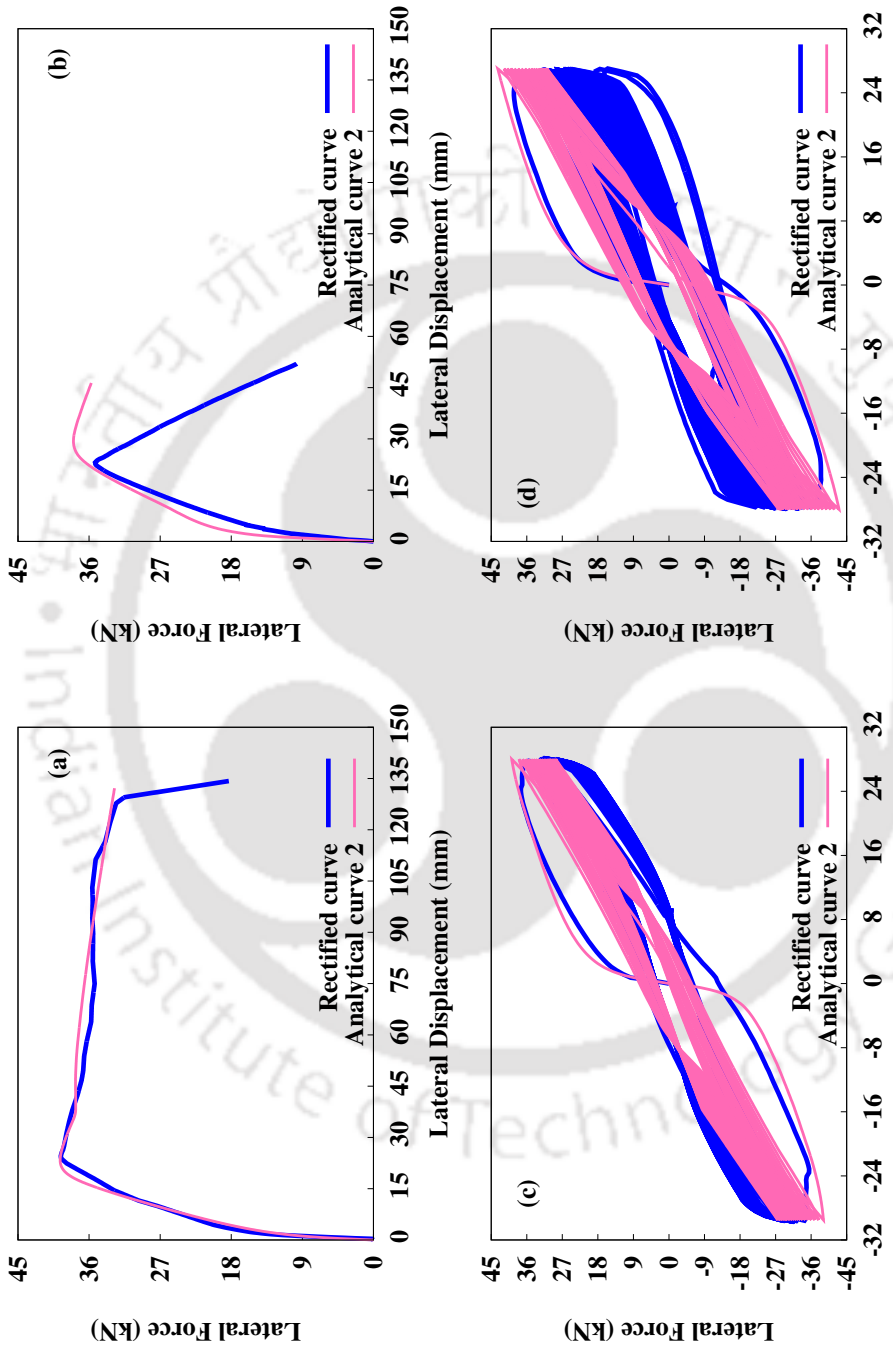

Figure 2.13: Comparison of the rectified and analytical H-Δ_r curves for different tests: (a) M1, (b) M2, (c) C1, (d) C2

2.5.2 Yield Parameters from Rectified Monotonic Pushover Curves

On the basis of the rectified pushover curve, the yield displacement and the yield strength can be estimated from r when it first reduces from unity, as shown in Figure 2.14. The elastic and plastic portions of Δ_r are also shown with respect to the duration of the experiment along with the rectified lateral force, H. The yield parameters are comparable with those obtained from a widely accepted empirical method [223], where the yield forces and yield displacements for M1 and M2 are determined to be 33.20, 30.93 kN and 15.03, 17.28 mm, respectively. The estimated values from the proposed method also show the expected trend of increasing yield strength (when normalized by f_c) with increasing axial load ratio [224]. The proposed estimate is free of any empirical/heuristic approach usually employed in finding the yield parameters of RC members.

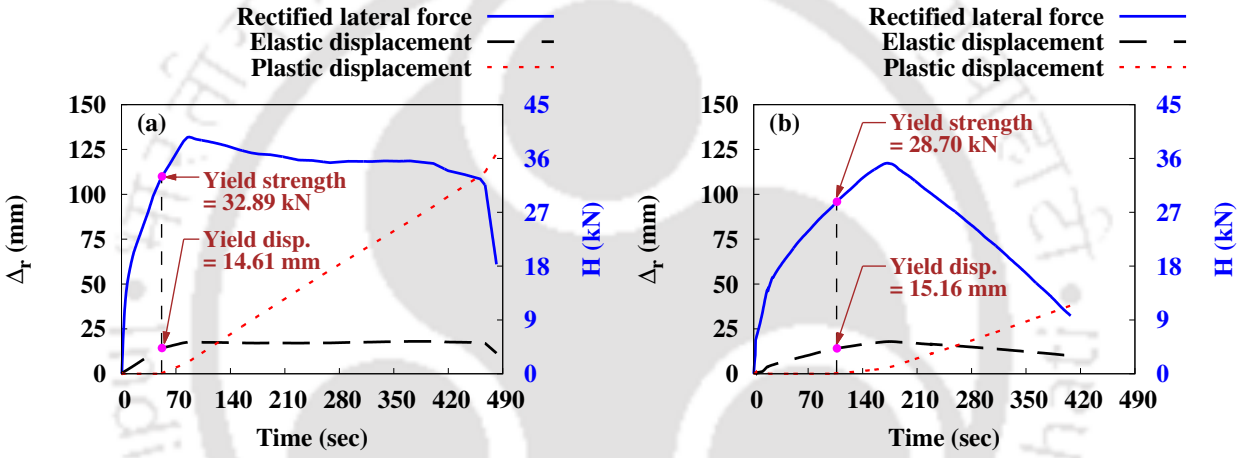

Figure 2.14: Estimation of yield parameters for different monotonic experiments from rectified pushover curves: (a) M1, (b) M2

2.6 Conclusions

Monotonic and cyclic tests on RC cantilever columns are usually carried out under unidirectional lateral loading and axial loading with different axial stress ratios. In most experimental setup the true cantilever behaviour is altered due to the fixing arrangement of the actuator heads with the specimen. Moreover, some interaction between the servo-controlled actuators through the specimen results in incorrect interpretation of lateral load behaviour of columns under combined axial and unidirectional lateral loading leading to further inaccuracies in capacity estimation. In the present study, a new mechanics-based approach is introduced to rectify the recorded behaviour of axially loaded RC columns subjected to unidirectional lateral loading by reckoning the effects of fixity and interactions between inclined horizontal and vertical actuators. Validation of the proposed methodology using a past experimental study [199] indicates that the rectified experimental recordings represent the true cantilever

nature of the tested column specimens. Following major conclusions can be drawn from the study.

- Using the proposed methodology it is possible to find out the elastic and plastic deformation separately at the member level from the experimental data. So, the yield displacement and yield strength can be estimated from the onset of plastic deformation. Thus, the proposed method can address the difficulties to find the location of the yield point and the yield strength due to the inherent nonlinearity of the RC section.

- An overall underestimation of the lateral strength, overestimation of the lateral displacement capacity, and overestimation of dissipated hysteresis energy of cantilever columns during various monotonic and cyclic tests are observed if the experimental data are not rectified. Further, the discrepancy of the lateral strength, displacement capacity and dissipated energy increases rapidly with higher axial stress ratio. This affects the nonlinear plastic behaviour (and the seismic damage estimation) of any column, designed using ductility-based design methods.

- The proposed method is independent of the incremental displacement readings of the vertical actuator that works on the force-based mechanism. The proposed method requires only the force readings of the vertical actuator and both displacement and force readings of the horizontal actuator to work, without compromising any computational effort.

- It is observed that the analytical models used for predicting the lateral load behaviour of cantilever columns can be calibrated with the rectified experimental data without changing the experimentally obtained strength related material properties. However, because of uncertainties in various material and element models some others indirect (derived) material properties have needed to be changed for the purpose of calibration.

In the current study several simplifications are made in the constitutive model in order to find various closed form relationships among unknown variables. A more accurate mechanics-based model (e.g., by considering bond-slip and distributed plasticity) can lead to more refined estimate for the true cantilever behaviour. The results of the present study may prove to be very useful in predicting the true response of RC columns in those cases when it is not possible to make some special arrangements to accurately measure the column tip movement and actuator rotations throughout the experiments.

3. Combined GDI formulae using recorded floor-displacement data for 2D RC frames

Contents

3.1 Introduction

In this chapter, a novel methodology has been proposed to predict the dissipated hysteresis energy-based weighted average [80] of modified Park and Ang-type 2D local damage model, $LDI_{2D\text{-}\mathrm{ST}}$ (refer to Table 1.1), at global level (denoted by $GDI_{2D\text{-}\mathrm{ST}}$ hereafter) using the floor-displacement measurements of an instrumented building (during an earthquake) as demand parameters instead of using the responses at section levels of the building obtained by nonlinear time-history analysis. A Park and Ang-type damage model, as mentioned, is chosen here because it is widely used for damage computation of RC structures [17, 25]. In this way, the complex and computationally demanding nonlinear time-history analysis of a building can be completely avoided in the estimation of $GDI_{2D\text{-}\mathrm{ST}}$ values. The capacity parameters for a structure or its members can be obtained using either a representative finite element model or the corresponding section properties, depending on the capacity parameter.

A finite element model is mandatory for estimating the global response-related capacity terms of a frame (e.g., ultimate displacement, displacement ductility) with the help of nonlinear static analysis or pushover analysis, whereas section properties (such as section dimensions, reinforcement arrangement, material properties) are sufficient to get the sectional response-related capacity terms for individual members (e.g., ultimate curvature, curvature ductility).

The proposed method can be used to predict $GDI_{2D\text{-ST}}$ values for the buildings equipped with acceleration measuring sensors after transforming the recorded responses into displacement values following the double integration approach in time domain [225] or frequency domain [226], whereas for the buildings equipped with displacement sensors the recorded responses can be used directly. Two different combined GDI formulae using the new methodology are proposed here for estimation of $GDI_{2D\text{-ST}}$ of 2D RC building frames. The difference in those formulae is the type of capacity parameters required in the evaluation of GDIs, i.e., global displacement ductility or curvature ductility of columns. Multilinear regression analyses and standard statistical tests are carried out to find explicit expressions (considering the variability of frames and ground motions) for the regression coefficients or the GDCs available in the GDI formulae and check the legitimacy of the physics-based non-cumulative and cumulative terms used in the formulae. Therefore, the GDIs estimated using the formulae map, through their regressed coefficients, the $GDI_{2D\text{-ST}}$ values. Although the application of the proposed method does not require nonlinear time-history analysis, the output of the latter is used in the present study for computation of $GDI_{2D\text{-ST}}$ [80] through the LDIs [1] at different plastic hinge locations. Nonlinear time-history analysis is also used to synthesize the floor-displacement responses because it is not possible to have a set of recorded floor-displacement data for systematically varying ground motion intensities for any given structure [227], which is very much necessary for training and validation purposes for any proposed regression model. For the practical usefulness of the proposed method in the field of structural engineering, the performances (in terms of accuracy, precision and recall measures) of the 2D GDI formulae to predict the post-disaster restoration-based global damage condition (i.e., no damage, repairable, irreparable and collapse) of a building from the estimated GDI values are compared with the damage conditions obtained using the limiting values [1] of modified Park and Ang damage model.

3.2 Details of Two-dimensional Reinforced Concrete Frames and Unidirectional Ground Motions

The nonlinear dynamic response obtained using various combinations of different types of 2D RC building frames and different spectrum-compatible unidirectional ground motions (DSCUGMs) are used in the present study for the training and validation purposes of the GDI evaluation method. The following sections briefly discuss the necessary details of the

considered 2D frames and the unidirectional ground motions.

3.2.1 Details of 2D RC Frames

Ten different 2D RC frames with two or five numbers of storeys are considered in this study. Those frames will be referred as sample frames in this thesis. Schematic details of a representative 2D frame with N_s number of storeys and N_b number of bays are shown in Figure 3.1. So, the frame has total $(N_s + 1)$ number of floors and the nth floor is termed as Floor n, e.g., the ground floor (GF) and the roof are termed as Floor 0 and Floor N_s, respectively. Similarly, the bays of the frame are represented by Bay m with m ranging from 1 to N_b as shown in the figure. Height of each story and length of each bay are denoted by h and l, respectively. The displacement DOF associated with the nth floor ($n \geqslant 1$) is denoted by $u_n(t)$. Table 3.1 shows the geometrical details of the ten sample frames considered for the present study. The provisions of IS 456: 2000 [208] and IS 13920: 2016 [228] are used to design the beams and the columns of the frames with external loading as per IS 875 (Part 1 and 2): 2008 [229, 230] and IS 1893 (Part 1): 2016 [3]. M25 grade concrete (with f_{ck} as 25 MPa and E_c as 25000 MPa) and Fe500 grade steel (with f_y as 500 MPa and E_s as 200 GPa) are used as material properties. The nomenclatures representing different sections of beams and columns (floor-wise) for all sample frames and the corresponding cross-sectional details are given in Table 3.1 and Figure 3.2, respectively.

Table 3.1: Details of different sample frames used for training or validation purpose

Sl. No.	Frame	N_s	N_b	h (m)	l (m)	Floor	Nomenclature of sections		Used for
							Beam	Column	
1	2F2B	2	2	3.0	4.0	1, 2	B1	C1	Training
2	2F3B	2	3	3.5	5.0	1, 2	B2	C2	Training
3	2F4B	2	4	3.0	4.0	1, 2	B1	C1	Training
4	2F5B	2	5	3.2	4.5	1, 2	B2	C3	Validation
5	2F6B	2	6	3.0	4.0	1, 2	B1	C1	Training
6	5F1B	5	1	3.0	4.0	1, 2	B3	C4	Training
						3, 4	B3	C5	
						5	B3	C6	
7	5F2B	5	2	3.2	5.0	1, 2, 3	B4	C7	Validation
						4, 5	B4	C8	
8	5F3B	5	3	3.0	4.0	1, 2	B3	C4	Training
						3, 4	B3	C5	
						5	B3	C6	
9	5F4B	5	4	3.5	4.5	1, 2, 3	B5	C9	Training
						4, 5	B5	C10	
10	5F5B	5	5	3.0	4.0	1, 2	B3	C4	Training
						3, 4	B3	C5	
						5	B3	C6	

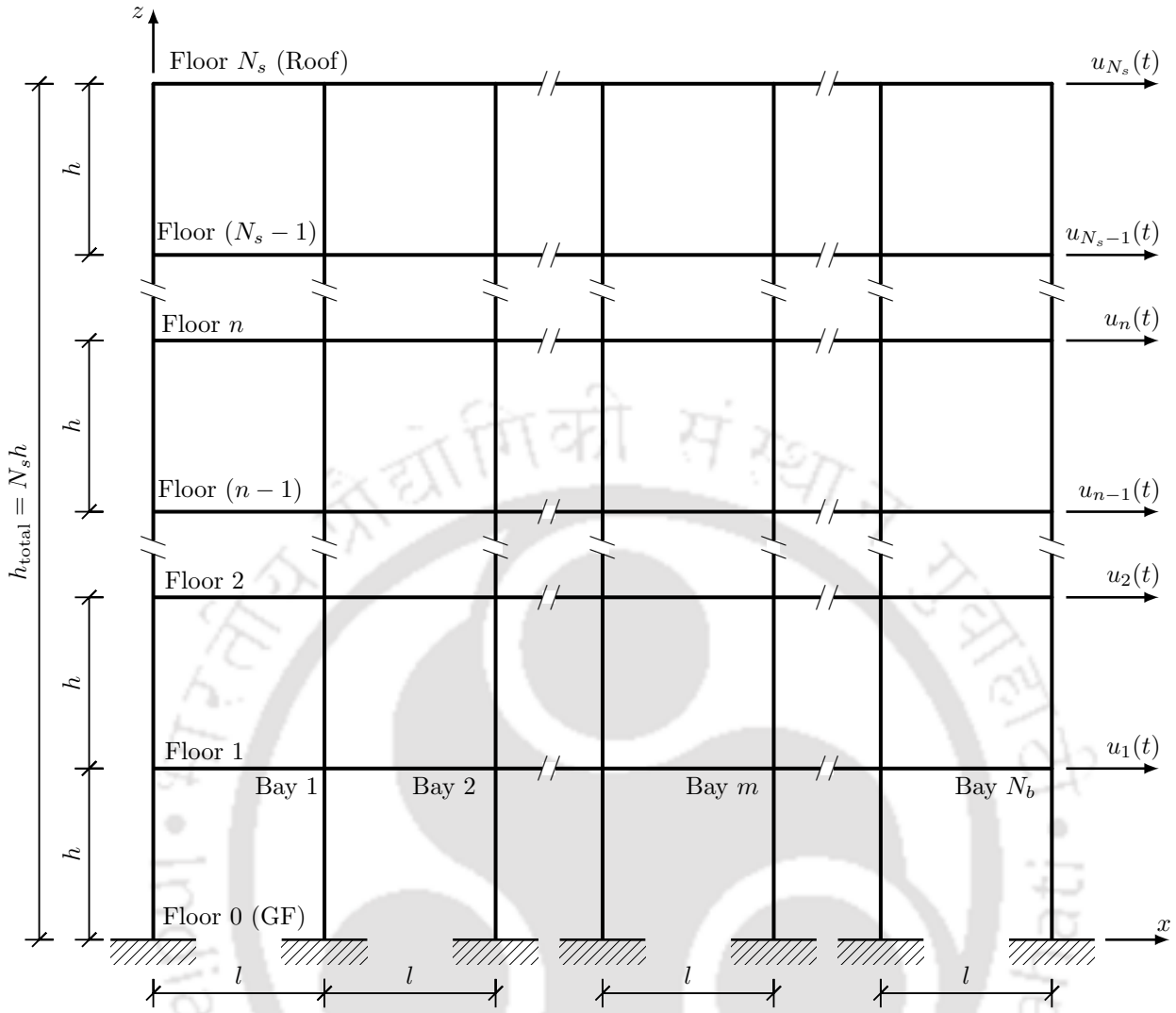

Figure 3.1: The schematic details of a generic 2D frame considered in the study

In this study, total ten numbers of finite element models corresponding to the sample frames are developed, among which the responses of eight finite element models are arbitrarily selected for the training purposes of the new method for GDI evaluation, and response of the other two finite element models are selected for the validation purpose (refer to Table 3.1). Further, the sample frames used for training and validation purposes will be termed training frames and validation frames, respectively, in the present study. The finite element models are developed using OpenSees framework [210] with the help of general details as shown in Table 3.2. The Giuffré-Menegotto-Pinto model [215, 216] in `Steel02` [217] with the values of f_y as 500MPa, E_s as 200GPa and the strain hardening ratio as 0.05 is used to develop the finite element models. The values for the parameters controlling the stress-strain transition during elastic to plastic behaviour (i.e., R_0, cR_1 and cR_2) associated with the analytical model 2 (calibrated with rectified experimental data as discussed in Subsection 2.5.1) are used in the finite element models. This will facilitate realistic damage characterization of the numerical

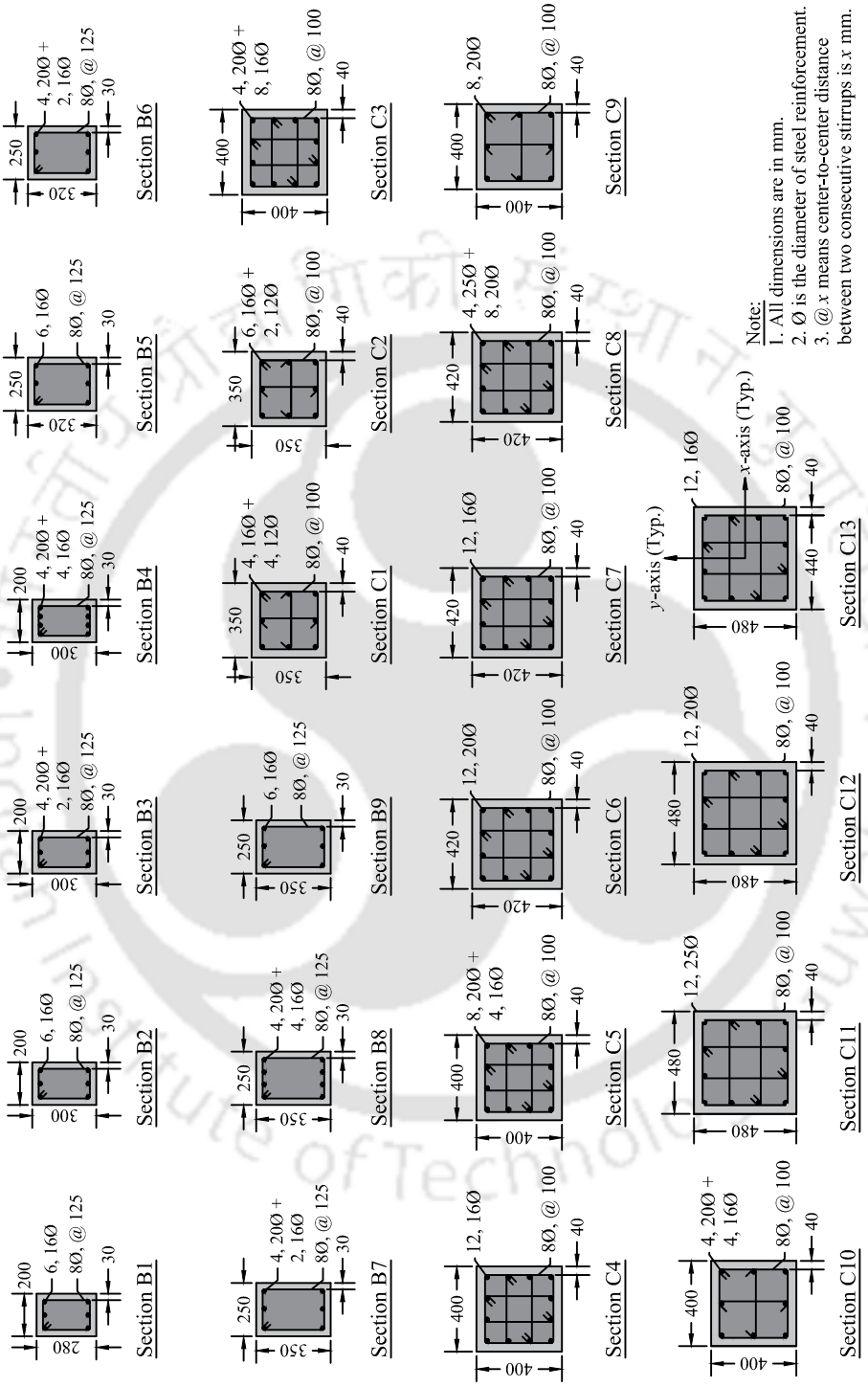

Figure 3.2: Cross-sectional details of different beam and column sections used in the sample RC frames (refer to Table 3.1)

models. The Chang-Mander stress-strain relationship [213, 214] in `Concrete07` [218] with $f_c = 25$ MPa is used to reproduce the behaviour of unconfined (cover) concrete and confined (core) concrete for the finite element models. The `beamWithHinges` [222] is used to model each beam and column to capture the material nonlinearity where the flexural plastic hinges will numerically form at a distance of one-half of the plastic hinge length (computed using Equation (2.4)) from either end of a flexural member.

Table 3.2: Details of finite element models for 2D RC frames developed in OpenSees framework [210]

Sl. No.	Object type	Object-specific input
1	Material model for reinforcement	`Steel02` [217]
2	Material model for unconfined cover concrete	`Concrete07` [218]
3	Material model for confined core concrete	`Concrete07` [218]
4	Geometric-transformation type for columns	`PDelta` [231]
5	Geometric-transformation type for beams	`Linear` [232]
6	SectionForceDeformation object type	`Fiber` [219, 220]
7	Element object type	`beamWithHinges` [222]

3.2.2 Details of Unidirectional Ground Motions

12 different unidirectional ground motions with different values of their strong motion duration as per Trifunac and Brady [233] are considered in the present study. The ground motions are taken from the PEER database [234], and some of their basic details are given in Table 3.3. Further, these motions are made compatible with design spectra [235] specified in IS 1893 (Part 1): 2016 [3] for three different types of soil conditions (hard soil, medium stiff soil and soft soil) to get structural responses from nonlinear time-history analysis due to design unidirectional ground motions. Hence, a total of 36 DSCUGMs are produced from 12 original ground motions. The comparisons of the design spectra [3] with the pseudo spectral accelerations or PSAs (for 5% damping) of the DSCUGMs for different types of soil conditions are shown in Figure 3.3. There are many ground motion selection methods available in literature based on scenario-specific information (e.g., earthquake magnitude, source-to-site distance, soil profile) or process-specific information (e.g., spectral properties or intensity measures of GM) to obtain DSCUGMs [236]. Those methods are mainly used for the purpose of designing structures by finding the mean (or the median or the maximum) response of a structure for a set of DSCUGMs selected such that the discrepancies in the nonlinear dynamic responses due to the DSCUGMs are reasonably low. However, such methods are not implemented here to select the considered ground motions (as shown in Table 3.3) before making them response spectra-compatible. This way, the performance of the new method for the evaluation of GDI can be examined due to the variability in the nonlinear dynamic responses of the sample frames due to arbitrarily selected ground motions. Among

Table 3.3: Details of different unidirectional ground motions

Sl. No.	Motion ID	Earthquake	Date	Recording station	Strong motion duration (s)	Peak ground acceleration (g)	Component (deg)	Used for
1	UGM01	Loma Prieta	18/10/1989	CDMG station 58373	15.08	0.089	090	Training
2	UGM02	Loma Prieta	18/10/1989	USGS station 1161	20.18	0.113	137	Training
3	UGM03	Kern County	21/07/1952	USGS station 135	31.78	0.042	090	Training
4	UGM04	Loma Prieta	18/10/1989	BV 5, Callens Ranch	17.60	0.069	220	Training
5	UGM05	Loma Prieta	18/10/1989	USGS Station 1652	15.62	0.064	250	Training
6	UGM06	Cape Mendocino	25/04/1992	CDMG station 89324	15.34	0.386	270	Training
7	UGM07	Cape Mendocino	25/04/1992	CDMG station 89156	16.08	0.663	090	Training
8	UGM08	Yorba Linda	03/09/2002	La Habra & Monte Vista	10.88	0.025	090	Training
9	UGM09	Park Field	28/06/1966	CDMG station 1016	26.56	0.063	320	Training
10	UGM10	Stone Canyon	04/09/1972	S.C. Observatory	3.94	0.213	177	Training
11	UGM11	Yorba Linda	03/09/2002	CSU Fullerton Grounds	14.12	0.029	090	Validation
12	UGM12	Yorba Linda	03/09/2002	Lake View & Riverdale	7.20	0.043	168	Validation

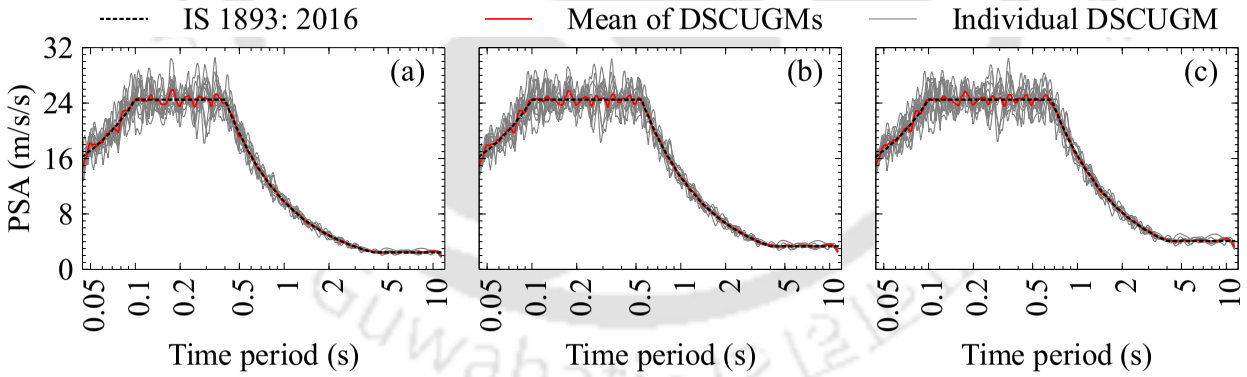

Figure 3.3: Comparisons of design spectra [3] with the PSAs (for 5% damping) of the DSCUGMs when the local soil type is (a) hard, (b) medium stiff, and (c) soft

all DSCUGMs, 30 DSCUGMs are selected randomly for the training purpose of the GDI evaluation method, and the remaining six DSCUGMs are selected for the validation purpose as shown in Table 3.3. Further, the DSCUGMs used for training and validation purposes will be called training DSCUGMs and validation DSCUGMs, respectively, in the present work.

3.3 New Method for Evaluation of 2D GDI

A new methodology utilizing the measured floor-displacement response of an instrumented building during any seismic activity as demand parameters is proposed in the present study to estimate the $GDI_{2D\text{-ST}}$ values. The main advancement in the new methodology is the use of floor-displacement measurements directly instead of conventionally used numerically computed section-level responses (e.g., sectional stress and strain resultants) due to seismic loading, which requires nonlinear time-history analyses of finite element models. Based on the new methodology, two different non-decreasing and non-dimensional combined GDI formulae are attempted in the following subsections. Among the two GDI formulae, one uses displacement ductility (global-level information) of an RC frame, whereas the other one uses curvature ductility (section-level information) of all columns present in the frame as capacity parameters. Also, according to the standard seismic design methodology, a structure is designed in such a manner that its ductility capacity is more than the ductility demand corresponding to a DSCUGM. Consequently, the structural deformability can be assumed to be strongly correlated with the product of ductility capacity and spectral displacement associated with the fundamental period of the structure.

3.3.1 2D GDI based on Displacement Ductility of Columns

A finite element model for a 2D RC frame is required to get the capacity terms used in the displacement ductility-based combined global damage index ($GDI_{2D\text{-}1}$) for the frame. The formula to find $GDI_{2D\text{-}1}$ value from the global responses of the frame has been introduced as

$$GDI_{2D\text{-}1} = \lambda_{2D\text{-}1}\frac{\langle \max|u_{N_s}(t)| - u_y\rangle}{u_u - u_y} + \psi_{2D\text{-}1}\sum_{n=1}^{N_s}\left[\frac{\sum_{s=1}^{T_d/\Delta t}\{(u_n(s\Delta t) - u_{n-1}(s\Delta t)) - (u_n((s-1)\Delta t) - u_{n-1}((s-1)\Delta t))\}^2}{(\bar{\mu}_{d_n}\cdot S_d)^2}\right] \tag{3.1}$$

$$\text{with} \qquad \langle \max|u_{N_s}(t)| - u_y\rangle = \begin{cases} \max|u_{N_s}(t)| - u_y, & \text{if} \quad \max|u_{N_s}(t)| > u_y \\ 0, & \text{otherwise} \end{cases} \tag{3.2}$$

$$\bar{\mu}_{d_n} = \frac{\sum_{d=1}^{C_{\text{frame}}} \left(F_n^{(d)} \cdot \mu_{d_n}^{(d)} \right)}{\sum_{d=1}^{C_{\text{frame}}} \left(F_n^{(d)} \right)} \tag{3.3}$$

where $\lambda_{2D\text{-}1}$ and $\psi_{2D\text{-}1}$ are the GDCs for $GDI_{2D\text{-}1}$, $u_{N_s}(t)$ is the measured roof displacement time-history of a frame, u_u is the ultimate displacement value of the frame, u_y is the yield displacement value of the frame, T_d is the total duration of displacement time-history record, Δt is the small-time interval for the recorded response, s is the index to represent incremental time-steps, $u_n(s\Delta t)$ is the displacement value for Floor n of the frame (refer to Figure 3.1) measured at time $s\Delta t$, $\bar{\mu}_{d_n}$ is the weighted average (based on the axial load demand of columns due to gravity loads) of displacement ductility values for all columns situated between Floor n and Floor $(n-1)$, $F_n^{(d)}$ and $\mu_{d_n}^{(d)}$ are the axial load demand due to gravity loads and the displacement ductility value, respectively, for the dth column between Floor n and Floor $(n-1)$, $C_{\text{frame}}(= N_b + 1)$ is the total number of columns present at each floor of the frame, and S_d is the spectral displacement value (obtained using the design response spectrum [3]) corresponding to the fundamental period (T_p) of the frame.

The first term of Equation (3.1) accounts for the consumption of structural deformability, whereas the second term accounts for the consumption of energy dissipation capacity. The non-cumulative part of $GDI_{2D\text{-}1}$ (or Equation (3.1)) is chosen to produce non-zero damage only when the building response exceeds its elastic range, similar to the modified Park and Ang damage index [1]. The global force-displacement relationships (or pushover curves) obtained from the nonlinear static analyses of the finite element models due to the static lateral load profile, as recommended in IS 1893 (Part 1): 2016 [3], are used to find u_u and u_y values (as shown in Table 3.4) here. The pushover curves (with the lateral displacement normalized by total height) for the considered sample frames are shown in Figure 3.4. The yield displacement of the equivalent and global elasto-plastic system with reduced stiffness corresponding to 75% of the ultimate lateral strength of the building [223], and the ultimate displacement corresponding to the 30% strength reduction after the occurrence of the ultimate lateral strength [237] are considered as u_y and u_u, respectively. The value of $\mu_{d_n}^{(d)}$ is obtained from the force-displacement relationship for the corresponding column under the action of $F_n^{(d)}$. For this purpose, nonlinear static analysis of a 2D line element with three DOFs (i.e., axial, transverse and rotational) at two end nodes and nonlinear material properties is sufficient to get the required response of a column. The yield displacement value for a column is obtained when either the strain of the longitudinal reinforcement (at the section near the plastic hinge location) reaches its yield limit or the confined concrete strain (at the extreme compression fiber of the section near the plastic hinge location) reaches its elastic strain limit [238]. Similarly, the ultimate displacement value is obtained when either the longitudinal reinforcement strain or the confined concrete strain reaches the corresponding ultimate limit first [238]. For column sections with multiple reinforcement layers at a face, the

strain at the center of gravity of the reinforcement layers will be considered for determining the corresponding displacement capacity parameters. Also, the rectified force-displacement responses (after removing the effects due to experimental arrangements as discussed in Section 2.3) obtained from a monotonic pushover test of a cantilever column of half the length of the actual one to match a symmetric double-curvature deformation profile with correct axial load and unidirectional lateral load can be used to determine the displacement capacity parameters. For estimating floor-wise displacement ductility ($\bar{\mu}_{d_n}$), the axial load demand of each column due to gravity loads is chosen as the weighing function to provide greater importance to the damage of a member, which will affect the global structural failure most. T_p values for the sample frames are calculated using eigenvalue analyses of the corresponding finite element models developed in the present study and provided (along with other necessary parameters for estimating $GDI_{2D\text{-}1}$) in Table 3.4.

Table 3.4: Different global and sectional parameter values of sample frames required for $GDI_{2D\text{-}1}$

Sl. No.	Frame	$\bar{\mu}_{d_n}$					T_p (s)	u_y (mm)	u_u (mm)
		$n=1$	$n=2$	$n=3$	$n=4$	$n=5$			
1	2F2B	6.076	6.981	×	×	×	0.655	86.31	700
2	2F3B	5.381	6.432	×	×	×	0.778	116.38	560
3	2F4B	5.841	6.699	×	×	×	0.667	88.38	480
4	2F5B	5.378	6.450	×	×	×	0.643	93.22	410
5	2F6B	5.838	6.711	×	×	×	0.672	82.35	290
6	5F1B	4.500	4.583	4.750	5.364	5.818	1.252	210.17	915
7	5F2B	4.075	4.149	4.393	5.054	5.378	1.400	234.57	1530
8	5F3B	4.195	4.274	4.648	4.987	5.762	1.230	197.83	975
9	5F4B	3.924	4.013	4.328	4.721	5.253	1.414	240.84	1340
10	5F5B	4.121	4.199	4.623	4.897	5.748	1.226	194.40	950

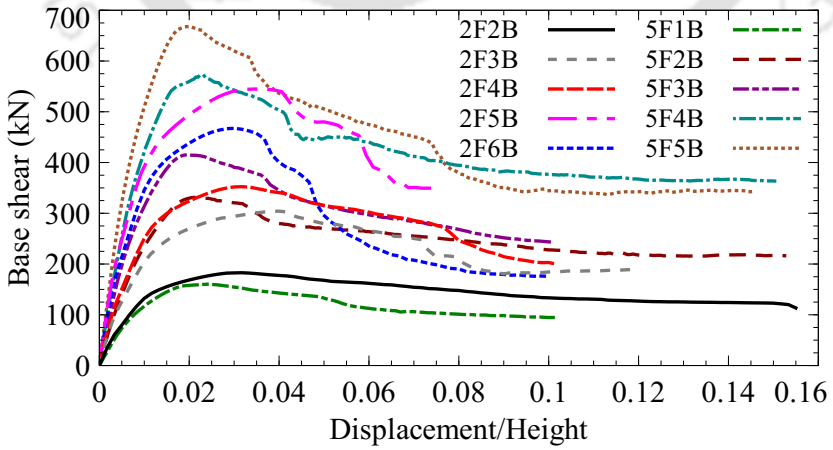

Figure 3.4: Pushover curves for different example 2D RC frames

3.3.2 2D GDI based on Curvature Ductility of Columns

The estimation of the curvature ductility-based combined global damage index ($GDI_{2D\text{-}2}$) value for a 2D building frame does not require any finite element model. The formula to get $GDI_{2D\text{-}2}$ value from the global responses of a frame has been introduced as

$$GDI_{2D\text{-}2} = \lambda_{2D\text{-}2}\frac{\max|u_{N_s}(t)|}{\bar{\mu}_\phi \cdot S'_d} + \psi_{2D\text{-}2}\sum_{n=1}^{N_s}\left[\frac{\sum_{s=1}^{T_d/\Delta t}\{(u_n(s\Delta t) - u_{n-1}(s\Delta t)) - (u_n((s-1)\Delta t) - u_{n-1}((s-1)\Delta t))\}^2}{\left(\bar{\mu}_{\phi_n} \cdot S'_d\right)^2}\right] + \gamma_{2D\text{-}2} \tag{3.4}$$

$$\text{with} \quad \bar{\mu}_{\phi_n} = \frac{\sum_{d=1}^{C_{\text{frame}}}\left(F_n^{(d)} \cdot \mu_{\phi_n}^{(d)}\right)}{\sum_{d=1}^{C_{\text{frame}}} F_n^{(d)}} \quad \text{and} \quad \bar{\mu}_\phi = \frac{\sum_{n=1}^{N_s}\left[\left(\sum_{d=1}^{C_{\text{frame}}} F_n^{(d)}\right) \cdot \bar{\mu}_{\phi_n}\right]}{\sum_{n=1}^{N_s}\left(\sum_{d=1}^{C_{\text{frame}}} F_n^{(d)}\right)} \tag{3.5}$$

where $\lambda_{2D\text{-}2}$, $\psi_{2D\text{-}2}$ and $\gamma_{2D\text{-}2}$ are the GDCs for $GDI_{2D\text{-}2}$, $\bar{\mu}_\phi$ is the weighted average of curvature ductility values for all columns of a frame, S'_d is the spectral displacement value [3] corresponding to the fundamental period (T'_p) of the frame, $\bar{\mu}_{\phi_n}$ and $\mu_{\phi_n}^{(d)}$ are the weighted average of the curvature ductility values for all columns and the curvature ductility value for the dth column, respectively, between Floor n and Floor $(n-1)$. Here, the axial load demand of each column due to gravity is used as the weighing function to estimate the values of $\bar{\mu}_\phi$ and $\bar{\mu}_{\phi_n}$ similarly as in the case of $\bar{\mu}_{d_n}$.

The first part of Equation (3.4) will produce some damage to the building while the floor-displacement responses are within the elastic range as the recoverable displacement portion is not removed from both the denominator and the numerator of that part. Therefore, another coefficient $\gamma_{2D\text{-}2}$ is included in $GDI_{2D\text{-}2}$ to make it consistent with the modified Park and Ang damage index [1]. For computing $\mu_{\phi_n}^{(d)}$ value of each column section from their moment-curvature relationship, the yield and the ultimate curvatures are obtained following the same material strain-based rules [238] (as described in Subsection 3.3.1) used to get similar displacement capacity parameters for individual column members. Moment-curvature relationship for a column section (with the corresponding axial load demand due to gravity loads) can be generated using the section geometry and the nonlinear material properties [238]. Unlike the displacement ductility-based 2D GDI, T'_p values are estimated from the eigen analysis of the sample frames, assuming them as shear buildings with masses lumped at each floor [239] for $GDI_{2D\text{-}2}$ (refer to Appendix A). The values of $\bar{\mu}_\phi$, $\bar{\mu}_{\phi_n}$ and T'_p for the sample frames are given in Table 3.5.

Table 3.5: Different global and sectional parameter values of sample frames required for $GDI_{2D\text{-}2}$

Sl. No.	Frame	$\bar{\mu}_{\phi_n}$					$\bar{\mu}_{\phi}$	T'_p (s)
		$n=1$	$n=2$	$n=3$	$n=4$	$n=5$		
1	2F2B	10.364	14.422	×	×	×	11.539	0.432
2	2F3B	10.422	14.344	×	×	×	11.561	0.472
3	2F4B	9.314	13.368	×	×	×	10.497	0.462
4	2F5B	10.873	14.710	×	×	×	11.993	0.403
5	2F6B	9.046	13.216	×	×	×	10.266	0.474
6	5F1B	6.147	6.708	9.000	10.310	12.611	7.716	0.522
7	5F2B	5.315	5.982	6.853	9.592	11.463	6.661	0.629
8	5F3B	5.463	6.060	7.889	9.505	12.196	6.968	0.593
9	5F4B	5.292	5.930	6.803	9.493	11.238	6.601	0.657
10	5F5B	5.298	5.904	7.622	9.313	12.100	6.788	0.614

3.3.3 Estimation of Required Global Damage Coefficients

The structural responses of the eight finite element models (developed for training frames as per Table 3.1) due to 30 training DSCUGMs (refer to Table 3.3) are obtained by carrying out nonlinear time-history analyses using OpenSees [210]. The section-level responses of those models are then used to calculate the LDI value for each plastic hinge according to the modified Park and Ang 2D damage index formula, $LDI_{2D\text{-ST}}$ [1, 124], as shown in Table 1.1. The value for the parameter β_{KRL} (representing the energy-based strength degradation of the material in the case of cyclic loading) is taken as 0.15 in the present study for structural members designed against seismic loading and accordingly provided with reinforcements for achieving ductile behaviour (refer to the discussions about β_{PA} and β_{KRL} in Subsection 1.2.1.1). The global damage index ($GDI_{2D\text{-ST}}$) value for a frame is calculated from the computed LDI values for all plastic hinges present in the frame using the dissipated hysteresis energy as the weighing factor [80] as.

$$GDI_{2D\text{-ST}} = \frac{\sum_{p=1}^{P_h} \left(LDI_{2D\text{-ST}_p} \cdot E_{2D\text{-}h_p} \right)}{\sum_{p=1}^{P_h} \left(E_{2D\text{-}h_p} \right)} \tag{3.6}$$

where P_h is the total number of plastic hinges present in the frame, $LDI_{2D\text{-ST}_p}$ is the LDI value for the pth plastic hinge and $E_{2D\text{-}h_p}$ is its total dissipated hysteresis energy due to uniaxial bending.

In the present study, each finite element model is analysed at least 20 times for a particular DSCUGM with different scale factors so that the $GDI_{2D\text{-ST}}$ values for the frame due to the factored DSCUGMs are distributed between 0 (i.e., no damage) and 1 (i.e., damage signifying collapse [124]) at intervals of around 0.05. In this way, the complete range of the $GDI_{2D\text{-ST}}$ values (to represent the light damage, the moderate damage, the strong damage and the

collapse state) for a frame due to a particular DSCUGM can be encapsulated. Therefore, each frame is analysed at least 200 times (for 10 training DSCUGMs per soil type) in the case of a particular soil type. The responses from those nonlinear time-history analyses are used to obtain the GDCs or regression coefficients (refer to Equations (3.1) and (3.4)) in the univariate multiple linear regression method (by minimizing the corresponding least squares function) individually for each pair of a frame and a soil type. For the regression analyses, the $GDI_{2D\text{-ST}}$ values are considered as the dependent (or response) variable, whereas the displacement-based (non-cumulative) part and the equivalent energy-based (cumulative) part present in the GDI formulae (i.e., $GDI_{2D\text{-}1}$ and $GDI_{2D\text{-}2}$) are considered as the independent (or predictor) variables.

The regressed GDCs apply to the individual pairs of training frame and soil type only, and hence, for wider applicability, there is a requirement to come up with more explicit expressions for the GDCs for any combination of a 2D frame and a soil type. To achieve this target, another set of regression analyses have been performed on the values of GDCs (obtained from 24 individual regression analyses for all combinations of eight training frames and three different soil types) with global properties of a frame, e.g., fundamental periods, total height, the ratio of the number of bays to that of floors, and the soil types as the independent variables.

3.4 Results and Discussions

3.4.1 Statistical Analyses for 2D GDIs

Results of the regression analyses for evaluating the GDCs, along with some other supporting results, are discussed here. For this purpose, three different indices, namely i, j and k, are used here for efficient representation of various results in the cases of GDI formulae and different combinations of training frame and soil type. The index i takes values equal to 1 and 2, and is used to represent the two GDI formulae (i.e., $GDI_{2D\text{-}1}$ and $GDI_{2D\text{-}2}$), respectively. The index j ranges from 1 to 3, and represents the hard soil, the medium stiff soil and the soft soil, respectively. The index k ranges from 1 to 8, and represents different training frames as shown in Tables 3.6 and 3.7. The values of the GDCs, $\lambda_{2D\text{-}i}^{(j,k)}$ and $\psi_{2D\text{-}i}^{(j,k)}$, associated with the ith 2D GDI formula and corresponding to the combination of the jth soil type and the kth frame are estimated for the complete ranges of i, j and k using regression analyses (as discussed in Section 3.3), whereas $\gamma_{2D\text{-}i}^{(j,k)}$ values are estimated for $i = 2$ (i.e., for $GDI_{2D\text{-}2}$) and complete ranges of j and k. The estimated values of those coefficients are provided in Tables 3.6 and 3.7. The values of the coefficients $\gamma_{2D\text{-}2}^{(j,k)}$ are found negative for all training cases as they offset the non-zero damage caused by the peak elastic response of any frame.

Since the proposed combined GDI evaluation method is the first of its kind, carrying out some statistical tests of hypotheses about the regression model parameters are obligatory for

Table 3.6: Different statistical results for $GDI_{2D\text{-}1}$

Sl. No.	i	j	Frame	k	$\lambda_{2D\text{-}i}^{(j,k)}$	$\psi_{2D\text{-}i}^{(j,k)}$	$\gamma_{2D\text{-}i}^{(j,k)}$	$q_{2D}^{(j,k)}$	$f_{0,2D}^{(i,j,k)}$	$\left\lvert t_{0,\lambda_{2D\text{-}i}}^{(j,k)} \right\rvert$	$\left\lvert t_{0,\psi_{2D\text{-}i}}^{(j,k)} \right\rvert$	$R^2_{\text{adj.}}\lvert_{2D\text{-}i}^{(j,k)}$	$R^2_{\text{pred.}}\lvert_{2D\text{-}i}^{(j,k)}$	$\rho_{\text{SM}}\lvert_{2D\text{-}i}^{(j,k)}$
1	1	1	2F2B	1	1.3389	9.6447	×	206	3943.86	1041.33	942.94	0.975	0.974	0.987
2	1	1	2F3B	2	0.9733	9.9153	×	203	3716.28	825.62	777.36	0.973	0.973	0.989
3	1	1	2F4B	3	0.9467	9.8569	×	203	2632.28	686.80	649.42	0.963	0.962	0.982
4	1	1	2F6B	4	0.6209	9.0099	×	207	2399.27	728.62	467.84	0.959	0.958	0.983
5	1	1	5F1B	5	0.7619	22.2708	×	204	2690.15	541.70	722.13	0.964	0.963	0.985
6	1	1	5F3B	6	0.9883	16.9171	×	203	3056.92	691.89	699.80	0.968	0.967	0.989
7	1	1	5F4B	7	1.1719	19.5782	×	203	1822.74	362.56	429.09	0.947	0.946	0.983
8	1	1	5F5B	8	1.0227	15.7030	×	200	2995.99	721.36	661.21	0.968	0.967	0.989
9	1	2	2F2B	1	1.3905	19.9403	×	204	4592.75	1172.57	1070.17	0.978	0.978	0.989
10	1	2	2F3B	2	0.9379	21.0902	×	202	3119.88	637.41	652.27	0.969	0.968	0.990
11	1	2	2F4B	3	0.9990	20.2098	×	205	2876.85	757.12	692.68	0.966	0.965	0.984
12	1	2	2F6B	4	0.6552	18.2953	×	209	2637.38	839.79	510.94	0.962	0.961	0.982
13	1	2	5F1B	5	0.7569	46.1103	×	203	2460.49	499.51	669.13	0.961	0.960	0.986
14	1	2	5F3B	6	0.9933	35.1639	×	201	2863.10	659.88	668.41	0.966	0.965	0.989
15	1	2	5F4B	7	1.2066	39.3446	×	201	1795.21	368.21	424.29	0.947	0.946	0.984
16	1	2	5F5B	8	1.0123	32.9511	×	201	2987.75	711.36	666.59	0.968	0.967	0.989
17	1	3	2F2B	1	1.5555	28.0365	×	206	5237.17	1387.07	1071.80	0.981	0.980	0.991
18	1	3	2F3B	2	1.0040	34.5995	×	201	3940.76	861.57	834.52	0.975	0.975	0.992
19	1	3	2F4B	3	1.1287	29.6502	×	207	3438.11	965.47	721.82	0.971	0.970	0.986
20	1	3	2F6B	4	0.7000	27.9933	×	208	2822.52	878.25	499.66	0.965	0.964	0.986
21	1	3	5F1B	5	0.7758	79.9626	×	202	2124.60	396.34	523.64	0.955	0.954	0.986
22	1	3	5F3B	6	1.0034	61.7273	×	204	2664.21	574.48	574.25	0.963	0.962	0.989
23	1	3	5F4B	7	1.2051	64.7601	×	206	1800.87	339.80	396.94	0.946	0.945	0.986
24	1	3	5F5B	8	1.0254	57.0169	×	200	2515.39	547.52	513.03	0.962	0.961	0.990

Table 3.7: Different statistical results for $GDI_{2D\text{-}2}$

Sl. No.	i	j	Frame	k	$\lambda_{2D\text{-}i}^{(j,k)}$	$\psi_{2D\text{-}i}^{(j,k)}$	$\gamma_{2D\text{-}i}^{(j,k)}$	$q_{2D}^{(j,k)}$	$f_{0,2D}^{(i,j,k)}$	$\left\lvert t_{0,\lambda_{2D\text{-}i}}^{(j,k)} \right\rvert$	$\left\lvert t_{0,\psi_{2D\text{-}i}}^{(j,k)} \right\rvert$	$R^2_{\text{adj.}}\lvert_{2D\text{-}i}^{(j,k)}$	$R^2_{\text{pred.}}\lvert_{2D\text{-}i}^{(j,k)}$	$\rho_{\text{SM}}\lvert_{2D\text{-}i}^{(j,k)}$
1	2	1	2F2B	1	2.5876	13.4852	−0.1548	206	4023.70	47.94	36.72	0.975	0.975	0.989
2	2	1	2F3B	2	2.6803	12.4255	−0.1316	203	5093.76	51.26	32.71	0.981	0.980	0.992
3	2	1	2F4B	3	2.7306	13.4890	−0.1686	203	2712.17	37.71	30.89	0.964	0.963	0.984
4	2	1	2F6B	4	3.3906	12.4376	−0.2082	207	2306.78	38.45	23.41	0.957	0.956	0.984
5	2	1	5F1B	5	0.9859	9.1079	−0.0972	204	3596.40	40.28	31.82	0.973	0.972	0.987
6	2	1	5F3B	6	1.1689	8.0868	−0.1173	203	4327.24	48.45	31.35	0.977	0.976	0.992
7	2	1	5F4B	7	1.0131	8.2523	−0.0756	203	3848.25	43.94	28.82	0.974	0.974	0.988
8	2	1	5F5B	8	1.2483	7.7548	−0.1245	200	4154.47	49.03	28.77	0.977	0.976	0.991
9	2	2	2F2B	1	2.8911	17.4599	−0.1603	204	4645.13	48.77	39.35	0.979	0.978	0.990
10	2	2	2F3B	2	3.0618	19.3559	−0.1174	202	4656.97	46.28	31.48	0.979	0.978	0.992
11	2	2	2F4B	3	3.2925	19.5556	−0.1723	205	2842.84	38.89	30.82	0.965	0.965	0.985
12	2	2	2F6B	4	4.2761	19.1958	−0.2297	209	2568.70	42.11	24.46	0.961	0.960	0.983
13	2	2	5F1B	5	1.2879	16.8307	−0.0919	203	3442.08	39.78	30.49	0.971	0.971	0.987
14	2	2	5F3B	6	1.6087	16.1506	−0.1142	201	4254.13	48.40	29.57	0.977	0.976	0.990
15	2	2	5F4B	7	1.4126	16.3380	−0.0783	201	3939.48	45.04	28.06	0.975	0.975	0.988
16	2	2	5F5B	8	1.6966	16.0211	−0.1240	201	4160.01	48.94	28.69	0.977	0.976	0.991
17	2	3	2F2B	1	3.2042	16.7616	−0.1759	206	5093.74	53.29	37.02	0.980	0.980	0.991
18	2	3	2F3B	2	3.2554	20.6663	−0.1295	201	5964.78	54.73	34.42	0.984	0.983	0.993
19	2	3	2F4B	3	3.7087	19.0400	−0.1998	207	3110.40	43.00	28.47	0.968	0.967	0.987
20	2	3	2F6B	4	4.5598	19.5385	−0.2489	208	2708.20	41.94	23.54	0.963	0.962	0.986
21	2	3	5F1B	5	1.3353	18.2985	−0.0864	202	3553.32	39.32	28.28	0.972	0.972	0.988
22	2	3	5F3B	6	1.7875	21.3336	−0.1101	204	4685.24	50.88	29.60	0.979	0.978	0.992
23	2	3	5F4B	7	1.7005	25.7481	−0.0712	206	4705.98	47.80	30.68	0.979	0.978	0.990
24	2	3	5F5B	8	1.9429	22.0833	−0.1136	200	4613.80	49.73	27.87	0.979	0.978	0.991

checking the existence of a linear relationship between the selected dependent variable (i.e., $GDI_{2D\text{-ST}}$) and the considered independent variables (i.e., non-cumulative and cumulative terms in $GDI_{2D\text{-}1}$ and $GDI_{2D\text{-}2}$) in the present study. Therefore, the F-test for significance of regression is used to examine the importance of the independent variables considered for the ith 2D GDI formula in the case of the jth soil type and the kth frame by assuming suitable null hypotheses (H_0) and alternative hypotheses (H_a) for ANOVA test as

$$H_{0,2D}^{(i,j,k)} : \lambda_{2D\text{-}i}^{(j,k)} = \psi_{2D\text{-}i}^{(j,k)} = 0 \ \forall \ i, j \text{ and } k \tag{3.7}$$

$$H_{a,2D}^{(i,j,k)} : \text{at least one between } \lambda_{2D\text{-}i}^{(j,k)} \text{ and } \psi_{2D\text{-}i}^{(j,k)} \neq 0 \ \forall \ i, j \text{ and } k \quad . \tag{3.8}$$

Now, $H_{0,2D}^{(i,j,k)}$ can be rejected if the value of the F-test statistic, $f_{0,2D}^{(i,j,k)}$, is found to be greater than the value of the percentage point of the F distribution at the α_s level of significance, $f_{\alpha_s,w,q_{2D}^{(j,k)}-v_i}$ [240]. Here, w is the number of independent variables for the GDI formulae (i.e., $w = 2$), $q_{2D}^{(j,k)}$ is the total number of data points in the regression dataset in the case of jth soil type and kth frame (refer to Tables 3.6 and 3.7), v_i is the number of GDCs for the ith 2D GDI formula (i.e., $v_i = 2$ for $i = 1$ and $v_i = 3$ for $i = 2$). $f_{0,2D}^{(i,j,k)}$ is computed as

$$f_{0,2D}^{(i,j,k)} = \frac{\left(q_{2D}^{(j,k)} - v_i\right) \sum_{g=1}^{q_{2D}^{(j,k)}} \left(GDI_{2D\text{-}i}^{(j,k,g)} - \overline{GDI}_{2D\text{-ST}}^{(j,k)}\right)^2}{w \sum_{g=1}^{q_{2D}^{(j,k)}} \left(GDI_{2D\text{-ST}}^{(j,k,g)} - GDI_{2D\text{-}i}^{(j,k,g)}\right)^2} \tag{3.9}$$

where $GDI_{2D\text{-}i}^{(j,k,g)}$ is the gth estimated value for the ith GDI formula, $GDI_{2D\text{-ST}}^{(j,k,g)}$ is the gth $GDI_{2D\text{-ST}}$ value used in the regression analysis, and $\overline{GDI}_{2D\text{-ST}}^{(j,k)}$ is the mean of all $GDI_{2D\text{-ST}}$ values in the case of the jth soil type and the kth frame. The $GDI_{2D\text{-}i}^{(j,k,g)}$ value is estimated using the corresponding independent variables and the GDCs for the ith GDI. The values of the F-test statistic of Equation (3.9) for complete ranges of i, j and k are calculated as shown in Tables 3.6 and 3.7. On the other hand, considering 5% level of significance (i.e., $\alpha_s = 0.05$), the maximum value of the parameter $f_{\alpha_s,w,q_{2D}^{(j,k)}-v_i}$ is equal to 3.04 for all training cases. Therefore, the null hypotheses of Equation (3.7) can be rejected, and it can be concluded that the dependent variable has a linear relationship with either or both of the considered independent variables in the cases of the GDI formulae and all possible combinations of the soil types and the training frames.

Student's t-test is carried out to examine the hypotheses on the individual independent variables and the partial contribution of an independent variable given the other independent variable is present in a GDI formula for all possible combinations of soil types and training frames. In this case, the suitable null and alternative hypotheses for the ANOVA test are

assumed as

$$H^{(j,k)}_{0,\lambda_{2D\text{-}i}} : \lambda^{(j,k)}_{2D\text{-}i} = 0 \ \forall \ i,j \text{ and } k \tag{3.10}$$
$$H^{(j,k)}_{a,\lambda_{2D\text{-}i}} : \lambda^{(j,k)}_{2D\text{-}i} \neq 0 \ \forall \ i,j \text{ and } k \tag{3.11}$$
$$H^{(j,k)}_{0,\psi_{2D\text{-}i}} : \psi^{(j,k)}_{2D\text{-}i} = 0 \ \forall \ i,j \text{ and } k \tag{3.12}$$
$$H^{(j,k)}_{a,\psi_{2D\text{-}i}} : \psi^{(j,k)}_{2D\text{-}i} \neq 0 \ \forall \ i,j \text{ and } k \quad . \tag{3.13}$$

Here, $H^{(j,k)}_{0,\lambda_{2D\text{-}i}}$ can be rejected if the absolute value of t-test statistic, $\left|t^{(j,k)}_{0,\lambda_{2D\text{-}i}}\right|$, is greater than the value of the percentage point of the Student's t distribution at the $\alpha_s/2$ level of significance, $t_{\alpha_s/2,q^{(j,k)}_{2D}-v_i}$ [240]. Same conclusion can be achieved for the hypothesis $H^{(j,k)}_{0,\psi_{2D\text{-}i}}$ satisfying similar condition, i.e., $\left|t^{(j,k)}_{0,\psi_{2D\text{-}i}}\right| > t_{\alpha_s/2,q^{(j,k)}_{2D}-v_i}$. The non-rejection of any null hypothesis of Equations (3.10) and (3.12) indicates confiscation of the associated independent variable from the corresponding GDI formula. The t-test statistics can be computed as

$$t^{(j,k)}_{0,\lambda_{2D\text{-}i}} = \lambda^{(j,k)}_{2D\text{-}i} \Big/ \text{SE}\left(\lambda^{(j,k)}_{2D\text{-}i}\right) \tag{3.14}$$
$$t^{(j,k)}_{0,\psi_{2D\text{-}i}} = \psi^{(j,k)}_{2D\text{-}i} \Big/ \text{SE}\left(\psi^{(j,k)}_{2D\text{-}i}\right) \tag{3.15}$$

with

$$\text{SE}\left(\lambda^{(j,k)}_{2D\text{-}i}\right) = \sqrt{\left\{\frac{\sum_{g=1}^{q^{(j,k)}_{2D}}\left(GDI^{(j,k,g)}_{2D\text{-ST}} - GDI^{(j,k,g)}_{2D\text{-}i}\right)^2}{\left(q^{(j,k)}_{2D} - v_i\right)}\right\} \cdot \left\{\sum_{g=1}^{q^{(j,k)}_{2D}}\left(\tilde{x}^{(j,k,g)}_{2D\text{-}i}\right)^2\right\}^{-1}} \tag{3.16}$$

$$\text{SE}\left(\psi^{(j,k)}_{2D\text{-}i}\right) = \sqrt{\left\{\frac{\sum_{g=1}^{q^{(j,k)}_{2D}}\left(GDI^{(j,k,g)}_{2D\text{-ST}} - GDI^{(j,k,g)}_{2D\text{-}i}\right)^2}{\left(q^{(j,k)}_{2D} - v_i\right)}\right\} \cdot \left\{\sum_{g=1}^{q^{(j,k)}_{2D}}\left(\tilde{y}^{(j,k,g)}_{2D\text{-}i}\right)^2\right\}^{-1}} \tag{3.17}$$

where $\tilde{x}^{(j,k,g)}_{2D\text{-}i}$ and $\tilde{y}^{(j,k,g)}_{2D\text{-}i}$ are the gth value of the first and second independent variable in the case of the jth soil type and the kth frame, respectively, present in the expression of $GDI_{2D\text{-}i}$. For example, the expression of $\tilde{x}_{2D\text{-}i}$ and $\tilde{y}_{2D\text{-}i}$ for $GDI_{2D\text{-}2}$ are

$$\tilde{x}_{2D\text{-}2} = \frac{\max|u_{N_s}(t)|}{\bar{\mu}_\phi \cdot S'_d} \quad \text{and} \quad \tilde{y}_{2D\text{-}2} = \sum_{n=1}^{N_s}\left[\frac{\sum_{s=1}^{T_d/\Delta t}\{(u_n(s\Delta t) - u_{n-1}(s\Delta t)) - (u_n((s-1)\Delta t) - u_{n-1}((s-1)\Delta t))\}^2}{\left(\bar{\mu}_{\phi_n} \cdot S'_d\right)^2}\right] \quad . \tag{3.18}$$

The estimated absolute values of the t-test statistics of Equations (3.14) and (3.15) are shown

in Tables 3.6 and 3.7, and the maximum value of the parameter $t_{\alpha_s/2,q_{2D}^{(j,k)}-v_i}$ is equal to 1.97 for all training cases. So, the null hypotheses of Equations (3.10) and (3.12) can be rejected, and it can be concluded that both independent variables contribute significantly to the corresponding GDI formula.

In multilinear regression analyses, the adjusted R^2 or $R^2_{\text{adj.}}$ is a better representation of the proportion of the variance in the dependent variable that can be predicted from the independent variables in comparison to the coefficient of determination, R^2. The main advantage of using $R^2_{\text{adj.}}$ over R^2 is that the former dictates the proportion of variation explained by only the independent variables that actually affect the dependent variable [240]. The adjusted R^2 value corresponding to the ith GDI in the case of the jth soil type and kth frame can be computed using the expression as

$$R^2_{\text{adj.}}\Big|_{2D\text{-}i}^{(j,k)} = 1 - \frac{\left(q_{2D}^{(j,k)} - 1\right)\sum_{g=1}^{q_{2D}^{(j,k)}}\left(GDI_{2D\text{-ST}}^{(j,k,g)} - GDI_{2D\text{-}i}^{(j,k,g)}\right)^2}{\left(q_{2D}^{(j,k)} - v_i\right)\sum_{g=1}^{q_{2D}^{(j,k)}}\left(GDI_{2D\text{-ST}}^{(j,k,g)} - \overline{GDI}_{2D\text{-ST}}^{(j,k)}\right)^2} \quad \forall\ i, j \text{ and } k \quad . \tag{3.19}$$

The estimated $R^2_{\text{adj.}}$ values (ranging from 0.946 to 0.984 as shown in Tables 3.6 and 3.7) for each GDI formula for different combinations of the soil types and the sample frames indicate a strong linear relationship between the independent and the dependent variables.

Another statistical term, predictive R^2 or $R^2_{\text{pred.}}$ is used to determine the capability of a regression model to make predictions for new observations [241]. $R^2_{\text{pred.}}$ can be obtained by systematically removing each observation from the existing data set, estimating the regression equation, and determining how well the model can predict the removed observation. Numerically, the parameter $R^2_{\text{pred.}}$ for the ith GDI in the case of the jth soil type and kth frame is computed as

$$R^2_{\text{pred.}}\Big|_{2D\text{-}i}^{(j,k)} = 1 - \frac{\sum_{g=1}^{q_{2D}^{(j,k)}}\left(GDI_{2D\text{-ST}}^{(j,k,g)} - GDI_{2D\text{-}i}^{(j,k,g)}\right)^2}{\sum_{g=1}^{q_{2D}^{(j,k)}}\left(GDI_{2D\text{-ST}}^{(j,k,g)} - \overline{GDI}_{2D\text{-ST}}^{(j,k)}\right)^2} \quad \forall\ i, j \text{ and } k \quad . \tag{3.20}$$

The estimated $R^2_{\text{pred.}}$ values (ranging from 0.945 to 0.983 as shown in Tables 3.6 and 3.7) for the GDI formulae for different cases indicate that the models have strong capability to predict a new observation.

Finally, the Spearman's rank-order correlation coefficients (ρ_{SM}) between the $GDI_{2D\text{-ST}}$ and the GDI formulae are estimated to measure the strength and the direction of the monotonic relationship between them beside concentrating on quantifying the proportion of variance presented in the GDI formulae that can be predicted from the independent variables. Here, the Spearman's rank-order correlation coefficient values between the ith 2D GDI for-

mula and $GDI_{2D\text{-ST}}$ for different combinations of the soil types and the training frames are computed separately as

$$\rho_{\text{SM}}|_{2D\text{-}i}^{(j,k)} = 1 - \frac{6\sum_{g=1}^{q_{2D}^{(j,k)}} \left(D_i^{(j,k,g)}\right)^2}{q_{2D}^{(j,k)}\left\{\left(q_{2D}^{(j,k)}\right)^2 - 1\right\}} \quad \forall\ i, j \text{ and } k \tag{3.21}$$

where $D_i^{(j,k,g)}$ is the difference between the ranks of the values associated with the pair $GDI_{2D\text{-}i}^{(j,k,g)}$ and $GDI_{2D\text{-ST}}^{(j,k,g)}$. Tables 3.6 and 3.7 show that the estimated values of $\rho_{\text{SM}}|_{2D\text{-}i}^{(j,k)}$ for all i, j and k values are ranging from 0.982 to 0.993, and thus, indicate a strong monotonically increasing relationship between the GDI formulae and the well-established modified Park and Ang damage index.

3.4.2 Explicit Expressions for Estimating GDCs of 2D GDI formulae

An attempt has been made here to find explicit expressions for estimating the GDCs, applicable to any combination of building frame and soil type, as outlined in Subsection 3.3.3. For this purpose, j and k indices are no longer relevant, and only the i index (for representing the GDI formulae) will be retained. The relations of some global parameters of a frame, such as the fundamental periods (T_p and T_p'), the total height ($h_{\text{total}} = N_s h$ as shown in Figure 3.1) and the frame ratio ($F_r = N_b/N_s$), along with the soil type (S) with the GDCs individually or for any possible linear combination of them are studied and used to produce the best-fitted explicit expression for each GDC separately. Also, the values for the parameter S are taken as 1, 2 and 3 for the hard soil, the medium stiff soil and the soft soil, respectively. Since the terms associated with the GDCs, $\lambda_{2D\text{-}1}$ and $\psi_{2D\text{-}1}$, use response due to a DSCUGM and structural properties (see Equations (3.1) and (3.4)), the explicit expressions for the coefficients, using soil type (which controls a design spectrum) and global parameters of a frame as independent variables, are considered in the present study as

$$\lambda_{2D\text{-}i} = g_{\lambda_{2D}}^{(c_1)}\left(\kappa_1^{(i)}, \kappa_2^{(i)}, \kappa_3^{(i)}, \kappa_4^{(i)}, T_p, h_{\text{total}}, F_r, S\right) \quad \forall\ c_1 = 1, 2, \cdots, 2^4 - 1 \text{ and } i = 1 \tag{3.22}$$

$$\psi_{2D\text{-}i} = g_{\psi_{2D}}^{(c_1)}\left(\kappa_5^{(i)}, \kappa_6^{(i)}, \kappa_7^{(i)}, \kappa_8^{(i)}, T_p, h_{\text{total}}, F_r, S\right) \quad \forall\ c_1 = 1, 2, \cdots, 2^4 - 1 \text{ and } i = 1 \tag{3.23}$$

where $\kappa_1^{(1)}, \kappa_2^{(1)}, \cdots, \kappa_8^{(1)}$ are the regression coefficients such that $\kappa_1^{(1)}$ to $\kappa_4^{(1)}$ are attached with T_p, h_{total}, F_r and S, respectively, for the coefficient $\lambda_{2D\text{-}1}$, and $\kappa_5^{(1)}$ to $\kappa_8^{(1)}$ are attached with the independent variables in the same order for $\psi_{2D\text{-}1}$. The index c_1 refers to all possible regression models considering the linear combinations of 4 numbers of independent variables available in Equations (3.22) and (3.23). Similarly, the explicit expressions for the GDCs,

$\lambda_{2D\text{-}2}$ and $\psi_{2D\text{-}2}$, are considered as

$$\lambda_{2D\text{-}i} = g_{\lambda_{2D}}^{(c_1)}\left(\kappa_1^{(i)}, \kappa_2^{(i)}, \kappa_3^{(i)}, \kappa_4^{(i)}, T_p', h_{\text{total}}, F_r, S\right) \quad \forall\ c_1 = 1, 2, \cdots, 2^4 - 1 \text{ and } i = 2 \tag{3.24}$$

$$\psi_{2D\text{-}i} = g_{\psi_{2D}}^{(c_1)}\left(\kappa_5^{(i)}, \kappa_6^{(i)}, \kappa_7^{(i)}, \kappa_8^{(i)}, T_p', h_{\text{total}}, F_r, S\right) \quad \forall\ c_1 = 1, 2, \cdots, 2^4 - 1 \text{ and } i = 2 \tag{3.25}$$

where the regression coefficients, $\kappa_1^{(2)}$ to $\kappa_4^{(2)}$ are attached with T_p', h_{total}, F_r and S, respectively, for the coefficient $\lambda_{2D\text{-}2}$, and $\kappa_5^{(2)}$ to $\kappa_8^{(2)}$ are attached with the independent variables in the same order for $\psi_{2D\text{-}2}$. Here, c_1 is also used in Equations (3.24) and (3.25), because the number of independent variables considered in these equations is same as Equations (3.22) and (3.23). Now, the other GDC, $\gamma_{2D\text{-}2}$, is related only to the structural properties of a frame (see Equation (3.4)). Therefore, the explicit expression for $\gamma_{2D\text{-}2}$ using only global parameters of a frame as independent variables are considered as

$$\gamma_{2D\text{-}i} = g_{\gamma_{2D}}^{(c_2)}\left(\kappa_9^{(i)}, \kappa_{10}^{(i)}, \kappa_{11}^{(i)}, T_p', h_{\text{total}}, F_r\right) \quad \forall\ c_2 = 1, 2, \cdots, 2^3 - 1 \text{ and } i = 2 \tag{3.26}$$

where $\kappa_9^{(2)}, \kappa_{10}^{(2)}$ and $\kappa_{11}^{(2)}$ are the regression coefficients associated with T_p', h_{total}, and F_r, respectively, for the coefficient $\gamma_{2D\text{-}2}$. The index c_2 refers to all possible linear regression models considering 3 numbers of independent variables. The units for T_p and T_P' are taken as second, whereas the unit for h_{total} as meter in Equations (3.22)-(3.26). The statistics of the considered models are studied thoroughly for all GDCs, and the values of the regression coefficients ($\kappa_1^{(i)}$ to $\kappa_{11}^{(i)}$) corresponding to the best-fitted models (obtained using the stepwise backward elimination of the independent variables [242]) among them are furnished in Table 3.8. For example, using the estimated regression coefficients (from Table 3.8) corresponding to $GDI_{2D\text{-}1}$, the expressions for the GDCs can be written as

$$\lambda_{2D\text{-}1} = 3.247T_p - 0.201h_{\text{total}} \quad \text{and} \quad \psi_{2D\text{-}1} = -85.981T_p + 7.545h_{\text{total}} + 16.441S \quad .$$

Table 3.8: Regression coefficients for the explicit expressions of the GDCs of 2D GDI formulae

Sl. No.	i	GDC	Values of regression coefficients in Equations (3.22)-(3.26)			
1	1	$\lambda_{2D\text{-}1}$	$\kappa_1^{(1)} = 3.247$	$\kappa_2^{(1)} = -0.201$	×	×
2	1	$\psi_{2D\text{-}1}$	$\kappa_5^{(1)} = -85.981$	$\kappa_6^{(1)} = 7.545$	×	$\kappa_8^{(1)} = 16.441$
3	2	$\lambda_{2D\text{-}2}$	$\kappa_1^{(2)} = 6.889$	$\kappa_2^{(2)} = -0.239$	$\kappa_3^{(2)} = 0.438$	$\kappa_4^{(2)} = 0.389$
4	2	$\psi_{2D\text{-}2}$	$\kappa_5^{(2)} = 21.270$	$\kappa_6^{(2)} = -0.445$	×	$\kappa_8^{(2)} = 4.926$
5	2	$\gamma_{2D\text{-}2}$	$\kappa_9^{(2)} = -0.616$	$\kappa_{10}^{(2)} = 0.017$	×	×

The importance of the corresponding independent variables for each GDC is checked with

the help of F-tests for significance of regression by assuming the following null and alternative hypotheses as

$$H_{0,\lambda_{2D\text{-}i}} : \kappa_{\xi}^{(i)} = 0 \text{ with } \xi = 1,2 \text{ for } i = 1 \text{ and } \xi = 1,2,3,4 \text{ for } i = 2 \tag{3.27}$$

$$H_{a,\lambda_{2D\text{-}i}} : \text{at least one among } \kappa_{\xi}^{(i)} \neq 0 \text{ with } \xi = 1,2 \text{ for } i = 1 \text{ and } \xi = 1,2,3,4 \text{ for } i = 2 \tag{3.28}$$

$$H_{0,\psi_{2D\text{-}i}} : \kappa_{\eta}^{(i)} = 0 \text{ with } \eta = 5,6,8 \ \forall \ i \tag{3.29}$$

$$H_{a,\psi_{2D\text{-}i}} : \text{at least one among } \kappa_{\eta}^{(i)} \neq 0 \text{ with } \eta = 5,6,8 \ \forall \ i \tag{3.30}$$

$$H_{0,\gamma_{2D\text{-}i}} : \kappa_{\zeta}^{(i)} = 0 \text{ with } \zeta = 9,10 \text{ for } i = 2 \tag{3.31}$$

$$H_{a,\gamma_{2D\text{-}i}} : \text{at least one among } \kappa_{\zeta}^{(i)} \neq 0 \text{ with } \zeta = 9,10 \text{ for } i = 2 \quad . \tag{3.32}$$

The F-test statistics, $f_{0,\lambda_{2D\text{-}i}}$, $f_{0,\psi_{2D\text{-}i}}$ and $f_{0,\gamma_{2D\text{-}i}}$, corresponding to the above null hypotheses tests are estimated (as shown in Table 3.9) following the similar method described in Subsection 3.4.1. Now, considering $\alpha_s = 0.05$, the maximum value of the percentage point of the F distribution are found to be 3.44 for all GDCs. Hence, the null hypotheses of Equations (3.27), (3.29) and (3.31) can be rejected, and it can be asserted that the dependent variable has a linear relationship with either or all of the considered independent variables.

Table 3.9: Different statistical results for the GDCs of 2D GDI formulae

Sl. No.	i	GDC	F-test statistic	Student's t-test statistic (absolute value)	$R^2_{\text{adj.}}$
1	1	$\lambda_{2D\text{-}1}$	$f_{0,\lambda_{2D\text{-}1}} = 176.1$	$t_{0,\lambda_{2D\text{-}1},\kappa_1} = 7.29$, $t_{0,\lambda_{2D\text{-}1},\kappa_2} = 5.23$	0.936
2	1	$\psi_{2D\text{-}1}$	$f_{0,\psi_{2D\text{-}1}} = 146.2$	$t_{0,\psi_{2D\text{-}1},\kappa_5} = 4.47$, $t_{0,\psi_{2D\text{-}1},\kappa_6} = 5.16$, $t_{0,\psi_{2D\text{-}1},\kappa_8} = 8.15$	0.948
3	2	$\lambda_{2D\text{-}2}$	$f_{0,\lambda_{2D\text{-}2}} = 755.0$	$t_{0,\lambda_{2D\text{-}2},\kappa_1} = 7.45$, $t_{0,\lambda_{2D\text{-}2},\kappa_2} = 7.91$, $t_{0,\lambda_{2D\text{-}2},\kappa_3} = 4.16$, $t_{0,\lambda_{2D\text{-}2},\kappa_4} = 6.87$	0.992
4	2	$\psi_{2D\text{-}2}$	$f_{0,\psi_{2D\text{-}2}} = 385.9$	$t_{0,\psi_{2D\text{-}2},\kappa_5} = 4.67$, $t_{0,\psi_{2D\text{-}2},\kappa_6} = 2.88$, $t_{0,\psi_{2D\text{-}2},\kappa_8} = 8.34$	0.980
5	2	$\gamma_{2D\text{-}2}$	$f_{0,\gamma_{2D\text{-}2}} = 304.4$	$t_{0,\gamma_{2D\text{-}2},\kappa_9} = 15.72$, $t_{0,\gamma_{2D\text{-}2},\kappa_{10}} = 9.82$	0.962

For carrying out the Student's t-test, the null and alternative hypotheses can be assumed as

$$H_{0,\lambda_{2D\text{-}i},\kappa_\xi} : \kappa_{\xi}^{(i)} = 0 \text{ with } \xi = 1,2 \text{ for } i = 1 \text{ and } \xi = 1,2,3,4 \text{ for } i = 2 \tag{3.33}$$

$$H_{a,\lambda_{2D\text{-}i},\kappa_\xi} : \kappa_{\xi}^{(i)} \neq 0 \text{ with } \xi = 1,2 \text{ for } i = 1 \text{ and } \xi = 1,2,3,4 \text{ for } i = 2 \tag{3.34}$$

$$H_{0,\psi_{2D\text{-}i},\kappa_\eta} : \kappa_{\eta}^{(i)} = 0 \text{ with } \eta = 5,6,8 \ \forall \ i \tag{3.35}$$

$$H_{a,\psi_{2D\text{-}i},\kappa_\eta} : \kappa_\eta^{(i)} \neq 0 \text{ with } \eta = 5, 6, 8 \; \forall \; i \tag{3.36}$$

$$H_{0,\gamma_{2D\text{-}i},\kappa_\zeta} : \kappa_\zeta^{(i)} = 0 \text{ with } \zeta = 9, 10 \text{ for } i = 2 \tag{3.37}$$

$$H_{a,\gamma_{2D\text{-}i},\kappa_\zeta} : \kappa_\zeta^{(i)} \neq 0 \text{ with } \zeta = 9, 10 \text{ for } i = 2 \quad . \tag{3.38}$$

The absolute values of the t-test statistics, $t_{0,\lambda_{2D\text{-}i},\kappa_\xi}, t_{0,\psi_{2D\text{-}i},\kappa_\eta}$ and $t_{0,\gamma_{2D\text{-}i},\kappa_\zeta}$, corresponding to the above null hypotheses tests are estimated following the similar method described in Subsection 3.4.1 and provided in Table 3.9. The maximum value of the percentage point of the Student's t distribution corresponding to $\alpha_s = 0.05$ is found to be 2.09 for all GDCs. Hence, the null hypotheses of Equations (3.33), (3.35) and (3.37) can be rejected, and the considered independent variables contribute significantly to the expressions of the GDCs. Finally, the adjusted R^2 values for the regression models of the GDCs are estimated using the method described in Subsection 3.4.1 and provided in Table 3.9. The estimated adjusted R^2 values establish strong linear relationships between the GDCs and the corresponding independent variables.

3.4.3 Correlation between Proposed 2D GDIs and Damage Conditions

The damage condition of a structure is used to evaluate its post-earthquake status and help to decide the future use of the structure based on its existing state. One way to identify the damage condition of a structure is to categorize the damage conditions with some limiting values of a damage index model capable of representing local or global damage of the structure. The limiting values for a damage index model can be estimated from experimental data, observational studies or both as discussed in Subsection 1.2.2. Due to the unavailability of such experimental data or observations in the present study, the limiting values of the proposed 2D GDI formulae related to different damage conditions may be considered similar to the recommendations offered by Stone and Taylor [1] as shown in Table 1.4.

Now, it is necessary to check the accuracies of the GDI formulae (i.e., $GDI_{2D\text{-}1}$ and $GDI_{2D\text{-}2}$) for identifying the damage conditions according to Table 1.4. For this purpose, the responses of the training frames due to the training DSCUGMs (with different scale factors) are utilized to find the values of $GDI_{2D\text{-}\mathrm{ST}}$ and the GDI values using the GDI formulae, followed by assigning the corresponding damage conditions based on the computed global damage values. The GDCs obtained from the explicit expressions (refer to Table 3.8) for different training frames and different soil types are used to calculate the values using GDI formulae. Finally, the comparisons of the damage conditions predicted by the GDI formulae and the actual damage conditions obtained by $GDI_{2D\text{-}\mathrm{ST}}$ values are shown in terms of confusion matrices in Figure 3.5. Here, each entry associated with the first 4 rows and the first 4 columns of the matrices is in the percentage of the total observations. The first 4 entries of the 5th row of the matrices are the precision measure representing the percentage of

correct predicted damage conditions for the GDI formulae, whereas the first 4 entries of the 5th column are the recall measure representing the percentage of actual damage conditions predicted by the GDI formulae. Finally, the last entry of the 5th row (or column) is the accuracy measure (i.e., the sum of the first four diagonal entries) representing the percentage of correct predicted damage conditions to the total observations. Higher values of precision, recall and accuracy measures demonstrate the better performance of a GDI formula.

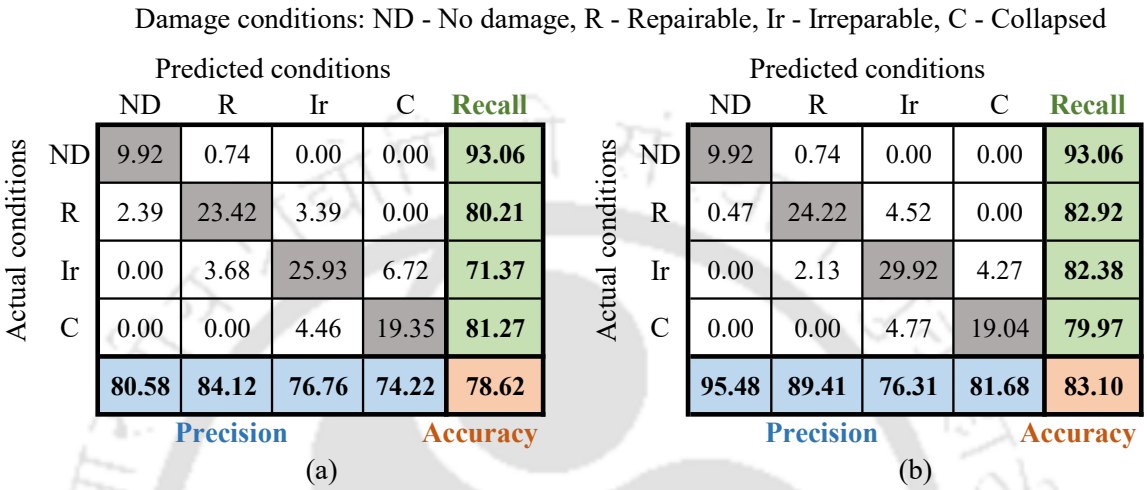

Figure 3.5: Confusion matrices (with values in percentage) of the actual and the predicted damage conditions for the training frames due to the training DSCUGMs in the case of (a) $GDI_{2D\text{-}1}$ and (b) $GDI_{2D\text{-}2}$

According to Figure 3.5, both GDI formulae have high accuracies (around 80%) in identifying the damage conditions for the training frames due to scaled training DSCUGMs. Also, the average values of the recall and the precision measures for all damage conditions are around 80% for $GDI_{2D\text{-}1}$ and around 85% for $GDI_{2D\text{-}2}$. Therefore, the limiting values of damage indices for different damage conditions, as provided in Table 1.4, can be used for the GDI formulae.

3.4.4 Validation of the Proposed Methodology

The GDI formulae, the explicit expressions for predicting the GDCs (refer to Table 3.8), and the applicability of the selected limiting damage index values for different damage conditions (refer to Table 1.4) will be validated in this section. For this purpose, the nonlinear dynamic responses of the validation frames (refer to Table 3.1) due to the training DSCUGMs (refer to Table 3.3) with different scale factors are used in multilinear regression analyses to compute the corresponding GDCs following the methodology described in Subsection 3.3.3. Those computed values of the coefficients for different validation frames and soil types are shown in Table 3.10 (e.g., $\lambda_{2D\text{-}2} = 2.74$, $\psi_{2D\text{-}2} = 13.45$ and $\gamma_{2D\text{-}2} = -0.16$ for frame 2F5B and hard soil). Also, the values of the GDCs for the frames are estimated using the explicit expressions as shown in Table 3.10 (e.g., $\lambda_{2D\text{-}2} = 2.73$, $\psi_{2D\text{-}2} = 10.65$ and $\gamma_{2D\text{-}2} = -0.14$ for

frame 2F5B and hard soil). Now, the nonlinear dynamic responses of the frames due to the validation DSCUGMs (refer to Table 3.3) with different scale factors are utilized to estimate global damage values (according to $GDI_{2D\text{-}1}$ and $GDI_{2D\text{-}2}$) separately using the corresponding GDCs obtained from explicit expressions and regression analyses. The responses of the frames are also used to obtain the corresponding $GDI_{2D\text{-ST}}$ values. Figures 3.6 and 3.7 show the comparisons of the monotonically non-decreasing evolution of the computed values using the GDI formulae and $GDI_{2D\text{-ST}}$ for frames 2F5B and 5F2B, respectively, due to different validation DSCUGMs and different soil conditions. The GDI values estimated using the coefficients obtained from regression analyses are represented as $GDI_{2D\text{-reg}}$, and the values estimated using the coefficients predicted by the explicit expressions as $GDI_{2D\text{-pred}}$ in those figures.

Table 3.10: Values of the GDCs for different 2D GDI formulae obtained from explicit expressions (refer to Table 3.8) and regression analyses for the validation frames and different soil types

Sl. No.	Frame	2D GDI formula	i	Soil type	Values of GDCs					
					From regression analyses			Using explicit expressions		
					$\lambda_{2D\text{-}i}$	$\psi_{2D\text{-}i}$	$\gamma_{2D\text{-}i}$	$\lambda_{2D\text{-}i}$	$\psi_{2D\text{-}i}$	$\gamma_{2D\text{-}i}$
1	2F5B	$GDI_{2D\text{-}1}$	1	Hard	1.02	8.08	×	0.80	9.46	×
2	2F5B	$GDI_{2D\text{-}1}$	1	Med.	1.13	15.14	×	0.80	25.90	×
3	2F5B	$GDI_{2D\text{-}1}$	1	Soft	1.05	25.77	×	0.80	42.34	×
4	2F5B	$GDI_{2D\text{-}2}$	2	Hard	2.74	13.45	−0.16	2.73	10.65	−0.14
5	2F5B	$GDI_{2D\text{-}2}$	2	Med.	2.82	14.81	−0.16	3.12	15.58	−0.14
6	2F5B	$GDI_{2D\text{-}2}$	2	Soft	3.03	15.60	−0.18	3.51	20.50	−0.14
7	5F2B	$GDI_{2D\text{-}1}$	1	Hard	2.52	8.15	×	1.32	16.80	×
8	5F2B	$GDI_{2D\text{-}1}$	1	Med.	2.56	19.88	×	1.32	33.24	×
9	5F2B	$GDI_{2D\text{-}1}$	1	Soft	2.51	33.76	×	1.32	49.68	×
10	5F2B	$GDI_{2D\text{-}2}$	2	Hard	1.22	6.46	−0.11	1.08	11.19	−0.11
11	5F2B	$GDI_{2D\text{-}2}$	2	Med.	1.65	12.97	−0.10	1.47	16.12	−0.11
12	5F2B	$GDI_{2D\text{-}2}$	2	Soft	1.98	18.09	−0.11	1.86	21.04	−0.11

The variability of the $GDI_{2D\text{-reg}}$ values from the $GDI_{2D\text{-ST}}$ values may be attributed to the inherent (or system) uncertainties present in the GDI formulae due to the approximations considered to get numerical values for global damage. Further, the variability of the $GDI_{2D\text{-pred}}$ values from the $GDI_{2D\text{-ST}}$ values increase as the explicit expressions for predicting the GDCs are associated with additional uncertainties. Although the quantification of global damage of a 2D frame using the proposed GDI formulae is influenced by these uncertainties, the estimated global damage indices predict the $GDI_{2D\text{-ST}}$ with acceptable accuracy from the floor-level observations.

Finally, the damage conditions (as per Table 1.4) for the validation frames due to the validation DSCUGMs are evaluated based on the corresponding $GDI_{2D\text{-pred}}$ and $GDI_{2D\text{-ST}}$ values. Figure 3.8 shows the comparison of the predicted (i.e., linked with $GDI_{2D\text{-pred}}$ values)

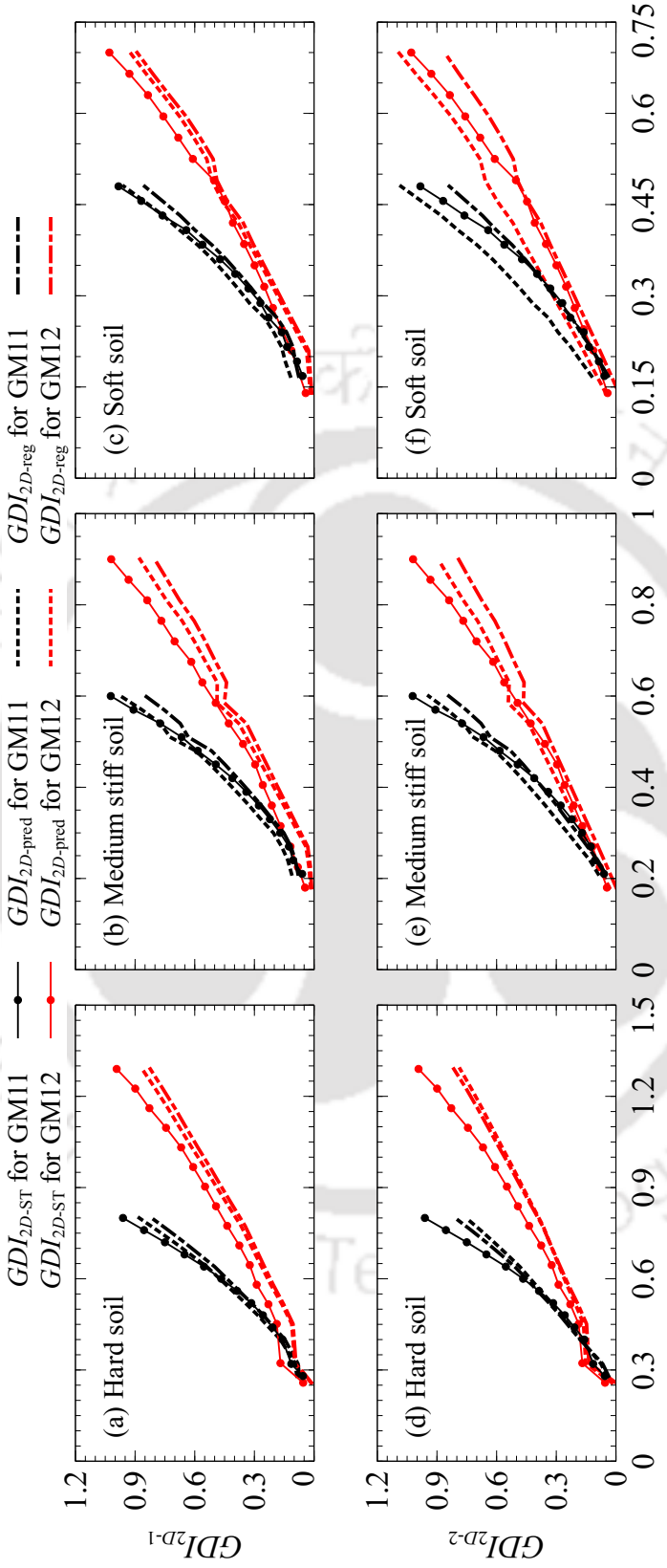

Figure 3.6: Comparisons of the GDI values estimated using the GDCs obtained from regression analyses and explicit expressions with $GDI_{2D\text{-ST}}$ values for frame 2F5B due to validation DSCUGMs for different soil types in the case of (a)-(c) $GDI_{2D\text{-}1}$, and (d)-(f) $GDI_{2D\text{-}2}$

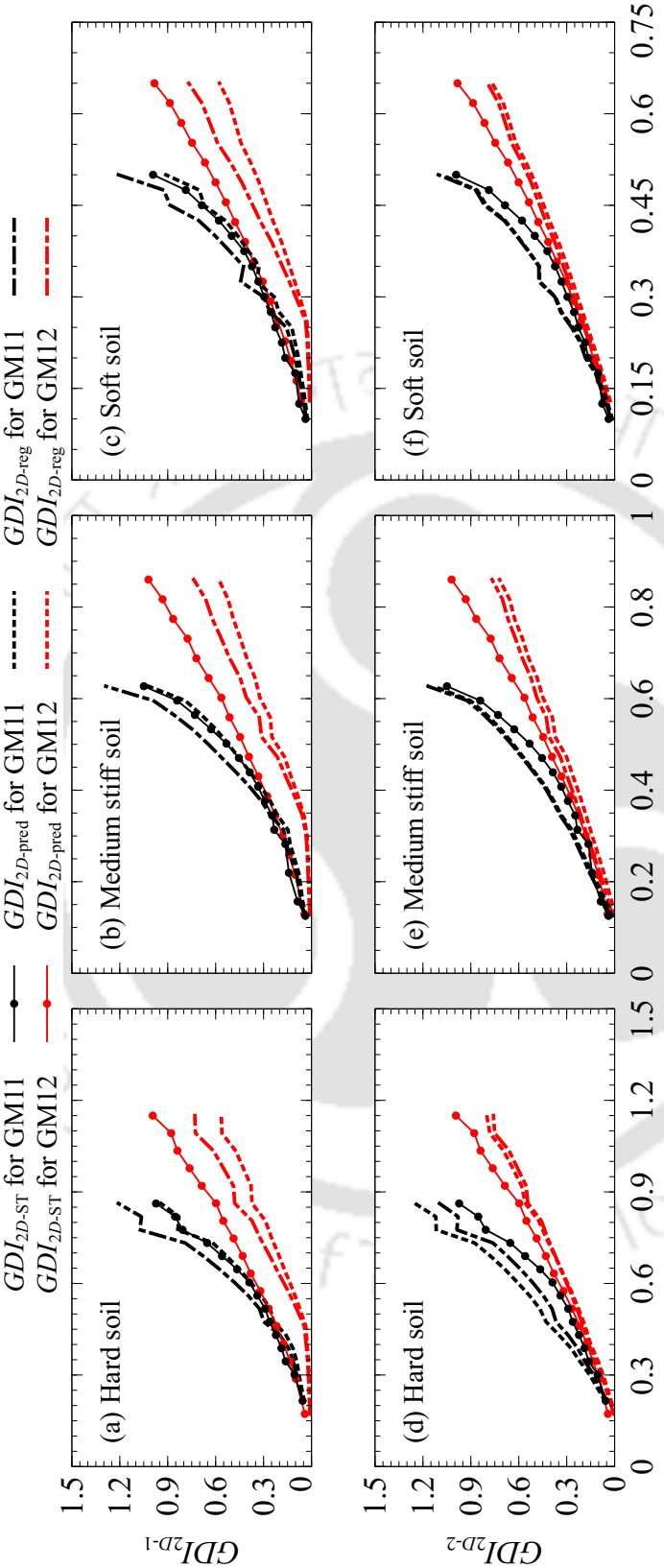

Figure 3.7: Comparisons of the GDI values estimated using the GDCs obtained from regression analyses and explicit expressions with $GDI_{2D\text{-}ST}$ values for frame 5F2B due to validation DSCUGMs for different soil types in the case of (a)-(c)$GDI_{2D\text{-}1}$, and (d)-(f) $GDI_{2D\text{-}2}$

and actual (i.e., linked with $GDI_{2D\text{-}ST}$ values) damage conditions in terms of confusion matrices. The accuracy measure for the GDI formulae is around 75%. In contrast, the average values of the other two measures (precision and recall) for all damage conditions are around 72% for $GDI_{2D\text{-}1}$ and 78% for $GDI_{2D\text{-}2}$. The obtained values of the performance parameters for the new GDI formulae can be considered satisfactory in the case of validation frames and validation DSCUGMs [227, 243]. Here, any suitable probabilistic approach can be used to further improve the assessment of damage conditions by the GDI formulae. The capacity terms used in $GDI_{2D\text{-}1}$ depend on global parameters of a frame (i.e., u_u, u_y and $\bar{\mu}_{d_n}$ as shown in Equation (3.1)), whereas the capacity terms used in $GDI_{2D\text{-}2}$ depend on sectional parameters (i.e., $\bar{\mu}_{\phi}$ and $\bar{\mu}_{\phi_n}$ as shown in Equation (3.4)) of all columns of a frame. Usually, the estimated sectional parameters are more meticulous than the estimated global parameters, as the global responses of a frame (or an individual member) are obtained by applying the integration method over the corresponding sectional responses. Therefore, $GDI_{2D\text{-}2}$ performs better than $GDI_{2D\text{-}1}$ as shown in Figure 3.8 (and Figure 3.5). However, $GDI_{2D\text{-}2}$ can be used only when the considered frame behaves as a shear building as it incorporates the fundamental period of the corresponding shear building (refer to Equation (3.4)). On the other hand, $GDI_{2D\text{-}1}$ can be used even if the considered frame does not behave as a shear building.

Damage conditions: ND - No damage, R - Repairable, Ir - Irreparable, C - Collapsed

Predicted conditions

Actual conditions	ND	R	Ir	C	Recall
ND	9.09	2.67	0.00	0.00	**77.30**
R	6.95	29.41	3.21	0.00	**74.32**
Ir	0.00	7.49	22.46	1.07	**72.40**
C	0.00	0.00	6.42	11.23	**63.63**
	56.67	**74.32**	**69.99**	**91.30**	**72.19**
	Precision				**Accuracy**

(a)

Predicted conditions

Actual conditions	ND	R	Ir	C	Recall
ND	9.10	2.67	0.00	0.00	**77.32**
R	0.53	31.55	7.49	0.00	**79.73**
Ir	0.00	2.67	24.60	3.74	**79.33**
C	0.00	0.00	5.88	11.77	**66.69**
	94.50	**85.52**	**64.79**	**75.89**	**77.02**
	Precision				**Accuracy**

(b)

Figure 3.8: Confusion matrices (with values in percentage) of the actual and the predicted damage conditions for the validation frames due to the validation DSCUGMs in the case of (a) $GDI_{2D\text{-}1}$ and (b) $GDI_{2D\text{-}2}$

3.5 Conclusion

A novel method is introduced, for the first time, to evaluate a combined GDI in the case of instrumented 2D RC frame utilizing floor-displacement measurements due to any seismic activity and some readily obtainable structural properties. Using the new methodology, two different combined GDI formulae are attempted for the prediction of dissipated hysteresis

energy-based weighted average of modified Park and Ang LDIs at global level ($GDI_{2D\text{-ST}}$) in the present study. The main advantage of the GDI formulae is that they do not need any complex and time-consuming nonlinear time-history analysis to get the section-level demand terms, unlike the existing combined global damage indices. Although, for the displacement ductility-based GDI formula nonlinear static analysis is required to get the yield and the ultimate displacement values. Among the two GDI formulae, the curvature ductility-based formula performs better in predicting the global damage state of a shear building-type frame based on limiting values of $GDI_{2D\text{-ST}}$. However, the displacement ductility-based formula can also be used for the frames that do not behave as a shear building. The displacement ductility-based GDI formula is suitable for any 2D RC frame and can be used with the help of a representative finite element model for the considered frame. The curvature ductility-based GDI formula is suitable for shear building-type frames and can be used without any finite element models. The GDCs of the formulae depend on the fundamental period, the geometry of the frame and the local soil type.

The adequacy of the GDI formulae and the corresponding coefficients are found to qualify standard statistical tests. The estimated values via the GDI formulae also enjoy a strong monotonically non-decreasing relationship with the corresponding $GDI_{2D\text{-ST}}$ values. Therefore, the chosen non-cumulative and cumulative terms for the GDI formulae may relate to the global damage state very well. The limiting values for the GDI formulae associated with different damage conditions are given to enhance their applicability in various engineering scenarios, e.g. post-earthquake assessments of instrumented buildings.

The current work on various GDI formulae proposed is carried out within a deterministic framework, where the statistical characterization of the residues in the prediction equations is not considered. However, a probabilistic approach incorporating such uncertainties (originating from residues) would lead to a more comprehensive characterization of damage prediction.

4. Combined GDI formulae using recorded floor-displacement data for 3D RC Buildings

Contents

4.1 Introduction

Structural Damages computed using 2D SDI models cannot capture the true extent of the seismic damage in actual 3D RC buildings due to biaxial bending about both of its principal axes resulting from the application of bidirectional ground motions [86, 244, 245]. Because the seismic resistance along a particular direction is usually reduced by the damage caused in the other direction and vice-versa, due to this coupling effect of both directions, the structural seismic resistance is reduced considerably [86]. Therefore, it is essential to consider the impact of biaxial bending and axial loading on the global damage of an RC building which cannot be apprehended by the new 2D GDI formulae introduced in the previous chapter. So, two different types of 3D GDI formulae are proposed in this chapter using the novel GDI evaluation methodology. The difference between the two 3D GDI formulae is the type of capacity parameters (i.e., displacement ductility and curvature ductility of columns, as

in the case of 2D GDI formulae) incorporated. The non-cumulative and cumulative terms of the 3D GDI formulae are considered (after modifying the corresponding terms available in the new 2D GDI formulae) to accommodate the recorded floor-displacement data along two orthogonal horizontal directions of an instrumented 3D RC building during any seismic activity.

The proposed 3D GDI formulae are trained via regression analysis to predict 3D GDI based on weighted average of the most comprehensive modified Park and Ang-type 3D local damage index model, $LDI_{3D\text{-GWLZD}}$ (refer to Equations (1.20)-(1.24)), computed at each possible plastic hinge locations of the building. The sum of the dissipated hysteresis energies along the two principal axes of a structural member due to bidirectional ground motions is used as the weighing function to get the GDI values in the present study. Similar to the 2D GDI formulae, univariate multilinear regression analyses and standard statistical tests are carried out to find the explicit expressions (considering the variability of buildings and ground motions) for the regression coefficients or the GDCs available in the 3D GDI formulae and check the legitimacy of the selected physics-based non-cumulative and cumulative terms used in the formulae. Further, for the practical usefulness of the new GDI evaluation methodology, the 3D GDI values obtained hereby are linked with overall damage conditions of the structural members in order to predict the post-earthquake restoration-based damage states of RC buildings.

4.2 Details of Three-dimensional Reinforced Concrete Buildings and Bidirectional Ground Motions

Nonlinear dynamic responses obtained using various combinations of different types of 3D RC buildings and different design spectra-compatible bidirectional ground motions (DSCBGMs) are used in this chapter for the training and validation purposes of the new 3D GDI evaluation method. The following sections briefly discuss the necessary details of the considered 3D buildings and the bidirectional ground motions.

4.2.1 Details of 3D RC Buildings

Nine different 3D RC buildings with varying numbers of storeys, bays along two orthogonal directions in horizontal plane (as shown in Table 4.1) are considered in the present study, and will be referred as sample buildings in the present study. Schematic details of one of the sample buildings, $4F4B_x3B_y$, with $N_s(=4)$ number of storeys, $N_{bx}(=4)$ number of bays along x-direction, and $N_{by}(=3)$ number of bays along y-direction are shown in Figure 4.1. The building has total $N_s+1(=5)$ number of floors and the nth floor is denoted by Floor n with $n=0,1,\cdots,N_s$. For example, the GF and the roof of building are denoted by Floor 0 and Floor N_s, respectively, as shown in Figure 4.1 (similar to 2D RC frames as discussed in

Subsection 3.2.1). The height of each storey is denoted by h, whereas the lengths of each bay along two orthogonal directions are denoted by l_x and l_y. Table 4.1 shows the geometrical details of the nine sample buildings considered for the present study. Two translational DOFs along x- and y-axis, and one in-plane rotational DOF attached at the center of mass of nth floor ($n \geq 1$) are denoted by $u_n(t)$, $v_n(t)$ and $\omega_n(t)$, respectively, as shown in Figure 4.1. The provisions of Indian loading standards [3, 229, 230] and design standards [208, 228] are used for designing the beams and the columns of the sample buildings. For this purpose, same material properties as in the case of 2D frames (i.e., M25 grade concrete and Fe500 grade steel) are considered. The nomenclatures representing different sections of beams and columns (floor-wise) for all sample buildings and the corresponding cross-sectional details are provided in Table 4.1 and Figure 4.2, respectively.

Table 4.1: Details of different sample buildings used for training or validation purpose

Sl. No.	Building	N_s	N_{bx}	N_{by}	h (m)	l_x (m)	l_y (m)	Floor	Nomenclature of sections			Used for
									Beam along		Column	
									x-axis	y-axis		
1	$2F2B_x5B_y$	2	2	5	3.0	4.0	4.5	1, 2	B1	B1	C1	Training
2	$2F3B_x4B_y$	2	3	4	3.2	4.5	5.0	1, 2	B2	B2	C2	Training
3	$3F2B_x4B_y$	3	2	4	3.2	5.0	4.5	1, 2	B3	B2	C9	Training
								3	B3	B2	C10	
4	$3F4B_x3B_y$	3	4	3	3.4	5.0	5.5	1, 2	B3	B4	C3	Validation
								3	B3	B4	C4	
5	$3F5B_x2B_y$	3	5	2	3.6	5.5	4.0	1, 2	B4	B2	C5	Training
								3	B4	B2	C4	
6	$4F3B_x5B_y$	4	3	5	3.0	5.0	4.0	1, 2	B6	B5	C6	Training
								3, 4	B6	B5	C7	
7	$4F4B_x3B_y$	4	4	3	3.6	4.5	5.0	1, 2	B5	B6	C8	Training
								3, 4	B5	B6	C8	
8	$5F2B_x5B_y$	5	2	5	3.2	5.5	4.0	1, 2	B8	B9	C11	Training
								3, 4	B8	B9	C12	
								5	B8	B9	C13	
9	$5F3B_x4B_y$	5	3	4	3.0	5.0	5.5	1, 2	B7	B8	C11	Training
								3, 4	B7	B8	C12	
								5	B7	B8	C13	

In this dissertation work, total nine numbers of 3D finite element models corresponding to the sample buildings are developed, among which the responses of eight models are arbitrarily selected for the training purpose of the new GDI evaluation method, and the responses of the other model are used for the validation purpose (refer to Table 4.1). Further, the sample buildings used for training and validation purposes will be termed as training buildings and validation building, respectively, in the present work. The finite element models are developed using OpenSees framework [210, 211] with the necessary details provided in Table 4.2. The Giuffré-Menegotto-Pinto model [215, 216] in `ReinforcingSteel` [246] is used to represent the cyclic strength degradation of the models, with $f_y = 500$ MPa, $f_u = 600$ MPa, $E_s = 200$ GPa, $E_{sh} = 10$ GPa, $\epsilon_{sh} = 0.005$ and $\epsilon_u = 0.12$, and the three parameters controlling stress-strain transition during elastic to plastic behaviour, i.e., R_1, R_2 and R_3 as 0.15, 20.0 and 0.925, respectively. The behaviour of unconfined and confined concrete for the models is replicated by the Chang-Mander stress-strain relation-

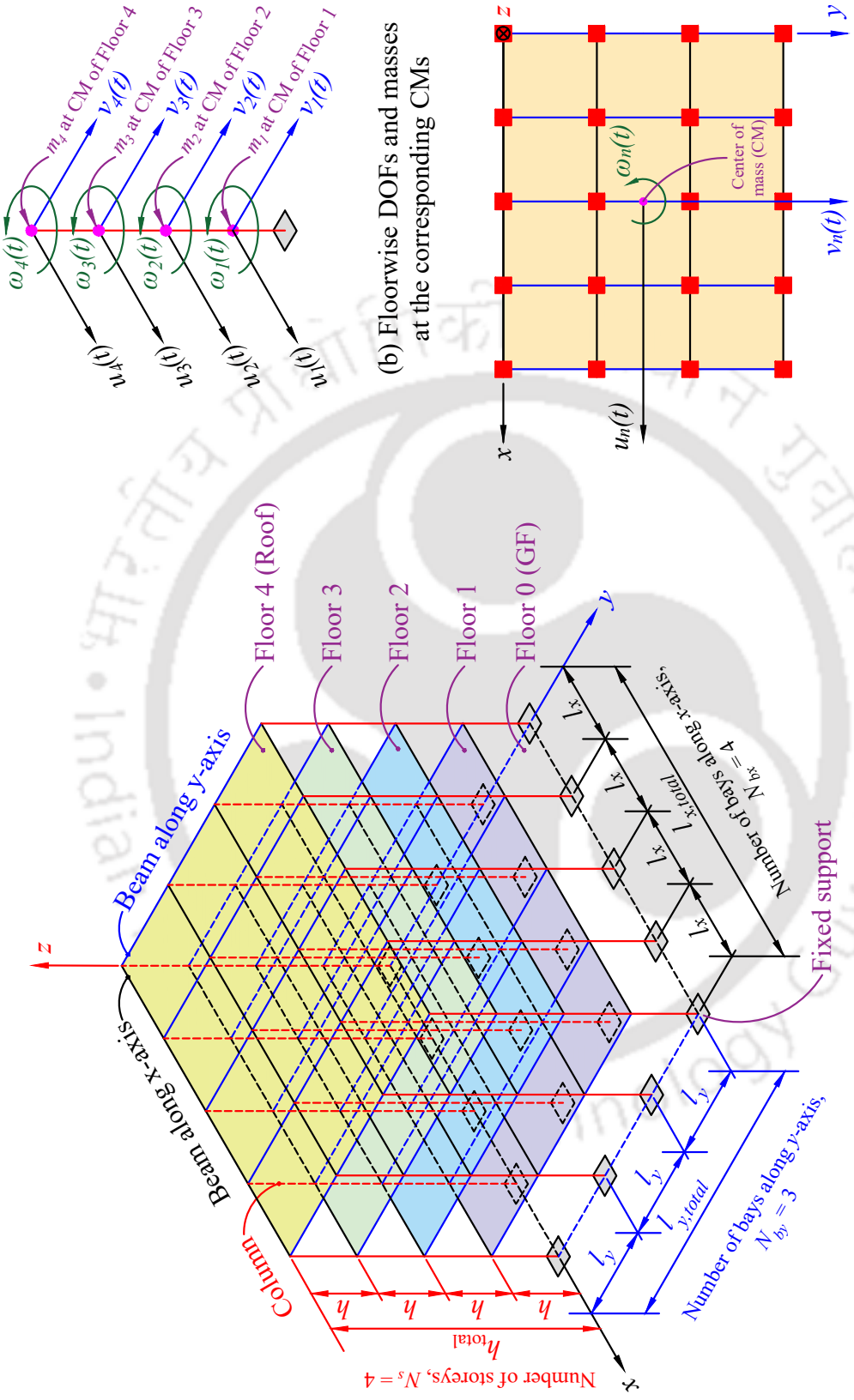

(a) Schematic details of the sample Building 4F4B$_x$3B$_y$ in isometric view

Figure 4.1: Various details for a representative sample building, 4F4B$_x$3B$_y$

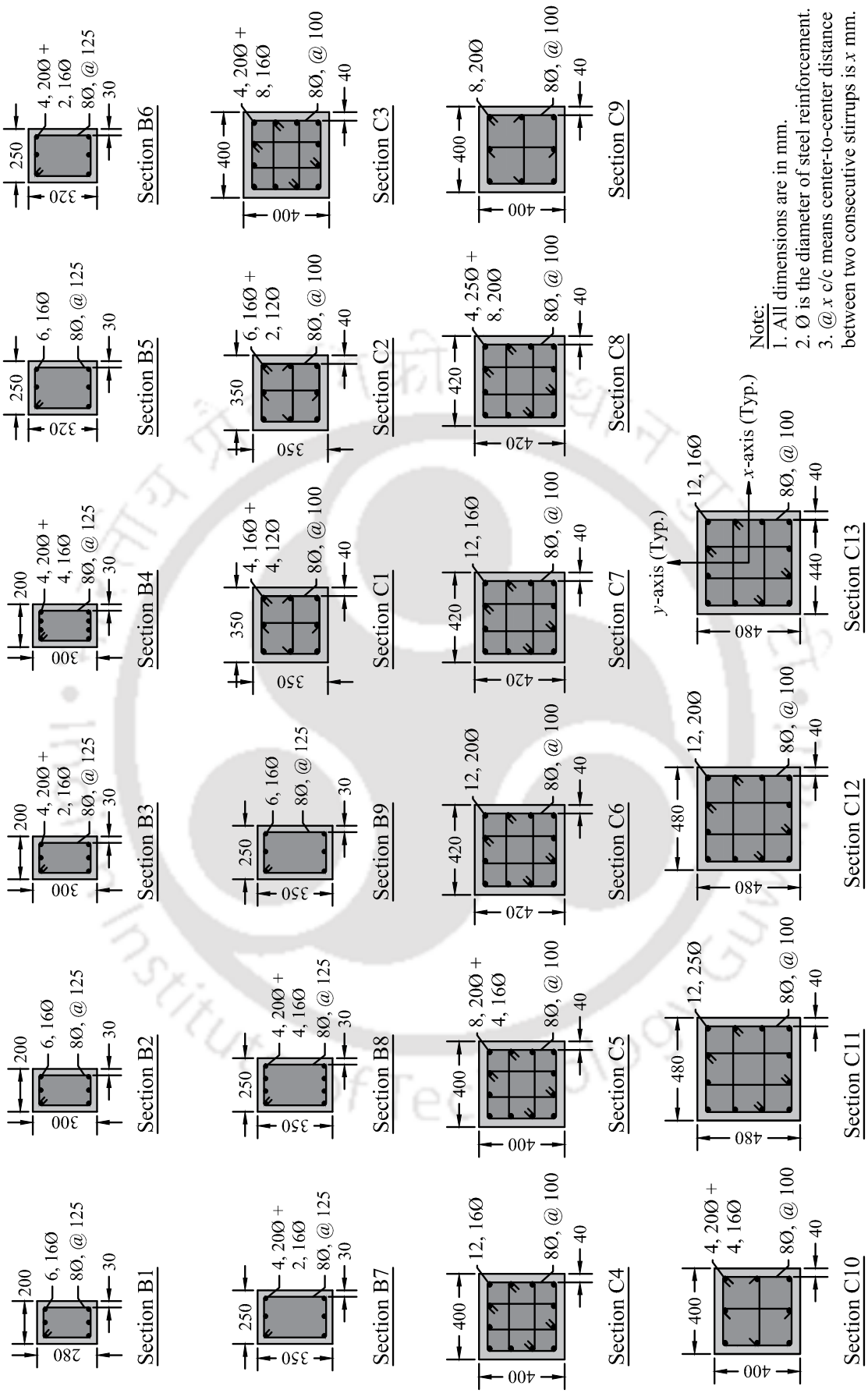

Figure 4.2: Cross-sectional details of different beam and column sections used in the sample RC buildings (refer to Table 4.1)

ships [213, 214] in `Concrete07` with $f_c = 25$ MPa. The material properties associated with the analytical model 2 of Chapter 2 are also used to model 3D RC buildings for the same reason as in the case of 2D RC frames. The behaviour of the slabs (with very high in-plane stiffness) subjected to lateral loads is achieved by using `rigidDiaphragm` [247] command in OpenSees. Here, deformations along the two translational DOFs and one in-plane rotational DOF are allowed at the center of mass for each floor as shown in Figure 4.1(b)-(c). The confined concrete portion for a column section is modeled with multiple subdivisions perpendicular to both its axes to capture the effect of the bidirectional bending along with the axial load on the materials. On the other hand, for a beam section, the confined area is modelled with multiple subdivisions perpendicular to its strong axis only to capture the effect of flexural loads on the materials. This simplification for the beam sections will reduce the overall computation cost, and also produce accurate section-level responses due to bidirectional lateral loads especially when the slab behaviour is modelled with `rigidDiaphragm` option. The displacement-based nonlinear beam-column element incorporating distributed plasticity with linear curvature distribution, i.e., `dispBeamColumn` [248] is used to model the behaviour of all beams and columns. Five numbers of integration points is used for the elements in the present work, as the post-peak softening of element-level force-displacement curves does not occur considering higher numbers of integration points for the structural members. Also, five numbers of `dispBeamColumn` element are used to achieve convergence of local responses (i.e., curvature) within some predefined tolerances for each column members.

Table 4.2: Details of finite element models for 3D RC buildings developed in OpenSees framework [210]

Sl. No.	Object type	Object-specific input
1	Material model for reinforcement	`ReinforcingSteel` [246]
2	Material model for unconfined cover concrete	`Concrete07` [218]
3	Material model for confined core concrete	`Concrete07` [218]
4	Geometric-transformation type for columns	`Corotational` [221]
5	Geometric-transformation type for beams	`Linear` [232]
6	SectionForceDeformation object type	`Fiber` [219, 220]
7	Element object type	`dispBeamColumn` [248]

4.2.2 Details of Bidirectional Ground Motions

14 different pairs of bidirectional ground motions from PEER database [234] are considered in the present study. Some of their basic details are given in Table 4.3. These bidirectional ground motions are required to be made compatible with a design spectrum to get realistic structural nonlinear dynamic responses (as in the case for the study of 2D frames in Subsection 3.2.2) due to design ground motions. But the available design spectra offer compatibility of unidirectional ground motions only. To make use of available design spectra,

a one-dimensional measure for a pair of ground motions along two orthogonal directions in horizontal plane is obligatory. The response spectrum RotDnn [249] is one such measure which is independent of the in-situ orientations of the recording sensors. The letter 'D' in RotDnn stands for period-dependent rotation angle (or orientation) associated with the resultant motion of the recorded bidirectional ground motions. Therefore, the RotDnn value for individual period of a single DOF oscillator is selected for the orientation of the resultant motion for which the response parameter (e.g., PSA, spectral acceleration or spectral displacement) value is maximum or any other predefined percentile value of the set. The 'nn' in RotDnn is the percentile value of the response parameter corresponding to the resultant motion for all plausible rotation angles ranging from 0° to 180° at a suitable interval. For example, RotD100, RotD50 and RotD00 represent the maximum, the median and the minimum values of a response parameter over all rotation angles, respectively. If $\ddot{u}_g(t)$ and $\ddot{v}_g(t)$ are the time-histories of bidirectional ground motion recorded along two orthogonal horizontal directions, $\vartheta(\in [0, 180))$ is the angle oriented from $\ddot{u}_g(t)$ to the corresponding resultant motion $\ddot{r}_g(t, \vartheta)$ in the counterclockwise sense, the time-history of $\ddot{r}_g(t, \vartheta)$ can be obtained as

$$\ddot{r}_g(t, \vartheta) = \ddot{u}_g(t) \cos \vartheta + \ddot{v}_g(t) \sin \vartheta \quad \forall\ \vartheta \in [0, 180) \quad . \tag{4.1}$$

In this dissertation work, maximum PSA (with 5% damping) observed in any direction of horizontal ground shaking or $\text{PSA}_{\text{RotD100}}$ for each bidirectional ground motion is matched with the target design spectra [3] for three different types of soil conditions (i.e., hard soil, medium stiff soil and soft soil). Hence, a total of 42 DSCBGMs are prepared from 14 recorded bidirectional ground motions (i.e., BGM01 to BGM14 in Table 4.3). The algorithm proposed by Montejo [250] is followed here to produce the DSCBGMs by considering the incremental interval of ϑ as 1°. This algorithm is capable of generating spectrally matched records with most of the characteristics (e.g., the period-dependent major axis orientations) of the original records preserved. The variations of the $\text{PSA}_{\text{RotD100}}$ for all DSCBGMs along with their mean values with respect to the target design spectra for different types of soils are found satisfactory as shown in Figure 4.3. The bidirectional ground motions are not selected using any ground motion selection method (based on scenario-specific or process-specific information) before making them design spectra-compatible for the same reason as in the case of selected unidirectional ground motions (refer to Subsection 3.2.2). Among all the DSCBGMs, 36 DSCBGMs are arbitrarily selected for the training purpose of the 3D GDI evaluation method, whereas the remaining six DSCBGMs are selected for the validation purpose as shown in Table 4.3. Further, the DSCBGMs used for training and validation purposes will be called training DSCBGMs and validation DSCBGMs, respectively, in the present study. Although the orthogonal components of DSCBGMs are applied along the structural principal axes for nonlinear time-history analysis, the random incidence angle of bidirectional ground motion is maintained in the present study because of the random orientations of the princi-

Table 4.3: Details of different bidirectional ground motions

Sl. No.	Motion ID	Earthquake	Date	Recording station	Strong motion duration (s)		Peak ground acceleration (g)		Recording orientation		Used for
					C1	C2	C1	C2	C1	C2	
1	BGM01	Coyote Lake	06/08/1979	CDMG Station 57383	3.24	3.62	0.434	0.316	S40W	S50E	Training
2	BGM02	Westmorland	26/04/1981	CDMG Station 5169	6.68	5.88	0.368	0.496	N00W	N90W	Training
3	BGM03	Imperial Valley	15/10/1979	USGS Station 5165	6.90	6.58	0.352	0.480	S00E	S90E	Training
4	BGM04	Irpinia	23/11/1980	Sturno Station	12.02	11.52	0.251	0.358	N90E	S00E	Training
5	BGM05	Loma Prieta	18/10/1989	Anderson Dam Downstream	10.50	10.84	0.244	0.240	S20W	S70E	Training
6	BGM06	Cape Mendocino	25/04/1992	CDMG Station 89156	17.74	16.08	0.590	0.663	N90E	N00E	Training
7	BGM07	Coalinga	02/05/1983	CDMG Station 36421	10.90	9.82	0.072	0.076	N90E	N00E	Training
8	BGM08	Kobe	16/01/1995	Kakogawa Station	13.14	12.86	0.252	0.345	N90E	N00E	Training
9	BGM09	Livermore	24/01/1980	CDMG Station 57063	19.62	20.08	0.050	0.073	N03W	S87W	Training
10	BGM10	Duzce	12/11/1999	Duzce Station	10.92	10.80	0.348	0.536	N90W	S00E	Training
11	BGM11	Big Bear	01/02/2001	Homeland - HWY & Sultanas	10.32	10.86	0.008	0.007	N90E	N00E	Training
12	BGM12	Landers	28/06/1992	CDMG STATION 24577	13.48	13.50	0.114	0.122	N90E	N00E	Training
13	BGM13	Morgan Hill	24/04/1984	USGS Station 1652	6.78	5.18	0.423	0.289	S20W	S70E	Validation
14	BGM14	Dinar	10/01/1995	Dinar Station	15.72	17.06	0.352	0.282	N00W	N90W	Validation

Note: C1 – Component 1 for the recorded bidirectional ground motion, C2 – Component 2 for the recorded bidirectional ground motion

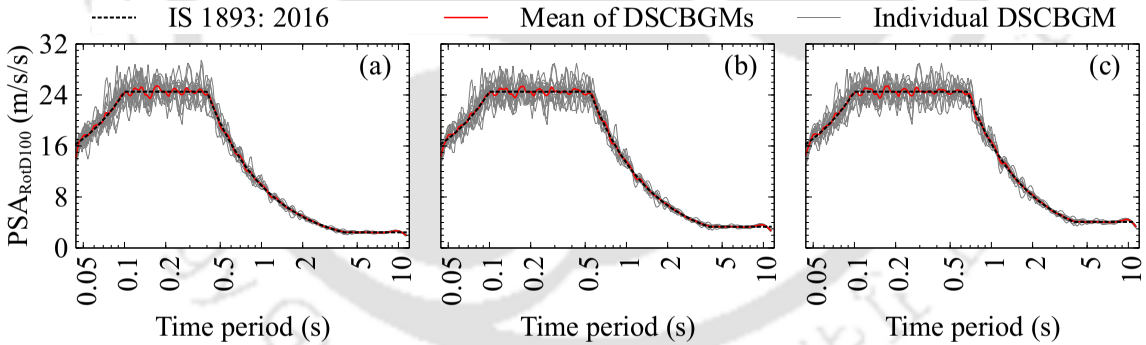

Figure 4.3: Comparisons of design spectra [3] with the $PSA_{RotD100}$ (for 5% damping) of the DSCBGMs when the local soil type is (a) hard, (b) medium stiff, and (c) soft

pal directions (both frequency-dependent and frequency-independent) of all selected ground motions with respect to the structural axes [251]. Further, using RotD100 for design spectrum compatibility assures the regularization of the direction-independent maximum linear response due to any bidirectional ground motions with a random incidence angle.

4.3 New Method for Evaluation of 3D GDI

The scope of the new methodology introduced in Section 3.3 (applicable for 2D RC frames) is extended for more generic 3D RC buildings in this section. Therefore, the new methodology can utilize the recorded floor-displacement responses along two orthogonal horizontal directions of an instrumented building during any earthquake for estimating the corresponding GDI value. However, necessary modifications to the cumulative and non-cumulative terms of the 3D GDI formulae based on the new methodology are introduced so that the formulae can accommodate structural responses considering biaxial bending and axial load developed due to bidirectional ground motions. Based on the new methodology, two different non-decreasing and non-dimensional GDI formulae depending on the type of capacity parameters (i.e., displacement ductility of building and columns, or curvature ductility of columns) are introduced here. Similar to the 2D GDI formulae, the structural deformability of a building is assumed to be strongly correlated with the product of ductility capacity and spectral displacement associated with the corresponding fundamental period of the building. However, the combination of those products along two orthogonal horizontal directions are used for the 3D GDI formulae to capture realistic capacity of buildings against bidirectional ground motions.

4.3.1 3D GDI based on Displacement Ductility of Columns

A finite element model for a 3D building is necessary to get the capacity terms used in the displacement ductility-based combined GDI ($GDI_{3D\text{-}1}$) for the building. The formula to find $GDI_{3D\text{-}1}$ value from the global responses of the building has been introduced as

$$GDI_{3D\text{-}1} = \lambda_{3D\text{-}1}\bar{\mu}_{d,m} + \psi_{3D\text{-}1}\sum_{n=1}^{N_s}\left[\sum_{s=1}^{T_d/\Delta t}\left(\frac{D_{d_n}^2(s\Delta t)}{C_{d_n}^2(s\Delta t)}\right)\right] \tag{4.2}$$

where $\lambda_{3D\text{-}1}$ and $\psi_{3D\text{-}1}$ are the GDCs, $\bar{\mu}_{d,m}$ is the maximum normalized global displacement ductility factor, $D_{d_n}^2(s\Delta t)$ is the displacement-based demand for Floor n at time $s\Delta t$, and $C_{d_n}(s\Delta t)$ is the corresponding displacement ductility-based capacity for Floor n. The first term of Equation 4.2 accounts for the consumption of structural deformability, whereas the second term accounts for the consumption of energy dissipation capacity, similarly as in the cases of the new 2D GDI formulae (refer to Equations 3.1 and 3.4). The non-cumulative part

of $GDI_{3D\text{-}1}$ is chosen to produce a non-zero damage only when the building response exceeds its elastic range similar to the modified Park and Ang damage index [2]. The details about different parameters used in Equation 4.2 are discussed below.

1. *Maximum normalized global displacement ductility factor* ($\bar{\mu}_{d,m}$): the deformation term of the non-cumulative part of $GDI_{3D\text{-}1}$ should anticipate the effect of bidirectional deformation. Therefore, the concept of displacement ductility due to unidirectional deformation is extended for the bidirectional deformation to compute $\bar{\mu}_{d,m}$ as

$$\bar{\mu}_{d,m} = \max |\bar{\mu}_d(s\Delta t)| \quad \forall\ s = 1, 2, \cdots, T_d/\Delta t \tag{4.3}$$

$$\text{with} \quad \bar{\mu}_d(s\Delta t) = \frac{\langle r_{N_s}(s\Delta t) - r_{N_s,y}(s\Delta t)\rangle}{r_{N_s,u}(s\Delta t) - r_{N_s,y}(s\Delta t)} \tag{4.4}$$

$$\langle r_{N_s}(s\Delta t) - r_{N_s,y}(s\Delta t)\rangle = \begin{cases} r_{N_s}(s\Delta t) - r_{N_s,y}(s\Delta t), & \text{if } r_{N_s}(s\Delta t) > r_{N_s,y}(s\Delta t) \\ 0, & \text{otherwise} \end{cases} \tag{4.5}$$

$$r_{N_s}(s\Delta t) = \sqrt{u_{N_s}^2(s\Delta t) + v_{N_s}^2(s\Delta t)} \tag{4.6}$$

where $\bar{\mu}_d(s\Delta t)$ is the normalized global displacement ductility factor at time $s\Delta t$, $r_{N_s}(s\Delta t)$ is the resultant displacement value for Floor N_s (or roof), $u_{N_s}(s\Delta t)$ and $v_{N_s}(s\Delta t)$ are the displacement values recorded at roof along x- and y-directions of the building (refer to Figure 4.1(b)), respectively. $r_{N_s,y}(s\Delta t)$ and $r_{N_s,u}(s\Delta t)$ are the corresponding resultant global yield displacement and resultant global ultimate displacement of the building, respectively, estimated along the direction of $r_{N_s}(s\Delta t)$, and can be expressed as

$$r_{N_s,y}(s\Delta t) = \left[u_y \cdot |u_{N_s}(s\Delta t)| + v_y \cdot |v_{N_s}(s\Delta t)|\right] / r_{N_s}(s\Delta t) \tag{4.7}$$

$$r_{N_s,u}(s\Delta t) = \left[u_u \cdot |u_{N_s}(s\Delta t)| + v_u \cdot |v_{N_s}(s\Delta t)|\right] / r_{N_s}(s\Delta t) \tag{4.8}$$

where u_y and v_y are the global yield displacements for the building along x- and y-directions, respectively. Similarly, u_u and v_u are the global ultimate displacements for the building along its respective directions.

The global force-displacement relationships obtained from nonlinear static analysis of the finite element models due to the static lateral load profile, as recommended in IS 1893 (Part 1): 2016 [3], along the x-direction are used to find u_y and u_u in the present study and their values are enlisted in Table 4.4. The yield displacement of the equivalent elasto-plastic system with reduced stiffness corresponding to 75% of the ultimate lateral strength of the building [223], and the ultimate displacement corresponding to 30% strength reduction after the occurrence of the ultimate lateral strength [237] are considered as u_y and u_u, respectively. v_y and v_u values (as shown in Table 4.5) for the finite element models are computed following the same methodology

(as their counterparts along x-direction) but for the corresponding static lateral load profile along y-direction only. The comparison of the pushover curves for different example RC buildings (refer to Table 4.1) along two orthogonal directions in horizontal plane (i.e., x- and y-directions) are shown in Figure 4.4.

Table 4.4: Different global and sectional parameter values associated with x-direction of the example RC buildings required for $GDI_{3D\text{-}1}$

Sl. No.	Building	$\bar{\mu}_{d_n}^{(x)}$					$T_p^{(x)}$ (s)	u_y (mm)	u_u (mm)
		$n=1$	$n=2$	$n=3$	$n=4$	$n=5$			
1	$2F2B_x5B_y$	6.829	9.463	×	×	×	0.49	110.29	915.0
2	$2F3B_x4B_y$	5.871	7.306	×	×	×	0.57	117.32	660.0
3	$3F2B_x4B_y$	4.841	5.220	7.159	×	×	0.81	198.89	1630.0
4	$3F4B_x3B_y$	6.081	6.819	10.076	×	×	0.92	218.40	1725.0
5	$3F5B_x2B_y$	6.188	6.791	10.558	×	×	0.91	260.48	2155.0
6	$4F3B_x5B_y$	5.731	6.111	8.316	11.514	×	0.88	232.67	1600.0
7	$4F4B_x3B_y$	5.432	5.787	7.681	10.993	×	1.14	259.98	1610.0
8	$5F2B_x5B_y$	4.923	5.139	6.102	7.134	14.041	1.12	319.21	2395.0
9	$5F3B_x4B_y$	4.779	5.011	5.801	6.741	13.365	1.06	268.77	1965.0

Table 4.5: Different global and sectional parameter values associated with y-direction of the example RC buildings required for $GDI_{3D\text{-}1}$

Sl. No.	Building	$\bar{\mu}_{d_n}^{(y)}$					$T_p^{(x)}$ (s)	v_y (mm)	v_u (mm)
		$n=1$	$n=2$	$n=3$	$n=4$	$n=5$			
1	$2F2B_x5B_y$	6.829	9.463	×	×	×	0.47	113.12	660.4
2	$2F3B_x4B_y$	6.116	8.124	×	×	×	0.57	124.40	706.0
3	$3F2B_x4B_y$	4.841	5.220	7.159	×	×	0.76	178.80	1535.0
4	$3F4B_x3B_y$	6.081	6.819	10.076	×	×	0.95	236.84	1780.0
5	$3F5B_x2B_y$	6.188	6.791	10.558	×	×	0.93	205.71	1495.0
6	$4F3B_x5B_y$	5.731	6.111	8.316	11.514	×	0.81	194.92	1425.0
7	$4F4B_x3B_y$	5.432	5.787	7.681	10.993	×	1.18	285.23	1667.5
8	$5F2B_x5B_y$	4.923	5.139	6.102	7.134	14.041	0.97	245.79	1885.0
9	$5F3B_x4B_y$	4.779	5.011	5.801	6.741	13.365	1.05	286.75	2065.0

2. *Displacement-based demand for each floor* ($D_{d_n}^2(s\Delta t)$): incorporating the translational responses of a building floor along two orthogonal directions in a horizontal plane due to bidirectional ground motions, the displacement-based demand for floor n can be expressed as

$$D_{d_n}^2(s\Delta t) = \{\Delta u_n(s\Delta t)\}^2 + \{\Delta v_n(s\Delta t)\}^2 \tag{4.9}$$

with

$$\Delta u_n(s\Delta t) = [u_n(s\Delta t) - u_{n-1}(s\Delta t)] - [u_n\{(s-1)\Delta t\} - u_{n-1}\{(s-1)\Delta t\}] \tag{4.10}$$

$$\Delta v_n(s\Delta t) = [v_n(s\Delta t) - v_{n-1}(s\Delta t)] - [v_n\{(s-1)\Delta t\} - v_{n-1}\{(s-1)\Delta t\}] \tag{4.11}$$

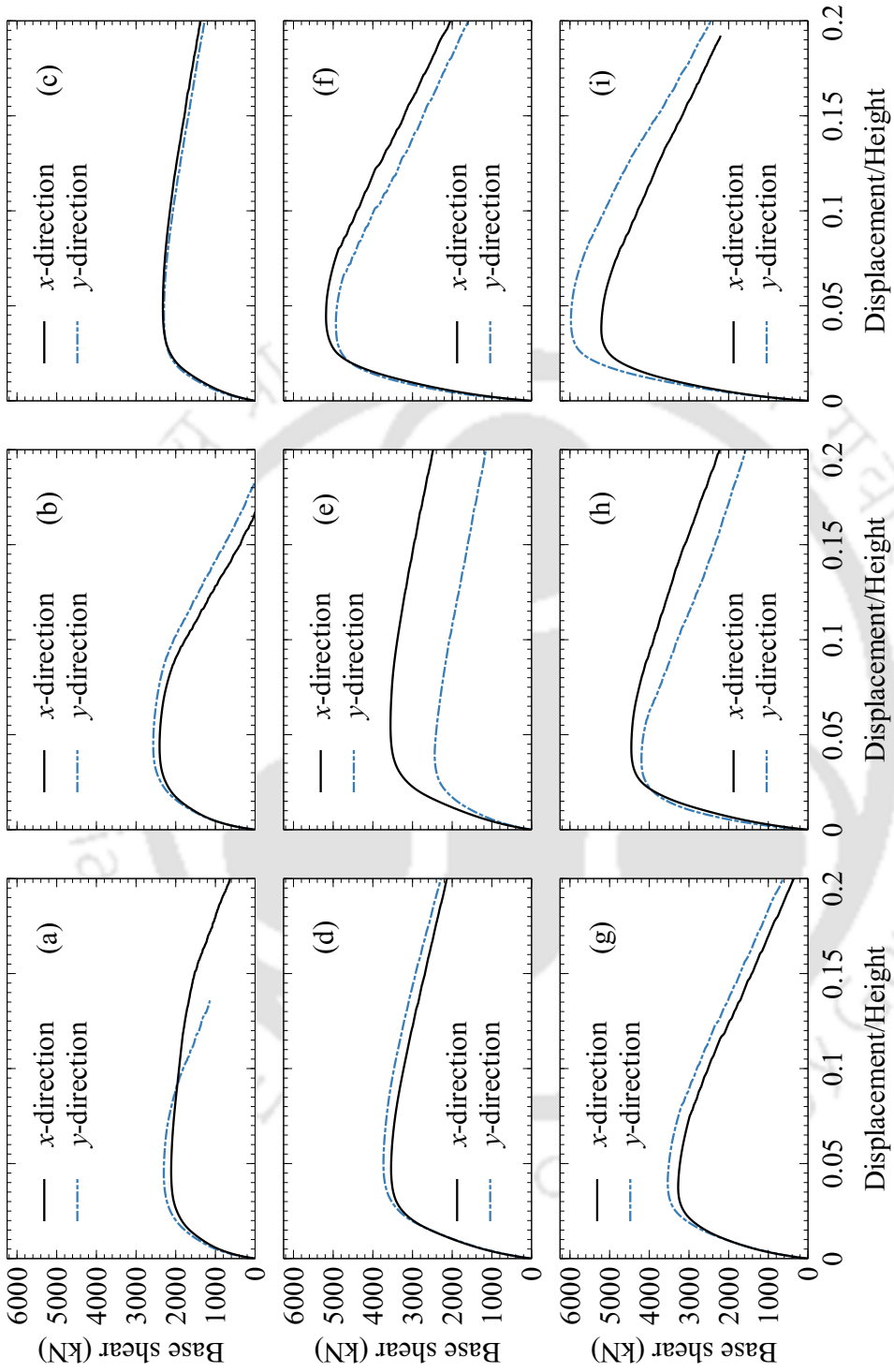

Figure 4.4: Comparison of the pushover curves along two orthogonal horizontal directions for different example 3D RC buildings: (a) $2F2B_x5B_y$, (b) $2F3B_x4B_y$, (c) $3F2B_x4B_y$, (d) $3F4B_x3B_y$, (e) $3F5B_x2B_y$, (f) $4F3B_x5B_y$, (g) $4F4B_x3B_y$, (h) $5F2B_x5B_y$, and (i) $5F3B_x4B_y$

where $\Delta u_n(s\Delta t)$ (and $\Delta v_n(s\Delta t)$) is the difference between the absolute interstory drifts of Floor n and Floor $(n-1)$ at time $s\Delta t$ and $(s-1)\Delta t$ along x- (and y-) direction of the building. $u_n(s\Delta t)$ and $v_n(s\Delta t)$ are the displacement values recorded at Floor n along x- and y-directions, respectively, of the building. The square power in $D_{d_n}^2(s\Delta t)$ is used to make the term equivalent with dissipated energy present as demand in the cumulative term of the modified Park and Ang 3D damage index [2].

3. *Displacement ductility-based capacity for each floor* ($C_{d_n}(s\Delta t)$): the displacement-based capacity for Floor n at time $s\Delta t$ along the direction of resultant displacement of the floor (i.e., $r_n(s\Delta t)$) can be computed as

$$C_{d_n}(s\Delta t) = \frac{\left[\bar{\mu}_{d_n}^{(x)} S_d(x) \cdot |u_n(s\Delta t)| + \bar{\mu}_{d_n}^{(y)} S_d(y) \cdot |v_n(s\Delta t)|\right]}{r_n(s\Delta t)} \tag{4.12}$$

where $\bar{\mu}_{d_n}^{(x)}$ and $\bar{\mu}_{d_n}^{(y)}$ are the weighted average (based on the axial load demand of columns due to gravity loads) of displacement ductility values along x- and y-directions of a building, respectively, for all columns situated between Floor n and Floor $(n-1)$. Their mathematical expressions can be represented as

$$\bar{\mu}_{d_n}^{(x)} = \frac{\sum_{d=1}^{C_{\text{building}}} \left(F_n^{(d)} \cdot \mu_{d_n}^{(d,x)}\right)}{\sum_{d=1}^{C_{\text{building}}} F_n^{(d)}} \quad \text{and} \quad \bar{\mu}_{d_n}^{(y)} = \frac{\sum_{d=1}^{C_{\text{building}}} \left(F_n^{(d)} \cdot \mu_{d_n}^{(d,y)}\right)}{\sum_{d=1}^{C_{\text{building}}} F_n^{(d)}} \tag{4.13}$$

where $C_{\text{building}} = (N_{bx}+1)(N_{by}+1)$ is the total number of columns present in a floor of a building. $F_n^{(d)}$ is the axial load demand due to gravity loads on the dth column situated between Floor n and Floor $(n-1)$, whereas $\mu_{d_n}^{(d,x)}$ and $\mu_{d_n}^{(d,y)}$ are the displacement ductility values along x- and y-directions, respectively, for the corresponding dth column. $r_n(s\Delta t)$ can be computed by replacing the index N_s with n in Equation 4.6, i.e.,

$$r_n(s\Delta t) = \sqrt{u_n^2(s\Delta t) + v_n^2(s\Delta t)} \quad . \tag{4.14}$$

$S_d^{(x)}$ and $S_d^{(y)}$ are the spectral displacement values [3] corresponding to the fundamental periods along x and y-directions $\left(\text{i.e., } T_p^{(x)} \text{ and } T_p^{(y)}\right)$, respectively, of the building. The capacity term, $C_{d_n}(s\Delta t)$, is squared before using in Equation 4.2 to make it dimensionally-compatible with the corresponding demand term, $D_{d_n}^2(s\Delta t)$.

The value of $\mu_{d_n}^{(d,x)}$ $\left(\text{and subsequently } \bar{\mu}_{d_n}^{(x)}\right)$ is derived from the force-displacement relationship for the corresponding column subjected to $F_n^{(d)}$. For this purpose, nonlinear static analysis of a 2D line element with three DOFs (i.e., axial, translational along global x-direction and rotational) at two end nodes and nonlinear material properties are sufficient to get the required response of a column. The yield displacement

and the ultimate displacement values for a column are obtained following the material strain-based rules as described in Subsection 3.3.1. Similarly, $\mu_{d_n}^{(d,y)}$ and $\bar{\mu}_{d_n}^{(y)}$ values can be derived by replacing the translational DOF along global x-direction with global y-direction. For estimating floor-wise displacement ductility values $\left(\bar{\mu}_{d_n}^{(x)} \text{ and } \bar{\mu}_{d_n}^{(y)}\right)$, the axial load demand of each column due to gravity loads is chosen as the weighing function to provide greater importance to the damage of a member which will affect the global structural failure most. The computed values of $\bar{\mu}_{d_n}^{(x)}$ and $\bar{\mu}_{d_n}^{(y)}$ for the sample buildings are enlisted in Tables 4.4 and 4.5, respectively. The fundamental periods, $T_p^{(x)}$ and $T_p^{(y)}$, for the sample buildings are obtained using eigenvalue analysis of the corresponding 3D finite element models and their values are shown in Tables 4.4 and 4.5.

4.3.2 3D GDI based on curvature Ductility of Columns

The estimation of the curvature-based combined GDI ($GDI_{3D\text{-}2}$) value for a 3D RC building does not require any finite element model. The formula to get $GDI_{3D\text{-}2}$ value from the global responses of a building has been introduced as

$$GDI_{3D\text{-}2} = \lambda_{3D\text{-}2}\bar{\mu}_{\phi,m} + \psi_{3D\text{-}2}\sum_{n=1}^{N_s}\left[\sum_{s=1}^{T_d/\Delta t}\left(\frac{D_{d_n}^2(s\Delta t)}{C_{\phi_n}^2(s\Delta t)}\right)\right] + \gamma_{3D\text{-}2} \tag{4.15}$$

where $\lambda_{3D\text{-}2}, \psi_{3D\text{-}2}$ and $\gamma_{3D\text{-}2}$ are the GDCs, $\bar{\mu}_{\phi,m}$ is the maximum overall curvature ductility factor, and $C_{\phi_n}(s\Delta t)$ is the corresponding resultant curvature ductility-based capacity for Floor n at time $s\Delta t$. It is obvious that some damage to the building will occur according to the first part of Equation (4.15) even if the floor-displacement responses are within the elastic range because the recoverable displacement portion is not removed from both the denominator and the numerator of that part, similarly as in the case of Equation (3.4). Therefore, another global damage coefficient $\gamma_{3D\text{-}2}$ is included in $GDI_{3D\text{-}2}$ (similar to GDI_{2D-2} in Subsection 3.3.2) to make it consistent with the modified Park and Ang-type 3D damage index [2]. The details about the different parameters used in Equation 4.15 are discussed below.

1. *Maximum overall curvature ductility factor* ($\bar{\mu}_{\phi,m}$): following the similar concept for finding $\bar{\mu}_{d,m}$, the parameter $\bar{\mu}_{\phi,m}$ can be computed as

$$\bar{\mu}_{\phi,m} = \max|\bar{\mu}_{\phi}(s\Delta t)| \quad \forall\ s = 1, 2, \cdots, T_d/\Delta t \tag{4.16}$$

$$\text{with} \quad \bar{\mu}_{\phi}(s\Delta t) = \frac{r_{N_s}(s\Delta t)}{C_{\phi}(s\Delta t)} \tag{4.17}$$

where $\bar{\mu}_{\phi}(s\Delta t)$ is the overall curvature ductility factor at time $s\Delta t$, $C_{\phi}(s\Delta t)$ is the overall curvature ductility-based capacity estimated along the direction of $r_{N_s}(s\Delta t)$,

and can be expressed as

$$C_{\phi}(s\Delta t) = \frac{\left[\bar{\mu}_{\phi}^{(x)} S_d'^{(x)} \cdot |u_{N_s}(s\Delta t)| + \bar{\mu}_{\phi}^{(y)} S_d'^{(y)} \cdot |v_{N_s}(s\Delta t)|\right]}{r_{N_s}(s\Delta t)} \tag{4.18}$$

with

$$\bar{\mu}_{\phi}^{(x)} = \frac{\sum_{n=1}^{N_s}\left[\left(\sum_{d=1}^{C_{\text{building}}} F_n^{(d)}\right) \cdot \bar{\mu}_{\phi_n}^{(x)}\right]}{\sum_{n=1}^{N_s}\left(\sum_{d=1}^{C_{\text{building}}} F_n^{(d)}\right)} \quad \text{and} \quad \bar{\mu}_{\phi_n}^{(x)} = \frac{\sum_{d=1}^{C_{\text{building}}}\left(F_n^{(d)} \cdot \mu_{\phi_n}^{(d,x)}\right)}{\sum_{d=1}^{C_{\text{building}}}\left(F_n^{(d)}\right)} \tag{4.19}$$

$$\bar{\mu}_{\phi}^{(y)} = \frac{\sum_{n=1}^{N_s}\left[\left(\sum_{d=1}^{C_{\text{building}}} F_n^{(d)}\right) \cdot \bar{\mu}_{\phi_n}^{(y)}\right]}{\sum_{n=1}^{N_s}\left(\sum_{d=1}^{C_{\text{building}}} F_n^{(d)}\right)} \quad \text{and} \quad \bar{\mu}_{\phi_n}^{(y)} = \frac{\sum_{d=1}^{C_{\text{building}}}\left(F_n^{(d)} \cdot \mu_{\phi_n}^{(d,y)}\right)}{\sum_{d=1}^{C_{\text{building}}}\left(F_n^{(d)}\right)} \tag{4.20}$$

where $\bar{\mu}_{\phi}^{(x)}$ is the weighted average of curvature ductility values for all columns of a building, $S_d'^{(x)}$ is the spectral displacement value [3] corresponding to the fundamental period, $T_p'^{(x)}$, of the building, $\bar{\mu}_{\phi_n}^{(x)}$ and $\mu_{\phi_n}^{(d,x)}$ are the weighted average of curvature ductility values for all columns and the curvature ductility value for the dth column, respectively, situated between Floor n and Floor $(n-1)$. Here, the axial load demand of each column due to gravity is used as the weighing function to estimate the values of $\bar{\mu}_{\phi}^{(x)}, \bar{\mu}_{\phi}^{(y)}, \bar{\mu}_{\phi_n}^{(x)}$ and $\bar{\mu}_{\phi_n}^{(y)}$, similarly as in the case of $\bar{\mu}_{d_n}^{(x)}$ and $\bar{\mu}_{d_n}^{(y)}$. The terms x and y in the superscripts of various parameters in Equations (4.18)-(4.20) represent the global direction of a building (refer to Figure 4.1) with which the parameters are associated. For computing $\mu_{\phi_n}^{(d,x)}$ or $\mu_{\phi_n}^{(d,y)}$ value of a column section from its moment-curvature relationship, the yield and the ultimate curvatures are obtained following the material strain-based rules (as described in Subsection 3.3.1) used to get similar displacement capacity parameters for column members. Moment-curvature relationships about x- and y-axes for a column section (with the corresponding axial load due to gravity loads) can be generated using the section geometry and the nonlinear material properties [238]. Unlike the displacement ductility-based $GDI_{3D\text{-}1}$, $T_p'^{(x)}$ and $T_p'^{(y)}$ values are estimated from the eigenvalue analysis of the sample buildings (refer to Appendix A), assuming two translational and one in-plane rotational DOFs are attached at the center of mass for each floor (as shown in Figure 4.1(b) and (c)) for $GDI_{3D\text{-}2}$. The values of different floor-wise and building-wise curvature ductility values, and fundamental periods along two orthogonal horizontal directions for the sample buildings are provided in Table 4.6. Here, the estimated values for $T_p'^{(x)}$ and $T_p'^{(y)}$ are found to be equal as expected in the case of all torsionally uncoupled sample buildings. So, these fundamental period-related

terms will be referred as T'_p onwards for the considered sample buildings.

Table 4.6: Different global and sectional parameter values associated with both orthogonal horizontal directions of the example RC buildings required for $GDI_{3D\text{-}2}$

Sl. No.	Building	$\bar{\mu}_{\phi_n}^{(x)} = \bar{\mu}_{\phi_n}^{(y)}$					$\bar{\mu}_{\phi}^{(x)} = \bar{\mu}_{\phi}^{(y)}$	$T_p'^{(x)} = T_p'^{(y)}$ (s)
		$n=1$	$n=2$	$n=3$	$n=4$	$n=5$		
1	$2F2B_x5B_y$	9.576	11.060	×	×	×	9.990	0.293
2	$2F3B_x4B_y$	9.930	11.059	×	×	×	10.247	0.363
3	$3F2B_x4B_y$	9.205	10.213	12.053	×	×	9.909	0.389
4	$3F4B_x3B_y$	14.674	15.543	16.060	×	×	15.144	0.483
5	$3F5B_x2B_y$	15.611	15.653	16.380	×	×	15.723	0.489
6	$4F3B_x5B_y$	15.162	16.326	15.310	16.771	×	15.670	0.423
7	$4F4B_x3B_y$	14.225	15.853	15.171	16.631	×	15.087	0.603
8	$5F2B_x5B_y$	13.790	15.530	16.270	15.943	17.556	15.215	0.453
9	$5F3B_x4B_y$	12.037	14.068	15.709	16.130	17.633	14.118	0.445

2. *Curvature ductility-based capacity for each floor* ($C_{\phi_n}^2(s\Delta t)$): the expression for computing floor-wise curvature ductility-based capacity at time $s\Delta t$ along the direction of $r_n(s\Delta t)$ is represented as

$$C_{\phi_n}(s\Delta t) = \frac{\left[\bar{\mu}_{\phi_n}^{(x)} S_d'^{(x)} \cdot |u_n(s\Delta t)| + \bar{\mu}_{\phi_n}^{(y)} S_d'^{(y)} \cdot |v_n(s\Delta t)|\right]}{r_n(s\Delta t)} \quad . \tag{4.21}$$

4.3.3 Estimation of Required Global Damage Coefficients

The structural responses of the eight training RC buildings (refer to Table 4.1) are obtained from nonlinear time-history analyses of the corresponding finite element models due to 36 training DSCBGMs (refer to Table 4.3) using OpenSees framework [210]. The LDI values for each plastic hinge are computed using the section-level responses of those finite element models according to the modified Park and Ang-type 3D damage index formula, $LDI_{3D\text{-GWLZD}}$ [2], represented by Equations (1.20)-(1.24). Further, total dissipated hysteresis energy, $E_{3D\text{-}h_p}$ (sum of the dissipated hysteresis energies associated with two principal axes for a member section), at pth plastic hinge location is used in the present study as weighing function over computed LDI values at all plausible plastic hinge locations to get the corresponding 3D global damage index value as

$$GDI_{3D\text{-GWLZD}} = \frac{\sum_{p=1}^{P_h} \left(LDI_{3D\text{-GWLZD}_p} \cdot E_{3D\text{-}h_p}\right)}{\sum_{p=1}^{P_h} \left(E_{3D\text{-}h_p}\right)} \quad . \tag{4.22}$$

Each finite element model, developed in the present study for various training buildings (refer to Table 4.1), is analysed several times, and each time both horizontal ground motions of a DSCBGM are multiplied with a particular scale factor. In this way, the structural

behaviour of each training building with different global damage states (i.e., no damage, repairable, irreparable and collapse) can be obtained thoroughly due to a particular DSCBGM. This procedure is repeated for all training DSCBGMs (refer to Table 4.3), and the set of corresponding nonlinear structural responses are used further to obtain the GDCs or (regression coefficients as shown in Equations (4.2) and (4.15)) through the univariate multiple linear regression analysis (by minimizing the corresponding least squares function) individually for each pair of a building and a soil type. The $GDI_{3D\text{-GWLZD}}$ values are utilized as the dependent variable, whereas the non-cumulative and the cumulative parts available in the new 3D GDI formulae ($GDI_{3D\text{-}1}$ and $GDI_{3D\text{-}2}$) are utilized as the independent variables for the multilinear regression analysis.

In the literature, no citation exists for estimating the global damage index value for a 3D RC building from the local damage indices of all plastic hinge locations using any suitable weighing function to date. Accordingly, limiting values for any 3D global damage index associated with different global damage states are also not available. Therefore, the correlation between $GDI_{3D\text{-GWLZD}}$ and the global collapse state is first established in the current study. The global collapse of a building usually occurs when no overall strength is reserved in the building to resist any seismic event. Numerically this condition can be identified for a particular building by applying factored bidirectional ground motions until a sharp change is observed in computed $GDI_{3D\text{-GWLZD}}$ values for a slight change in the scale factor. Figure 4.5 shows such evolution of computed $GDI_{3D\text{-GWLZD}}$ values for two training buildings, $5F2B_x5B_y$ and $5F3B_x4B_y$, due to factored DSCBGMs associated with arbitrarily selected three training bidirectional ground motions, i.e., BGM05, BGM09 and BGM11. For all considered training buildings and training DSCBGMs, it has been found that the global collapses (as demarcated in Figure 4.5 for $5F2B_x5B_y$ and $5F3B_x4B_y$ only) occur when 50% of GF columns or 10% of GF columns along with 50% of beams at any floor are collapsed. Here, the local damage states of individual members (columns and beams) can be determined using the limiting range for $LDI_{3D\text{-GWLZD}}$ values proposed by Guo et al. [2] (refer to Table 1.4). The responses from the nonlinear time-history analysis in the case of a particular pair of a training building and a training DSCBGM with different scale factors until the corresponding global collapse occurs are considered further for the linear regression study.

The average of the computed $GDI_{3D\text{-GWLZD}}$ values associated with the global collapse condition due to training DSCBGMs for different local soil types and different training buildings are shown in Table 4.7. Unlike 2D frames, the computed GDI values for globally collapsed 3D buildings are not equal to 1.0. Also, the GDI values vary within a large range (from 0.302 to 0.624) for different training buildings as shown in Table 4.7. This is because the number of members (mainly beams on any floor and columns on upper floors) with no damage to moderate damage in a 3D building is quite large (in comparison with its 2D representation as a frame) when other members (especially columns in the GF) are severely damaged or on the verge of collapse. So, such low-damaged members constitute a large portion of the

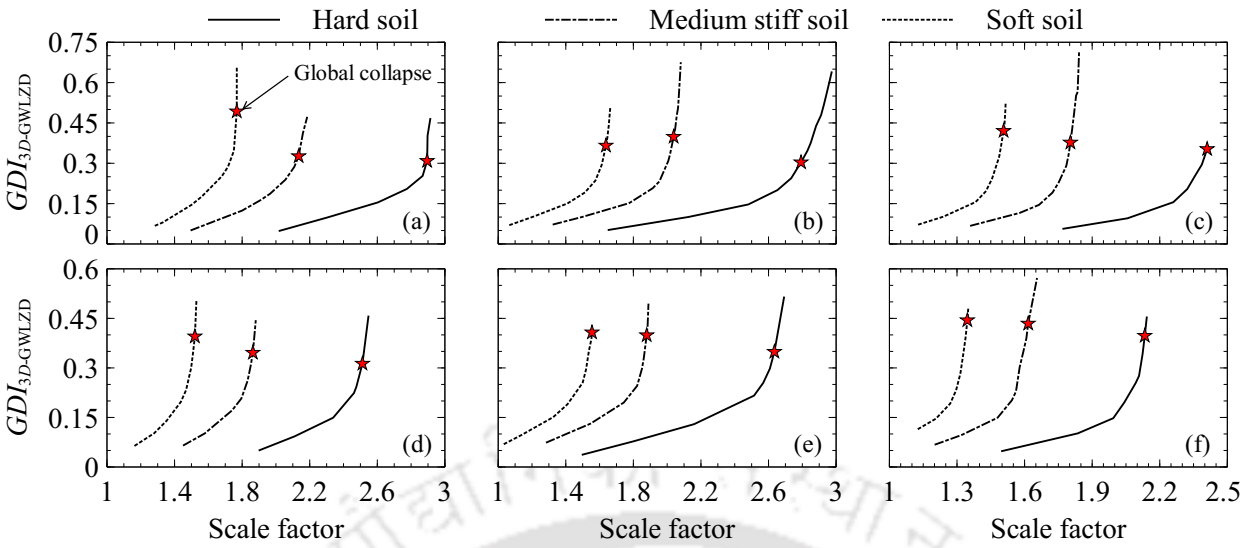

Figure 4.5: Evolution of computed $GDI_{3D\text{-}GWLZD}$ values with scale factors of DSCBGMs in the case of (a) $5F2B_x5B_y$ and BGM05, (b) $5F2B_x5B_y$ and BGM09, (c) $5F2B_x5B_y$ and BGM11, (d) $5F3B_x4B_y$ and BGM05, (e) $5F3B_x4B_y$ and BGM09, and (f) $5F3B_x4B_y$ and BGM11

total dissipated hysteresis energy and reduce the GDI value of a building significantly even though the overall strength of the building is nearly exhausted. Since the disparity in the number of low-damaged members increases with the number of storeys in a building, smaller $GDI_{3D\text{-}GWLZD}$ values are observed for the training buildings with 4 to 5 storeys than that of the buildings with 2 to 3 storeys in the present study as reported in Table 4.7.

Table 4.7: Average of $GDI_{3D\text{-}GWLZD}$ values for globally collapsed training buildings due to training DSCBGMs for different local soil types

Sl. No.	Building	Average $GDI_{3D\text{-}GWLZD}$ values associated with global collapse state due to training DSCBGMs for different soil conditions		
		Hard soil	Medium stiff soil	Soft soil
1	$2F2B_x5B_y$	0.584	0.588	0.624
2	$2F3B_x4B_y$	0.566	0.582	0.594
3	$3F2B_x4B_y$	0.428	0.458	0.476
4	$3F5B_x2B_y$	0.434	0.475	0.501
5	$4F3B_x5B_y$	0.302	0.344	0.358
6	$4F4B_x3B_y$	0.331	0.341	0.355
7	$5F2B_x5B_y$	0.304	0.344	0.354
8	$5F3B_x4B_y$	0.361	0.408	0.405

For most of the available SDI models, the collapse of a member (or a whole structure) is usually apprehended when the value of the corresponding damage index becomes 1.0. Therefore, the normalization factors for each training building and each soil type (considering all associated training DSCBGMs) are obtained to match the average $GDI_{3D\text{-}GWLZD}$ values with

1.0 when global collapse occurs for a building in the case of different soil types. Basically, the normalization factor for a particular building and a soil type is the inverse of the corresponding average $GDI_{3D\text{-GWLZD}}$ value enlisted in Table 4.7. These normalization factors are further multiplied with all computed $GDI_{3D\text{-GWLZD}}$ values for the corresponding buildings and the factored DSCBGMs (responsible for less damage than global collapse) before using the GDI values directly as the dependent variable in the multilinear regression analysis. Such normalization will not only scale the estimated $GDI_{3D\text{-GWLZD}}$ value for a building to 1.0 to represent the global collapse but also pave the way for a uniform limiting range of the 3D GDI values for other global damage states applicable to all 3D RC buildings. Hereafter, the $GDI_{3D\text{-GWLZD}}$ values multiplied with the normalization factors will be referred as the normalized $GDI_{3D\text{-GWLZD}}$ or $\widetilde{GDI}_{3D\text{-GWLZD}}$ values for better clarity in this thesis. On the other hand, the normalization factors are not applied to the independent variables (i.e., non-cumulative and cumulative terms of the 3D GDI formulae, $GDI_{3D\text{-}1}$ and $GDI_{3D\text{-}2}$) in the regression analysis, because the regression coefficients (or the GDCs) can inherently take care of the effect of the normalization factors in the predicted $GDI_{3D\text{-GWLZD}}$ values.

Similar to the GDCs (i.e., $\lambda_{2D\text{-}1}, \lambda_{2D\text{-}2}, \psi_{2D\text{-}1}, \psi_{2D\text{-}2}$ and $\gamma_{2D\text{-}2}$) available in the new 2D GDI formulae, the GDCs (i.e., $\lambda_{3D\text{-}1}, \lambda_{3D\text{-}2}, \psi_{3D\text{-}1}, \psi_{3D\text{-}2}$ and $\gamma_{3D\text{-}2}$) of $GDI_{3D\text{-}1}$ and $GDI_{3D\text{-}2}$ are also needed to be expressed explicitly for any combination of a 3D RC building and a soil type for wider applicability. Therefore, another set of regression analyses is performed on the values of GDCs (obtained from 24 individual regression analyses regarding all combinations of eight training buildings and three different types of soil) with some global building parameters (e.g., fundamental periods, numbers of bays and floors, total height, total bay widths along orthogonal directions) and the soil type as the independent variables.

4.4 Results and Discussions

4.4.1 Statistical Analyses for 3D GDIs

Results of the regression analyses for evaluating the GDCs and some other supporting results are discussed and represented efficiently in this section with the help of the same indices (i.e., i, j and k) used in the cases of $GDI_{2D\text{-}1}$ and $GDI_{2D\text{-}2}$ (refer to Subsection 3.4.1). However, the indices i and k represent different GDI formulae and different training buildings in this chapter. For example, the index i with the values equal to 1 and 2 is used to represent the formulae $GDI_{3D\text{-}1}$ and $GDI_{3D\text{-}2}$, respectively, and the index k with the values equal 1 to 8 is used to represent different training buildings as shown in Tables 4.8 and 4.9. On the other hand, the index j takes the same values (as considered in Subsection 3.4.1) ranging from 1 to 3 for representing the different soil types. Therefore, the values of the GDCs, $\lambda_{3D\text{-}i}^{(j,k)}$ and $\psi_{3D\text{-}i}^{(j,k)}$, associated with the ith 3D GDI formula and corresponding to the combination of the jth soil type and the kth building are estimated for the complete ranges of i, j and k using the

regression analyses, whereas $\gamma_{3D\text{-}i}^{(j,k)}$ values are estimated for $i = 2$ (i.e., for $GDI_{3D\text{-}2}$ formula) and the complete ranges of j and k. Their estimated values are provided in Tables 4.8 and 4.9. As expected, the values of the coefficients $\gamma_{3D\text{-}2}^{(j,k)}$ are found negative for all training cases as they offset the non-zero damage resulting from the peak elastic response of any building.

Since the scope of the new GDI evaluation methodology (introduced in Chapter 3) is extended for 3D RC buildings with some necessary modifications to the non-cumulative and the cumulative terms of the GDI formulae in the current chapter, some statistical tests of hypotheses about the regression model parameters are also required to be carried out for examining the existence of a linear relationship between the selected dependent variable (i.e., $\widetilde{GDI}_{3D\text{-GWLZD}}$) and the corresponding independent variables (i.e., non-cumulative and cumulative terms of $GDI_{3D\text{-}1}$ and $GDI_{3D\text{-}2}$). Therefore, the F-test and Student's t-test for significance of regression are performed to examine various suitable null and alternative hypotheses associated with the ith 3D GDI formula in the case of the jth soil type and the kth building. The null hypotheses and the alternative hypotheses corresponding to the F-test are considered as

$$H_{0,3D}^{(i,j,k)} : \lambda_{3D\text{-}i}^{(j,k)} = \psi_{3D\text{-}i}^{(j,k)} = 0 \ \forall \ i, j \text{ and } k \tag{4.23}$$

$$H_{a,3D}^{(i,j,k)} : \text{at least one between } \lambda_{3D\text{-}i}^{(j,k)} \text{ and } \psi_{3D\text{-}i}^{(j,k)} \neq 0 \ \forall \ i, j \text{ and } k \quad . \tag{4.24}$$

The corresponding F-test statistic, $f_{0,3D}^{(i,j,k)}$, can be estimated from Equation 3.9 by replacing the values of different parameters associated with ith 2D GDI formula (i.e., $q_{2D}^{(j,k)}$, $GDI_{2D\text{-}i}^{(j,k,g)}$, $GDI_{2D\text{-ST}}^{(j,k,g)}$ and $\overline{GDI}_{2D\text{-ST}}^{(j,k)}$) with their counterparts for the ith 3D GDI formula (i.e., $q_{3D}^{(j,k)}$, $GDI_{3D\text{-}i}^{(j,k,g)}$, $\widetilde{GDI}_{3D\text{-GWLZD}}^{(j,k,g)}$ and the mean of all $\widetilde{GDI}_{3D\text{-GWLZD}}^{(j,k,g)}$ values). The values of v_i and w for $GDI_{3D\text{-}i}$ are same as for $GDI_{2D\text{-}i}$, and the values for the parameter $q_{3D}^{(j,k)}$ are provided in Table 4.8 (or Table 4.9). The estimated values of $f_{0,3D}^{(i,j,k)}$ for all combinations of two new 3D GDI formulae, three different types of soil and the considered training buildings are shown in Tables 4.8 and 4.9. On the other hand, the maximum value of the corresponding percentage point of the F-distribution at the 5% level of significance is equal to 3.16 for all training cases. So, the null hypotheses of Equation (4.23) can be rejected which signifies the fact that the dependent variable has a linear relationship with either or both of independent variables considered in the cases of the two 3D GDI formulae and all possible combinations of the soil types and the training frames [240].

Now, for carrying out Student's t-test the following null and alternative hypotheses are considered as

$$H_{0,\lambda_{3D\text{-}i}}^{(j,k)} : \lambda_{3D\text{-}i}^{(j,k)} = 0 \ \forall \ i, j \text{ and } k \tag{4.25}$$

$$H_{a,\lambda_{3D\text{-}i}}^{(j,k)} : \lambda_{3D\text{-}i}^{(j,k)} \neq 0 \ \forall \ i, j \text{ and } k \tag{4.26}$$

$$H_{0,\psi_{3D\text{-}i}}^{(j,k)} : \psi_{3D\text{-}i}^{(j,k)} = 0 \ \forall \ i, j \text{ and } k \tag{4.27}$$

$$H_{a,\psi_{3D\text{-}i}}^{(j,k)} : \psi_{3D\text{-}i}^{(j,k)} \neq 0 \ \forall \ i, j \text{ and } k \quad . \tag{4.28}$$

Table 4.8: Different statistical results for $GDI_{3D\text{-}1}$

Sl. No.	i	j	Building	k	$\lambda_{3D\text{-}i}^{(j,k)}$	$\psi_{3D\text{-}i}^{(j,k)}$	$\gamma_{3D\text{-}i}^{(j,k)}$	$q_{3D}^{(j,k)}$	$f_{0,3D}^{(i,j,k)}$	$\left\lvert t_{0,\lambda_{3D\text{-}i}}^{(j,k)} \right\rvert$	$\left\lvert t_{0,\psi_{3D\text{-}i}}^{(j,k)} \right\rvert$	$R^2_{\text{adj.}}\lvert_{3D\text{-}i}^{(j,k)}$	$R^2_{\text{pred.}}\lvert_{3D\text{-}i}^{(j,k)}$	$\rho_{3D\text{-SM}}^{(i,j,k)}$
1	1	1	2F2B$_x$5B$_y$	1	0.4387	0.7580	×	119	631.37	155.11	183.03	0.912	0.910	0.961
2	1	1	2F3B$_x$4B$_y$	2	0.4662	0.9391	×	123	509.65	146.15	158.45	0.892	0.889	0.956
3	1	1	3F2B$_x$4B$_y$	3	0.9539	0.3850	×	96	274.92	143.25	63.60	0.848	0.843	0.927
4	1	1	3F5B$_x$2B$_y$	4	0.2093	0.3013	×	146	445.82	77.42	89.08	0.901	0.895	0.960
5	1	1	4F3B$_x$5B$_y$	5	0.5933	0.0837	×	73	817.43	481.14	114.13	0.958	0.955	0.979
6	1	1	4F4B$_x$3B$_y$	6	0.3770	0.1089	×	70	2106.1	1173.1	515.35	0.984	0.984	0.990
7	1	1	5F2B$_x$5B$_y$	7	0.6194	0.0382	×	61	539.86	371.20	66.58	0.939	0.936	0.968
8	1	1	5F3B$_x$4B$_y$	8	0.5166	0.0576	×	79	896.77	494.38	176.64	0.959	0.957	0.980
9	1	2	2F2B$_x$5B$_y$	1	0.5428	1.0900	×	117	455.16	146.94	128.24	0.883	0.879	0.955
10	1	2	2F3B$_x$4B$_y$	2	0.5506	1.4910	×	128	526.05	181.45	145.38	0.890	0.886	0.958
11	1	2	3F2B$_x$4B$_y$	3	0.9973	0.5230	×	102	250.48	162.93	50.71	0.826	0.822	0.914
12	1	2	3F5B$_x$2B$_y$	4	0.3477	0.1856	×	125	394.11	194.41	48.69	0.886	0.854	0.934
13	1	2	4F3B$_x$5B$_y$	5	0.5503	0.1663	×	83	981.06	568.03	152.83	0.960	0.958	0.979
14	1	2	4F4B$_x$3B$_y$	6	0.4225	0.1707	×	73	1301.6	1032.7	285.17	0.974	0.972	0.984
15	1	2	5F2B$_x$5B$_y$	7	0.6068	0.0854	×	72	649.37	420.84	99.06	0.941	0.937	0.973
16	1	2	5F3B$_x$4B$_y$	8	0.5095	0.1009	×	93	1097.3	600.88	208.38	0.961	0.959	0.979
17	1	3	2F2B$_x$5B$_y$	1	0.6213	0.8950	×	120	455.80	163.06	102.14	0.883	0.879	0.954
18	1	3	2F3B$_x$4B$_y$	2	0.6639	1.3691	×	131	455.21	182.04	96.74	0.869	0.864	0.953
19	1	3	3F2B$_x$4B$_y$	3	0.9316	0.9192	×	106	282.79	146.02	55.69	0.834	0.829	0.928
20	1	3	3F5B$_x$2B$_y$	4	0.2945	0.5308	×	131	746.54	184.98	93.57	0.932	0.930	0.967
21	1	3	4F3B$_x$5B$_y$	5	0.5641	0.2676	×	79	860.48	513.45	133.19	0.954	0.952	0.972
22	1	3	4F4B$_x$3B$_y$	6	0.4301	0.2748	×	68	1772.6	1451.1	426.76	0.982	0.981	0.990
23	1	3	5F2B$_x$5B$_y$	7	0.6303	0.1281	×	77	825.48	535.26	113.31	0.953	0.950	0.974
24	1	3	5F3B$_x$4B$_y$	8	0.5564	0.1379	×	82	1042.6	621.12	157.48	0.963	0.961	0.980

Table 4.9: Different statistical results for $GDI_{3D\text{-}2}$

Sl. No.	i	j	Building	k	$\lambda_{3D\text{-}i}^{(j,k)}$	$\psi_{3D\text{-}i}^{(j,k)}$	$\gamma_{3D\text{-}i}^{(j,k)}$	$q_{3D}^{(j,k)}$	$f_{0,3D}^{(i,j,k)}$	$\left\lvert t_{0,\lambda_{3D\text{-}i}}^{(j,k)} \right\rvert$	$\left\lvert t_{0,\psi_{3D\text{-}i}}^{(j,k)} \right\rvert$	$R^2_{\text{adj.}}\lvert_{3D\text{-}i}^{(j,k)}$	$R^2_{\text{pred.}}\lvert_{3D\text{-}i}^{(j,k)}$	$\rho_{3D\text{-SM}}^{(i,j,k)}$
1	2	1	$2F2B_x5B_y$	1	0.3085	0.2427	−0.0661	119	779.38	8.79	18.41	0.930	0.926	0.970
2	2	1	$2F3B_x4B_y$	2	0.9197	0.4963	−0.2010	123	494.05	10.90	10.47	0.890	0.886	0.947
3	2	1	$3F2B_x4B_y$	3	0.6845	0.2553	−0.1630	96	381.72	12.15	6.95	0.889	0.885	0.940
4	2	1	$3F5B_x2B_y$	4	0.4057	0.0979	−0.0826	146	903.25	40.11	3.33	0.926	0.920	0.966
5	2	1	$4F3B_x5B_y$	5	0.7021	0.0597	−0.0574	73	748.49	15.77	6.78	0.954	0.951	0.978
6	2	1	$4F4B_x3B_y$	6	0.5538	0.0981	−0.0338	70	1504.0	14.71	13.84	0.978	0.976	0.988
7	2	1	$5F2B_x5B_y$	7	0.5032	0.0296	−0.0247	61	449.65	11.86	4.67	0.937	0.932	0.973
8	2	1	$5F3B_x4B_y$	8	0.4033	0.0469	−0.0182	79	821.87	14.33	10.88	0.955	0.952	0.978
9	2	2	$2F2B_x5B_y$	1	0.4404	0.2372	−0.1250	117	658.76	10.80	14.77	0.919	0.914	0.965
10	2	2	$2F3B_x4B_y$	2	1.0637	0.3672	−0.2040	128	402.41	10.25	7.23	0.863	0.858	0.940
11	2	2	$3F2B_x4B_y$	3	0.6507	0.2205	−0.1410	102	359.51	12.15	6.90	0.877	0.873	0.938
12	2	2	$3F5B_x2B_y$	4	0.5380	0.0650	−0.0802	125	2142.2	61.14	2.15	0.972	0.971	0.983
13	2	2	$4F3B_x5B_y$	5	0.6393	0.0780	−0.0176	83	806.93	14.24	8.33	0.952	0.948	0.979
14	2	2	$4F4B_x3B_y$	6	0.9063	0.1444	−0.0634	73	933.06	15.34	8.26	0.963	0.960	0.979
15	2	2	$5F2B_x5B_y$	7	0.5640	0.0459	−0.0286	72	591.05	13.24	7.40	0.943	0.937	0.975
16	2	2	$5F3B_x4B_y$	8	0.4683	0.0507	−0.0310	93	922.06	15.76	10.44	0.952	0.950	0.978
17	2	3	$2F2B_x5B_y$	1	0.4924	0.2014	−0.1360	120	657.85	11.50	11.91	0.917	0.912	0.966
18	2	3	$2F3B_x4B_y$	2	1.2597	0.2928	−0.2640	131	489.41	12.76	5.63	0.883	0.878	0.948
19	2	3	$3F2B_x4B_y$	3	0.5631	0.2417	−0.0867	106	367.33	10.54	7.29	0.875	0.870	0.945
20	2	3	$3F5B_x2B_y$	4	0.5816	0.1498	−0.0897	131	2659.1	70.69	4.59	0.976	0.974	0.986
21	2	3	$4F3B_x5B_y$	5	0.6062	0.0929	−0.0044	79	1069.8	15.05	10.20	0.965	0.962	0.974
22	2	3	$4F4B_x3B_y$	6	1.0879	0.1799	−0.0896	68	996.01	16.77	8.57	0.967	0.966	0.985
23	2	3	$5F2B_x5B_y$	7	0.5595	0.0498	−0.0174	77	607.20	13.04	7.45	0.941	0.937	0.970
24	2	3	$5F3B_x4B_y$	8	0.4659	0.0545	−0.0123	82	1110.0	15.81	9.86	0.965	0.963	0.984

The corresponding t-test statistics for 3D GDI formulae, $t^{(j,k)}_{0,\lambda_{3D\text{-}i}}$ and $t^{(j,k)}_{0,\psi_{3D\text{-}i}}$, can be obtained from Equations (3.14) to (3.17) by replacing the values of different parameters associated with ith 2D GDI formula with their counterparts for the ith 3D GDI formula. In this case, the values of $\tilde{x}_{2D\text{-}i}$ and $\tilde{y}_{2D\text{-}i}$ for $GDI_{3D\text{-}1}$ and $GDI_{3D\text{-}2}$, respectively, can be obtained using the following expressions

$$\tilde{x}_{3D\text{-}1} = \bar{\mu}_{d,m} \quad \text{and} \quad \tilde{y}_{3D\text{-}1} = \sum_{n=1}^{N_s} \left[\sum_{s=1}^{T_d/\Delta t} \left(\frac{D^2_{d_n}(s\Delta t)}{C^2_{d_n}(s\Delta t)} \right) \right] \tag{4.29}$$

$$\tilde{x}_{3D\text{-}2} = \bar{\mu}_{\phi,m} \quad \text{and} \quad \tilde{y}_{3D\text{-}2} = \sum_{n=1}^{N_s} \left[\sum_{s=1}^{T_d/\Delta t} \left(\frac{D^2_{d_n}(s\Delta t)}{C^2_{\phi_n}(s\Delta t)} \right) \right] \quad . \tag{4.30}$$

The estimated absolute values of $t_{0,\lambda_{2D\text{-}i}}$ and $t_{0,\psi_{2D\text{-}i}}$ are provided in Tables 4.8 and 4.9. The maximum value of the corresponding percentage point of the Student's t-distribution at the $\alpha_s/2$ level of significance is found to be 2.0 for all training cases. So, the null hypotheses of Equations (4.25) and (4.27) can be rejected emphasizing the fact that both independent variables contribute significantly to the corresponding GDI formula [240].

Further, for the 3D GDI formulae and the complete ranges of the indices j and k, the values of the adjusted R^2 $\left(\text{i.e., } R^2_{\text{adj.}}\big|^{(j,k)}_{3D\text{-}i}\right)$ and the predicted R^2 $\left(\text{i.e., } R^2_{\text{pred.}}\big|^{(j,k)}_{3D\text{-}i}\right)$ are computed (following the framework of Equations 3.19 and 3.20, respectively) and enlisted in Tables 4.8 and 4.9. The values of $R^2_{\text{adj.}}\big|^{(j,k)}_{3D\text{-}i}$ are ranging from 0.826 to 0.984 for $GDI_{3D\text{-}1}$, and from 0.863 to 0.978 for $GDI_{3D\text{-}2}$, whereas the values of $R^2_{\text{pred.}}\big|^{(j,k)}_{3D\text{-}i}$ are ranging from 0.822 to 0.984, and from 0.858 to 0.976 for $GDI_{3D\text{-}1}$ and $GDI_{3D\text{-}2}$, respectively. Although the adjusted and predicted R^2 values for 3D GDI formulae are less than that for 2D GDI formulae, the obtained $R^2_{\text{adj.}}\big|^{(j,k)}_{3D\text{-}i}$ and $R^2_{\text{pred.}}\big|^{(j,k)}_{3D\text{-}i}$ values can be considered satisfactory especially taking into account the higher amount of uncertainties involved in replicating the structural response of 3D RC building due to bidirectional ground motions through nonlinear time-history analysis of a representative finite element model. Hence, the independent non-cumulative and cumulative terms of the 3D GDI formulae enjoy strong linear relationships with $\widetilde{GDI}_{3D\text{-GWLZD}}$ [240], and the GDI formulae have strong capability to predict a new observation [241]. Finally, the Spearman's rank-order correlation coefficient, $\rho_{\text{SM}}\big|^{(j,k)}_{3D\text{-}i}$, are estimated (similarly as $\rho_{\text{SM}}\big|^{(j,k)}_{2D\text{-}i}$ following the framework of Equation (3.21)) to measure the strength and the direction of the monotonic relationship between $\widetilde{GDI}_{3D\text{-GWLZD}}$ and the GDI formulae, $GDI_{3D\text{-}1}$ and $GDI_{3D\text{-}2}$. The ranges of the $\rho_{\text{SM}}\big|^{(j,k)}_{3D\text{-}i}$ parameter for all j and k values are from 0.914 to 0.990 for $GDI_{3D\text{-}1}$, and from 0.938 to 0.988 for $GDI_{3D\text{-}2}$ as shown in Tables 4.8 and 4.9. Hence, there is a strong monotonically increasing relationship between the 3D GDI formulae and the modified Park and Ang 3D damage model.

4.4.2 Explicit Expressions for Estimating GDCs of 3D GDI formulae

This section explores various functions to find most suitable explicit expressions for estimating the GDCs of 3D GDI formulae, as discussed in Subsection 4.3.3. For this purpose, the relations of some global parameters of a 3D building, such as its fundamental periods ($T_p^{(x)}, T_p^{(y)}$, and T_p'), floor and bays numbers (N_{bx}, N_{by} and N_s), the total dimensions (i.e., h_{total}, total width along x-direction, $l_{x,\text{total}} = N_{bx}l_x$, and total width along y-direction, $l_{y,\text{total}} = N_{by}l_y$, as shown in Figure 4.1), various building shape ratios ($R_{s1} = N_{bx}/N_s, R_{s2} = N_{by}/N_s$ and $R_{s3} = N_{bx}N_{by}/N_s^2$) and building dimensional ratios ($R_{d1} = l_{x,\text{total}}/h_{\text{total}}, R_{d2} = l_{y,\text{total}}/h_{\text{total}}$ and $R_{d3} = l_{x,\text{total}}l_{y,\text{total}}/h_{\text{total}}^2$), along with the soil type (S) with the GDCs individually or for any linear combination of them are studied. These relations are used through stepwise backward elimination of the independent variables [242] to produce the best-fitted explicit expression for each GDCs separately. Also, only the index i will be used hereafter, similarly as in the cases of the explicit expression for the GDCs associated with 2D GDI formulae.

The non-cumulative and cumulative terms (of $GDI_{3D\text{-}1}$ in Equation (4.2)), associated with $\lambda_{3D\text{-}1}$ and $\psi_{3D\text{-}1}$, use responses due to DSCBGMs and structural properties. So, the explicit expressions for the coefficients are considered as

$$\begin{aligned}\lambda_{3D\text{-}i} = g_{\lambda_{3D}}^{(c_3)}\Big(&\kappa_{12}^{(i)},\kappa_{13}^{(i)},\kappa_{14}^{(i)},\kappa_{15}^{(i)},\kappa_{16}^{(i)},\kappa_{17}^{(i)},\kappa_{18}^{(i)},\kappa_{19}^{(i)},\kappa_{20}^{(i)},\kappa_{21}^{(i)},\kappa_{22}^{(i)},\kappa_{23}^{(i)},\kappa_{24}^{(i)},\kappa_{25}^{(i)},\kappa_{26}^{(i)},\\ &T_p^{(x)},T_p^{(y)},N_{bx},N_{by},N_s,h_{\text{total}},l_{x,\text{total}},l_{y,\text{total}},R_{s1},R_{s2},R_{s3},R_{d1},R_{d2},R_{d3},S\Big)\\ &\forall\ c_3 = 1,2,\cdots,2^{15}-1 \text{ and } i = 1 \qquad (4.31)\end{aligned}$$

$$\begin{aligned}\psi_{3D\text{-}i} = g_{\psi_{3D}}^{(c_3)}\Big(&\kappa_{27}^{(i)},\kappa_{28}^{(i)},\kappa_{29}^{(i)},\kappa_{30}^{(i)},\kappa_{31}^{(i)},\kappa_{32}^{(i)},\kappa_{33}^{(i)},\kappa_{34}^{(i)},\kappa_{35}^{(i)},\kappa_{36}^{(i)},\kappa_{37}^{(i)},\kappa_{38}^{(i)},\kappa_{39}^{(i)},\kappa_{40}^{(i)},\kappa_{41}^{(i)},\\ &T_p^{(x)},T_p^{(y)},N_{bx},N_{by},N_s,h_{\text{total}},l_{x,\text{total}},l_{y,\text{total}},R_{s1},R_{s2},R_{s3},R_{d1},R_{d2},R_{d3},S\Big)\\ &\forall\ c_3 = 1,2,\cdots,2^{15}-1 \text{ and } i = 1 \qquad (4.32)\end{aligned}$$

where the regression coefficients, $\kappa_{12}^{(i)}$ to $\kappa_{26}^{(i)}$ are attached with $T_p^{(x)}$, $T_p^{(y)}$, N_{bx}, N_{by}, N_s, h_{total}, $l_{x,\text{total}}$, $l_{y,\text{total}}$, R_{s1}, R_{s2}, R_{s3}, R_{d1}, R_{d2}, R_{d3} and S, respectively, for the coefficient $\lambda_{3D\text{-}1}$, and $\kappa_{27}^{(i)}$ to $\kappa_{41}^{(i)}$ are attached with the independent variables in the same order for $\psi_{3D\text{-}1}$. The index c_3 refers to all possible regression models considering the linear combinations of the corresponding independent variables available in Equations (4.31) and (4.32). Similarly, the explicit expressions for the GDCs associated with the non-cumulative and the cumulative terms of $GDI_{3D\text{-}2}$, $\lambda_{3D\text{-}2}$ and $\psi_{3D\text{-}2}$, are considered as

$$\begin{aligned}\lambda_{3D\text{-}i} = g_{\lambda_{3D}}^{(c_4)}\Big(&\kappa_{12}^{(i)},\kappa_{14}^{(i)},\kappa_{15}^{(i)},\kappa_{16}^{(i)},\kappa_{17}^{(i)},\kappa_{18}^{(i)},\kappa_{19}^{(i)},\kappa_{20}^{(i)},\kappa_{21}^{(i)},\kappa_{22}^{(i)},\kappa_{23}^{(i)},\kappa_{24}^{(i)},\kappa_{25}^{(i)},\kappa_{26}^{(i)},\\ &T_p',N_{bx},N_{by},N_s,h_{\text{total}},l_{x,\text{total}},l_{y,\text{total}},R_{s1},R_{s2},R_{s3},R_{d1},R_{d2},R_{d3},S\Big)\\ &\forall\ c_4 = 1,2,\cdots,2^{14}-1 \text{ and } i = 2 \qquad (4.33)\end{aligned}$$

$$\psi_{3D\text{-}i} = g_{\psi_{3D}}^{(c_4)}\Big(\kappa_{27}^{(i)}, \kappa_{29}^{(i)}, \kappa_{30}^{(i)}, \kappa_{31}^{(i)}, \kappa_{32}^{(i)}, \kappa_{33}^{(i)}, \kappa_{34}^{(i)}, \kappa_{35}^{(i)}, \kappa_{36}^{(i)}, \kappa_{37}^{(i)}, \kappa_{38}^{(i)}, \kappa_{39}^{(i)}, \kappa_{40}^{(i)}, \kappa_{41}^{(i)}, T_p', N_{bx}, N_{by}, N_s, h_{\text{total}}, l_{x,\text{total}}, l_{y,\text{total}}, R_{s1}, R_{s2}, R_{s3}, R_{d1}, R_{d2}, R_{d3}, S\Big) \quad \forall\ c_4 = 1, 2, \cdots, 2^{14} - 1 \text{ and } i = 2 \tag{4.34}$$

where the regression coefficients, $\kappa_{12}^{(i)}$ and $\kappa_{14}^{(i)}$ to $\kappa_{26}^{(i)}$ are attached with T_p', N_{bx}, N_{by}, N_s, h_{total}, $l_{x,\text{total}}$, $l_{y,\text{total}}$, R_{s1}, R_{s2}, R_{s3}, R_{d1}, R_{d2}, R_{d3} and S, respectively, for the coefficient $\lambda_{3D\text{-}2}$, whereas the regression coefficients, $\kappa_{27}^{(i)}$ and $\kappa_{29}^{(i)}$ to $\kappa_{41}^{(i)}$ are attached with the independent variables in the same order for $\psi_{3D\text{-}2}$. The index c_4 refers to all possible regression models considering the linear combinations of the corresponding independent variables available in Equations (4.33) and (4.34). Now, the other GDC of $GDI_{3D\text{-}2}$, $\gamma_{3D\text{-}2}$, is related only to the structural properties of a building (refer to Equation (4.15)). Therefore, the explicit expression for $\gamma_{3D\text{-}2}$ using only global parameters of a building (same as $\gamma_{2D\text{-}2}$) as independent variables are considered as

$$\gamma_{3D\text{-}i} = g_{\gamma_{3D}}^{(c_5)}\Big(\kappa_{42}^{(i)}, \kappa_{43}^{(i)}, \kappa_{44}^{(i)}, \kappa_{45}^{(i)}, \kappa_{46}^{(i)}, \kappa_{47}^{(i)}, \kappa_{48}^{(i)}, \kappa_{49}^{(i)}, \kappa_{50}^{(i)}, \kappa_{51}^{(i)}, \kappa_{52}^{(i)}, \kappa_{53}^{(i)}, \kappa_{54}^{(i)}, T_p', N_{bx}, N_{by}, N_s, h_{\text{total}}, l_{x,\text{total}}, l_{y,\text{total}}, R_{s1}, R_{s2}, R_{s3}, R_{d1}, R_{d2}, R_{d3}\Big) \quad \forall\ c_5 = 1, 2, \cdots, 2^{13} - 1 \text{ and } i = 2 \tag{4.35}$$

where the regression coefficients, $\kappa_{42}^{(i)}$ to $\kappa_{54}^{(i)}$ are attached with T_p', N_{bx}, N_{by}, N_s, h_{total}, $l_{x,\text{total}}$, $l_{y,\text{total}}$, R_{s1}, R_{s2}, R_{s3}, R_{d1}, R_{d2}, and R_{d3}, respectively, for the coefficient $\gamma_{3D\text{-}2}$. The index c_5 refers to all possible regression models considering the linear combinations of the corresponding independent variables available in Equation (4.35). The units for the fundamental periods are taken as second, and the units for the total widths of a building along two orthogonal horizontal directions are taken as meter in Equations (4.31)-(4.35). The statistics of the considered models are studied for all GDCs, and the corresponding best-fitted model can be expressed as

$$\lambda_{3D\text{-}1} = 8.5611T_p^{(x)} - 3.8124T_P^{(y)} - 0.3327h_{\text{total}} - 2.3685R_{s1} - 1.1010R_{s2} + 1.3120R_{d1} + 0.9270R_{d2} + 0.0323S \ \left(\text{with } R^2_{\text{adj.}} = 0.993\right) \tag{4.36}$$

$$\psi_{3D\text{-}1} = -0.0223h_{\text{total}} + 0.1697R_{d3} + 0.1285S \ \left(\text{with } R^2_{\text{adj.}} = 0.933\right) \tag{4.37}$$

$$\lambda_{3D\text{-}2} = 2.4914T_p' - 0.1795N_s - 1.1485R_{s3} + 0.5727R_{d3} + 0.0627S \ \left(\text{with } R^2_{\text{adj.}} = 0.951\right) \tag{4.38}$$

$$\psi_{3D\text{-}2} = 0.6478T_p' - 0.0103l_{x,\text{total}} - 0.0084l_{y,\text{total}} + 0.0682R_{d3} + 0.5991 \times 10^{-3}S \ \left(\text{with } R^2_{\text{adj.}} = 0.898\right) \tag{4.39}$$

$$\gamma_{3D\text{-}2} = -1.1504T_p' + 0.2444N_{bx} + 0.0589N_{by} + 0.0231h_{\text{total}} - 0.0344l_{x,\text{total}} - 0.0127l_{y,\text{total}} - 0.0619R_{s3} \ \left(\text{with } R^2_{\text{adj.}} = 0.925\right) \quad . \tag{4.40}$$

The importance of the corresponding independent variables for each 3D GDC (similar to

their 2D counterparts in Subsection 3.4.2) is checked through the F-tests for significance of regression by assuming the following suitable null and alternative hypotheses as

$$H_{0,\lambda_{3D\text{-}i}} : \kappa_{\xi}^{(i)} = 0 \text{ with } \xi = 12, 13, 17, 20, 21, 23, 24, 26 \text{ for } i = 1, \text{ and } \xi = 12, 16, 22, 25, 26 \text{ for } i = 2 \quad (4.41)$$

$$H_{a,\lambda_{3D\text{-}i}} : \text{at least one among } \kappa_{\xi}^{(i)} \neq 0 \text{ with } \xi = 12, 13, 17, 20, 21, 23, 24, 26 \text{ for } i = 1, \text{ and } \xi = 12, 16, 22, 25, 26 \text{ for } i = 2 \quad (4.42)$$

$$H_{0,\psi_{3D\text{-}i}} : \kappa_{\eta}^{(i)} = 0 \text{ with } \eta = 32, 40, 41 \text{ for } i = 1, \text{ and } \eta = 27, 33, 34, 40, 41 \text{ for } i = 2 \quad (4.43)$$

$$H_{a,\psi_{3D\text{-}i}} : \text{at least one among } \kappa_{\eta}^{(i)} \neq 0 \text{ with } \eta = 32, 40, 41 \text{ for } i = 1, \text{ and } \eta = 27, 33, 34, 40, 41 \text{ for } i = 2 \quad (4.44)$$

$$H_{0,\gamma_{3D\text{-}i}} : \kappa_{\zeta}^{(i)} = 0 \text{ with } \zeta = 42, 43, 44, 46, 47, 48, 51 \text{ for } i = 2 \quad (4.45)$$

$$H_{a,\gamma_{3D\text{-}i}} : \text{at least one among } \kappa_{\zeta}^{(i)} \neq 0 \text{ with } \zeta = 42, 43, 44, 46, 47, 48, 51 \text{ for } i = 2 \quad . \quad (4.46)$$

The corresponding F-test statistics, $f_{0,\lambda_{3D\text{-}i}}$, $f_{0,\psi_{3D\text{-}i}}$ and $f_{0,\gamma_{3D\text{-}i}}$, are estimated following the similar method described in Subsection 3.4.1 and provided in Table 4.10. Since the corresponding maximum value of the percentage point of the F-distribution is 3.072 (considering $\alpha_s = 0.05$) for all GDCs, the null hypotheses of Equations (4.41), (4.43) and (4.45) can be rejected.

Table 4.10: Different statistical results for the GDCs of 3D GDI formulae

Sl. No.	i	GDC	F-test statistic	Student's t-test statistic (absolute value)
1	1	$\lambda_{3D\text{-}1}$	$f_{0,\lambda_{3D\text{-}1}} = 445.2$	$t_{0,\lambda_{3D\text{-}1},\kappa_{12}} = 9.87$, $t_{0,\lambda_{3D\text{-}1},\kappa_{13}} = 5.67$, $t_{0,\lambda_{3D\text{-}1},\kappa_{17}} = 13.92$, $t_{0,\lambda_{3D\text{-}1},\kappa_{20}} = 14.23$, $t_{0,\lambda_{3D\text{-}1},\kappa_{21}} = 5.14$, $t_{0,\lambda_{3D\text{-}1},\kappa_{23}} = 12.56$, $t_{0,\lambda_{3D\text{-}1},\kappa_{24}} = 6.82$, $t_{0,\lambda_{3D\text{-}1},\kappa_{26}} = 2.68$
2	1	$\psi_{3D\text{-}1}$	$f_{0,\psi_{3D\text{-}1}} = 112.9$	$t_{0,\psi_{3D\text{-}1},\kappa_{32}} = 3.69$, $t_{0,\psi_{3D\text{-}1},\kappa_{40}} = 10.87$, $t_{0,\psi_{3D\text{-}1},\kappa_{41}} = 3.27$
3	2	$\lambda_{3D\text{-}2}$	$f_{0,\lambda_{3D\text{-}2}} = 93.12$	$t_{0,\lambda_{3D\text{-}2},\kappa_{12}} = 5.05$, $t_{0,\lambda_{3D\text{-}2},\kappa_{16}} = 3.38$, $t_{0,\lambda_{3D\text{-}2},\kappa_{22}} = 3.48$, $t_{0,\lambda_{3D\text{-}2},\kappa_{25}} = 3.87$, $t_{0,\lambda_{3D\text{-}2},\kappa_{26}} = 1.68$
4	2	$\psi_{3D\text{-}2}$	$f_{0,\psi_{3D\text{-}2}} = 43.23$	$t_{0,\psi_{3D\text{-}2},\kappa_{27}} = 2.94$, $t_{0,\psi_{3D\text{-}2},\kappa_{33}} = 2.53$, $t_{0,\psi_{3D\text{-}2},\kappa_{34}} = 2.49$ $t_{0,\psi_{3D\text{-}2},\kappa_{40}} = 7.77$, $t_{0,\psi_{3D\text{-}2},\kappa_{41}} = 0.04$
5	2	$\gamma_{3D\text{-}2}$	$f_{0,\gamma_{3D\text{-}2}} = 43.46$	$t_{0,\gamma_{3D\text{-}2},\kappa_{42}} = 5.10$, $t_{0,\gamma_{3D\text{-}2},\kappa_{43}} = 4.71$, $t_{0,\gamma_{3D\text{-}2},\kappa_{44}} = 3.56$, $t_{0,\gamma_{3D\text{-}2},\kappa_{46}} = 3.02$, $t_{0,\gamma_{3D\text{-}2},\kappa_{47}} = 4.27$, $t_{0,\gamma_{3D\text{-}2},\kappa_{48}} = 2.86$, $t_{0,\gamma_{3D\text{-}2},\kappa_{51}} = 2.93$

For carrying out the Student's t-test, the following null and alternative hypotheses can be assumed as

$$H_{0,\lambda_{3D\text{-}i},\kappa_{\xi}} : \kappa_{\xi}^{(i)} = 0 \text{ with } \xi = 12, 13, 17, 20, 21, 23, 24, 26 \text{ for } i = 1,$$

$$\text{and } \xi = 12, 16, 22, 25, 26 \text{ for } i = 2 \tag{4.47}$$

$$H_{a,\lambda_{3D\text{-}i},\kappa_\xi} : \kappa_\xi^{(i)} \neq 0 \text{ with } \xi = 12, 13, 17, 20, 21, 23, 24, 26$$
$$\text{for } i = 1, \text{ and } \xi = 12, 16, 22, 25, 26 \text{ for } i = 2 \tag{4.48}$$

$$H_{0,\psi_{3D\text{-}i},\kappa_\eta} : \kappa_\eta^{(i)} = 0 \text{ with } \eta = 32, 40, 41 \text{ for } i = 1, \text{ and } \eta = 27, 33, 34, 40, 41 \text{ for } i = 2 \tag{4.49}$$

$$H_{a,\psi_{3D\text{-}i},\kappa_\eta} : \kappa_\eta^{(i)} \neq 0 \text{ with } \eta = 32, 40, 41 \text{ for } i = 1, \text{ and } \eta = 27, 33, 34, 40, 41 \text{ for } i = 2 \tag{4.50}$$

$$H_{0,\gamma_{3D\text{-}i},\kappa_\zeta} : \kappa_\zeta^{(i)} = 0 \text{ with } \zeta = 42, 43, 44, 46, 47, 48, 51 \text{ for } i = 2 \tag{4.51}$$

$$H_{a,\gamma_{3D\text{-}i},\kappa_\zeta} : \kappa_\zeta^{(i)} \neq 0 \text{ with } \zeta = 42, 43, 44, 46, 47, 48, 51 \text{ for } i = 2 \quad . \tag{4.52}$$

Table 4.10 shows the estimated values of the corresponding absolute t-test statistics, $t_{0,\lambda_{3D\text{-}i},\kappa_\xi}$, $t_{0,\psi_{3D\text{-}i},\kappa_\eta}$ and $t_{0,\gamma_{3D\text{-}i},\kappa_\zeta}$. The maximum value of the percentage point of the Student's t-distribution with $\alpha_s = 0.05$ is found to be 2.07 for all GDCs. Hence, the null hypotheses of Equations (4.47), (4.49) and (4.51) for various independent variables can be rejected except S (representing soil type) in the selected regression models for $\lambda_{3D\text{-}2}$ (of Equation (4.38)) and $\psi_{3D\text{-}2}$ (of Equation (4.39)), as the absolute values of the t-test statistics, $t_{0,\lambda_{3D\text{-}2},\kappa_{26}}$ and $t_{0,\psi_{3D\text{-}2},\kappa_{41}}$, are less than 2.07. However, the parameter is kept in the explicit expressions of $\lambda_{3D\text{-}2}$ and $\psi_{3D\text{-}2}$ here to include the physical effect of local soil type on the damages occurred to buildings due to bidirectional ground motions. This will make the expressions of those GDCs more realistic. Also, the importance of the parameter when used with other independent variables is established through the F-test of the corresponding regression models (refer to Equations (4.41) and (4.43) for $i = 2$) as shown in Table 4.10. Finally, the $R^2_{\text{adj.}}$ values for the best-fitted regression models of the GDCs are estimated (as shown in Equations (4.36)-(4.40)) which refers to strong linear relationships between the GDCs and the corresponding independent variables.

4.4.3 Correlation between Proposed 3D GDIs and Damage Conditions

In the present research works, the collapse of a 3D building is defined (to represent no reserved strength) in terms of physical damage conditions of its members (i.e., when at least 50% of GF columns or 10% of GF columns along with 50% of beams on any floor are collapsed) as discussed in Subsection 4.3.3. Similarly, other necessary intermediate and lowest (post-earthquake restoration-based) global damage states are also defined in terms of members-damage conditions as shown in Table 4.11. The local damage state of the members is decided from the corresponding $LDI_{3D\text{-GWLZD}}$ values [2] (refer to Table 1.4). The limiting values for normalized $GDI_{3D\text{-GWLZD}}$ are obtained for different global damage states considering the nonlinear dynamic responses of all training buildings due to all training DSCBGMs with varying scale factors and shown in Table 4.11.

Since the limiting ranges for a 3D GDI model are proposed for the first time in this study,

Table 4.11: Limiting values for the 3D GDI formulae ($\widetilde{GDI}_{3D\text{-GWLZD}}$, $GDI_{3D\text{-}1}$ and $GDI_{3D\text{-}2}$) associated with different post-earthquake restoration-based global damage conditions

Sl. No.	Global damage state	Physical damage state of members	Limiting values of 3D GDIs
1	Collapse	At least 50% of GF columns or 10% of GF columns along with 50% of beams on any floor are collapsed	$0.95 \leq GDI_{3D}$
2	Irreparable	At least 50% of GF columns or 10% of GF columns along with 50% of beams on any floor are irreparable	$0.45 \leq GDI_{3D} < 0.95$
3	Repairable	At least 50% of GF columns or 10% of GF columns along with 50% of beams on any floor are repairable	$0.14 \leq GDI_{3D} < 0.45$
4	No damage	Otherwise	$GDI_{3D} < 0.14$

the performance of the $\widetilde{GDI}_{3D\text{-GWLZD}}$ values is needed to be checked at first for identifying the damage conditions (according to Table 4.11) from its computed values using confusion matrix as shown in Figure 4.6. Here, the predicted damage condition of a building is obtained by $\widetilde{GDI}_{3D\text{-GWLZD}}$ value, whereas the actual damage condition is obtained using the physical damage states of the GF columns and beams of all floors of the building. The accuracy of $\widetilde{GDI}_{3D\text{-GWLZD}}$ is more than 80% for all training buildings, and the average values of recall and precision measures are around 75%. Therefore, the limiting values of 3D damage indices for different damage conditions can be used for the $\widetilde{GDI}_{3D\text{-GWLZD}}$ values.

The same limiting ranges as in Table 4.11 can also be used for the new GDI formulae as they are tuned (through regression analysis) to match the corresponding $\widetilde{GDI}_{3D\text{-GWLZD}}$ value. Finally, the performances of $GDI_{3D\text{-}1}$ and $GDI_{3D\text{-}2}$ formulae, similarly as $\widetilde{GDI}_{3D\text{-GWLZD}}$, are checked using confusion matrices as shown in Figure 4.6. For this purpose, the GDCs obtained from Equations (4.36)-(4.40) for different training buildings and different soil types are used to estimate the values of $GDI_{3D\text{-}1}$ and $GDI_{3D\text{-}2}$ from the corresponding nonlinear dynamic responses, followed by assigning the corresponding global damage conditions (i.e., the predicted conditions) based on the estimated values. The accuracies obtained by the GDI formulae are around 80% in the cases of all training buildings and all training DSCBGMs. Although the confusion matrices of Figure 4.6 represent the overall performances of the GDI models for all training buildings and training DSCBGMs, the performances of the models in the case of individual training buildings and all training DSCBGMs are also found satisfactory. It reflects the importance of using the $\widetilde{GDI}_{3D\text{-GWLZD}}$ values in multilinear regression analysis to get a uniform range of 3D GDI values (linked with different global damage states) applicable for any RC building (similar to the considered sample buildings) as discussed in Subsection 4.3.3.

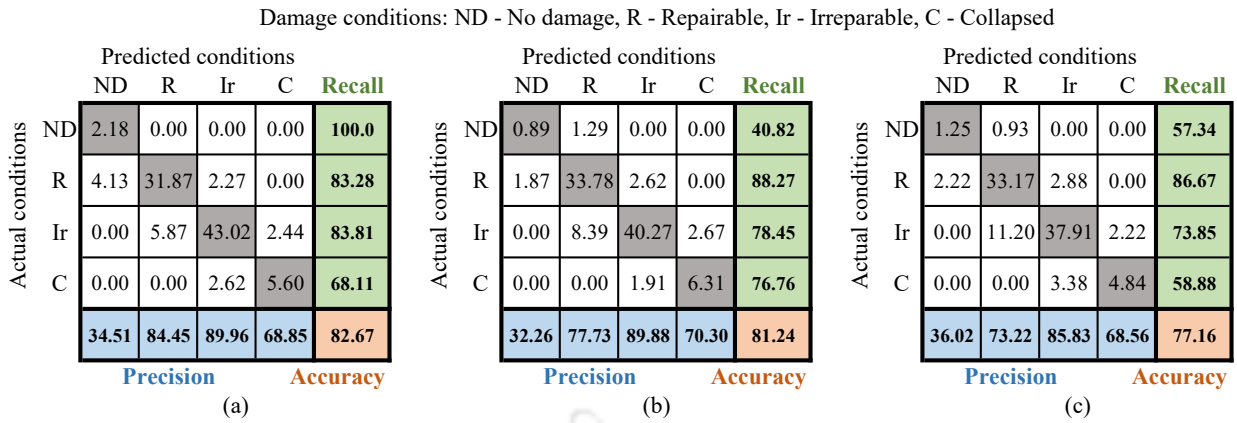

Figure 4.6: Confusion matrices (with values in percentage) of the actual and the predicted damage conditions for the training buildings due to the training DSCBGMs in the case of (a) $\widetilde{GDI}_{3D\text{-GWLZD}}$, (b) $GDI_{3D\text{-}1}$ and (c) $GDI_{3D\text{-}2}$

4.4.4 Validation of the Proposed Methodology

In this section, the new 3D GDI formulae (Equations (4.2) and (4.15)), the explicit expressions (Equations (4.36)-(4.40)) for predicting the corresponding GDCs, and the applicability of the selected limiting damaging index values for different damage states (refer to Table 4.11) will be validated. For this purpose, the values of 3D GDCs for the validation building (i.e., $3F4B_x3B_y$ as shown in Table 4.1) are estimated as $\gamma_{3D\text{-}2} = -0.1435$, and

$$\lambda_{3D\text{-}1} = 0.7063, \psi_{3D\text{-}1} = 0.4393, \lambda_{3D\text{-}2} = 1.0128, \psi_{3D\text{-}2} = 0.1852 \text{ for } S = 1 \ ,$$
$$\lambda_{3D\text{-}1} = 0.7386, \psi_{3D\text{-}1} = 0.5678, \lambda_{3D\text{-}2} = 1.0755, \psi_{3D\text{-}2} = 0.1858 \text{ for } S = 2 \ ,$$
$$\lambda_{3D\text{-}1} = 0.7709, \psi_{3D\text{-}1} = 0.6963, \lambda_{3D\text{-}2} = 1.1382, \psi_{3D\text{-}2} = 0.1864 \text{ for } S = 3 \ .$$

The nonlinear dynamic responses of the building due to the validation DSCBGMs (refer to Table 4.3) with different scale factors are used to compute normalized $GDI_{3D\text{-GWLZD}}$ values and to estimate global damage values using the new GDI formulae. It should be mentioned that the validation building is first analysed due to the training DSCBGMs for different local soil types to get the normalization factors linked with the global collapse state for the building (similarly for the training buildings as discussed in Subsection 4.3.3). These normalization factors are applied to the computed $GDI_{3D\text{-GWLZD}}$ values (as per Equation (4.22)) for all validation DSCBGMs (with different scale factors) to yield the $\widetilde{GDI}_{3D\text{-GWLZD}}$ values for comparing them with the corresponding computed $GDI_{3D\text{-}1}$ and $GDI_{3D\text{-}2}$ values. However, the normalization factors are not applied to the computed $GDI_{3D\text{-}1}$ and $GDI_{3D\text{-}2}$ values for the same reason as in the case of training buildings and training DSCBGMs, i.e., the GDCs available in the new GDI formulae will deal with the effect of the normalization. The comparisons of the monotonically non-decreasing evolution of those estimated GDI values for different local soil types are shown in Figure 4.7. It can be seen in the Figure that the global

damage values estimated by $GDI_{3D\text{-}1}$ and $GDI_{3D\text{-}2}$ formulae can predict the corresponding normalized $GDI_{3D\text{-GWLZD}}$ values with satisfactory accuracy despite some inherent uncertainties resulting from the approximations considered to get the global damage values and the proposed explicit expressions of the GDCs.

The global damage conditions (as per Table 4.11) for the validation building due to the validation DSCBGMs are evaluated from the corresponding $GDI_{3D\text{-}1}$, $GDI_{3D\text{-}2}$ and normalized $GDI_{3D\text{-GWLZD}}$ values. The comparison of the predicted and actual damage conditions for different GDI models in terms of confusion matrices are shown in Figure 4.8. The accuracy measures for normalized $GDI_{3D\text{-GWLZD}}$ values and the new GDI formulae are found to be more than 75%. Hence, the obtained values of the performance parameters for $GDI_{3D\text{-}1}$ and $GDI_{3D\text{-}2}$ can be considered satisfactory (like their 2D counterparts) in the case of validation buildings and validation DSCBGMs [227, 243]. Any suitable probabilistic approach can also be used to improve further the damage assessment of 3D buildings by the GDI formulae. Although $GDI_{3D\text{-}1}$ and $GDI_{3D\text{-}2}$ formulae perform similarly for damage assessment of a building, $GDI_{3D\text{-}2}$ applies to the building behaving as a linear shear building model (attached with two translational and one rotational DOFs at each storey), whereas $GDI_{3D\text{-}1}$ applies to more general type of buildings.

4.5 Conclusion

The scope of the novel GDI evaluation method (introduced in the previous chapter) has been extended for instrumented 3D RC building to get combined GDI values during an earthquake from recorded floor-displacement data and some readily obtainable structural properties. Using the methodology, two different combined GDI formulae have been proposed to predict the $\widetilde{GDI}_{3D\text{-GWLZD}}$ value. The values obtained from new formulae are tuned with the $\widetilde{GDI}_{3D\text{-GWLZD}}$ to achieve the GDI value equal to 1.0 for a building with globally collapsed condition. The non-cumulative and cumulative terms of the new 3D GDI formulae are modified (concerning their 2D counterparts) accordingly to accommodate the combined effect of biaxial bending and axial loading, usually generated due to bidirectional ground motions on the damage of structural members. The 3D GDI formulae also enjoy similar advantage as the 2D GDI formulae, i.e., the independence from any computationally intensive and time-consuming nonlinear time-history analysis for their application.

Among the new GDI formulae, the displacement ductility-based GDI formula is applicable for any 3D RC buildings and can be used with the help of a corresponding representative finite element model. On the other hand, the curvature ductility-based GDI formula applies to those buildings whose behaviour can be idealized as a shear building model attached with three DOFs (two translational and one rotational) for each story. Also, the curvature ductility-based GDI model does not need any representative finite element model to compute GDI values. The explicit expressions for the global damage coefficients of the new 3D GDI

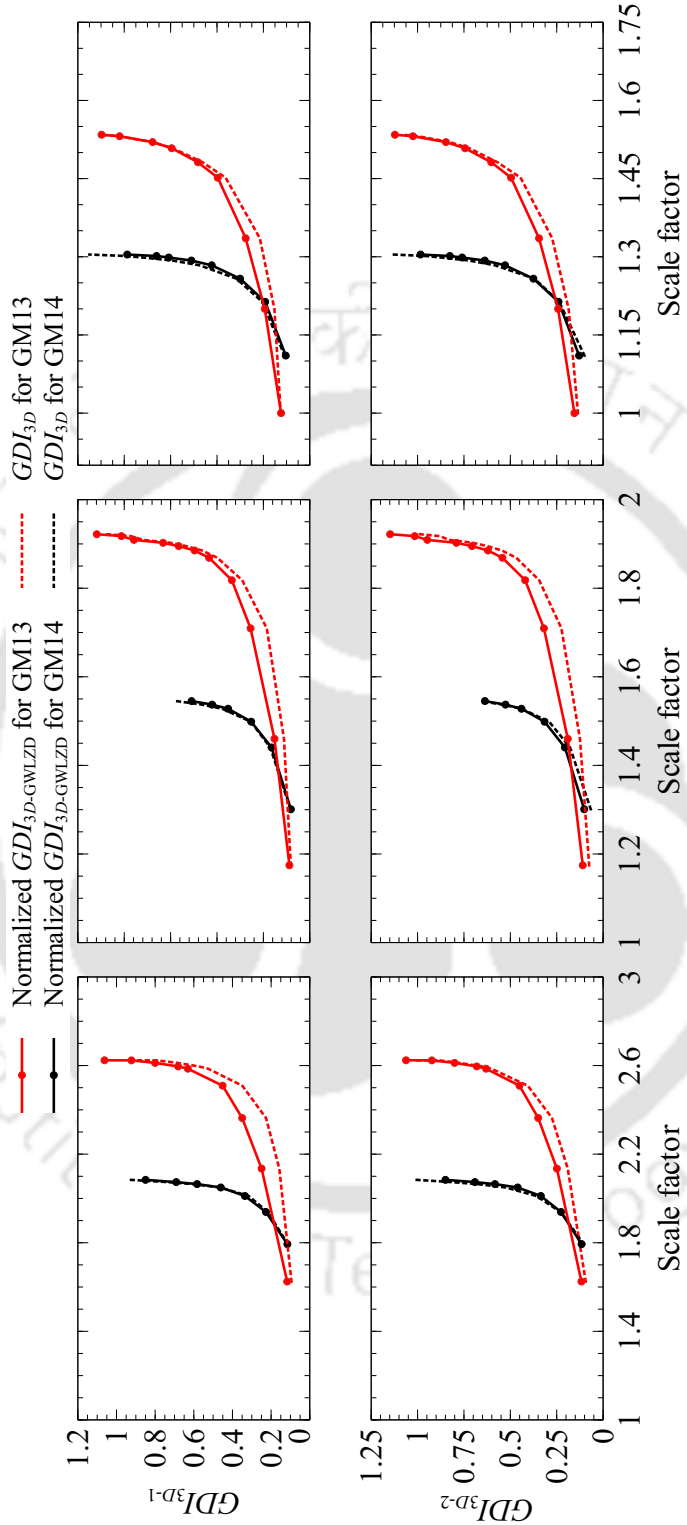

Figure 4.7: Comparisons of the GDI values estimated using the GDCs obtained from explicit expressions with $\widetilde{GDI}_{3D\text{-}GWLZD}$ values for building $3F4B_x3B_y$ due to validation DSCBGMs for different soil types in the case of (a)-(c) $GDI_{3D\text{-}1}$, and (d)-(f) $GDI_{3D\text{-}2}$

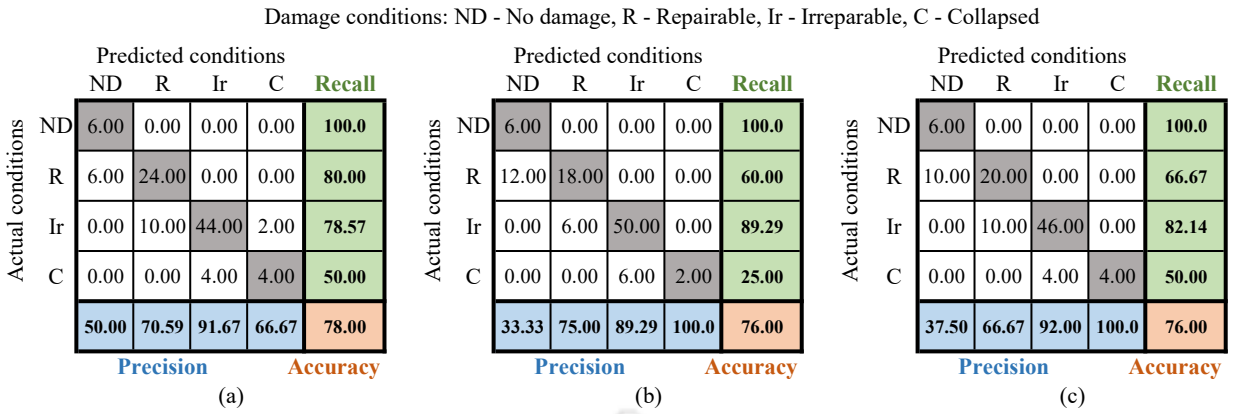

Figure 4.8: Confusion matrices (with values in percentage) of the actual and the predicted damage conditions for the validation building due to the validation DSCBGMs in the case of (a) $\widetilde{GDI}_{3D\text{-GWLZD}}$, (b) $GDI_{3D\text{-}1}$ and (c) $GDI_{3D\text{-}2}$

formulae are provided as a function of some readily obtainable global parameters of the buildings (e.g., fundamental periods, building shape ratio, building dimensional ratio etc.) and the local soil type.

The adequacy of the 3D GDI formulae, along with the associated global damage coefficients, are found satisfactory through some standard statistical tests, and the damage values estimated using the GDI formulae enjoy a strong monotonically non-decreasing relationship with the corresponding values of $\widetilde{GDI}_{3D\text{-GWLZD}}$. So, the selected non-cumulative and cumulative terms for the new GDI formulae may relate to the global damage state obtained from $\widetilde{GDI}_{3D\text{-GWLZD}}$ values very well. For wider applicability of the GDI formulae, their limiting values representing appropriate global damage conditions are also proposed in this study. The global damage state of a building is linked with the physical damage states of structural members (i.e., columns and beams) in different storeys of the building.

The statistical characterization of the residues in the predicting equations is not considered in this study through the deterministic framework for the 3D GDI formulae like their 2D counterparts. So, a probabilistic approach utilizing such uncertainties due to residues would lead to a more comprehensive characterization of damage prediction for 3D RC buildings.

5. Concluding Remarks

Contents

5.1 Overview

Any seismic damage index model can be used to compute earthquake-induced structural damage of a building. Most researchers prefer combined damage index models due to their ability to consider the effect of both maximum and cyclic deformations on structural damage. All such combined damage models require section-level responses (e.g., sectional stress and strain resultants, dissipated hysteresis energy) through nonlinear time-history analysis, and cannot compute global damage index using global-level responses (e.g., lateral floor-response) alone. Utilizing the structural dynamic responses recorded by modern sensors, there is a scope for developing a new combined GDI evaluation method which uses such recorded data and avoids the requirement of numerically obtained sectional responses. On the other hand, the acceptability of the computed damage of a building using any damage index model through the output of a representative finite element model depends on the authenticity of the experimental data with which the finite element model is calibrated. The lateral output of any finite element model is usually calibrated with experimental results of axially-loaded cantilever columns subjected to unidirectional horizontal quasi-static loading. For most of the experimental setups (especially the economic ones), the true lateral behaviour of a cantilever column is altered because of the undesirable orientations of the actuators and the fixing arrangements between the actuator heads and the column tip. Therefore, the results obtained from such experiments must be rectified to generate true lateral load-deformation behaviour before using them directly for calibration of any finite element model. Many previous research works also emphasized the need to rectify such experimental data [86, 194, 203]. Therefore,

a novel mechanics-based formulation to reproduce the true lateral load-deformation curve of cantilever columns from experimental data and a novel combined GDI evaluation method incorporating recorded floor-displacement responses for instrumented buildings during any seismic event are developed in the present study. This chapter presents a summary of the completed research work, followed by significant contributions and limitations associated with the study. Finally, different branches of possible future works based on the current topic are suggested.

5.2 Summary of the Research

The experimental results of four cantilever column specimens subjected to constant axial loading along with unidirectional horizontal quasi-static monotonic and cyclic loadings (carried out in a separate research work [199]) are used to study the effect of real-time inclination of the actuators and fixing arrangements on the lateral behaviour of the specimens. During the experiments, inclined positions of both horizontal and vertical actuators are responsible for altercations in the actual lateral and vertical forces acting on a specimen from the corresponding actuator readings. Also, the eccentric force (concerning the column tip) developed from the inclined actuator results in an extra moment and, subsequently, an additional column tip deformation. The effect of these anomalies should be removed (especially in the case of large displacement or high axial load) from the test result to get exact force and deformation components. However, their values depend on the unknown column tip rotation, which cannot be determined directly from the actuator readings. Geometric configurations of the actuators and column specimen, displacement compatibility, equilibrium equations and constitutive relationships (including geometric stiffness) are used to find implicit expressions for column tip rotation in terms of lateral displacement. Now, the configurations depend on the loading directions of actuators and vice-versa, and the constitutive relationship primarily depends on the initially unknown proportion of elastic and plastic deformation. Therefore, a nested iteration procedure based on a detailed mechanics-oriented approach is used to get the exact solution for the tip rotation. The proposed formulation applies to get the true lateral load-displacement relationship of RC columns when some special arrangements are not available for procuring accurate measurements of the column tip movement and actuator rotations during the experiments. It can also find the yield parameters from the monotonic test results by tracking the onset of plastic deformation.

The values of various parameters (e.g., column tip rotation and displacement, inclinations of actuators with their initial positions, stress-resultants at base) predicted by the proposed mechanics-based formulation are validated satisfactorily with experimentally obtained observations and results in the case of monotonic test with the largest column deformation. Further, the evolution of plastic behaviour of the column specimens obtained from the proposed formulation is found as expected theoretically during the monotonic and cyclic experiments.

The application of the formulation shows that the original experimental results underestimate the lateral strength and overestimate the lateral displacement capacity of a cantilever column, especially with a high axial stress ratio. For cyclic experiments, an overestimation of dissipated hysteresis energy is also observed when the experimental result is not rectified using the proposed formulation. Such incorrect estimation of capacity parameters and energy dissipation for a column will not result in its realistic damage estimation due to seismic loading.

Further, the importance of rectification via the mechanics-based formulation is critically reviewed by studying analytical model 1 and analytical model 2 (developed using the OpenSees framework [210, 211]) calibrated with the original experimental data and the rectified data, respectively. It has been found that some directly obtained material properties (through material tests) of concrete (i.e., compressive cube strength) and reinforcing steel (i.e., yield and ultimate strength) can be used directly in the analytical model 2 to predict the rectified curves with good accuracy. On the contrary, those material properties are reduced for calibrating the analytical model with the original experimental results to match the corresponding underestimated lateral strength. However, a few necessary indirectly obtained properties of concrete (e.g., elastic modulus, unconfined and confined concrete properties) are changed for both analytical models because of the inherent uncertainty in the material models and other modelling issues. Now, finite element models for various 2D RC frames and 3D RC buildings are developed (in the OpenSees framework) using the material properties calibrated with the rectified experimental lateral load-deformation curve to capture the realistic sectional and global structural responses. The nonlinear dynamic responses of those finite element models due to different design spectrum-compatible unidirectional and bidirectional ground motions are studied thoroughly to introduce a novel combined GDI evaluation method for instrumented buildings utilizing the floor-displacement data recorded during any seismic loading along with some easily obtainable structural properties and local soil type (i.e., hard soil, medium stiff soil or soft soil).

The new GDI evaluation method can predict the dissipated hysteresis energy-based weighted average of suitable modified Park and Ang-type combined local damage index models [1, 2] for 2D RC frames and 3D RC buildings. The main advantage of the new method (unlike the existing damage index models) is its independence on the demand parameters in terms of the section-level responses (i.e., stress and strain resultants, dissipated hysteresis energy) of a structure usually generated by the complex and computationally demanding nonlinear time-history analysis. Because it replaces those section-level demand terms for a building with the recorded displacement values at each storey of the building to consider the effect of both maximum and cyclic structural responses on the global damage. The capacity parameters for a structure or its members to be used in the new GDI evaluation method can be procured using either a representative finite element model or the corresponding section properties. A finite element model is necessary to estimate the global response-based capacity

terms of a frame/building (e.g., ultimate displacement, yield displacement or displacement ductility) through nonlinear static analysis. On the contrary, the sectional response-based capacity terms (e.g., ultimate curvature, curvature ductility) can be estimated from section properties such as section dimensions, reinforcement arrangement, and material properties. Two combined GDI formulae based on different types of capacity parameters (i.e., global displacement ductility or curvature ductility of columns) are introduced for 2D RC frames using the new methodology in this thesis. Now, to get a better idea of the damages that occurred in a building, one should consider the combined (sectional or global) responses along two orthogonal horizontal directions of the complete 3D building due to bidirectional ground motions instead of selecting a corner or internal 2D frame (as a representation of the complete building) subjected to the resultant unidirectional motion. Because the latter study regarding 2D frames cannot utilize the effect of biaxial bending and axial loading, usually developed due to bidirectional ground motions, on the sustained damage. Therefore, another two combined GDI formulae are also proposed in the case of 3D RC buildings by suitably modifying the non-cumulative and cumulative terms of their 2D counterparts to account for the responses due to biaxial bending and axial loading.

Univariate multilinear regression analyses and some standard statistical tests are performed to find the explicit expressions (considering the variability of 2D frames, 3D buildings and ground motions) for the regression coefficients or the global damage coefficients available in the new GDI formulae and examine the legitimacy of the physics-based non-cumulative and cumulative terms considered in the formulae. As a result, the estimated damage index values using the new GDI formulae (both for 2D frames and 3D buildings) represent, through their regressed coefficients, the corresponding GDI values obtained from dissipated hysteresis energy-based weighted average of modified Park and Ang-type combined local damage models [1, 2]. In the case of the modified Park and Ang-type 3D GDI model, the sum of the dissipated hysteresis energy along two principal axes of each structural member is used as the weighing function followed by normalization of the GDI values in such a way that the value associated with the global collapse condition for a 3D building becomes 1.0. Although the application of the proposed GDI formulae does not need nonlinear time-history analysis, the latter's output is used in this research work to compute the GDI values through the corresponding LDIs at different plastic hinge locations. The nonlinear time-history analysis is also performed to generate the floor-displacement response because it is impossible to procure a set of recorded floor-displacement data for systematically varying ground motion intensities for any given frame or building [227], which is very much necessary for training and validation purposes for any proposed regression model.

A new (global or local) damage index model would be impractical if its user cannot understand the post-seismic damage state or performance level of a building or its member from the computed damage index. Therefore, the correlation between the proposed GDI formulae and the post-earthquake restoration-based damage states (i.e., no damage, repairable,

irreparable and collapse) is also carried out in the present research work. For 2D GDI formulae, the available limiting ranges (proposed by Stone and Taylor [1]) of the weighted average of modified Park and Ang-type 2D local damage index model (considered in the present study) to represent different global damage states are found satisfactory. No such limiting ranges for normalized values of modified Park and Ang-type 3D global damage model (with which the proposed 3D GDI formulae are tuned) are currently available. Therefore, new limiting ranges for the GDI values linked with different global damage states for 3D buildings are introduced in the present research work. Finally, the performance of the new GDI formulae, explicit expressions for the GDCs and limiting ranges for different global damage states are examined for various validation frames or buildings due to different validation design spectrum-compatible unidirectional or bidirectional round motions.

5.3 Contributions of the Research

The focus of the current research primarily revolves around the major advancements in the investigation of capturing the true lateral behaviour of columns through quasi-static experiments and conducting a comprehensive global damage characterization for instrumented RC structures due to seismic loading. These advancements have been elaborated upon in-depth in the preceding chapters. The outlines of the key contributions associated with each of these advancements are provided below.

5.3.1 Mechanics-based formulation to rectify experimental data

- ✍ A mechanics-based formulation has been proposed to rectify the experimentally obtained load-deformation curve for the cantilever column subjected to unidirectional lateral load and constant axial load by reckoning the effects of fixity and interactions between the actuators and the specimen and generate the curve representing true cantilever behaviour.

- ✍ The proposed formulation is applicable in the cases where it is not possible to make some special arrangements to accurately measure the column tip movement and actuator rotations during experiments.

- ✍ An overall underestimation and overestimation of lateral strength and lateral displacement capacity for cantilever columns, respectively, are observed when the experimental data are not rectified. The amount of deviation in the true behaviour from the experimentally-obtained one increases with axial stress and lateral displacement of a column specimen.

- ✍ The analytical models for predicting the lateral load-deformation behaviour of cantilever columns can be calibrated using the rectified data without changing the experi-

mentally obtained material properties (e.g., compressive strength of concrete, yield and ultimate strengths of steel).

- ✍ The proposed formulation can directly identify the yield displacement and the yield strength for a cantilever column from the rectified data by identifying the emergence of its plastic displacement.

5.3.2 Combined GDIs for 2D RC frames

- ✍ A novel combined GDI evaluation method has been proposed to predict GDI values obtained as the weighted average of modified Park and Ang-type local damage model for 2D RC frames. The dissipated hysteresis energies at each plastic hinge location are used as a weighing function to get the GDI values from the LDI values computed using the modified Park and Ang-type 2D damage model.

- ✍ The new GDI evaluation method utilizes the recorded floor-displacement data for a 2D frame due to seismic loading as the demand parameters, and therefore, negates the requirement of complex and computationally demanding nonlinear time-history analysis to generate the demand terms used in conventional damage models.

- ✍ Two combined GDI formulae applicable to 2D RC frames have been introduced using the new methodology in the present study. The difference in those formulae is the type of capacity terms used in the 2D GDI formulae, i.e., displacement ductility of frames and columns or curvature ductility of columns.

- ✍ The displacement ductility-based 2D GDI formula is suitable for any 2D RC frame. The corresponding capacity parameters can be computed from a representative finite element model for the considered frame.

- ✍ The curvature ductility-based 2D GDI formula is suitable for those frames whose behaviour can be idealized as a shear building model. Sectional information, material properties and eigenvalue analysis of the idealized shear building model can be used to get the corresponding capacity parameters.

- ✍ Use of the selected physics-based non-cumulative and cumulative terms in the new combined 2D GDI formulae have been found satisfactory through various standard statistical tests and statistical parameters.

- ✍ For wider applicability of the 2D GDI formulae, general expressions of the GDCs used in the 2D GDI formulae have been proposed to make the formulae applicable for other frames similar to the ones considered in the present study. The GDCs are expressed in terms of the fundamental period, the total height, the frame ratio for a frame and the local soil type.

- ✍ The available limiting ranges for modified Park and Ang-type damage index model have been used for verifying the performance of the new 2D GDI formulae to identify the post-earthquake restoration-based global damage states, i.e., no damage, repairable, irreparable and collapse, for a frame as the new formulae are tuned with the same damage values.

5.3.3 Combined GDIs for 3D RC buildings

- ✍ The scope of the new GDI evaluation methodology has been extended for 3D RC buildings by introducing another two combined GDI formulae, which can consider the effect of biaxial bending and axial load developed due to bidirectional ground motions on the global damage through the recorded dynamic responses along two orthogonal horizontal directions.

- ✍ The new combined 3D GDI formulae can predict the normalized GDI values for 3D RC buildings, where the GDI values obtained as the weighted average of modified Park and Ang-type 3D local damage model. The sum of dissipated hysteresis energies associated with two principal axes for a member section at each plastic hinge location are used as a weighing function to get the GDI values from the corresponding LDIs.

- ✍ The normalization of the GDI values is implemented to get the GDI value equal to 1.0 for a building in the case of globally collapsed condition. It has also helped to develop uniform limiting ranges for new 3D GDI formulae to represent different post-earthquake restoration-based global damage states for RC buildings.

- ✍ The new 3D GDI formulae utilizes different type of capacity terms (similar to their 2D counterparts), i.e., displacement ductility of building and columns or curvature ductility of columns, for their applications.

- ✍ The displacement ductility-based 3D GDI formula is suitable for any 3D RC building with the help of a representative finite element model to find the required capacity parameters.

- ✍ The curvature ductility-based 3D GDI formula is applicable to those buildings whose behaviour can be idealized as a shear building model. The required capacity parameters can be computed from the material properties, sectional information and eigenvalue analysis of the idealized shear building model.

- ✍ Similar to 2D GDI formulae, the non-cumulative and cumulative terms of the 3D GDI formulae are found satisfactory. Also, general expressions of the corresponding GDCs for the 3D GDI formulae have been developed in terms of the fundamental period, total

height, total widths along orthogonal horizontal directions, different shape ratios and dimensional ratios for a building and the local soil type.

✍ The correlation between the damage values estimated using new 3D GDI formulae and the global damage states are established in this study through the overall damage conditions of the structural members (i.e., columns and beams). Accordingly, suitable limiting ranges associated with those damage states for the new 3D GDI formulae have been introduced.

5.4 Limitations of the Study

The presented results as outcomes of the current research works are subjected to following limitations, though the conclusions extracted from those results remain unaffected.

- The proposed mechanics-based formulation does not consider the effect of bond-slip and distributed plasticity in the constitutive model to rectify cantilever-test data when the actuators do not keep their initial orientation during an experiment.
- The columns of the considered 2D RC frames and 3D RC buildings are assumed to be fixed at their base (or ground floor level) without accounting for soil-structure interaction.
- Low-rise to mid-rise buildings (with maximum five storeys and six bays) are considered for the study about the novel GDI evaluation method in this thesis.
- Combined effect of shear-flexure and torsion on the damage of RC members is not considered, and thus the new GDI formulae are applicable to the buildings which damaged mainly due to flexure or shear-flexure interaction.
- The effect of geometric irregularities in vertical or horizontal or both planes of a building is not accounted for in the proposed GDI formulae.

5.5 Branch of Future Research

The current study introduces a promising mechanics-based formulation to get true cantilever behaviour from test data and a novel GDI evaluation method for RC frames and buildings from their recorded floor responses during any seismic event. Although the necessary validations for the present research works and some allied practical engineering applications are demonstrated in this thesis satisfactorily, there are some scopes for further improvement apart from eliminating the limitations mentioned in the preceding section. With this in view, the following branches are identified for further research.

- For studying the behaviour of columns in 3D buildings due to seismic loading, many quasi-static (monotonic and cyclic) experiments on axially-loaded cantilever columns under the action of bidirectional lateral loadings have been carried out in recent times. Therefore, the scope of the proposed mechanics-based rectification formulation can be extended for columns attached with two horizontal actuators and one vertical actuator during such experiments to get the true cantilever behaviour from the test results.

- The current research works on the proposed GDI formulae for 2D RC frames and 3D RC buildings are carried out within a deterministic framework, where the statistical characterization of the residues in the prediction equations is not considered. Therefore, a probabilistic approach incorporating such uncertainties could be used to get more comprehensive characterization of damage prediction.

- The study about the proposed GDI evaluation method (from establishing the selected non-cumulative and cumulative terms to formulate suitable expressions for the global damage coefficients through statistical tests and numerical validation) for RC buildings can be applied as a proof-of-concept to propose other global damage indices applicable to the structures with other materials. For this purpose, GDI values computed using other appropriate damage models (e.g., low cycle fatigue-based damage model for metals), in lieu of modified Park and Ang-type combined damage models used in the present study, can be utilized as dependent variable in the proposed GDI evaluation methodology to come up with new combined GDI formulae.

A. Eigen Analysis

Definition A.1 *If* $\mathbf{T}$ *is a linear transformation from a vector space* $\mathbf{V}$ *over a field* $\mathbf{F}$ *into itself and* $\overrightarrow{v}$ *is a nonzero vector in* $\mathbf{V}$*, then* $\overrightarrow{v}$ *is an eigenvector of* $\mathbf{T}$ *if* $\mathbf{T}\overrightarrow{v}$ *is a scalar multiplier of* $\overrightarrow{v}$*, i.e.,*

$$\mathbf{T}\overrightarrow{v} = \Lambda\overrightarrow{v}$$

where Λ *(a scalar in* $\mathbf{F}$*) is known as the eigenvalue or characteristic value associated with the eigenvector* $\overrightarrow{v}$*. If* $\mathbf{V}$ *is finite-dimensional, the above expression is equivalent to*

$$\mathbf{A}\overrightarrow{u} = \Lambda\overrightarrow{u}$$

where $\mathbf{A}$ *is the matrix representation of* $\mathbf{T}$ *and* $\overrightarrow{u}$ *is the coordinate vector of* $\overrightarrow{v}$*.*

A.1 Eigen Analysis for structures

In structural engineering, eigen analysis of structures are used for various engineering applications such as free vibration of structures, buckling analysis, analysis of heat conduction. However, the application of eigen analysis in studying the undamped free vibration of RC structures will be discussed briefly in this section. The free vibration of a linear multi degree of freedom system or MDOF system with N degrees of freedom and no damping can be represented by the following set of coupled ordinary differential equations as

$$\mathbf{M}\ddot{\mathbf{u}}(t) + \mathbf{K}\mathbf{u}(t) = \mathbf{0} \tag{A.1}$$

where $\mathbf{M}_{N\times N}$ and $\mathbf{K}_{N\times N}$ are the *mass matrix* and the *stiffness matrix*, respectively, for the system, $\ddot{\mathbf{u}}_{N\times 1}(t)$ and $\mathbf{u}_{N\times 1}(t)$ are the acceleration and displacement vectors, respectively, at time t associated with the respective DOFs of the system, and $\mathbf{0}_{N\times 1}$ is the null vector representing zero external force. To uncouple the above set of equations, the physical coordinates $\mathbf{u}(t)$ can be expressed in terms of generalized coordinates $\boldsymbol{\eta}_{N\times 1}(t)$ and time-independent modal matrix $\boldsymbol{\Phi}_{N\times N}$ as

$$\mathbf{u}(t) = \boldsymbol{\Phi}\boldsymbol{\eta}(t) = \sum_{n=1}^{N} \boldsymbol{\phi}_n \eta_n(t) \tag{A.2}$$

where $\boldsymbol{\phi}_n$ is the nth mode shape and $\eta_n(t)$ is the generalized coordinate associated with the nth degree of freedom. Assuming $\eta_n(t) = A_n \sin\omega_n(t) + B_n \cos\omega_n(t)$, similar to the free

vibration response of an SDOF system, Equation (A.1) can be expressed as

$$\left[-\omega_n^2 \mathbf{M}\boldsymbol{\phi}_n + \mathbf{K}\boldsymbol{\phi}_n\right] \eta_n(t) = \mathbf{0} \quad . \tag{A.3}$$

Here, ω_n is the *natural frequency* for nth mode, and A_n and B_n are constants associated with the nth mode depending on the initial condition(s) of the MDOF system. Equation (A.3) can be satisfied if either $\eta_n(t) = 0$ (which is a trivial solution implying $\mathbf{u}(t) = \mathbf{0}$ or no motion), or ω_n and $\boldsymbol{\phi}_n$ must satisfy the following equation

$$\left[\mathbf{K} - \omega_n^2 \mathbf{M}\right] \boldsymbol{\phi}_n = \mathbf{0} \tag{A.4}$$

$$\Rightarrow \left[\mathbf{D}^{-1} - \omega_n^2 \mathbf{I}\right] \boldsymbol{\phi}_n = \mathbf{0} \quad \text{or} \quad \left[\mathbf{D} - \gamma_n^2 \mathbf{I}\right] \boldsymbol{\phi}_n = \mathbf{0} \quad \text{with} \quad \mathbf{D} = \mathbf{K}^{-1}\mathbf{M},\ \gamma_n = 1/\omega_n \tag{A.5}$$

$$\Rightarrow \mathbf{D}^{-1}\boldsymbol{\phi}_n = \omega_n^2 \boldsymbol{\phi}_n \quad \text{or} \quad \mathbf{D}\boldsymbol{\phi}_n = \gamma_n^2 \boldsymbol{\phi}_n \tag{A.6}$$

where $\mathbf{D}_{N\times N}$ is known as the dynamical matrix and $\mathbf{I}_{N\times N}$ is the identity matrix. Equation (A.4) is known as the *generalized eigenvalue problem*, whereas Equation (A.5) or (A.6) is known as the *standard eigenvalue problem*. The set of N homogeneous algebraic equations of Equation (A.4) always has the trivial solution $\boldsymbol{\phi}_n = \mathbf{0}$ (implying no motion), and nontrivial solution if

$$\det\left[\mathbf{K} - \omega_n^2 \mathbf{M}\right] = 0 \quad . \tag{A.7}$$

Equation (A.7) yields a polynomial of order N in ω_n^2, and it is known as the *characteristic equation* or the *frequency equation*. For shear building (or any other passive system without any rigid body movement), $\mathbf{K}$ and $\mathbf{M}$ are symmetric[1] and positive definite[2] matrices. Therefore, Equation (A.7) has N real[3] and positive roots for ω_n^2 in the case of a shear building. These N roots of the characteristic equation are known as *eigenvalues* or *characteristic values* or *normal values*. The square root of the eigenvalues are the N natural frequencies of the MDOF system, which can be further used to find the *fundamental periods* as $T_n = 2\pi/\omega_n$. After knowing a natural frequency, the corresponding *eigenvector* or *natural mode shape of vibration* in terms of the relative values of the N displacements ϕ_{jn} ($\forall j = 1, 2, \cdots, N$) can be obtained from Equation (A.4). There are different types of numerical method [252, 253] available for solving eigen value problems such as vector iterative methods (e.g., the forward iteration and inverse iteration methods), transformation methods (e.g., general Jacobi method and Lanczos method), Sturm sequence method, factorization method (e.g., QR factorization). The expressions of $\mathbf{M}$ and $\mathbf{K}$ matrices for 2D RC frames and 3D RC buildings (as considered in Chapters 3 and 4) are provided in the following sections to get T_n values through eigen analysis as discussed here.

[1] Matrix $\mathbf{A}_{N\times N}$ is symmetric if $A_{ij} = A_{ji}\ \forall\ i, j = 1, 2, \cdots, N$.

[2] Matrix $\mathbf{A}$ is positive definite if all of its sub matrices and the matrix itself have nonzero determinant, i.e., $\mathbf{v}^T\mathbf{A}\mathbf{v} > 0\ \forall\ \mathbf{v}$.

[3] The roots of eigen analysis are either real valued or they occur in complex-conjugate pairs for damped system.

A.1.1 Mass and stiffness matrices for 2D RC frames

Figure A.1 shows the schematic details of a 2D RC frame with N_s number of storeys and N_b number of bays. The frame is assumed to behave as a shear building for which the masses are concentrated at floors only with high in-plane rigidity, and they are supported by massless inextensible columns. Therefore, the frame has N_s DOFs (i.e., $u_1(t), u_2(t), \cdots, u_{N_s}(t)$) along the lateral direction as shown in the figure. The mass acting at ith floor ($\forall\ i = 1, 2, \cdots, N_s$) of the frame is denoted by m_i which is lumped at the corresponding DOF, $u_i(t)$. Since all columns situated between Floor i and Floor $(i-1)$ of the shear building have equal lateral displacement, the combined elastic stiffness of the columns (against flexural loading) can be expressed as

$$k_i = \sum_{c=1}^{N_b+1} \left(\frac{12 E_c I_c}{h_i^3} \right) \tag{A.8}$$

where E_c and I_c as the modulus of elasticity and the area moment of inertia, respectively, for the cth column situated in the corresponding storey, and h_i is the distance between Floor i and Floor $(i-1)$ for the frame.

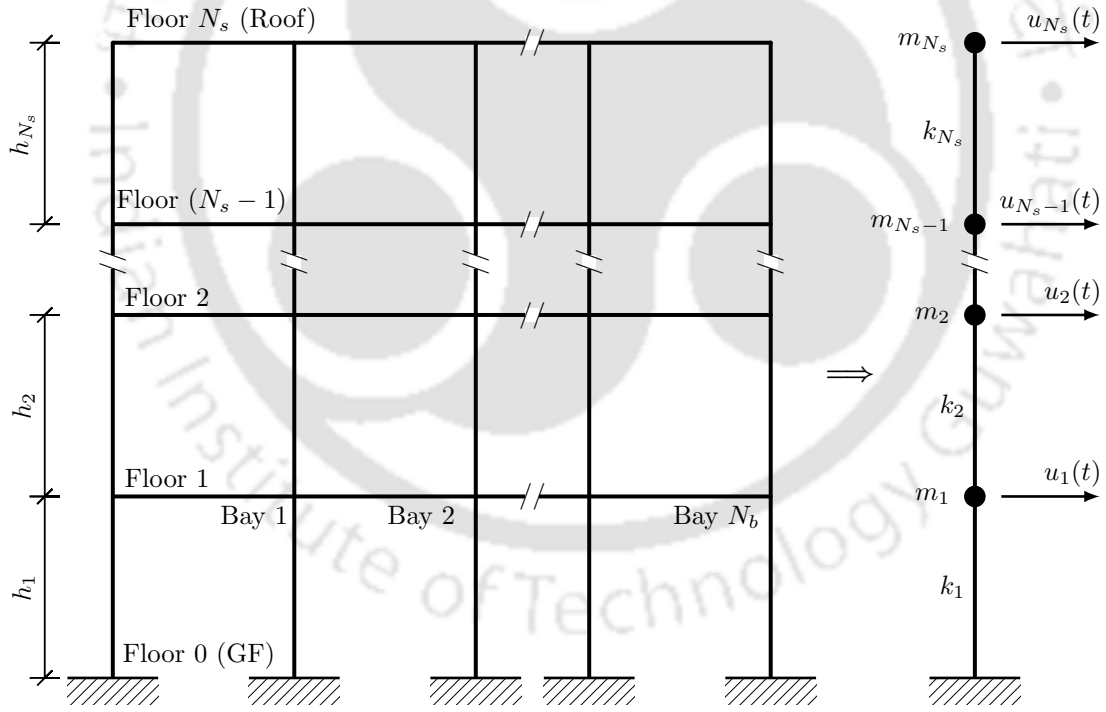

Figure A.1: The schematic details of a 2D RC frame along with the corresponding lumped-mass system

The elements of the lumped mass matrix $\mathbf{M}_{N_s \times N_s}$ for the 2D frame can be expressed as

$$M_{ij} = \begin{cases} m_i, & \text{if} \quad i = j \\ 0, & \text{otherwise} \end{cases} \tag{A.9}$$

where the lumped mass coefficient M_{ij} represents the contribution of mass along DOF i when unit deformation is applied at DOF j. The index i (and j) ranges from 1 to N_s, and represents the DOFs in the order of $u_1(t), u_2(t), \cdots, u_{N_s}(t)$. The elements of the stiffness matrix $\mathbf{K}_{N_s \times N_s}$ for the frame can be expressed as

$$K_{ij} = \begin{cases} k_i + k_{i+1}, & \text{if} \quad i = j \text{ and } i < N_s \\ k_i, & \text{if} \quad i = j = N_s \\ -k_{\max(i,j)}, & \text{if} \quad i = j \pm 1 \\ 0, & \text{otherwise} \end{cases} \tag{A.10}$$

where the stiffness coefficient K_{ij} represents the contribution of stiffness along DOF i when unit deformation is applied at DOF j.

A.1.2 Mass and stiffness matrices for 3D RC buildings

Consider a 3D RC building with N_s number of storeys, and N_{bx} and N_{by} numbers of bays along x- and y-directions, respectively. The height of all floors from their respective previous floors are $\{h_1, h_2, \cdots, h_{N_s}\}$, whereas the widths of each bay along two orthogonal directions are $\{l_{x1}, l_{x2}, \cdots, l_{xN_{bx}}\}$ and $\{l_{y1}, l_{y2}, \cdots, l_{yN_{by}}\}$. Figure A.2 shows the details of a 3D building, similar to the one of Figure 4.1, but with different dimensions in all directions. Three degrees of freedom (two translational and one rotational) are attached at the center of mass for each floor as shown in Figure A.2. Therefore, total degrees of freedom for the building are equal to $3N_s$. The mass of each floor is considered as $\{m_1, m_2, \cdots, m_{N_s}\}$ for the building. Now, for better representation of column stiffnesses, three indices, q, r and s, are introduced. q (ranging from 1 to $N_{bx}+1$) represents the location of a column in the direction of x-axis, r (ranging from 1 to $N_{by}+1$) represents the location of the column in the direction of y-axis, and s (ranging from 1 to N_s) represents its location in the direction of z-axis. Therefore, stiffness of individual column along two orthogonal directions are represented by $k_{sqr}^{(x)}$ and $k_{sqr}^{(y)}$, respectively. Numerically their values can be obtained as

$$k_{sqr}^{(x)} = \frac{12 E_{sqr} I_{sqr}^{(x)}}{h_s^3} \quad \text{and} \quad k_{sqr}^{(y)} = \frac{12 E_{sqr} I_{sqr}^{(y)}}{h_s^3} \tag{A.11}$$

where E_{sqr} is the modulus of elasticity of the corresponding column, and $I_{sqr}^{(x)}$ and $I_{sqr}^{(x)}$ are the area moment of inertia of the column about x- and y-axis respectively. Further, the distance of any column (in plan) from the center of mass along x-axis (Δx_q) and y-axis (Δy_r) can be represented as

$$\Delta x_q = CM_x - \sum_{i=1}^{q} l_{xi} \quad \text{and} \quad \Delta y_r = CM_y - \sum_{i=1}^{r} l_{yi} \tag{A.12}$$

where (CM_x, CM_y) is the coordinate of the center of mass as shown in Figure A.2.

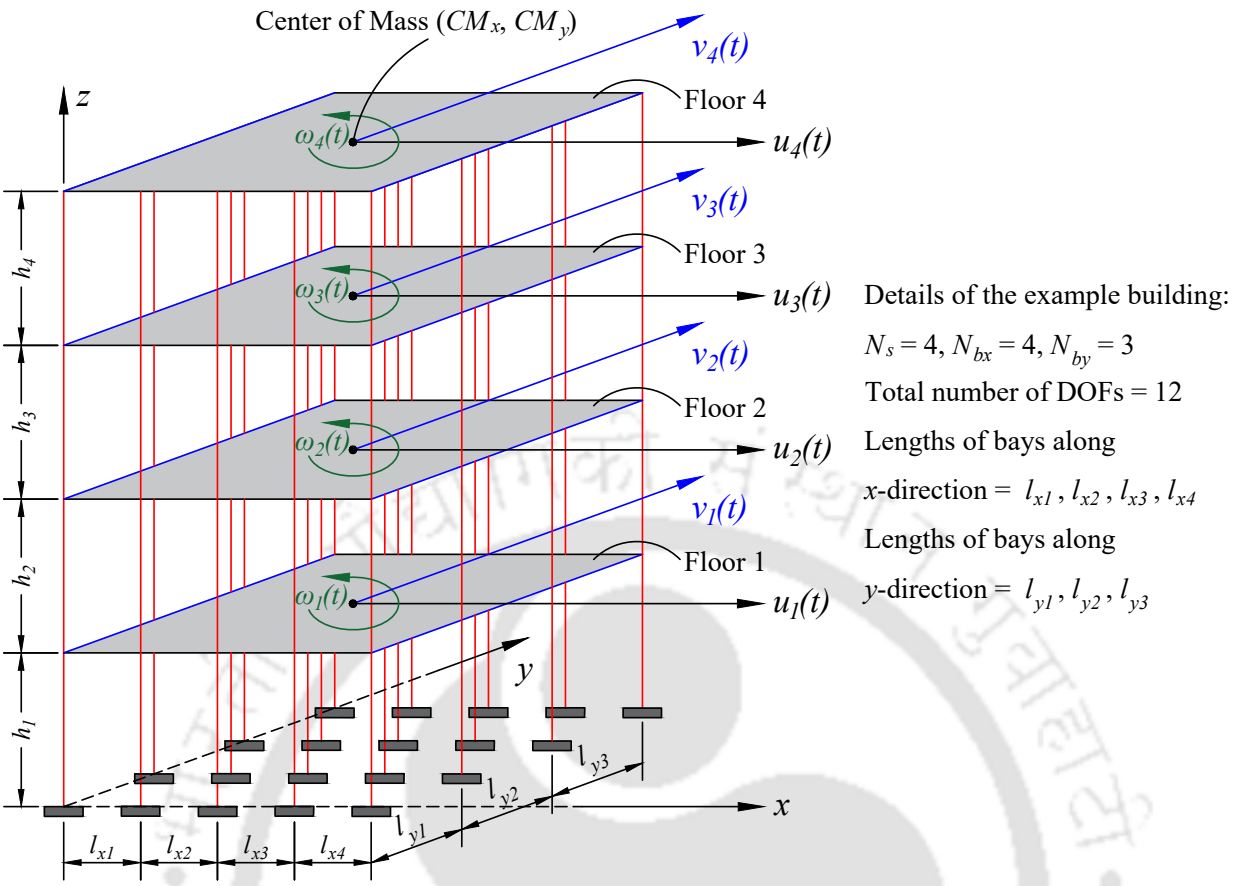

Figure A.2: Various details of an example 3D RC building

The elements of the mass matrix $\mathbf{M}_{3N_s \times 3N_s}$ for the 3D building can be expressed as

$$M_{ij} = \begin{cases} m_s, & \text{if} \quad i = j \text{ and } (j \bmod 3) \neq 0 \\ \dfrac{m_s}{12}\left(l_{x,\text{total}}^2 + l_{y,\text{total}}^2\right), & \text{if} \quad i = j \text{ and } (j \bmod 3) = 0 \\ 0, & \text{otherwise} \end{cases} \tag{A.13}$$

$$\text{with} \quad s = \lceil j/3 \rceil \tag{A.14}$$

where the index i (and j) ranges from 1 to $3N_s$, and represents the DOFs in the order of $u_1(t), v_1(t), \omega_1(t), \cdots, u_{N_s}(t), v_{N_s}(t), \omega_{N_s}(t)$. $\lceil \bullet \rceil$ represents the *ceiling function* (which returns the smallest integer greater than or equal to a given real number), $(f \bmod g)$ is the remainder of the Euclidean division of f by g provided both f and g are positive numbers. $l_{x,\text{total}}$ and $l_{y,\text{total}}$ are the total width of bays along x- and y-directions, respectively, for the building, and can be expressed as

$$l_{x,\text{total}} = \sum_{i=1}^{N_{bx}} l_{xi} \quad \text{and} \quad l_{y,\text{total}} = \sum_{i=1}^{N_{by}} l_{yi} \quad . \tag{A.15}$$

The elements of stiffness matrix $\mathbf{K}_{3N_s \times 3N_s}$ associated with the translational degrees of freedom along x-direction (i.e., $u_1(t), u_2(t), u_3(t)$ and $u_4(t)$ for the example building as shown

in Figure A.2) for 3D building can be expressed as

$$K_{ij} = \begin{cases} \sum_{q=1}^{N_{bx}+1}\sum_{r=1}^{N_{by}+1}\left[k_{sqr}^{(x)} + k_{(s+1)qr}^{(x)}\right], & \text{if } \; i=j,\ (j \bmod 3)=1 \text{ and } s<N_s \\ \sum_{q=1}^{N_{bx}+1}\sum_{r=1}^{N_{by}+1}\left[k_{sqr}^{(x)}\right], & \text{if } \; i=j,\ (j \bmod 3)=1 \text{ and } s=N_s \\ \sum_{q=1}^{N_{bx}+1}\sum_{r=1}^{N_{by}+1}\left[k_{sqr}^{(x)} + k_{(s+1)qr}^{(x)}\right](\Delta y_r), & \text{if } \; i=j+2,\ (j \bmod 3)=1 \text{ and } s<N_s \\ \sum_{q=1}^{N_{bx}+1}\sum_{r=1}^{N_{by}+1}\left[k_{sqr}^{(x)}\right](\Delta y_r), & \text{if } \; i=j+2,\ (j \bmod 3)=1 \text{ and } s=N_s \\ \sum_{q=1}^{N_{bx}+1}\sum_{r=1}^{N_{by}+1}\left[-k_{(s+1)qr}^{(x)}\right], & \text{if } \; i=j+3,\ (j \bmod 3)=1 \text{ and } s<N_s \\ \sum_{q=1}^{N_{bx}+1}\sum_{r=1}^{N_{by}+1}\left[k_{(s+1)qr}^{(x)}\right](-\Delta y_r), & \text{if } \; i=j+5,\ (j \bmod 3)=1 \text{ and } s<N_s \\ \sum_{q=1}^{N_{bx}+1}\sum_{r=1}^{N_{by}+1}\left[-k_{sqr}^{(x)}\right], & \text{if } \; i=j-3,\ (j \bmod 3)=1 \text{ and } s>1 \\ \sum_{q=1}^{N_{bx}+1}\sum_{r=1}^{N_{by}+1}\left[k_{sqr}^{(x)}\right](-\Delta y_r), & \text{if } \; i=j-1,\ (j \bmod 3)=1 \text{ and } s>1 \\ 0, & \text{for all other values of } i \text{ when } (j \bmod 3)=1 \end{cases} . \tag{A.16}$$

Similarly, the elements of stiffness matrix $\mathbf{K}$ associated with the translational degrees of freedom along y-direction (i.e., $v_1(t), v_2(t), v_3(t)$ and $v_4(t)$ for the example building of Figure A.2) can be expressed as

$$K_{ij} = \begin{cases} \sum_{q=1}^{N_{bx}+1}\sum_{r=1}^{N_{by}+1}\left[k_{sqr}^{(y)} + k_{(s+1)qr}^{(y)}\right], & \text{if } \; i=j,\ (j \bmod 3)=2 \text{ and } s<N_s \\ \sum_{q=1}^{N_{bx}+1}\sum_{r=1}^{N_{by}+1}\left[k_{sqr}^{(y)}\right], & \text{if } \; i=j,\ (j \bmod 3)=2 \text{ and } s=N_s \\ \sum_{q=1}^{N_{bx}+1}\sum_{r=1}^{N_{by}+1}\left[k_{sqr}^{(y)} + k_{(s+1)qr}^{(y)}\right](-\Delta x_q), & \text{if } \; i=j+1,\ (j \bmod 3)=2 \text{ and } s<N_s \\ \sum_{q=1}^{N_{bx}+1}\sum_{r=1}^{N_{by}+1}\left[k_{sqr}^{(y)}\right](-\Delta x_q), & \text{if } \; i=j+1,\ (j \bmod 3)=2 \text{ and } s=N_s \\ \sum_{q=1}^{N_{bx}+1}\sum_{r=1}^{N_{by}+1}\left[-k_{(s+1)qr}^{(y)}\right], & \text{if } \; i=j+3,\ (j \bmod 3)=2 \text{ and } s<N_s \\ \sum_{q=1}^{N_{bx}+1}\sum_{r=1}^{N_{by}+1}\left[k_{(s+1)qr}^{(y)}\right](\Delta x_q), & \text{if } \; i=j+4,\ (j \bmod 3)=2 \text{ and } s<N_s \\ \sum_{q=1}^{N_{bx}+1}\sum_{r=1}^{N_{by}+1}\left[-k_{sqr}^{(y)}\right], & \text{if } \; i=j-3,\ (j \bmod 3)=2 \text{ and } s>1 \\ \sum_{q=1}^{N_{bx}+1}\sum_{r=1}^{N_{by}+1}\left[k_{sqr}^{(y)}\right](\Delta x_q), & \text{if } \; i=j-2,\ (j \bmod 3)=2 \text{ and } s>1 \\ 0, & \text{for all other values of } i \text{ when } (j \bmod 3)=2 \end{cases} . \tag{A.17}$$

Finally, the elements of stiffness matrix $\mathbf{K}$ associated with the rotational degrees of freedom (i.e., $\omega_1(t), \omega_2(t), \omega_3(t)$ and $\omega_4(t)$ for the example building of Figure A.2) can be expressed as

$$K_{ij} = \begin{cases} \sum_{q=1}^{N_{bx}+1} \sum_{r=1}^{N_{by}+1} \left[\left\{ k_{sqr}^{(x)} + k_{(s+1)qr}^{(x)} \right\} (\Delta y_r)^2 + \left\{ k_{sqr}^{(y)} + k_{(s+1)qr}^{(y)} \right\} (\Delta x_q)^2 \right], & \text{if} \quad i = j,\ (j \bmod 3) = 0 \text{ and } s < N_s \\ \sum_{q=1}^{N_{bx}+1} \sum_{r=1}^{N_{by}+1} \left[k_{sqr}^{(x)} (\Delta y_r)^2 + k_{sqr}^{(y)} (\Delta x_q)^2 \right], & \text{if} \quad i = j,\ (j \bmod 3) = 0 \text{ and } s = N_s \\ \sum_{q=1}^{N_{bx}+1} \sum_{r=1}^{N_{by}+1} \left[k_{(s+1)qr}^{(x)} \right] (-\Delta y_r), & \text{if} \quad i = j+1,\ (j \bmod 3) = 0 \text{ and } s < N_s \\ \sum_{q=1}^{N_{bx}+1} \sum_{r=1}^{N_{by}+1} \left[k_{(s+1)qr}^{(y)} \right] (\Delta x_q), & \text{if} \quad i = j+2,\ (j \bmod 3) = 0 \text{ and } s < N_s \\ \sum_{q=1}^{N_{bx}+1} \sum_{r=1}^{N_{by}+1} - \left[k_{(s+1)qr}^{(x)} (\Delta y_r)^2 + k_{(s+1)qr}^{(y)} (\Delta x_q)^2 \right], & \text{if} \quad i = j+3,\ (j \bmod 3) = 0 \text{ and } s < N_s \\ \sum_{q=1}^{N_{bx}+1} \sum_{r=1}^{N_{by}+1} \left[k_{sqr}^{(x)} \right] (-\Delta y_r), & \text{if} \quad i = j-5,\ (j \bmod 3) = 0 \text{ and } s > 1 \\ \sum_{q=1}^{N_{bx}+1} \sum_{r=1}^{N_{by}+1} \left[k_{sqr}^{(y)} \right] (\Delta x_q), & \text{if} \quad i = j-4,\ (j \bmod 3) = 0 \text{ and } s > 1 \\ \sum_{q=1}^{N_{bx}+1} \sum_{r=1}^{N_{by}+1} - \left[k_{sqr}^{(x)} (\Delta y_r)^2 + k_{sqr}^{(y)} (\Delta x_q)^2 \right], & \text{if} \quad i = j-3,\ (j \bmod 3) = 0 \text{ and } s > 1 \\ \sum_{q=1}^{N_{bx}+1} \sum_{r=1}^{N_{by}+1} \left[k_{sqr}^{(x)} + k_{(s+1)qr}^{(x)} \right] (\Delta y_r), & \text{if} \quad i = j-2,\ (j \bmod 3) = 0 \text{ and } s < N_s \\ \sum_{q=1}^{N_{bx}+1} \sum_{r=1}^{N_{by}+1} \left[k_{sqr}^{(x)} \right] (\Delta y_r), & \text{if} \quad i = j-2,\ (j \bmod 3) = 0 \text{ and } s = N_s \\ \sum_{q=1}^{N_{bx}+1} \sum_{r=1}^{N_{by}+1} \left[k_{sqr}^{(y)} + k_{(s+1)qr}^{(y)} \right] (-\Delta x_q), & \text{if} \quad i = j-1,\ (j \bmod 3) = 0 \text{ and } s < N_s \\ \sum_{q=1}^{N_{bx}+1} \sum_{r=1}^{N_{by}+1} \left[k_{sqr}^{(x)} \right] (-\Delta x_q), & \text{if} \quad i = j-1,\ (j \bmod 3) = 0 \text{ and } s = N_s \\ 0, & \text{for all other values of } i \text{ when } (j \bmod 3) = 0 \quad . \end{cases} \tag{A.18}$$

List of Publications

Refereed Journals

- **Subhadip Naskar**, Sandip Das, and Hemant B Kaushik. "Retrieval of true lateral load-deformation behaviour of axially loaded columns from experimental data." In: *Journal of Structural Engineering* 146.3 (2020), pp. 04020007. DOI: 10.1061/(ASCE)ST.1943-541X.0002522.

- **Subhadip Naskar**, Sandip Das, and Hemant B Kaushik. "A novel method to evaluate combined global seismic damage index using recorded floor-displacement data for RC plane frames." In: *Bulletin of Earthquake Engineering* (2023) (under review).

- **Subhadip Naskar**, Sandip Das, and Hemant B Kaushik. "Combined global seismic damage for 3D RC buildings using recorded floor-displacement data." In: *Journal of Earthquake Engineering* (2024), pp. 1-31. DOI: 10.1080/13632469.2024.2310067.

Book Chapter

- **Subhadip Naskar**, Sandip Das, and Hemant B Kaushik. "Modification and modeling of experiments with bi-directional loading on reinforced concrete columns." In: *Lecture Notes in Mechanical Engineering: Advances in Structural Vibration, Springer Nature Singapore Pte. Ltd.* (2020), pp. 185-198. DOI: 10.1007/978-981-15-5862-7_16.

International Conferences

- Sandip Das, **Subhadip Naskar**, and Hemant B Kaushik. "Evaluation of global seismic damage index based on the measurable response quantities of structures." In: *17th World Conference on Earthquake Engineering*, Sendai, Japan, 2020-21.
  URL: https://wcee.nicee.org/wcee/article/17WCEE/2c-0253.pdf (visited on Feb. 19, 2024).

- **Subhadip Naskar**, Sandip Das, and Hemant B Kaushik. "Combined global damage index for 3D reinforced concrete frame using recorded floor-displacement data." In: *18th World Conference on Earthquake Engineering*, Milan, Italy, 2024 (paper accepted).
  URL: https://services2.aimgroup.eu/ASPClient/files/5002/Abstract/372_20231031085355.pdf (visited on March 26, 2024).

Bibliography

[1] William C Stone and Andrew W Taylor. "Seismic performance of circular bridge columns designed in accordance with AASHTO/CALTRANS standards". In: *NIST Building Science Series 170, US Department of Commerce, National Institute of Standards and Technology* (1993). URL: https://nehrpsearch.nist.gov/article/PB96-146352/XAB (visited on Feb. 19, 2023) (See pp. xviii, xxii, xxiii, 7, 11, 12, 21, 22, 54, 61, 63, 64, 74, 115–117).

[2] J Guo, JJ Wang, Y Li, WG Zhao, and YL Du. "Three dimensional extension for Park and Ang damage model". In: *Structures* 7 (2016), pp. 184–194. DOI: 10.1016/j.istruc.2016.06.008 (See pp. xxii, xxiii, 4, 7, 17, 20–22, 90, 93, 94, 96, 97, 107, 115, 116).

[3] *IS 1893: Criteria for earthquake resistant design of structures (Part 1: General provision and buildings)*. Standard. New Delhi: Bureau of Indian Standard, 2016. URL: https://www.services.bis.gov.in/php/BIS_2.0/bisconnect/standard_review/Standard_review/Isdetails?ID=ODQwMQ%3D%3D (visited on Aug. 15, 2022) (See pp. xxiv, 55, 58, 59, 61, 63, 83, 87, 88, 90, 93, 95).

[4] M_w 9.5-1960*: Great Chilean (Valvidia) Earthquake*. URL: https://earthquake.usgs.gov/earthquakes/eventpage/official19600522191120_30/executive (visited on May 22, 2023) (See p. 1).

[5] M_w 9.1-2004*: Sumatra-Andaman Islands Earthquake*. URL: https://earthquake.usgs.gov/earthquakes/eventpage/official20041226005853450_30/executive (visited on May 22, 2023) (See p. 1).

[6] M_w 9.1-2011*: Great Tohoku Earthquake, Japan*. URL: https://earthquake.usgs.gov/earthquakes/eventpage/official20110311054624120_30/executive (visited on May 22, 2023) (See p. 1).

[7] M_{fa} 7.9-1868*: Great Ka'u Earthquake, Hawaii*. URL: https://earthquake.usgs.gov/earthquakes/eventpage/official18680403023000000/executive (visited on May 22, 2023) (See p. 1).

[8] M_w 7.7-1975*: 17 km SSW of Leilani Estates, Hawaii*. URL: https://earthquake.usgs.gov/earthquakes/eventpage/hv19755025/executive (visited on May 22, 2023) (See p. 1).

[9] M_w 7.1-1990*: 0 km ESE of Union, Philippines*. URL: https://earthquake.usgs.gov/earthquakes/eventpage/usp0004ag6/executive (visited on May 22, 2023) (See p. 1).

[10] M_w 9.2-1964*: Prince William Sound Earthquake, Alaska*. URL: https://earthquake.usgs.gov/earthquakes/eventpage/iscgem869809/executive (visited on May 22, 2023) (See p. 1).

[11] M_d 5.7-1980*: 38 km NNE of Amboy, Washington*. URL: https://earthquake.usgs.gov/earthquakes/eventpage/uw10084803/executive (visited on May 22, 2023) (See p. 1).

[12] *M_w 6.7-1994: 1 km NNW of Reseda, California*. URL: https://earthquake.usgs.gov/earthquakes/eventpage/ci3144585/executive (visited on May 22, 2023) (See p. 1).

[13] *Earthquakes-Overview*. URL: https://www.who.int/health-topics/earthquakes#tab=tab_1 (visited on May 22, 2023) (See p. 1).

[14] Shannon Doocy, Amy Daniels, Catherine Packer, Anna Dick, and Thomas D Kirsch. "The human impact of earthquakes: a historical review of events 1980-2009 and systematic literature review". In: *PLoS currents* 5 (2013). URL: https://www.ncbi.nlm.nih.gov/pmc/articles/PMC3644288/ (visited on Oct. 15, 2022) (See p. 1).

[15] YS Chung, C Meyer, and M Shinozuka. *Seismic damage assessment of reinforced concrete members*. Vol. 87. 0022. National Center for Earthquake Engineering Research, State University of New York, Buffalo, USA, 1987. URL: https://nehrpsearch.nist.gov/static/files/NSF/PB88150867.pdf (visited on Feb. 19, 2018) (See pp. 2, 3, 7, 8).

[16] A Ghobarah, H Abou-Elfath, and Ashraf Biddah. "Response-based damage assessment of structures". In: *Earthquake engineering & structural dynamics* 28.1 (1999), pp. 79–104. DOI: 10.1002/(SICI)1096-9845(199901)28:1<79::AID-EQE805>3.0.CO;2-J (See pp. 2, 3, 7, 18).

[17] DA Makhloof, AR Ibrahim, and Xiaodan Ren. "Damage Assessment of Reinforced Concrete Structures through Damage Indices: A State-of-the-Art Review". In: *CMES-COMPUTER MODELING IN ENGINEERING & SCIENCES* 128.3 (2021), pp. 849–874. DOI: 10.32604/cmes.2021.016882 (See pp. 2, 3, 53).

[18] Majdi Flah, Itzel Nunez, Wassim Ben Chaabene, and Moncef L Nehdi. "Machine learning algorithms in civil structural health monitoring: A systematic review". In: *Archives of computational methods in engineering* 28 (2021), pp. 2621–2643. DOI: 0.1007/s11831-020-09471-9 (See p. 2).

[19] Vahid Reza Gharehbaghi et al. "A critical review on structural health monitoring: Definitions, methods, and perspectives". In: *Archives of computational methods in engineering* (2021), pp. 1–27. DOI: 10.1007/s11831-021-09665-9 (See p. 2).

[20] Brian López-Castro, Ana Gabriela Haro-Baez, Diego Arcos-Aviles, Marco Barreno-Riera, and Bryan Landázuri-Avilés. "A systematic review of structural health monitoring systems to strengthen post-earthquake assessment procedures". In: *Sensors* 22.23 (2022), p. 9206. DOI: 10.3390/s22239206 (See pp. 2, 21).

[21] Rakesh Katam, Venkata Dilip Kumar Pasupuleti, and Prafulla Kalapatapu. "A review on structural health monitoring: past to present". In: *Innovative Infrastructure Solutions* 8.9 (2023), p. 248. DOI: 10.1007/s41062-023-01217-3 (See p. 2).

[22] Adrian M Chandler and Nelson TK Lam. "Performance-based design in earthquake engineering: a multi-disciplinary review". In: *Engineering structures* 23.12 (2001), pp. 1525–1543. DOI: 10.1016/S0141-0296(01)00070-0 (See p. 2).

[23] Ahmed Ghobarah. "Performance-based design in earthquake engineering: state of development". In: *Engineering structures* 23.8 (2001), pp. 878–884. DOI: 10.1016/S0141-0296(01)00036-0 (See p. 2).

[24] Rivka Oxman. "Performance-based design: current practices and research issues". In: *International journal of architectural computing* 6.1 (2008), pp. 1–17. DOI: https://doi.org/10.1260/147807708784640090 (See p. 2).

[25] M Zameeruddin and K K Sangle. "Review on Recent developments in the performance-based seismic design of reinforced concrete structures". In: *Structures* 6 (2016), pp. 119–133. DOI: 10.1016/j.istruc.2016.03.001 (See pp. 2, 3, 53).

[26] SS Mehanny and GG Deierlein. "Modelling of assessment of seismic performance of composite frames with reinforced concrete columns and steel beams." In: *Report No. 135, John A. Blume Earthquake Engineering Center, Stanford University, Sanford, USA* (2000). URL: https://searchworks.stanford.edu/view/ht920mc7943 (visited on Sept. 1, 2022) (See pp. 2, 3).

[27] Comité Euro-International du Béton. *RC frames under earthquake loading: state of the art report*. Vol. 231. Thomas Telford, London, 1996. ISBN: 978-0-7277-2085-6. URL: https://www.fib-international.org/publications/ceb-bulletins/rc-frames-under-earthquake-loading-pdf-detail.html (visited on Mar. 26, 2018) (See pp. 2, 23).

[28] Martin S Williams and Robert G Sexsmith. "Seismic damage indices for concrete structures: a state-of-the-art review". In: *Earthquake spectra* 11.2 (1995), pp. 319–349. DOI: 10.1193/1.1585817 (See pp. 2, 3, 6, 9, 11, 19, 24).

[29] AJ Kappos. "Seismic damage indices for RC buildings: evaluation of concepts and procedures". In: *Progress in Structural Engineering and materials* 1.1 (1997), pp. 78–87. DOI: 10.1002/pse.2260010113 (See pp. 2, 4, 18).

[30] B Mohebi, A.H. Chegini. T, and A.R. Miri. T. "A new damage index for steel MRFs based on incremental dynamic analysis". In: *Journal of Constructional Steel Research* 156 (2019), pp. 137–154. DOI: 10.1016/j.jcsr.2019.02.005 (See p. 2).

[31] A Bassam, A Iranmanesh, and F Ansari. "A simple quantitative approach for post earthquake damage assessment of flexure dominant reinforced concrete bridges". In: *Engineering Structures* 33.12 (2011), pp. 3218–3225. DOI: 10.1016/j.engstruct.2011.06.024 (See p. 2).

[32] Stephanie G Paal, Jong-Su Jeon, Ioannis Brilakis, and Reginald DesRoches. "Automated damage index estimation of reinforced concrete columns for post-earthquake evaluations". In: *Journal of Structural Engineering* 141.9 (2015), p. 04014228. DOI: 10.1061/(ASCE)ST.1943-541X.0001200 (See p. 2).

[33] J-A Goulet, C Michel, and AD Kiureghian. "Data-driven post-earthquake rapid structural safety assessment". In: *Earthquake Engineering & Structural Dynamics* 44.4 (2015), pp. 549–562. DOI: 10.1002/eqe.2541 (See p. 2).

[34] Andreas J Kappos and EG Dimitrakopoulos. "Feasibility of pre-earthquake strengthening of buildings based on cost-benefit and life-cycle cost analysis, with the aid of fragility curves". In: *Natural hazards* 45 (2008), pp. 33–54. DOI: 10.1007/s11069-007-9155-9 (See p. 2).

[35] Konstantinos Kostinakis, Asimina Athanatopoulou, and Konstantinos Morfidis. "Correlation between ground motion intensity measures and seismic damage of 3D R/C buildings". In: *Engineering Structures* 82 (2015), pp. 151–167. DOI: 10.1016/j.engstruct.2014.10.035 (See p. 2).

[36] Konstantinos Kostinakis, Ioanna-Kleoniki Fontara, and Asimina M Athanatopoulou. "Scalar structure-specific ground motion intensity measures for assessing the seismic performance of structures: a review". In: *Journal of Earthquake Engineering* 22.4 (2018), pp. 630–665. DOI: 10.1080/13632469.2016.1264323 (See p. 2).

[37] Yikun Qiu, Changdong Zhou, and A Siha. "Correlation between earthquake intensity parameters and damage indices of high-rise RC chimneys". In: *Soil Dynamics and Earthquake Engineering* 137 (2020), p. 106282. DOI: 10.1016/j.soildyn.2020.106282 (See p. 2).

[38] Xian-Liang Rong, Jing-heng Yang, Luo Jun, Yi-Xin Zhang, Shan-Suo Zheng, and Liguo Dong. "Optimal ground motion intensity measure for seismic assessment of high-rise reinforced concrete structures". In: *Case Studies in Construction Materials* 18 (2023), e01678. DOI: 10.1016/j.cscm.2022.e01678 (See p. 2).

[39] C Davis, V Keilis-Borok, G Molchan, P Shebalin, P Lahr, and C Plumb. "Earthquake prediction and disaster preparedness: Interactive analysis". In: *Natural Hazards Review* 11.4 (2010), pp. 173–184. DOI: 10.1061/(ASCE)NH.1527-6996.0000020 (See p. 2).

[40] Craig A Davis. "Loss functions for temporal and spatial optimizing of earthquake prediction and disaster preparedness". In: *Pure and applied geophysics* 169.11 (2012), pp. 1989–2010. DOI: 10.1007/s00024-012-0502-8 (See p. 2).

[41] Maria Battarra, Burcu Balcik, and Huifu Xu. "Disaster preparedness using risk-assessment methods from earthquake engineering". In: *European journal of operational research* 269.2 (2018), pp. 423–435. DOI: 10.1016/j.ejor.2018.02.014 (See p. 2).

[42] Amador Teran-Gilmore and James O Jirsa. "A damage model for practical seismic design that accounts for low cycle fatigue". In: *Earthquake spectra* 21.3 (2005), pp. 803–832. DOI: 10.1193/1.1979500 (See pp. 3, 8).

[43] R Sinha and SR Shiradhonkar. "Seismic damage index for classification of structural damage–closing the loop". In: Proceedings of the 15th World Conference on Earthquake Engineering. Libosa, Portugal, 2012. URL: https://iitk.ac.in/nicee/wcee/article/WCEE2012_2941.pdf (visited on Aug. 3, 2022) (See p. 3).

[44] Aparna Roy, Gautam Bhattacharya, and Rana Roy. "Maximum credible damage of RC bridge pier under bi-directional seismic excitation for all incidence angles". In: *Engineering Structures* 152 (2017), pp. 251–273. DOI: 10.1016/j.engstruct.2017.09.008 (See pp. 3, 4, 7, 15, 17).

[45] Pritam Hait, Arjun Sil, and Satyabrata Choudhury. "Modified Damage Assessment Method for Reinforced Concrete Buildings". In: *Practice Periodical on Structural Design and Construction* 26.4 (2021), p. 04021039. DOI: 10.1061/(ASCE)SC.1943-5576.0000605 (See p. 3).

[46] Helmut Krawinkler and Mahmud Zohrei. "Cumulative damage in steel structures subjected to earthquake ground motions". In: *Computers & Structures* 16.1-4 (1983), pp. 531–541. DOI: 10.1016/0045-7949(83)90193-1 (See p. 3).

[47] Carlo A Castiglioni and Luis Calado. "Comparison of two cumulative damage approaches for the assessment of behaviour factors for low-rise steel buildings". In: *Journal of Constructional Steel Research* 40.1 (1996), pp. 39–61. DOI: 10.1016/S0143-974X(96)00042-9 (See p. 3).

[48] ML Daali and RM Korol. "Adequate ductility in steel beams under earthquake-type loading". In: *Engineering structures* 18.2 (1996), pp. 179–189. DOI: 10.1016/0141-0296(95)00064-X (See p. 3).

[49] Amadeo Benavent-Climent. "An energy-based damage model for seismic response of steel structures". In: *Earthquake engineering & structural dynamics* 36.8 (2007), pp. 1049–1064. DOI: 10.1002/eqe.671 (See p. 3).

[50] E Bojórquez, A Reyes-Salazar, A Terán-Gilmore, and SE Ruiz. "Energy-based damage index for steel structures". In: *Steel and Composite Structures* 10.4 (2010), pp. 331–348. DOI: 10.12989/scs.2010.10.4.331 (See p. 3).

[51] George S Kamaris, George D Hatzigeorgiou, and Dimitri E Beskos. "A new damage index for plane steel frames exhibiting strength and stiffness degradation under seismic motion". In: *Engineering Structures* 46 (2013), pp. 727–736. DOI: 10.1016/j.engstruct.2012.07.037 (See p. 3).

[52] P Rajeev and KK Wijesundara. "Energy-based damage index for concentrically braced steel structure using continuous wavelet transform". In: *Journal of Constructional Steel Research* 103 (2014), pp. 241–250. DOI: 10.1016/j.jcsr.2014.09.011 (See p. 3).

[53] Sergio A Díaz, Luis G Pujades, Alex H Barbat, Diego A Hidalgo-Leiva, and Yeudy F Vargas-Alzate. "Capacity, damage and fragility models for steel buildings: a probabilistic approach". In: *Bulletin of earthquake engineering* 16.3 (2018), pp. 1209–1243. DOI: 10.1007/s10518-017-0237-0 (See pp. 3, 4).

[54] ZG Zhou and YW Li. "Experimental investigation on cumulative damage indices for steel members under ultra-low-cycle loading". In: *Journal of Constructional Steel Research* 172 (2020), p. 106223. DOI: 10.1016/j.jcsr.2020.106223 (See p. 3).

[55] Mohammed Samier Sebaq, Yi Xiao, and Ge Song. "Damage indices of steel moment-resisting frames equipped with fluid viscous dampers". In: *Journal of Asian Architecture and Building Engineering* (2023), pp. 1–20. DOI: 10.1080/13467581.2023.2182645 (See p. 3).

[56] H Mao and S Mahadevan. "Fatigue damage modelling of composite materials". In: *Composite Structures* 58.4 (2002), pp. 405–410. DOI: 10.1016/S0263-8223(02)00126-5 (See p. 3).

[57] Hsing-Sung Chen and Shun-Fa Hwang. "A fatigue damage model for composite materials". In: *Polymer composites* 30.3 (2009), pp. 301–308. DOI: 10.1002/pc.20556 (See p. 3).

[58] Ramadan A Esmaeel and Farid Taheri. "Delamination detection in laminated composite beams using the empirical mode decomposition energy damage index". In: *Composite Structures* 94.5 (2012), pp. 1515–1523. DOI: 10.1016/j.compstruct.2011.12.029 (See p. 3).

[59] Shahab Torkamani, Samit Roy, Mark E Barkey, Edward Sazonov, Susan Burkett, and Sushma Kotru. "A novel damage index for damage identification using guided waves with application in laminated composites". In: *Smart Materials and Structures* 23.9 (2014), p. 095015. DOI: 10.1088/0964-1726/23/9/095015 (See p. 3).

[60] Carlo Boursier Niutta, Andrea Tridello, Raffaele Ciardiello, Giovanni Belingardi, and Davide Salvatore Paolino. "Assessment of residual elastic properties of a damaged composite plate with combined damage index and finite element methods". In: *Applied Sciences* 9.12 (2019), p. 2579. DOI: 10.3390/app9122579 (See p. 3).

[61] Sheng Peng et al. "A modified Park-Ang model for seismic damage assessment of recycled aggregate concrete-filled square steel tube columns". In: *Case Studies in Construction Materials* 17 (2022), e01692. DOI: 10.1016/j.cscm.2022.e01692 (See p. 3).

[62] V Bertero and B Bresler. *Developing methodologies for evaluating the earthquake safety of existing buildings*. Vol. 77. 06. Earthquake Engineering Research Center, University of California, Berkeley, USA, 1977. URL: https://files.eric.ed.gov/fulltext/ED154514.pdf (visited on June 26, 2023) (See p. 3).

[63] T Blejwas and Boris Bresler. *Damageability in existing buildings*. Vol. 78. 12. Earthquake Engineering Research Center, University of California, USA, 1979. URL: https://nehrpsearch.nist.gov/article/PB80-166978/XAB (visited on June 26, 2023) (See pp. 3, 6).

[64] Koji Mizuhata and Yukinori Maeda. "Study on evaluation of cumulative damage earthquake response of structures based on computer-actuator on-line test". In: vol. 4. Proceedings 9th World Conference on Earthquake Engineering. Tokyo-Kyoto, Japan, 1988, pp. 83–88. URL: https://www.iitk.ac.in/nicee/wcee/article/9_vol4_83.pdf (visited on May 4, 2023) (See p. 3).

[65] Graham H Powell and Rakesh Allahabadi. "Seismic damage prediction by deterministic methods: concepts and procedures". In: *Earthquake engineering & structural dynamics* 16.5 (1988), pp. 719–734. DOI: 10.1002/eqe.4290160507 (See pp. 3, 6, 7).

[66] JM Bracci, AM Reinhorn, JB Mander, and SK Kunnath. *Deterministic model for seismic damage evaluation of reinforced concrete structures*. Vol. 89. 0033. National Center for Earthquake Engineering Research, State University of New York, Buffalo, USA, 1989. URL: https://www.buffalo.edu/mceer/catalog.host.html/content/shared/www/mceer/publications/NCEER-89-0033.detail.html (visited on June 13, 2022) (See pp. 3, 7, 14, 19, 20, 22).

[67] Young Soo Chung, Christian Meyer, and Masanobu Shinozuka. "Modeling of concrete damage". In: *Structural Journal* 86.3 (1989), pp. 259–271. DOI: 10.14359/2895 (See pp. 3, 7, 8).

[68] Panagiotis E Mergos and Andreas J Kappos. "Seismic damage analysis including inelastic shear–flexure interaction". In: *Bulletin of Earthquake Engineering* 8 (2010), pp. 27–46. DOI: 10.1007/s10518-009-9161-2 (See pp. 3, 7, 8).

[69] Akenori Shibata and Mete A Sozen. "Substitute-structure method for seismic design in R/C". In: *Journal of the structural division* 102.1 (1976), pp. 1–18. DOI: 10.1061/JSDEAG.0004250 (See pp. 3, 6, 7).

[70] Hooshang Banon, John M Biggs, and H Max Irvine. "Seismic damage in reinforced concrete frames". In: *Journal of the Structural Division* 107.9 (1981), pp. 1713–1729. DOI: 10.1061/JSDEAG.0005778. (Visited on Feb. 3, 2023) (See pp. 3, 6, 7, 10).

[71] Magdy SL Roufaiel and Christian Meyer. "Analytical modeling of hysteretic behavior of R/C frames". In: *Journal of Structural Engineering* 113.3 (1987), pp. 429–444. DOI: 10.1061/(ASCE)0733-9445(1987)113:3(429) (See pp. 3, 6, 7, 18).

[72] P.S. Skjærbæk, S.R.K. Nielsen, and A.Ş. Çakmak. "Identification of damage in reinforced concrete structures from earthquake records— optimal location of sensors". In: *Soil Dynamics and Earthquake Engineering* 15.6 (1996), pp. 347–358. ISSN: 0267-7261. DOI: 10.1016/0267-7261(96)00018-8 (See pp. 3, 7, 19).

[73] JM Ko, ZG Sun, and YQ Ni. "Multi-stage identification scheme for detecting damage in cable-stayed Kap Shui Mun Bridge". In: *Engineering structures* 24.7 (2002), pp. 857–868. DOI: 10.1016/S0141-0296(02)00024-X (See pp. 3, 7, 19).

[74] Jer-Fu Wang, Chi-Chang Lin, and Shih-Min Yen. "A story damage index of seismically-excited buildings based on modal frequency and mode shape". In: *Engineering Structures* 29.9 (2007), pp. 2143–2157. DOI: 10.1016/j.engstruct.2006.10.018 (See pp. 3, 7, 19, 24).

[75] Ali Massumi and Ehsan Moshtagh. "A new damage index for RC buildings based on variations of nonlinear fundamental period". In: *The structural design of tall and special buildings* 22.1 (2013), pp. 50–61. DOI: 10.1002/tal.656 (See pp. 3, 7, 19).

[76] E DiPasquale and AS Cakmak. *Identification of the serviceability limit state and detection of seismic structural damage*. Vol. 88. 0022. National Center for Earthquake Engineering Research, State University of New York, Buffalo, USA, 1987. URL: https://nehrpsearch.nist.gov/static/files/NSF/PB89122188.pdf (visited on Jan. 29, 2023) (See pp. 3, 7, 19).

[77] E DiPasquale and AS Cakmak. "Seismic damage assessment using linear models". In: *Soil Dynamics and Earthquake Engineering* 9.4 (1990), pp. 194–215. DOI: 10.1016/S0267-7261(05)80010-7 (See pp. 3, 4, 7, 19).

[78] Edmondo DiPasquale, Jiann-Wen Ju, Attila Askar, and Ahmet S Çakmak. "Relation between global damage indices and local stiffness degradation". In: *Journal of Structural Engineering* 116.5 (1990), pp. 1440–1456. DOI: 10.1061/(ASCE)0733-9445(1990)116:5(1440). (Visited on July 17, 2022) (See pp. 3, 7, 19).

[79] KJ Mørk. "Stochastic analysis of reinforced concrete frames under seismic excitation". In: *Soil Dynamics and Earthquake Engineering* 11.3 (1992), pp. 145–161. DOI: 10.1016/0267-7261(92)90028-C (See pp. 3, 4, 7, 19).

[80] Young-Ji Park, Alfredo H-S Ang, and Yi Kwei Wen. "Seismic damage analysis of reinforced concrete buildings". In: *Journal of Structural Engineering* 111.4 (1985), pp. 740–757. DOI: 10.1061/(ASCE)0733-9445(1985)111:4(740) (See pp. 3, 7, 10, 19, 20, 22, 53, 54, 64).

[81] Mohammad Reza Tabeshpour, Ali Bakhshi, and Ali A Golafshani. "Vulnerability and damage analyses of existing buildings". In: 1261. 13th World Conference on Earthquake Engineering. Vancouver, Canada, 2004. URL: https://www.iitk.ac.in/nicee/wcee/article/13_1261.pdf (visited on Oct. 16, 2022) (See pp. 3, 7, 19).

[82] Seong-Hoon Jeong and Amr S Elnashai. "New three-dimensional damage index for RC buildings with planar irregularities". In: *Journal of Structural Engineering* 132.9 (2006), pp. 1482–1490. DOI: 10.1061/(ASCE)0733-9445(2006)132:9(1482) (See pp. 3, 7, 19).

[83] Shuijing Xiao, Longhe Xu, and Xiao Lu. "Nonlinear damage model for seismic damage assessment of reinforced concrete frame members and structures". In: *Acta Mechanica Sinica* 34.5 (2018), pp. 949–962. DOI: 10.1007/s10409-018-0779-7 (See pp. 3, 7, 12, 13, 19–22).

[84] M Ciampoli, R Giannini, C Nuti, and PE Pinto. "Seismic reliability of non-linear structures with stochastic parameters by directional simulation". In: *Structural Safety and Reliability*. American Society of Civil Engineers. 1989, pp. 1121–1128. URL: https://cedb.asce.org/CEDBsearch/record.jsp?dockey=0064423 (visited on June 13, 2023) (See pp. 4, 11).

[85] S.R.K. Nielsen, H.U. Köylüoğlu, and A.Ş. Çalmak. "One and two-dimensional maximum softening damage indicators for reinforced concrete structures under seismic excitation". In: *Soil Dynamics and Earthquake Engineering* 11.8 (1992), pp. 435–443. ISSN: 0267-7261. DOI: 10.1016/0267-7261(92)90007-Z (See pp. 4, 7, 19).

[86] Fawei Qiu, Wenfeng Li, Peng Pan, and Jiaru Qian. "Experimental tests on reinforced concrete columns under biaxial quasi-static loading". In: *Engineering structures* 24.4 (2002), pp. 419–428. DOI: 10.1016/S0141-0296(01)00108-0. (Visited on Sept. 1, 2022) (See pp. 4, 7, 15, 23, 25, 81, 113).

[87] Hugo Rodrigues, António Arêde, Humberto Varum, and Aníbal Costa. "Damage evolution in reinforced concrete columns subjected to biaxial loading". In: *Bulletin of earthquake Engineering* 11 (2013), pp. 1517–1540. DOI: 10.1007/s10518-013-9439-2 (See pp. 4, 7, 15, 16, 20).

[88] Noriyuki Takahashi and Hitoshi Shiohara. "Life cycle economic loss due to seismic damage of nonstructural elements". In: vol. 203. 13th World Conference on Earthquake Engineering. Vancouver, Canada, 2004. URL: https://www.iitk.ac.in/nicee/wcee/article/13_203.pdf (visited on Oct. 16, 2022) (See p. 4).

[89] *FEMA P-58-2: Seismic Performance Assessment of Buildings (Volume 2 - Implementation Guide)*. Standard. California: Applied Technology Council, 2018. URL: https://femap58.atcouncil.org/documents/fema-p-58/25-fema-p-58-volume-2-implementation-second-edition/file (visited on Feb. 29, 2024) (See p. 4).

[90] *FEMA P-58-6: Guidelines for Performance-Based Seismic Design of Buildings*. Standard. California: Applied Technology Council, 2018. URL: https://femap58.atcouncil.org/documents/fema-p-58/28-fema-p-58-6-guidelines-for-design/file (visited on Feb. 29, 2024) (See p. 4).

[91] Pritam Hait, Arjun Sil, and Satyabrata Choudhury. "Overview of damage assessment of structures". In: *Current Science* 117.1 (2019), pp. 64–70. ISSN: 00113891. URL: https://www.jstor.org/stable/27138204 (See p. 4).

[92] Martino Zito, Roberto Nascimbene, Paolo Dubini, Danilo D'Angela, and Gennaro Magliulo. "Experimental Seismic Assessment of Nonstructural Elements: Testing Protocols and Novel Perspectives". In: *Buildings* 12.11 (2022), p. 1871. DOI: 10.3390/buildings12111871 (See pp. 4, 5).

[93] Robert Reitherman. "A review of earthquake damage estimation methods". In: *Earthquake Spectra* 1.4 (1985), pp. 805–847. DOI: 10.1193/1.1585293 (See p. 5).

[94] A Kappos, K Stylianidis, and George G Penelis. "Analytical prediction of the response of structures to future earthquakes". In: *European Earthquake Engineering* 1 (1991), pp. 10–21 (See p. 5).

[95] Surya Kumar V Gunturi and Haresh C Shah. "Mapping structural damage to monetary damage". In: *Structural Engineering in Natural Hazards Mitigation*. American Society of Civil Engineers. 1993, pp. 1331–1336 (See p. 5).

[96] AJ Kappos, KC Stylianidis, and CN Michailidis. "A methodology for developing loss scenarios, with an application to the city of Thessaloniki". In: Proceedings of the 11th world conference on earthquake engineering. Acapulco, Mexico, 1996. URL: https://www.iitk.ac.in/nicee/wcee/article/11_2057.PDF (visited on Aug. 14, 2022) (See p. 5).

[97] Russell Blong. "A new damage index". In: *Natural hazards* 30 (2003), pp. 1–23. DOI: 10.1023/A:1025018822429 (See p. 5).

[98] Luís Martins, Vítor Silva, Mário Marques, Helen Crowley, and Raimundo Delgado. "Development and assessment of damage-to-loss models for moment-frame reinforced concrete buildings". In: *Earthquake Engineering & Structural Dynamics* 45.5 (2016), pp. 797–817. DOI: 10.1002/eqe.2687 (See p. 5).

[99] Nathan Mortimore Newmark and Emilio Rosenblueth. "Fundamentals of earthquake engineering". In: *Civil engineering and engineering mechanics series* 12 (1971). URL: https://trid.trb.org/View/1057938 (visited on Jan. 25, 2023) (See pp. 6, 7).

[100] Magdy SL Roufaiel and Christian Meyer. *Nonlinear analysis of reinforced concrete frames for dynamic loading*. Department of Civil Engineering and Engineering Mechanics, Columbia University, New York City, USA, 1981 (See pp. 6, 7).

[101] Edoardo Cosenza, Gaetano Manfredi, and Roberto Ramasco. "The use of damage functionals in earthquake engineering: a comparison between different methods". In: *Earthquake engineering & structural dynamics* 22.10 (1993), pp. 855–868. DOI: 10.1002/eqe.4290221003 (See pp. 6, 7, 11).

[102] Vinay K Gupta, Søren RK Nielsen, and Poul H Kirkegaard. "A preliminary prediction of seismic damage-based degradation in RC structures". In: *Earthquake engineering & structural dynamics* 30.7 (2001), pp. 981–993. DOI: 10.1002/eqe.45 (See pp. 7, 8).

[103] SK Kunnath and C Jenne. "Seismic damage assessment of inelastic RC structures". In: vol. 1. 5th US national conference on earthquake engineering. EERI Chicago, Illinois, 1994, pp. 55–64 (See pp. 6, 7).

[104] Payam Khashaee. "Damage-based seismic design of structures". In: *Earthquake spectra* 21.2 (2005), pp. 371–387. DOI: 10.1193/1.1896366 (See pp. 6, 7).

[105] Julian Carrillo. "Damage index based on stiffness degradation of low-rise RC walls". In: *Earthquake Engineering & Structural Dynamics* 44.6 (2015), pp. 831–848. DOI: 10.1002/eqe.2488 (See pp. 6, 7).

[106] Narendra K Gosain, Russell H Brown, and James O Jirsa. "Shear requirements for load reversals on RC members". In: *Journal of the Structural Division* 103.7 (1977), pp. 1461–1476. DOI: 10.1061/JSDEAG.0004677 (See pp. 7–9).

[107] Hooshang Banon and Daniele Veneziano. "Seismic safety of reinforced concrete members and structures". In: *Earthquake Engineering & Structural Dynamics* 10.2 (1982), pp. 179–193. DOI: 10.1002/eqe.4290100202 (See pp. 7, 8, 10).

[108] Jerry E Stephens and James TP Yao. "Damage assessment using response measurements". In: *Journal of Structural Engineering* 113.4 (1987), pp. 787–801. DOI: 10.1061/(ASCE)0733-9445(1987)113:4(787) (See pp. 7, 8, 11).

[109] Ming-Liang Wang and Surendra P Shah. "Reinforced concrete hysteresis model based on the damage concept". In: *Earthquake Engineering & Structural Dynamics* 15.8 (1987), pp. 993–1003. DOI: 10.1002/eqe.4290150806 (See pp. 7, 9).

[110] Garrett D Jeong and Wilfred D Iwan. "The effect of earthquake duration on the damage of structures". In: *Earthquake engineering & structural dynamics* 16.8 (1988), pp. 1201–1211. URL: https://onlinelibrary.wiley.com/doi/pdf/10.1002/eqe.4290160808 (visited on Mar. 1, 2023) (See pp. 7, 8).

[111] ML Wang and J Wang. "Nonlinear dynamic analysis of reinforced concrete shear wall structures". In: *Soil Dynamics and Earthquake Engineering* 11.5 (1992), pp. 255–268. DOI: 10.1016/0267-7261(92)90042-C (See pp. 7, 9).

[112] Sameh SF Mehanny and Gregory G Deierlein. "Seismic damage and collapse assessment of composite moment frames". In: *Journal of Structural engineering* 127.9 (2001), pp. 1045–1053. DOI: 10.1061/(ASCE)0733-9445(2001)127:9(1045) (See pp. 7, 9).

[113] SL McCabe and WJ Hall. "Assessment of seismic structural damage". In: *Journal of Structural Engineering* 115.9 (1989), pp. 2166–2183. DOI: 10.1061/(ASCE)0733-9445(1989)115:9(2166) (See pp. 7, 9).

[114] Sashi K Kunnath, Ashraf El-Bahy, Andrew W Taylor, and William C Stone. "Cumulative seismic damage of reinforced concrete bridge piers". In: NISTIR 6075. National Institute of Standards and Technology, US Department of Commerce Technology Administration, 1997. URL: https://rosap.ntl.bts.gov/view/dot/40706 (visited on Feb. 19, 2023) (See pp. 7, 9, 20, 21).

[115] Riyadh A Hindi and Robert G Sexsmith. "A proposed damage model for RC bridge columns under cyclic loading". In: *Earthquake Spectra* 17.2 (2001), pp. 261–290. DOI: 10.1193/1.1586175 (See pp. 7, 9).

[116] Tze-How Hwang. "Effects of variation in load history on cyclic response of concrete flexural members". Illinois, USA: University of Illinois at Urbana-Champaign, 1982 (See pp. 7, 9).

[117] Tze-How Hwang and Charles F Scribner. "R/C member cyclic response during various loadings". In: *Journal of Structural Engineering* 110.3 (1984), pp. 477–489. DOI: 10.1061/(ASCE)0733-9445(1984)110:3(477) (See pp. 7, 9).

[118] David Darwin and Charles K Nmai. "Energy dissipation in RC beams under cyclic load". In: *Journal of Structural Engineering* 112.8 (1986), pp. 1829–1846. DOI: 10.1061/(ASCE)0733-9445(1986)112:8(1829) (See pp. 7, 9).

[119] Charles K Nmai and David Darwin. "Lightly reinforced concrete beams under cyclic load". In: *ACI Journal* 83.5 (1986), pp. 777–783. DOI: 10.14359/10672 (See pp. 7, 9).

[120] WB Krätzig, IF Meyer, and K Meskouris. "Damage evolution in reinforced concrete members under cyclic loading". In: *Structural safety and reliability*. American Society of Civil Engineers. 1989, pp. 795–804. URL: https://cedb.asce.org/CEDBsearch/record.jsp?dockey=0064381 (visited on June 16, 2022) (See pp. 7, 9).

[121] Antonella Colombo and Paolo Negro. "A damage index of generalised applicability". In: *Engineering Structures* 27.8 (2005), pp. 1164–1174. DOI: 10.1016/j.engstruct.2005.02.014 (See pp. 7, 10).

[122] Mario E Rodriguez and Daniel Padilla. "A damage index for the seismic analysis of reinforced concrete members". In: *Journal of Earthquake Engineering* 13.3 (2009), pp. 364–383. DOI: 10.1080/13632460802597893 (See pp. 7, 10).

[123] S.S. Prakash and A Belarbi. "Towards damage-based design approach for RC bridge columns under combined loadings using damage index models". In: *Journal of Earthquake Engineering* 14.3 (2010), pp. 363–389. DOI: 10.1080/13632460903214695 (See pp. 7, 9, 12, 13, 20–22).

[124] Sashi K Kunnath, Andrei M Reinhorn, and RF Lobo. "IDARC Version 3.0: A program for the inelastic damage analysis of reinforced concrete structures". In: Technical Report NCEER-92-0022. State University of New York, USA: US National Center for Earthquake Engineering Research, 1992. URL: https://www.buffalo.edu/mceer/catalog.host.html/content/shared/www/mceer/publications/NCEER-92-0022.detail.html (visited on Aug. 21, 2022) (See pp. 7, 11, 12, 17, 19, 64).

[125] Peter Fajfar and Peter Gašperšič. "The N2 method for the seismic damage analysis of RC buildings". In: *Earthquake engineering & structural dynamics* 25.1 (1996), pp. 31–46. DOI: 10.1002/(SICI)1096-9845(199601)25:1<31::AID-EQE534>3.0.CO;2-V (See pp. 7, 12, 13, 19).

[126] Young-Ji Park and Alfredo H-S Ang. "Mechanistic seismic damage model for reinforced concrete". In: *Journal of structural engineering* 111.4 (1985), pp. 722–739. DOI: 10.1061/(ASCE)0733-9445(1985)111:4(722) (See pp. 7, 10).

[127] YH Chai, KM Romstad, and SM Bird. "Energy-based linear damage model for high-intensity seismic loading". In: *Journal of Structural Engineering* 121.5 (1995), pp. 857–864. DOI: 10.1061/(ASCE)0733-9445(1995)121:5(857) (See pp. 7, 11, 12).

[128] Y Bozorgnia and V.V. Bertero. "Damage spectrum and its applications to performance-based earthquake engineering". In: 1497. Proceedings of the 13th World Conference on Earthquake Engineering. Vancouver, Canada, 2004, pp. 1–8. URL: https://www.iitk.ac.in/nicee/wcee/article/13_1497.pdf (visited on Oct. 15, 2022) (See pp. 7, 12, 13).

[129] Djordje Ladjinovic and Radomir Folic. "Application of improved damage index for designing of earthquake resistant structures". In: 2135. Proceedings of the 13th World Conference on Earthquake Engineering. Vancouver, Canada, 2004, pp. 1–15. URL: https://www.iitk.ac.in/nicee/wcee/article/13_2135.pdf (visited on Oct. 15, 2022) (See pp. 7, 12, 13).

[130] Huanjun Jiang, Bo Fu, Xilin Lu, and Linzhi Chen. "Seismic damage assessment of RC members by a modified Park-Ang model". In: *Advances in Structural Engineering* 18.3 (2015), pp. 353–364. DOI: 10.1260/1369-4332.18.3.353 (See pp. 7, 11, 12, 20–22).

[131] Wei Huang, Jiang Qian, and Zhi Zhou. "Seismic damage assessment of steel reinforced concrete members by a modified Park-Ang model". In: *Journal of Asian Architecture and Building Engineering* 15.3 (2016), pp. 605–611. DOI: 10.3130/jaabe.15.605 (See pp. 7, 12, 13, 20–22).

[132] K Nishigaki and K Mizuhata. "Experimental Study on Low-Cycle Fatigue on Reinforced Concrete Columns". In: *Transaction of the Architectural Institute of Japan* (1983) (See pp. 7, 14).

[133] K Mizuhata. "Evaluation of seismic safety for reinforced concrete structures due to low-cycle fatigue". In: *Laboratory of Japanese Architectural Society, Japan* 10.4 (1985) (See pp. 7, 14).

[134] Christian Meyer, Magdy SL Roufaiel, and Serafim G Arzoumanidis. "Analysis of damaged concrete frames for cyclic loads". In: *Earthquake Engineering & Structural Dynamics* 11.2 (1983), pp. 207–228. DOI: 10.1002/eqe.4290110205 (See pp. 7, 18).

[135] Edmondo DiPasquale and AS Cakmak. *On the relation between local and global damage indices*. Vol. 89. 0034. National Center for Earthquake Engineering Research, State University of New York, Buffalo, USA, 1989. URL: https://nehrpsearch.nist.gov/static/files/NSF/PB90173865.pdf (See pp. 7, 19).

[136] Young-Ji Park, A HS Ang, and Yi Kwei Wen. "Damage-limiting aseismic design of buildings". In: *Earthquake spectra* 3.1 (1987), pp. 1–26. DOI: 10.1193/1.1585416 (See pp. 7, 11, 19, 20, 22).

[137] Young Soo Chung, Christian Meyer, and Masanobu Shinozuka. "Automatic seismic design of reinforced concrete building frames". In: *Structural Journal* 87.3 (1990), pp. 326–340. DOI: 10.14359/3115 (See pp. 7, 9, 19).

[138] Sashi K Kunnath, Andrei M Reinhorn, and Young J Park. "Analytical modeling of inelastic seismic response of R/C structures". In: *Journal of Structural Engineering* 116.4 (1990), pp. 996–1017. DOI: 10.1061/(ASCE)0733-9445(1990)116:4(996) (See pp. 7, 19).

[139] Ming L Wang. "Comparison of responses of various nonlinear reinforced concrete models". In: *Soil Dynamics and Earthquake Engineering* 12.7 (1993), pp. 433–444. DOI: 10.1016/0267-7261(93)90006-D (See p. 9).

[140] Tony F Zahrah and William J Hall. "Earthquake energy absorption in SDOF structures". In: *Journal of structural Engineering* 110.8 (1984), pp. 1757–1772. DOI: 10.1061/(ASCE)0733-9445(1984)110:8(1757) (See p. 9).

[141] Santiago Rodríguez-Gómez and AS Cakmak. *Evaluation of seismic damage indices for reinforced concrete structures*. Vol. 90. 0022. National Center for Earthquake Engineering Research, State University of New York, Buffalo, USA, 1990. URL: https://nehrpsearch.nist.gov/static/files/NSF/PB91171322.pdf (visited on June 26, 2022) (See pp. 10, 19).

[142] YJ Park, AM Reinhorn, and SK Kunnath. "Seismic damage analysis of reinforced concrete buildings". In: 9th World Conference on Earthquake Engineering. Tokyo-Kyoto, Japan: International Association for Earthquake Engineering (IAEE), 1988, pp. 211–216. URL: https://www.iitk.ac.in/nicee/wcee/article/9_vol7_211.pdf (visited on Jan. 20, 2022) (See p. 10).

[143] Young-Ji Park, AH-S Ang, and Yi-Kwei Wen. *Seismic damage analysis and damage-limiting design of RC buildings*. Report No. UILU-ENG-84-2007, Department of Civil Engineering, University of Illinois, Urbana, USA, 1984. URL: https://hdl.handle.net/2142/14124 (visited on Feb. 24, 2022) (See p. 10).

[144] Siddhartha Ghosh, Debarati Datta, and Abhinav A Katakdhond. "Estimation of the Park–Ang damage index for planar multi-storey frames using equivalent single-degree systems". In: *Engineering Structures* 33.9 (2011), pp. 2509–2524. DOI: 10.1016/j.engstruct.2011.04.023 (See pp. 10–12).

[145] Enrique Alarcón et al. "A repairability index for reinforced concrete members based on fracture mechanics". In: *Engineering Structures* 23.6 (2001), pp. 687–697. DOI: 10.1016/S0141-0296(00)00075-4 (See p. 11).

[146] Stephen A Mahin and Vitelmo V Bertero. "An evaluation of inelastic seismic design spectra". In: *Journal of the Structural Division* 107.9 (1981), pp. 1777–1795. DOI: 10.1061/JSDEAG.0005782 (See p. 12).

[147] Nicola Bonora. "A nonlinear CDM model for ductile failure". In: *Engineering fracture mechanics* 58.1-2 (1997), pp. 11–28. DOI: 10.1016/S0013-7944(97)00074-X (See p. 13).

[148] MA Sozen. "Review of earthquake response of reinforced concrete buildings with a view to drift control". In: *State-of-the-art in Earthquake Engineering* (1981), pp. 383–418 (See p. 18).

[149] Pritam Hait, Arjun Sil, and Satyabrata Choudhury. "Damage assessment of reinforced concrete-framed building considering multiple demand parameters in Indian codal provisions". In: *Iranian Journal of Science and Technology, Transactions of Civil Engineering* 44 (2020), pp. 121–139. DOI: 10.1007/s40996-020-00380-2 (See p. 18).

[150] AK Pandey, M Biswas, and MM Samman. "Damage detection from changes in curvature mode shapes". In: *Journal of sound and vibration* 145.2 (1991), pp. 321–332. DOI: 10.1016/0022-460X(91)90595-B (See p. 19).

[151] Marc Hill and Tiziana Rossetto. "Comparison of building damage scales and damage descriptions for use in earthquake loss modelling in Europe". In: *Bulletin of Earthquake Engineering* 6 (2008), pp. 335–365. DOI: 10.1007/s10518-007-9057-y (See p. 20).

[152] MP Hill and T Rossetto. "Do existing damage scales meet the needs of seismic loss estimation". In: *Proceedings of the 14th World Conference on Earthquake Engineering*. Vol. 6. 2. Beijing, China, 2008, pp. 335–365. URL: https://www.iitk.ac.in/nicee/wcee/article/14_S01-02-003.PDF (visited on Aug. 3, 2022) (See p. 20).

[153] Alfredo HS Ang, Won Jong Kim, and Sung Bae Kim. "Damage estimation of existing bridge structures". In: *Structural Engineering in natural Hazards mitigation*. American Society of Civil Engineers. 1993, pp. 1137–1142 (See pp. 20, 22).

[154] A Sivasuriyan, D.S. Vijayan, W Górski, Ł Wodzyński, M.D. Vaverková, and E Koda. "Practical implementation of structural health monitoring in multi-story buildings". In: *Buildings* 11.6 (2021), p. 263. DOI: 10.3390/buildings11060263 (See p. 21).

[155] A Sofi, J Jane Regita, Bhagyesh Rane, and Hieng Ho Lau. "Structural health monitoring using wireless smart sensor network–An overview". In: *Mechanical Systems and Signal Processing* 163 (2022), p. 108113. DOI: 10.1016/j.ymssp.2021.108113 (See p. 21).

[156] Erica Lenticchia, Rosario Ceravolo, and Paola Antonaci. "Sensor placement strategies for the seismic monitoring of complex vaulted structures of the modern architectural heritage". In: *Shock and Vibration* 2018 (2018). DOI: 10.1155/2018/3739690 (See p. 21).

[157] Francesco Clementi, Antonio Formisano, Gabriele Milani, and Filippo Ubertini. "Structural health monitoring of architectural heritage: From the past to the future advances". In: *International Journal of Architectural Heritage* 15.1 (2021), pp. 1–4. DOI: 10.1080/15583058.2021.1879499 (See p. 21).

[158] Vinoth Kanna Gopinath and Ravi Ramadoss. "Review on structural health monitoring for restoration of heritage buildings". In: *Materials Today: Proceedings* 43 (2021), pp. 1534–1538. DOI: 10.1016/j.matpr.2020.09.318 (See p. 21).

[159] Atefeh Soleymani, Hashem Jahangir, and Moncef L Nehdi. "Damage detection and monitoring in heritage masonry structures: Systematic review". In: *Construction and Building Materials* 397 (2023), p. 132402. DOI: 10.1016/j.conbuildmat.2023.132402 (See p. 21).

[160] Vladimir Mihailov, Mehmet Celebi, and Kosta Talaganov. "Seismic monitoring of structures-an important element of seismic hazard reduction". In: 0894. Auckland, New Zealand, 2000, pp. 1–8 (See p. 21).

[161] Mehmet Çelebi. "Seismic monitoring of structures and new developments". In: *Earthquakes and health monitoring of civil structures* (2013), pp. 37–84. DOI: 10.1007/978-94-007-5182-8_2 (See p. 21).

[162] Farzad Naeim. "Real-time damage detection and performance evaluation for buildings". In: *Earthquakes and health monitoring of civil structures* (2013), pp. 167–196. DOI: 10.1007/978-94-007-5182-8_7 (See p. 21).

[163] Derek A Skolnik and John W Wallace. "Critical assessment of interstory drift measurements". In: *Journal of structural engineering* 136.12 (2010), pp. 1574–1584. DOI: 10.1061/(ASCE)ST.1943-541X.0000255 (See p. 21).

[164] Gokhan Kilic and Mehmet S Unluturk. "Testing of wind turbine towers using wireless sensor network and accelerometer". In: *Renewable Energy* 75 (2015), pp. 318–325. DOI: 10.1016/j.renene.2014.10.010 (See p. 21).

[165] MJ Chae, HS Yoo, JY Kim, and Moon-Young Cho. "Development of a wireless sensor network system for suspension bridge health monitoring". In: *Automation in Construction* 21 (2012), pp. 237–252. DOI: 10.1016/j.autcon.2011.06.008 (See p. 21).

[166] M Majumder, TK Gangopadhyay, AK Chakraborty, K Dasgupta, and DK Bhattacharya. "Fibre Bragg gratings in structural health monitoring—Present status and applications". In: *Sensors and Actuators A: Physical* 147.1 (2008), pp. 150–164. DOI: 10.1016/j.sna.2008.04.008 (See p. 21).

[167] Paulo Fernando da Costa Antunes et al. "Optical fiber accelerometer system for structural dynamic monitoring". In: *IEEE Sensors Journal* 9.11 (2009), pp. 1347–1354. DOI: 10.1109/JSEN.2009.2026548 (See p. 21).

[168] S Kavitha, R Joseph Daniel, and K Sumangala. "Design and analysis of MEMS comb drive capacitive accelerometer for SHM and seismic applications". In: *Measurement* 93 (2016), pp. 327–339. DOI: 10.1016/j.measurement.2016.07.029 (See p. 22).

[169] Seok Been Im, Stefan Hurlebaus, and Young Jong Kang. "Summary review of GPS technology for structural health monitoring". In: *Journal of Structural Engineering* 139.10 (2013), pp. 1653–1664. DOI: 10.1061/(ASCE)ST.1943-541X.0000475 (See p. 22).

[170] Mosbeh R Kaloop, Emad Elbeltagi, Jong Wan Hu, and Ahmed Elrefai. "Recent advances of structures monitoring and evaluation using GPS-time series monitoring systems: A review". In: *ISPRS International Journal of Geo-Information* 6.12 (2017), p. 382. DOI: 10.3390/ijgi6120382 (See p. 22).

[171] Cemal Ozer Yigit and Eralp Gurlek. "Experimental testing of high-rate GNSS precise point positioning (PPP) method for detecting dynamic vertical displacement response of engineering structures". In: *Geomatics, natural hazards and risk* 8.2 (2017), pp. 893–904. DOI: 10.1080/19475705.2017.1284160 (See p. 22).

[172] Gongkang Fu and Adil G Moosa. "An optical approach to structural displacement measurement and its application". In: *Journal of Engineering Mechanics* 128.5 (2002), pp. 511–520. DOI: 10.1061/(ASCE)0733-9399(2002)128:5(511) (See p. 22).

[173] Jong-Woong Park, Jong-Jae Lee, Hyung-Jo Jung, and Hyun Myung. "Vision-based displacement measurement method for high-rise building structures using partitioning approach". In: *Ndt & E International* 43.7 (2010), pp. 642–647. DOI: 10.1016/j.ndteint.2010.06.009 (See p. 22).

[174] Hyun Myung, Seungmok Lee, and Bumjoo Lee. "Paired structured light for structural health monitoring robot system". In: *Structural Health Monitoring* 10.1 (2011), pp. 49–64. DOI: 10.1177/1475921710365413 (See p. 22).

[175] A Mazen Wahbeh, John P Caffrey, and Sami F Masri. "A vision-based approach for the direct measurement of displacements in vibrating systems". In: *Smart materials and structures* 12.5 (2003), p. 785. DOI: 10.1088/0964-1726/12/5/016 (See p. 22).

[176] Tara C Hutchinson and Falko Kuester. "Monitoring global earthquake-induced demands using vision-based sensors". In: *IEEE Transactions on Instrumentation and Measurement* 53.1 (2004), pp. 31–36. DOI: 10.1109/TIM.2003.821481 (See pp. 22, 23).

[177] Iwao Matsuya et al. "Development of lateral displacement sensor for real-time detection of structural damage". In: *IEEJ transactions on electrical and electronic engineering* 6.3 (2011), pp. 266–272. DOI: 10.1002/tee.20654 (See p. 23).

[178] Iwao Matsuya et al. "Relative-story displacement sensor for measuring five-degree-of-freedom movement of building layers". In: vol. 7981. Sensors, Smart Structures Technologies for Civil, Mechanical, and Aerospace Systems 2011. San Diego, California, USA: SPIE - International Society for Optics and Photonics, 2011, p. 79810C. DOI: 10.1117/12.871138 (See p. 23).

[179] Enbang Li and Jianquan Yao. "Laser-based displacement measurement of a remote object". In: vol. 6344. Advanced Laser Technologies 2005. Tianjin, China: SPIE - International Society for Optics and Photonics, 2006, p. 634431. DOI: 10.1117/12.694434 (See p. 23).

[180] Kiyoshi Kanekawa et al. "An experimental study on relative displacement sensing using phototransistor array for building structures". In: *IEEJ transactions on electrical and electronic engineering* 5.2 (2010), pp. 251–255. DOI: 10.1002/tee.20524 (See p. 23).

[181] Kim D Bennett and Cynthia B Batroney. "Interstory drift monitoring in smart buildings using laser crosshair projection". In: *Optical Engineering* 36.7 (1997), pp. 1889–1892. DOI: 10.1117/1.601396 (See p. 23).

[182] Weimin Chen, Kim D. Bennett, Jun Feng, Yi-Ping Wang, and Shanglian Huang. "Laser technique for measuring three-dimensional interstory drift". In: ed. by S Huang, K.D. Bennett, and D.A. Jackson. Vol. 3555. International Society for Optics and Photonics. SPIE, 1998, pp. 305–310. DOI: 10.1117/12.318209 (See p. 23).

[183] Giovanni Ausanio, AC Barone, C Hison, Vincenzo Iannotti, G Mannara, and Luciano Lanotte. "Magnetoelastic sensor application in civil buildings monitoring". In: *Sensors and Actuators A: Physical* 123 (2005), pp. 290–295. DOI: 10.1016/j.sna.2005.03.027 (See p. 23).

[184] Bengi Aygün and Vehbi Cagri Gungor. "Wireless sensor networks for structure health monitoring: recent advances and future research directions". In: *Sensor Review* 31.3 (2011), pp. 261–276. DOI: 10.1108/02602281111140038 (See p. 23).

[185] XW Ye, YH Su, and JP Han. "Structural health monitoring of civil infrastructure using optical fiber sensing technology: A comprehensive review". In: *The Scientific World Journal* 2014 (2014). DOI: 10.1155/2014/652329 (See p. 23).

[186] Swagato Das and Purnachandra Saha. "A review of some advanced sensors used for health diagnosis of civil engineering structures". In: *Measurement* 129 (2018), pp. 68–90. DOI: 10.1016/j.measurement.2018.07.008 (See p. 23).

[187] Mohammed Abdulkarem, Khairulmizam Samsudin, Fakhrul Zaman Rokhani, and Mohd Fadlee A Rasid. "Wireless sensor network for structural health monitoring: A contemporary review of technologies, challenges, and future direction". In: *Structural Health Monitoring* 19.3 (2020), pp. 693–735. DOI: 10.1177/1475921719854528 (See p. 23).

[188] Jerome P Lynch, Hoon Sohn, and Ming L Wang. *Sensor technologies for civil infrastructures: Volume 1: Sensing hardware and data collection methods for performance assessment*. Second Edition. Woodhead Publishing, 2022. ISBN: 9780081026960. DOI: 10.1016/C2017-0-02662-9 (See p. 23).

[189] Daniel P Abrams. "Influence of axial force variations on flexural behavior of reinforced concrete columns". In: *ACI Structural Journal* 84.3 (1987), pp. 246–254. DOI: 10.14359/2691 (See p. 23).

[190] M Ala Saadeghvaziri and Douglas A Foutch. "Behavior of RC columns under nonproportionally varying axial load". In: *Journal of Structural Engineering* 116.7 (1990), pp. 1835–1856. DOI: 10.1061/(ASCE)0733-9445(1990)116:7(1835) (See p. 23).

[191] Murat Saatcioglu and Guney Ozcebe. "Response of reinforced concrete columns to simulated seismic loading". In: *ACI Structural Journal* 86.1 (1989), pp. 3–12. DOI: 10.14359/2607 (See p. 23).

[192] SN Bousias, G Verzelleti, MN Fardis, and G Magonette. "RC columns in cyclic biaxial bending and axial load". In: *Proceedings of the 10th World Conference on Earthquake Engineering*. Balkema, Rotterdam, 1992, pp. 3041–3046. URL: https://www.iitk.ac.in/nicee/wcee/article/10_vol5_3041.pdf (visited on Aug. 3, 2022) (See p. 23).

[193] Jin-Keun Kim and Sang-Soon Lee. "The behavior of reinforced concrete columns subjected to axial force and biaxial bending". In: *Engineering Structures* 23 (2000), pp. 1518–1528. DOI: 10.1016/S0141-0296(99)00090-5 (See p. 23).

[194] Shuenn-Yih Chang. "Experimental studies of reinforced concrete bridge columns under axial load plus biaxial bending". In: *Journal of Structural Engineering* 136.1 (2009), pp. 12–25. DOI: 10.1061/(ASCE)0733-9445(2010)136:1(12) (See pp. 23, 25, 113).

[195] Umut Akguzel and Stefano Pampanin. "Effects of variation of axial load and bidirectional loading on seismic performance of GFRP retrofitted reinforced concrete exterior beam-column joints". In: *Journal of Composites for Construction* 14.1 (2010), pp. 94–104. DOI: 10.1061/(ASCE)1090-0268(2010)14:1(94) (See p. 23).

[196] Hugo Rodrigues, António Arêde, Humberto Varum, and Aníbal G Costa. "Experimental evaluation of rectangular reinforced concrete column behaviour under biaxial cyclic loading". In: *Earthquake Engineering & Structural Dynamics* 42.2 (2013), pp. 239–259. DOI: 10.1002/eqe.2205 (See p. 23).

[197] H Rodrigues, A Furtado, and A Arêde. "Behavior of rectangular reinforced-concrete columns under biaxial cyclic loading and variable axial loads". In: *Journal of Structural Engineering* 142.1 (2016), p. 04015085. DOI: 10.1061/(ASCE)ST.1943-541X.0001345 (See p. 23).

[198] Hugo Rodrigues, António Arêde, André Furtado, and Patrício Rocha. "Seismic rehabilitation of RC columns under biaxial loading: an experimental characterization". In: *Structures* 3 (2015), pp. 43–56. DOI: 10.1016/j.istruc.2015.03.001 (See p. 23).

[199] Harshad Yadav. "Influence of axial load on low cyclic fatigue behaviour of RC columns". Assam: Department of Civil Engineering, Indian Institute of Technology Guwahati, 2015 (See pp. 23, 29–31, 51, 114).

[200] Giuseppe Campione, Liborio Cavaleri, Fabio Di Trapani, Giuseppe Macaluso, and Gaia Scaduto. "Biaxial deformation and ductility domains for engineered rectangular RC cross-sections: a parametric study highlighting the positive roles of axial load, geometry and materials". In: *Engineering Structures* 107 (2016), pp. 116–134. DOI: 10.1016/j.engstruct.2015.10.030 (See p. 23).

[201] Timothy J Sullivan, Rui Pinho, and Alberto Pavese. *An introduction to structural testing techniques in earthquake engineering*. Report No. ROSE-2004/01, Multimedia Cardano, Pavia, Italy, 2004 (See pp. 23, 25).

[202] Hugo Rodrigues, Humberto Varum, Antonio Arêde, and Aníbal G Costa. "Behaviour of reinforced concrete column under biaxial cyclic loading—state of the art". In: *International Journal of Advanced Structural Engineering* 5.4 (2013), pp. 1–12. URL: https://link.springer.com/article/10.1186/2008-6695-5-4 (visited on Dec. 23, 2022) (See p. 23).

[203] Oya Mercan, James M Ricles, Richard Sause, and Thomas Marullo. "Kinematic transformations for planar multi-directional pseudodynamic testing". In: *Earthquake Engineering & Structural Dynamics* 38.9 (2009), pp. 1093–1119. DOI: 10.1002/eqe.886 (See pp. 25, 113).

[204] Gaston A Fermandois and Billie F Spencer. "Model-based framework for multi-axial real-time hybrid simulation testing". In: *Earthquake Engineering and Engineering Vibration* 16.4 (2017), pp. 671–691. DOI: 10.1007/s11803-017-0407-8 (See p. 25).

[205] Thomas Paulay and MJ Nigel Priestley. *Seismic design of reinforced concrete and masonry buildings*. John Wiley & Sons INC., New York, USA, 1992. ISBN: 9780471549154. DOI: 10.1002/9780470172841 (See p. 33).

[206] *Building Code Requirements for Structural Concrete (ACI 318-14) and Commentary (ACI 318R-14)*. Standard. Farmington Hills: American Concrete Institute. ACI, 2014 (See p. 37).

[207] Dan Earle Branson and Gene Alan Metz. *Instantaneous and time-dependent deflections of simple and continuous reinforced concrete beams*. Department of Civil Engineering and Auburn Research Foundation, Auburn University, 1963. URL: https://rosap.ntl.bts.gov/view/dot/42307 (visited on Oct. 16, 2022) (See p. 37).

[208] *IS 456: Plain and Reinforced concrete – Code of Practice*. Standard. New Delhi: Bureau of Indian Standard, 2005. URL: https://www.services.bis.gov.in/php/BIS_2.0/bisconnect/standard_review/Standard_review/Isdetails?ID=MTEyNDk%3D (visited on Oct. 24, 2022) (See pp. 37, 55, 83).

[209] S. Unnikrishna Pillai and Devdas Menon. *Reinforced concrete design*. Tata McGraw Hill Publishing Company Limited, New Delhi, 1998. ISBN: 9789354601026. URL: https://www.mheducation.co.in/reinforced-concrete-design-9789354601026-india (visited on Mar. 1, 2022) (See p. 37).

[210] Frank McKenna. "OpenSees: a framework for earthquake engineering simulation". In: *Computing in Science & Engineering* 13.4 (2011), pp. 58–66. DOI: 10.1109/MCSE.2011.66 (See pp. 47, 48, 56, 58, 64, 83, 86, 96, 115).

[211] *OpenSees*. 2006. URL: https://opensees.berkeley.edu/ (visited on July 30, 2022) (See pp. 47, 83, 115).

[212] Robert L'Hermite. *Idées actuelles sur la technologie du béton*. La Documentation technique du batiment et des travaux publics, 1955 (See p. 47).

[213] John B Mander, Michael JN Priestley, and R Park. "Theoretical stress-strain model for confined concrete". In: *Journal of structural engineering* 114.8 (1988), pp. 1804–1826. DOI: 10.1061/(ASCE)0733-9445(1988)114:8(1804) (See pp. 47, 58, 86).

[214] GA Chang and John B Mander. "Seismic energy based fatigue damage analysis of bridge columns: Part 1-evaluation of seismic capacity". In: *NCEER Technical Rep. No. NCEER-94-0006, State University of New York, Buffalo* 6 (1994). URL: https://nehrpsearch.nist.gov/article/PB94-219185/XAB (visited on Aug. 21, 2022) (See pp. 47, 58, 86).

[215] M Menengotto. "Method of Analysis for Cyclically Loaded Reinforced Concrete Plane Frames Including Changes in Geometry and Nonelastic Behavior of Elements under Combined Normal Force and Bending". In: *IABSE Symposium on Resistance and Ultimate Deformability of Structures Acted on by Well-Defined Repeated Loads, Final Report, Li.* 1973 (See pp. 47, 56, 83).

[216] FC Filippou, EP Popov, and VV Bertero. "Effects of bond deterioration on hysteretic behavior of reinforced concrete joints". In: *Rep. No. UCB/EERC-83/19, Earthquake Engineering Research Center, University of California Berkeley* (1983). URL: https://nehrpsearch.nist.gov/article/PB84-192020/XAB (visited on Feb. 19, 2023) (See pp. 47, 56, 83).

[217] Filip Filippou and Silvia Mazzoni. *Steel02 Material – Giuffré-Menegotto-Pinto Model with Isotropic Strain Hardening*. 2012. URL: https://opensees.berkeley.edu/wiki/index.php/Steel02_Material_--_Giuffr%C3%A9-Menegotto-Pinto_Model_with_Isotropic_Strain_Hardening (visited on Feb. 15, 2023) (See pp. 48, 56, 58).

[218] Jonathan Waugh and Sri Sritharan. *Concrete07 – Chang & Mander's 1994 Concrete Model*. 2013. URL: https://opensees.berkeley.edu/wiki/index.php/Concrete07_%E2%80%93_Chang_%26_Mander%E2%80%99s_1994_Concrete_Model (visited on Dec. 11, 2022) (See pp. 48, 58, 86).

[219] *Fiber*. 2011. URL: https://opensees.berkeley.edu/wiki/index.php/Fiber (visited on Jan. 8, 2023) (See pp. 48, 58, 86).

[220] Enrico Spacone, Filip C Filippou, and Fabio F Taucer. "Fibre beam–column model for non-linear analysis of R/C frames: Part I. Formulation". In: *Earthquake Engineering & Structural Dynamics* 25.7 (1996), pp. 711–725. DOI: 10.1002/(SICI)1096-9845(199607)25:7<711::AID-EQE576>3.0.CO;2-9. (Visited on Aug. 14, 2022) (See pp. 48, 58, 86).

[221] Remo M de Souza. *Corotational Transformation*. 2014. URL: https://opensees.berkeley.edu/wiki/index.php/Corotational_Transformation (visited on June 29, 2023) (See pp. 48, 86).

[222] Michael H. Scott. *Beam With Hinges Element*. 2014. URL: https://opensees.berkeley.edu/wiki/index.php/Beam_With_Hinges_Element (visited on Feb. 18, 2023) (See pp. 48, 58).

[223] MJN Priestley and R Park. "Strength and ductility of concrete bridge columns under seismic loading". In: *ACI Structural Journal* 84.1 (1987), pp. 61–76. DOI: 10.14359/2800 (See pp. 51, 61, 90).

[224] Asad Esmaeily and Yan Xiao. "Behavior of reinforced concrete columns under variable axial loads: analysis". In: *ACI Structural Journal* 102.5 (2005), pp. 736–744. DOI: 10.14359/14669 (See p. 51).

[225] Ki-Tae Park, Sang-Hyo Kim, Heung-Suk Park, and Kyu-Wan Lee. "The determination of bridge displacement using measured acceleration". In: *Engineering Structures* 27.3 (2005), pp. 371–378. DOI: 10.1016/j.engstruct.2004.10.013 (See p. 54).

[226] Xu Liu, Jian Wang, Jie Zhen, Houzeng Han, and Craig Hancock. "GNSS-aided accelerometer frequency domain integration approach to monitor structural dynamic displacements". In: *International Journal of Image and Data Fusion* 12.4 (2021), pp. 268–281. DOI: 10.1080/19479832.2021.1967468 (See p. 54).

[227] Sanjeev Bhatta and Ji Dang. "Seismic damage prediction of RC buildings using machine learning". In: *Earthquake Engineering & Structural Dynamics* (2023). DOI: 10.1002/eqe.3907 (See pp. 54, 79, 110, 116).

[228] *IS 13920: Ductile design and detailing of reinforced concrete structures subjected to seismic forces - code of practice*. Standard. New Delhi: Bureau of Indian Standard, 2016. URL: https://www.services.bis.gov.in/php/BIS_2.0/bisconnect/standard_review/Standard_review/Isdetails?ID=NTcyNA%3D%3D (visited on Jan. 26, 2023) (See pp. 55, 83).

[229] *IS 875: Code of practice for design loads (other than earthquake) for buildings and structures (Part 1: Dead loads - unit weight of building materials and stored materials)*. Standard. New Delhi: Bureau of Indian Standard, 2008. URL: https://www.services.bis.gov.in/php/BIS_2.0/bisconnect/standard_review/Standard_review/Isdetails?ID=MTU5MzE%3D (visited on Sept. 7, 2022) (See pp. 55, 83).

[230] *IS 875: Code of practice for design loads (other than earthquake) for buildings and structures (Part 2: Imposed loads)*. Standard. New Delhi: Bureau of Indian Standard, 2008. URL: https://www.services.bis.gov.in/php/BIS_2.0/bisconnect/standard_review/Standard_review/Isdetails?ID=MTU5MzI%3D (visited on Nov. 29, 2022) (See pp. 55, 83).

[231] Remo Magalhaes de Souza. *PDelta Transformation*. 2014. URL: https://opensees.berkeley.edu/wiki/index.php/PDelta_Transformation (visited on May 7, 2023) (See p. 58).

[232] Remo Magalhaes de Souza. *Linear Transformation*. 2020. URL: https://opensees.berkeley.edu/wiki/index.php/Linear_Transformation (visited on Dec. 24, 2022) (See pp. 58, 86).

[233] Mihailo Dimitrije Trifunac and A Gerald Brady. "A study on the duration of strong earthquake ground motion". In: *Bulletin of the Seismological Society of America* 65.3 (1975), pp. 581–626. DOI: 10.1785/BSSA0650030581 (See p. 58).

[234] *PEER Ground Motion Database: Pacific Earthquake Engineering Research Center*. 2017. URL: http://ngawest2.berkeley.edu/ (visited on Dec. 22, 2022) (See pp. 58, 86).

[235] Suparno Mukhopadhyay, Sandip Das, and Vinay K Gupta. "Wavelet-based generation of accelerogram-consistent, spectrum-compatible motions: new algorithms and short-period overestimation". In: *Soil Dynamics and Earthquake Engineering* 121 (2019), pp. 327–340. DOI: 10.1016/j.soildyn.2019.02.001 (See p. 58).

[236] Evangelos I Katsanos, Anastasios G Sextos, and George D Manolis. "Selection of earthquake ground motion records: A state-of-the-art review from a structural engineering perspective". In: *Soil dynamics and earthquake engineering* 30.4 (2010), pp. 157–169. DOI: 10.1016/j.soildyn.2009.10.005 (See p. 58).

[237] R Park. "Ductility evaluation from laboratory and analytical testing". In: 9th World Conference on Earthquake Engineering. Tokyo-Kyoto, Japan: International Association for Earthquake Engineering (IAEE), 1988, pp. 605–616. URL: http://www.iitk.ac.in/nicee/wcee/article/9_vol8_605.pdf (visited on Jan. 20, 2022) (See pp. 61, 90).

[238] Michael N Fardis. *Seismic design, assessment and retrofitting of concrete buildings: based on EN-Eurocode 8*. Vol. 8. Springer, Berlin, 2009. ISBN: 978-1-4020-9841-3. DOI: 10.1007/978-1-4020-9842-0 (See pp. 61, 63, 95).

[239] Mario Paz and William Leigh. *Structural dynamics theory and computation*. Kluwer Academic Publishers, Massachusetts, USA, 2004. ISBN: 978-1-4020-7667-1. DOI: 10.1007/978-1-4615-0481-8 (See p. 63).

[240] Douglas C Montgomery and George C Runger. *Applied statistics and probability for engineers*. John Wiley & Sons, 2018. ISBN: 978-1-119-40036-3. URL: https://www.wiley.com/en-us/Applied+Statistics+and+Probability+for+Engineers%2C+7th+Edition-p-9781119400363 (visited on Jan. 12, 2023) (See pp. 68–70, 100, 103).

[241] Ronald E Walpole, Raymond H Myers, Sharon L Myers, and Keying Ye. *Probability and statistics for engineers and scientists*. Pearson, 2012. ISBN: 13: 9780137273546. URL: https://www.pearson.com/en-us/subject-catalog/p/probability--statistics-for-engineers--scientists/P200000007119/9780137273546 (visited on Nov. 29, 2022) (See pp. 70, 103).

[242] A Elenas. "Seismic-parameter-based statistical procedures for the approximate assessment of structural damage". In: *Mathematical Problems in Engineering* 2014 (2014). DOI: 10.1155/2014/916820 (See pp. 72, 104).

[243] Sujith Mangalathu, Seong-Hoon Hwang, Eunsoo Choi, and Jong-Su Jeon. "Rapid seismic damage evaluation of bridge portfolios using machine learning techniques". In: *Engineering Structures* 201 (2019), p. 109785. DOI: 10.1016/j.engstruct.2019.109785 (See pp. 79, 110).

[244] David A Pecknold. "Inelastic structural response to 2D ground motion". In: *journal of the Engineering Mechanics Division* 100.5 (1974), pp. 949–963. DOI: 10.1061/JMCEA3.0001953 (See p. 81).

[245] Toshihiko HISADA, Masamitsu MIYAMURA, Satoshi KAN, and Yasuyuki HIRAO. "Studies on the orthogonal effects in seismic analyses". In: vol. 5. 9th World Conference on Earthquake Engineering. Tokyo-Kyoto, Japan, 1988, pp. 191–196. URL: https://www.iitk.ac.in/nicee/wcee/article/9_vol5_191.pdf (visited on May 4, 2023) (See p. 81).

[246] *Reinforcing Steel Material*. 2022. URL: https://opensees.berkeley.edu/wiki/index.php/Reinforcing_Steel_Material (visited on July 2023) (See pp. 83, 86).

[247] *RigidDiaphragm command*. 2022. URL: https://opensees.berkeley.edu/wiki/index.php/RigidDiaphragm_command (visited on May 22, 2023) (See p. 86).

[248] Michael H. Scott. *Displacement-Based Beam-Column Element*. 2014. URL: https://opensees.berkeley.edu/wiki/index.php/Displacement-Based_Beam-Column_Element (visited on Jan. 23, 2023) (See p. 86).

[249] David M Boore. "Orientation-independent, nongeometric-mean measures of seismic intensity from two horizontal components of motion". In: *Bulletin of the Seismological Society of America* 100.4 (2010), pp. 1830–1835. DOI: 10.1785/0120090400 (See p. 87).

[250] Luis A Montejo. "Response spectral matching of horizontal ground motion components to an orientation-independent spectrum (RotDnn)". In: *Earthquake Spectra* 37.2 (2021), pp. 1127–1144. DOI: 10.1177/8755293020970981 (See p. 87).

[251] Naskar, Subhadip and Das, Sandip. "Bi-directional ground motions: Stochastic simulation and frequency-dependent modal combination rule". In: *Earthquake Engineering & Structural Dynamics* 50.14 (2021), 3872–3893. DOI: https://doi.org/10.1002/eqe.3537 (See p. 89).

[252] Prab Bhatt. *Programming the dynamic analysis of structures*. First Edition. Spon Press, New York, USA, 2002. ISBN: 0-419-15610-0 (See p. 123).

[253] Gene H Golub and Charles F Van Loan. *Matrix computations*. Fourth Edition. The John Hopkins University Press, Baltimore, USA, 2013. ISBN: 9781421407944. DOI: 10.56021/9781421407944 (See p. 123).

Index